UNIVERSITY OF CALIFORNIA
RIVERSIDE

Intermediate and Vacillating Redox in Ancient Marine Settings and their Biological Implications

A Dissertation submitted in partial satisfaction
of the requirements for the degree of

Doctor of Philosophy

in

Geological Sciences

by

Dalton Shane Hardisty

August 2016

Dissertation Committee:
Dr. Timothy W. Lyons, Chairperson
Dr. Gordon D. Love
Dr. Andrey Bekker

The Dissertation of Dalton Shane Hardisty is approved:

_____

_____

_____

Committee Chairperson

University of California, Riverside

ACKNOWLEDGMENTS

The last five years really have been an adventure. A small town Hoosier doesn't usually get the opportunities I've enjoyed, with the pursuit of my interests most limited by my own ability. I have a lot of people to thank for that. This spans from the mentorship, collaboration, and training I've received, to the friends and family who've provided me the support and motivation to pursue my goals and have made it easy along the way. In many cases the distinction between these have blurred, which is what I'm most lucky for.

I want to first thank those I've been lucky enough to call my mentors and friends. Tim, you are the hardest working person I know and I don't think I'm currently capable of grasping the time, energy, resources, and patience you've given me along the way. It's really a debt that you'll never receive full payment for, regardless of what I give back. I'm beyond grateful and respect the hell out of you. Gordon, despite that you are a golf foe, I consider you a close friend and respect you as a gentleman and a scholar. Thanks for everything. Zunli, I seriously couldn't have done this without you. Thanks for keeping me afloat, putting your trust in me with your proxy, and for the good times along the way. Others I consider essential include Noah Planavsky, Steve Bates, Andrey Bekker, Jeremy Owens, and Natascha Riedinger.

The list is long of folks I've gotten to work with and now consider, and even their families in in some cases, close friends. These include Robyn Dahl, Alex and Ashley Zumberge, Chris Reinhard, Lidya Tarhan, Konstantin Choumiline, Bridget Lee, Charles Diamond, Carina Lee, Stephanie Olson, Andy Robinson, Kevin Nguyen, Sarah Simpson, Davy Crockett, and Brett Holdaway. You are each awesome in your own way and it's thanks to you that Riverside has become home to me. Thank you.

Of course the bulk of the thanks goes to my family, particularly my Mom (Dee), Dad (Dale), brother (Dylan), Grandma and Papaw Hardisty, Grandma and Grandpa Orman, and more recently my fiancé (and favorite collaborator) Leanne. I've always been encouraged to pursue what I'm passionate about and you've continually steered me toward the right path, whether I knew it or not. I don't take that for granted. Regardless of what anyone thinks of or gets from this dissertation, it really has been a lot of work and has involved sacrifices along the way too — particularly the experiences I've missed with you. Thank you for your inspiration, understanding, and unwavering support, the bleachers have never been empty. I dedicate this dissertation to you.

ABSTRACT OF THE DISSERTATION

Intermediate and Vacillating Redox in Ancient Marine Settings and their Biological Implications

by

Dalton Shane Hardisty

Doctor of Philosophy, Graduate Program in Geological Sciences
University of California, Riverside, August 2016
Dr. Timothy W. Lyons, Chairperson

The presence of marine oxygen is an essential precursor for faunal habitability, driving distribution in coastal systems today and linked to evolutionary patterns throughout the geologic past. In oxygen-deficient marine systems, the reducing capacity can be defined by the zonation of redox-sensitive elements (e.g. O, I, N, Mn, Fe, S, C), with their availability in the rock record in some cases linked to the water column redox state during deposition and subsequent burial processes. In this dissertation, I reconstruct paleoredox in environments defined by water column oxygen deficiency at biologically critical levels, specifically extreme low oxygen to mildly sulfidic, a redox window most representative of reducing systems today but largely underexplored in the geologic past.

First, I present the initial surface ocean-specific Precambrian redox record, the location and period hosting the emergence of both oxygenic photosynthesis and multicellular life, evaluated through iodine-to-calcium-magnesium ratios in mostly shallow carbonate and supplemented through study of iodine retention during carbonate diagenesis. Oxygen became widespread in shallow marginal marine settings starting in the Paleoproterozoic, likely at levels

necessary to support simple animals. The ensuing Proterozoic record was dynamic, with oxygen fluctuating at and below thresholds similar to waters within and directly overlying modern oxygen minimum zones and largely constrained to shallow settings, a condition particularly exacerbated during the middle Proterozoic. This is a new view of the Precambrian surface ocean and such variability and spatially restricted marine oxygen at critically low levels is hypothesized to explain the delayed emergence of animals until the Neoproterozoic.

A second study defines natural variations in water column redox in the Baltic Sea over the Holocene, the world's largest modern anthropogenically forced and spatially and temporally variable low-oxygen basin. An iron-manganese-molybdenum geochemical approach reveals distinct phases of large-scale anoxia during the Holocene, with the magnitude and frequency of anoxia increasing with increasing distance from the sill, but never beyond mild sulfide accumulation. This work specifically indicates that spatial and temporal variability in Baltic redox appears to have driven both long-term oxygen depletion and restrained the maximum reducing potential over the Holocene.

Table of Contents

List of Figures

List of Tables

INTRODUCTION AND MOTIVATION

The presence and secular evolution of molecular oxygen (O_2) is a first order control on faunal habitation in marine settings. Geologic evidence for eukaryotes and eventually animals does not appear in the rock record until after indications of widespread atmospheric oxidation through the Precambrian (prior to 541 million years ago) (Farquhar and others, 2000; Knoll, 2014; Planavsky and others, 2014b), Phanerozoic (541 million years ago until the present) extinction events are in some cases tied to intervals of widespread marine anoxia (Hallam and Wignall, 1997), and the expansion of relatively low oxygen or anoxic settings from the anthropogenically forced warming and nutrient loading observed today has critical effects on marine fisheries (Diaz and Rosenberg, 2008). The oxygen requirement for the evolutionary onset and sustained presence of eukaryotic complexity in marine systems is a function of the large metabolic energy yield from molecular oxygen relative to other oxidants (Froelich and others, 1979). This energy is essential for the synthesis of proteins and membrane lipids (Summons and others, 2006; Towe, 1970) as well as maintaining large body sizes, motility and intricate food webs (Catling and others, 2005; Sperling and others, 2013). Despite our appreciation of molecular oxygen as a fundamental requirement for multi-cellular life and a growing understanding of the spatiotemporal distribution of oxygen in the atmosphere and oceans through time (Lyons and others, 2014), multiple fundamental open questions concerning their relationship remain — When did oxygenic photosynthesis evolve and can we constrain its onset from the rock record? What is the temporal relationship between oxygen accumulation in the atmosphere and oceans? Did surface ocean oxygen levels accumulate to levels capable of hosting animals precede the earliest fossil records? To what degree are observations of modern human-induced marine oxygen depletion and associated ecological extirpation analogous to natural events and local pre-anthropogenic baselines?

Molecular oxygen is produced as a waste product during oxygenic photosynthesis (simplified in Equation 1), which is the only major source of molecular oxygen and the most significant primary organic carbon source on Earth today. During oxygenic photosynthesis, light provides the initial energy within Photosystem II to strip electrons from chlorophyll. This initiates an electron transport chain that, together with Photosystem I and additional light, generates energy and reductants (ATP and NADPH). The electrons are replenished in Photosystem II when a manganese-based catalytic complex oxidizes a water molecule to produce molecular oxygen. Carbon fixation occurs in a second process known as the Calvin Cycle in which ATP and NADPH from the light reactions provide the energy and reducing capacity to produce carbohydrates (oversimplified as CH_2O) from ambient CO_2.

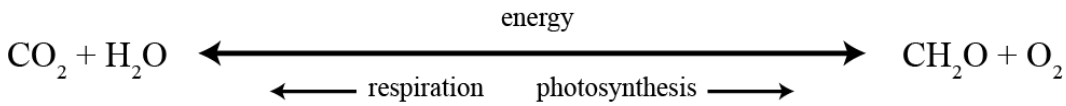

Through a seminal work, Froelich and others (1979) first demonstrated that oxidants are sequentially reduced in the order of the highest to lowest free energy change per mole of organic carbon oxidized (Figure 1). This is referred to as the redox (reduction-oxidation) ladder, and provides constraints on oxygen availability by describing the relative abundance of oxidants with known energetic yields at a given time or location. When oxygen is available, respiration is the most favorable metabolism — yielding nearly an order of magnitude more energy than anaerobic metabolisms — and oxygen abundance in the modern ocean is responsible for the overwhelming majority of organic matter remineralization within the water column. Due to water column respiration, <1% of organic matter actually reaches the sediments.

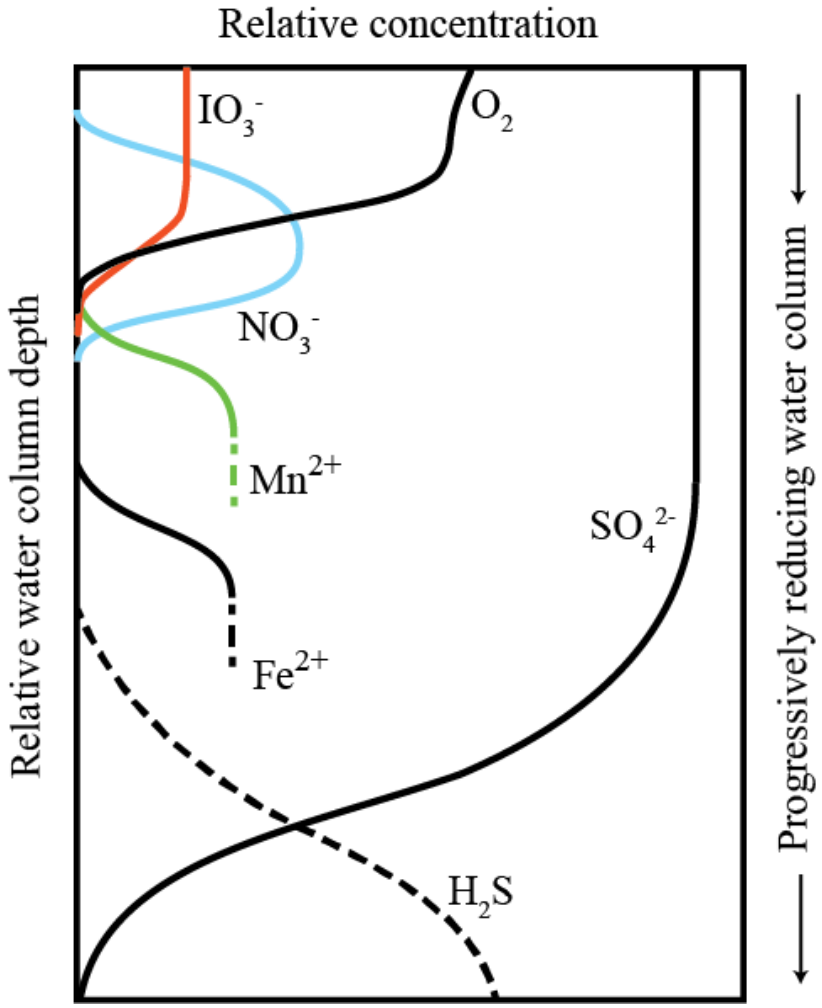

Figure 1. Idealized and simplified vertical water column profile showing the reduction of dissolved oxidants with progressive oxidation of organic matter and associated dissolved reductive products. A similar progression is also observed in marine pore waters. Highlighted species represent elements with active redox cycles while oxygen is present but at low levels. Dashed lines indicate dissolved reductive products that are particularly prone to precipitate from solution.

Initial signs of widespread atmospheric oxygen accumulation appear in the rock record nearly 2.4 billion years ago (Farquhar and others, 2011), and oxygenic photosynthesis perhaps evolved sooner (Planavsky and others, 2014a). The accumulation of molecular oxygen is most strongly dependent on export production of organic carbon from the marine photic zone and net burial in sediments, with other inorganic sources and sinks playing a more minor role (Berner,

1984; Berner and Canfield, 1989; Holland, 1978). This allows for an oxygen surplus as organic carbon produced during primary production escapes respiration, i.e. oxygen consumption through the oxidation of organic matter (Equation 1). Through this intimate link to the carbon cycle, global surface oxygen accumulation through time can be partially traced using the carbon isotopic composition of carbonate in the rock record. Carbonate precipitation captures the isotopic composition of dissolved inorganic carbon in seawater. This provides a means of tracking organic carbon burial as Rubisco, the enzyme that catalyzes the first step of the Calvin Cycle, exerts an isotope fractionation preferential to the lighter carbon isotope (^{12}C) during organic carbon production from carbon dioxide, influencing the carbon isotope composition of dissolved inorganic carbon of seawater. In this way, 'excursions' of carbonate carbon isotope values from steady state most simply reflect periods of net organic carbon burial versus oxidation and hence changes in Earth's oxidation state over time. Net oxygen production over time has resulted in profound impacts on the abiotic and biotic geochemical cycling of a large range of elements, transforming Earth's surface and resulting in oxygen accumulation to ~21% of our atmosphere.

In marine environments characterized by high rates of primary production and-or stratification between the photic zone and underlying waters — such as areas of coastal nutrient upwelling or restricted basins — organic matter respiration may consume water-column oxygen (Figure 1). In these 'oxygen minimum zones' or OMZs, reduction of nitrate, iodate, manganese oxides, and other oxidized chemical species provide pathways for organic matter remineralization and their vertical profiles afford constraints on the extent of local oxygen depletion (Rue and others, 1997). Each of these oxidants require the presence of oxygen for accumulation but also become energetically favorable for reduction while oxygen is still present but at extreme low levels (Clement and others, 2009; Thamdrup and others, 2012), thus showing decreasing concentrations and increases in reductive products both within and at the OMZ boundary (Rue

and others, 1997). The redox conditions of OMZs and seasonally low oxygen coastal basins best reflect the reducing conditions most typical in the modern ocean (Figure 2). In reducing systems characterized by the complete absence of oxygen, the reduction of other oxidants, such as iron oxides or sulfate, will occur (Figure 1). Such conditions are the norm in sedimentary pore fluids and account for the majority of post-depositional or diagenetic remineralization of organic matter. However, the accumulation of their reaction products, dissolved iron (ferruginous) and hydrogen sulfide (euxinic), are not typical in modern marine water columns outside of restricted basins, representing <0.1% of the modern seafloor (Figure 2).

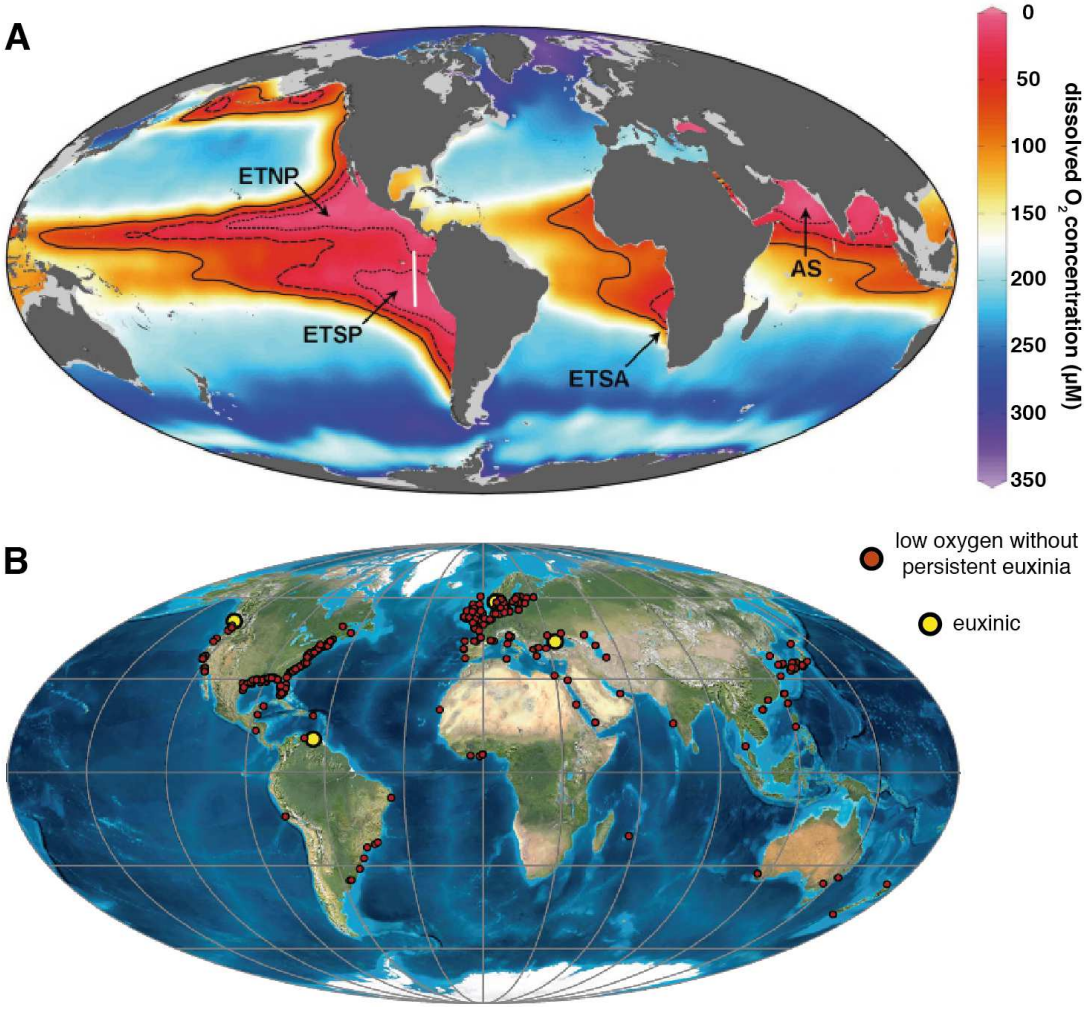

Figure 2. (A) The oxygen concentration (right scale bar in μM) at 300 m water depth throughout the ocean. The four major oxygen minimum zones are labeled: Eastern Tropical North Pacific (ETNP), Eastern Tropical South Pacific (ETSP), Arabian Sea (AS) and Eastern Tropical South Atlantic (ETSA). The plot is taken from the 2008 World Ocean Atlas/Max Planck Institute for Marine Microbiology. (B) Occurrences of coastal low oxygen or anoxic settings not characterized by persistent euxinia or anoxia (red). The majority of these localities represent seasonal low oxygen waters. Also shown are euxinic localities (yellow). Data are taken from Diaz and Rosenberg (Diaz and Rosenberg, 2008) and the map is from the PALEOMAP Project (Scotese, 2008). Part B compilation courtesy of Jeremy Owens.

Oxygen concentrations of ambient waters or atmospheres cannot be directly measured from the geologic past. However, spatiotemporal variations in past oxygen availability can be defined within the context of the redox ladder or from redox sensitive elements (e.g. iron, sulfur,

carbon) or minerals (e.g. pyrite, siderite) that are preserved in the rock record (Figure 3). This requires the calibration of 'paleoredox proxies' relevant to terrestrial or marine sediments in modern well-understood natural sediments, water columns and pore fluids, as well as laboratory experiments. For instance, the initial signs of atmospheric oxygen accumulation in Earth history were first partially constrained by a switch from presence to absence of detrital pyrite and the absence to presence of red beds containing oxidized iron near the Archean-Proterozoic boundary (Farquhar and others, 2011), now termed the Great Oxidation Event or GOE (Figure 3). The levels of atmospheric oxygen increase associated with the GOE were later refined by a switch from the presence to absence of mass independent sulfur isotope fractionations in sedimentary pyrite, which laboratory and modeling efforts indicate requires atmospheric oxygen concentrations <0.001% of present atmospheric levels for expression (Farquhar and others, 2000; Pavlov and Kasting, 2002). More recent work using chromium isotopes (Planavsky and others, 2014b) suggests a second oxidation event later in the Proterozoic (Figure 3). Interestingly, basic models indicate that *in situ* oxygenic photosynthesis could have allowed for local oxygen accumulation in the marine photic zone that is elevated relative to the current constraints on Archean and Proterozoic atmospheres (Kasting, 1992; Olson and others, 2013) as well as that necessary to sustain simple animals (Mills and others, 2014). However, this has not been empirically demonstrated, as no comprehensive record of Precambrian surface ocean redox exists and paleoredox proxies specific to marine oxygen availability versus absence are few. This leaves open the questions of both when oxygenic photosynthesis first evolved relative to the GOE (Farquhar and others, 2011; Kasting, 1992; Olson and others, 2013; Planavsky and others, 2014a) and when surface ocean oxygen reached levels capable of supporting early animals (Fischer, 1965).

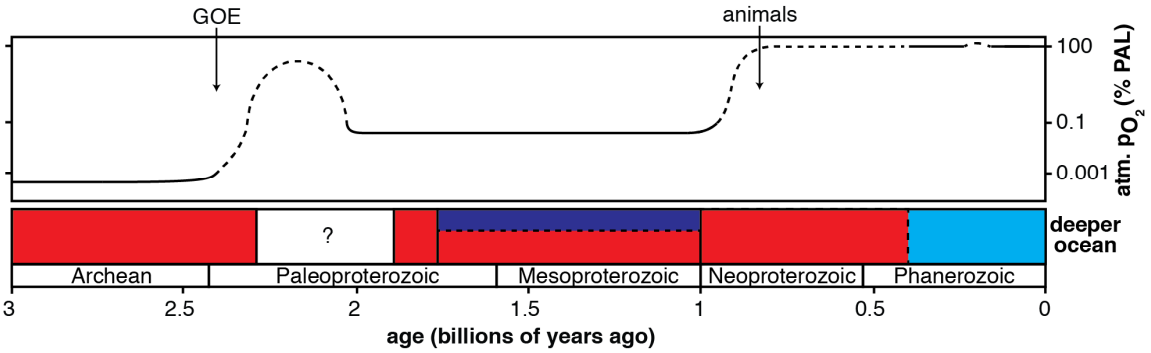

Figure 3. Current constraints on the secular evolution of atmospheric oxygen relative to present atmospheric levels (PAL). Also shown is deep ocean redox, with ferruginous (red), euxinic (purple), and oxygenated (blue) conditions. Dashed lines represent intervals where evidence for redox transitions exist but without quantitative constraints. This figure is largely modeled after Lyons and others (2014) and the decades of research discussed therein. However, the figure is updated to include recent advances, including middle Proterozoic atmospheric oxygen constraints (Planavsky and others, 2014b), combinations of ferruginous and euxinic waters in the middle Proterozoic deeper ocean (Sperling and others, 2015), as well as evidence for deeper ocean anoxia extending into the Paleozoic (Sperling and others, 2015). Details regarding the timing of the Great Oxidation Event (GOE) and the appearance of animals are also shown (Farquhar and others, 2011; Knoll, 2014). The figure does not include evidence for pre-GOE oxygen, which is still debated (Farquhar and others, 2011; Planavsky and others, 2014a). A comprehensive temporal record of surface ocean oxygen accumulation does not currently exist.

Using the modern euxinic Black Sea as an analogue, the most well understood and commonly applied marine paleoredox proxies stem largely from the dynamics of sulfur, carbon, iron, and related geochemical cycles (e.g. molybdenum) as tracers of pyrite formation. These proxies are specific to deeper siliclastic sediments and not the redox conditions of the photic zone. The Black Sea is a restricted basin with a sill forcing seawater input and freshwater output through a single location, resulting in salinity stratification and an environment prone to the development of anoxic, and in this case euxinic, bottom waters (Figure 2). Extensive calibration of proxies specific to euxinic conditions in such basins (Algeo and Lyons, 2006; Canfield and others, 1996; Lyons and Severmann, 2006; Raiswell and Canfield, 1998) have allowed for an ongoing characterization of an anoxic ocean with dissolved iron and sulfide accumulation in the water column for much of Earth history, including the Phanerozoic (Figure 3). Local anoxic conditions are certainly hostile to epifaunal habitation (Rhoads and Morse, 1971) and may have

played a role in limiting the presence-absence of animals throughout the course of biological evolution.

In contrast to the euxinic conditions of the Black Sea, the most common reducing marine environments today are oscillatory reducing basins, transitioning between oxic to anoxic conditions on seasonal or other geological short timescales, and intermediately reducing waters defined by extreme low but present oxygen with active manganese, nitrogen, and iodine redox cycling (Figure 2). This is important, as such systems are reducing enough to have major ecological effects, excluding higher order animals while providing refuge from carnivores to simpler less metabolically demanding and low oxygen-tolerant species (Diaz and Rosenberg, 2008; Sperling and others, 2013). This dissertation is a treatise illuminating that such conditions are difficult to determine with current marine paleoredox proxies and are therefore under characterized in ancient settings. The next step forward in characterizing the co-evolution of marine paleoredox and biology is the calibration and application of proxies specific to constraining the presence opposed to absence of dissolved oxygen from a range of discrete concentrations (e.g. relative to nitrate, iodate, manganese), timescales (e.g. seasonal, inter-annual, permanent), and vertically defined portions of the ocean (e.g. photic zone, marginal marine).

This thesis provides a context for the use of elements sensitive to oxygen variations near the oxic-anoxic threshold — specifically iodine, manganese, and associated elemental cycles — as indicators of redox regimes relevant to faunal habitability. This is done specifically through a focus on: **(1)** the Proterozoic surface ocean, the location and time period hosting the emergence and diversification of the first animals, and; **(2)** a modern basin — the Baltic Sea — with observed redox variations and spatiotemporal heterogeneities representative of that seen most often in modern reducing coastal systems (Figure 2b). The first and second chapters use iodine in carbonate to provide the first comprehensive record of near-surface oxygen availability through

the Proterozoic. To compliment this work, I have also provided a context on modern iodine cycling in carbonate sediments through evaluation of iodine concentrations in carbonate during progressive stages of burial and associated diagenetic carbonate recrystallization. A third chapter outlines an approach for determining the paleo presence of sulfide accumulation in pore fluids, as opposed to the water column, and therefore a means of constraining the relevance of sulfide stress on benthic animals from ancient settings. Finally, the fourth and fifth chapters use sediments from the International Ocean Drilling Program Expedition 347 to provide a detailed baseline for natural variations in oxygen depletion in the Baltic Sea over the course of the Holocene, which are then compared to the current anthropogenic-forced low oxygen Baltic water column. The chapters are presented in journal manuscript form, with the first for *Geology*, second for *Proceedings of the National Academy of Sciences*, third and fourth for *American Journal of Science,* and fifth *Chemical Geology*.

REFERENCES

Algeo, T. J. and Lyons, T. W., 2006, Mo–total organic carbon covariation in modern anoxic marine environments: Implications for analysis of paleoredox and paleohydrographic conditions: Paleoceanography, v. 21, p.

Berner, R. A., 1984, Sedimentary pyrite formation: an update: Geochimica et Cosmochimica Acta, v. 48, p. 605-615.

Berner, R. A. and Canfield, D. E., 1989, A new model for atmospheric oxygen over Phanerozoic time: Am. J. Sci, v. 289, p. 333-361.

Canfield, D. E., Lyons, T. W. and Raiswell, R., 1996, A model for iron deposition to euxinic Black Sea sediments: American Journal of Science, v. 296, p. 818-834.

Catling, D. C., Glein, C. R., Zahnle, K. J. and McKay, C. P., 2005, Why O2 Is Required by Complex Life on Habitable Planets and the Concept of Planetary" Oxygenation Time": Astrobiology, v. 5, p. 415-438.

Clement, B. G., Luther, G. W. and Tebo, B. M., 2009, Rapid, oxygen-dependent microbial Mn (II) oxidation kinetics at sub-micromolar oxygen concentrations in the Black Sea suboxic zone: Geochimica et Cosmochimica Acta, v. 73, p. 1878-1889.

Diaz, R. J. and Rosenberg, R., 2008, Spreading dead zones and consequences for marine ecosystems: Science, v. 321, p. 926-929.

Farquhar, J., Bao, H. and Thiemens, M., 2000, Atmospheric influence of Earth's earliest sulfur cycle: Science, v. 289, p. 756-758.

Farquhar, J., Zerkle, A. L. and Bekker, A., 2011, Geological constraints on the origin of oxygenic photosynthesis: Photosynthesis Research, v. 107, p. 11-36.

Fischer, A. G., 1965, Fossils, early life, and atmospheric history: Proceedings of the National Academy of Sciences, v. 53, p. 1205-1215.

Froelich, P. N., Klinkhammer, G., Bender, M. a. a., Luedtke, N., Heath, G. R., Cullen, D., Dauphin, P., Hammond, D., Hartman, B. and Maynard, V., 1979, Early oxidation of organic matter in pelagic sediments of the eastern equatorial Atlantic: suboxic diagenesis: Geochimica et Cosmochimica Acta, v. 43, p. 1075-1090.

Hallam, A. and Wignall, P. B., 1997, Mass extinctions and their aftermath. Oxford University Press, UK.

Holland, H. D., 1978, The chemistry of the atmosphere and oceans New York, Wiley, v., p. 351.

Kasting, J., 1992, Models relating to Proterozoic atmospheric and ocean chemistry: The Proterozoic Biosphere: A Multidisciplinary Study, v., p. 1185-1187.

Knoll, A. H., 2014, Paleobiological perspectives on early eukaryotic evolution: Cold Spring Harbor perspectives in biology, v. 6, p. a016121.

Lyons, T. W., Reinhard, C. T. and Planavsky, N. J., 2014, The rise of oxygen in Earth/'s early ocean and atmosphere: Nature, v. 506, p. 307-315.

Lyons, T. W. and Severmann, S., 2006, A critical look at iron paleoredox proxies: new insights from modern euxinic marine basins: Geochimica et Cosmochimica Acta, v. 70, p. 5698-5722.

Mills, D. B., Ward, L. M., Jones, C., Sweeten, B., Forth, M., Treusch, A. H. and Canfield, D. E., 2014, Oxygen requirements of the earliest animals: Proceedings of the National Academy of Sciences, v. 111, p. 4168-4172.

Olson, S. L., Kump, L. R. and Kasting, J. F., 2013, Quantifying the areal extent and dissolved oxygen concentrations of Archean oxygen oases: Chemical Geology, v. 362, p. 35-43.

Pavlov, A. and Kasting, J., 2002, Mass-independent fractionation of sulfur isotopes in Archean sediments: strong evidence for an anoxic Archean atmosphere: Astrobiology, v. 2, p. 27-41.

Planavsky, N. J., Asael, D., Hofmann, A., Reinhard, C. T., Lalonde, S. V., Knudsen, A., Wang, X., Ossa, F. O., Pecoits, E. and Smith, A. J., 2014a, Evidence for oxygenic photosynthesis half a billion years before the Great Oxidation Event: Nature Geoscience, v. 7, p. 283-286.

Planavsky, N. J., Reinhard, C. T., Wang, X., Thomson, D., McGoldrick, P., Rainbird, R. H., Johnson, T., Fischer, W. W. and Lyons, T. W., 2014b, Low Mid-Proterozoic atmospheric oxygen levels and the delayed rise of animals: Science, v. 346, p. 635-638.

Raiswell, R. and Canfield, D. E., 1998, Sources of iron for pyrite formation in marine sediments: American Journal of Science, v. 298, p. 219-245.

Rhoads, D. C. and Morse, J. W., 1971, Evolutionary and ecologic significance of oxygen□ deficient marine basins: Lethaia, v. 4, p. 413-428.

Rue, E. L., Smith, G. J., Cutter, G. A. and Bruland, K. W., 1997, The response of trace element redox couples to suboxic conditions in the water column: Deep Sea Research Part I: Oceanographic Research Papers, v. 44, p. 113-134.

Sperling, E. A., Frieder, C. A., Raman, A. V., Girguis, P. R., Levin, L. A. and Knoll, A. H., 2013, Oxygen, ecology, and the Cambrian radiation of animals: Proceedings of the National Academy of Sciences, v. 110, p. 13446-13451.

Sperling, E. A., Wolock, C. J., Morgan, A. S., Gill, B. C., Kunzmann, M., Halverson, G. P., Macdonald, F. A., Knoll, A. H. and Johnston, D. T., 2015, Statistical analysis of iron geochemical data suggests limited late Proterozoic oxygenation: Nature, v. 523, p. 451-454.

Summons, R. E., Bradley, A. S., Jahnke, L. L. and Waldbauer, J. R., 2006, Steroids, triterpenoids and molecular oxygen: Philosophical Transactions of the Royal Society of London B: Biological Sciences, v. 361, p. 951-968.

Thamdrup, B., Dalsgaard, T. and Revsbech, N. P., 2012, Widespread functional anoxia in the oxygen minimum zone of the Eastern South Pacific: Deep Sea Research Part I: Oceanographic Research Papers, v. 65, p. 36-45.

Towe, K. M., 1970, Oxygen-collagen priority and the early metazoan fossil record: Proceedings of the National Academy of Sciences, v. 65, p. 78.

CHAPTER 1

An iodine record of Paleoproterozoic surface ocean oxygenation

ABSTRACT

Constraining oxygen levels in the early Precambrian surface ocean has been a longstanding goal, but efforts have been challenged by the availability of suitable proxies. Here we present a novel approach, iodine geochemistry, which broadens our perspective by providing constraints on shallow, carbonate-dominated marine settings. Iodate (IO_3^-) persists exclusively in oxic waters and is the sole iodine species incorporated into carbonate minerals, allowing iodine-to-calcium ratios (I/Ca) in shallow carbonates to be used as a paleoredox indicator. Our data from a series of Mesoarchean through Paleoproterozoic carbonates deposited under shallow-marine conditions reveal a progressive surface ocean oxygenation in the early Paleoproterozoic. Our data seem to indicate that a largely anoxic surface ocean extended throughout the Archean until the Great Oxidation Event (GOE) at ca. 2.4 billion year ago (Ga), implying that previous inferences of pre-GOE oxygen production may reflect oxygen oases, transient oxidation events, or oxygen levels below those required for IO_3^- production. Our data suggest formation and persistence of IO_3^- and, consequently, surface ocean oxygen concentrations at least 1 μM during the GOE. Following the initial rise of oxygen, carbonate-associated iodine in globally extensive carbonate units deposited during the Lomagundi positive carbon isotope excursion (LE) at ca. 2.22–2.1 Ga suggest a widespread aerobic iodine cycle beyond that before and after the event, synchronous with high relative rates of organic carbon burial and apparent expansion of oxidative conditions.

INTRODUCTION

Measurements of iodine speciation in anoxic basins demonstrate that IO_3^- undergoes complete reduction to iodide (I^-) nearly simultaneously with O_2 depletion (Emerson and others, 1979; Luther III and Campbell, 1991; Wong and Brewer, 1977; Wong and others, 1985). It was recently observed that during calcite precipitation, concentrations of carbonate-associated iodine increase linearly with those of IO_3^- in the precipitating medium, but I^- is completely excluded (Lu

and others, 2010). Coupled with the well-known redox behavior of iodine, its seawater residence time of ~300 kyr (Broecker and others, 1982), and concentrations near 450 nM in the modern ocean, this correlation suggests that I/Ca ratios in carbonates can be used as a robust indicator of the presence or absence of IO_3^-, and hence oxygen, in the water column. Further, post-depositional alteration of carbonates through diagenesis have been shown —if anything—to decrease the original I/Ca ratios (Loope and others, 2013), making post-depositional increases in I/Ca ratios highly unlikely.

Molybdenum and chromium geochemistry, each sensitive to aerobic manganese cycling, suggests mild and/or transient atmospheric oxygenation starting as early as 3.0 Ga (Crowe and others, 2013; Planavsky and others, 2014). Permanent accumulation of appreciable O_2 during the GOE at roughly 2.3 Ga is further inferred from non-mass dependent sulfur isotope (NMD-S) fractionations (Bekker and others, 2004). However, constraints on surface ocean oxidation are limited both before and after the GOE, despite assumptions and mounting evidence that early oxygen was sourced from the marine photic zone following the advent of oxygenic photosynthesis 300–600 million years prior to the GOE (Lyons and others, 2014). Here, we use a novel approach, I/(Ca+Mg) ratios in shallow-water carbonates, to determine the timing of the onset of marine aerobic iodine cycling and construct the first temporal record of early oxygen production specific to the surface ocean.

MATERIALS AND METHODS

I/(Ca+Mg) ratios were measured in 190 samples from 20 carbonate units ranging in age from 3.5 to 1.94 Ga, with a focus on capturing the key periods of the earliest progressive oxygen expansion (Table 1). Magnesium is included to account for dolomitization, as all measured units are dolostones. Carbonates that experienced metamorphic temperatures greater than greenschist facies were not included in this study, since previous work has shown significant iodine loss in

shale at metamorphic temperatures > 400°C (Muramatsu and Hans Wedepohl, 1998). We generated fresh powders from carbonate samples to minimize the effects of weathering and surface contamination. Measurements of I, Ca, and Mg were performed on a quadrupole ICP-MS (Bruker M90) at Syracuse University according to the method of Lu and others, (2010). The precision of I-127 is typically better than 1% and not reported separately for each sample. The standard deviation in counts per second (cps) for three blanks in a row is typically below 300 cps, while the sensitivity for 1 ppb standard is 80,000-120,000 cps. The detection limit for I/(Ca+Mg) is usually better than 0.1 μmol/mol—a value that loosely corresponds to 10 nM IO_3^- based on carbonate precipitation experiments in Lu et al. (2010).

Table 1.1. Carbonates used in this study and plotted in Figure 1.1

Geologic Formation	Age (Ga)	n	% containing iodine
Dresser Fm., Warrawoona Group	ca. 3.5	8	0
Steep Rock Group	2.801-2.757	14	0
Tumbiana Fm., Fortescue Group	2.729-2.719	18	0
Cheshire Fm., Ngezi Group	2.650-2.552	3	0
Wittenoom Fm., Hamersley Group	2.56-2.50	16	0
Campbellrand Subgroup	2.563-2.541	6	0
Tongwane Fm., Chunniespoort Group	2.486-2.32	5	20
Duitschland Fm., Pretoria Group	2.486-2.32	2	0
Espanola Fm., Huronian Supergroup	2.475-2.32	8	0
Carbonates of Turee Creek Group	2.45-2.40	29	28
Gandarela Fm., Minas Supergroup	~2.42	3	0
Gordon Lake Fm., Huronian Supergroup	2.32	9	11
Bad River Dolomite, Chocolay Group	2.32-2.22	2	0
Saunders Fm., Chocolay Group	2.32-2.22	1	0
Cercadinho Fm., Minas Supergroup	~2.22	2	0
Lucknow Fm., Olifantshoek Group	2.15	5	80
Mcheka Fm., Lomagundi Group	2.15	37	95
Lower Albanel Fm., Mistassini Group	2.1	10	80
Aquas Claras Fm., Serra Pelada Sequence	2.1	8	50
Aluminium River Fm., Amer Group	1.95-1.91	4	0

Note: References to ages and data are available in Supplementary 1.2

RESULTS AND DISCUSSION

Archean

All carbonate samples predating ~2.45 Ga record iodine concentrations analytically indistinguishable from blank values (Fig. 1; Table 1), indicating I^- as the dominant inorganic iodine species in the water column. A lack of appreciable IO_3^- accumulation in the Archean shallow-marine carbonates suggests deposition under anoxic conditions. Overall, such a notion agrees well with significant NMD-S isotope signatures in the rock record until ca. 2.4 Ga (Bekker and others, 2004) constraining atmospheric oxygen concentrations to less than 10^{-5} of present atmospheric levels (PAL; Pavlov and Kasting, 2002). Though the sample set predating 2.5 Ga only includes six out of the 20 carbonates measured (Table 1), our work focuses on key units directly leading up to the GOE and some, such as the Tumbiana Formation, used for previous inferences of aerobiosis (Thomazo and others, 2011). Nevertheless, this limited sample scheme leaves open the possibility of surface ocean oxygen production beyond the resolution of our data. Regardless, the I/(Ca+Mg) record does not, at face value, support the idea of widespread, persistent surface ocean oxygen prior to the GOE.

Reservoir control seems unlikely for the lack of carbonate-associated iodine prior to the GOE. Overall, the largest iodine sink in modern oceans is organic matter (OM) burial, particularly marine algae (Lu and others, 2010). Without effective sequestration with marine algae and other organisms, iodine would be more abundant in the ocean as we observe for other hydrophilic halogens such as Br and Cl (Sharp and Draper, 2013). We propose that the absence of advanced marine algae and fewer biological sinks in the Archean would yield a seawater iodine reservoir much larger than today. Considering this, the first appearance of carbonate-associated iodine would be solely dependent on redox conditions allowing for IO_3^- production and accumulation from either I^- or intermediate forms.

For the Neoarchean, initially low I/(Ca+Mg) ratios, as would be expected if IO_3^- accumulated at only trace levels, may have been particularly vulnerable to diagenetic loss, limiting the record of rising I/(Ca+Mg) to intervals of sufficient O_2 production and concomitant IO_3^- accumulation. Similarly, post-GOE carbonates lacking iodine (Table 1) may have been deposited under locally anoxic conditions despite a general rise in surface ocean oxygen availability, but without a more comprehensive geological context, diagenesis cannot yet be ruled out. Further work is needed that specifically addresses IO_3^- incorporation into primary dolomite and its retention during dolomitization of primary calcite. However, retention of primary fabrics in Precambrian dolostones compared to fabric destruction in most Phanerozoic dolostones suggests early dolomite formation in equilibrium with seawater, opposed to late-stage dolomitization replacing primary calcite in reducing pore fluids (Tucker, 1982). Given this, Precambrian dolostones may be well suited to preserve primary seawater trends, analogous to calcites precipitated in Phanerozoic calcite seas (Stanley and Hardie, 1998). Regardless, the observation that I/(Ca+Mg) ratios are all below the detection limit from the carbonates ranging in ages from 3.5 Ga, well before most estimates of initial O_2 production and accumulation, to 2.5 Ga (Table 1) is unlikely solely a relic of local diagenetic loss, arguing against appreciable and persistent iodine redox cycling throughout the Archean within the resolution of our data.

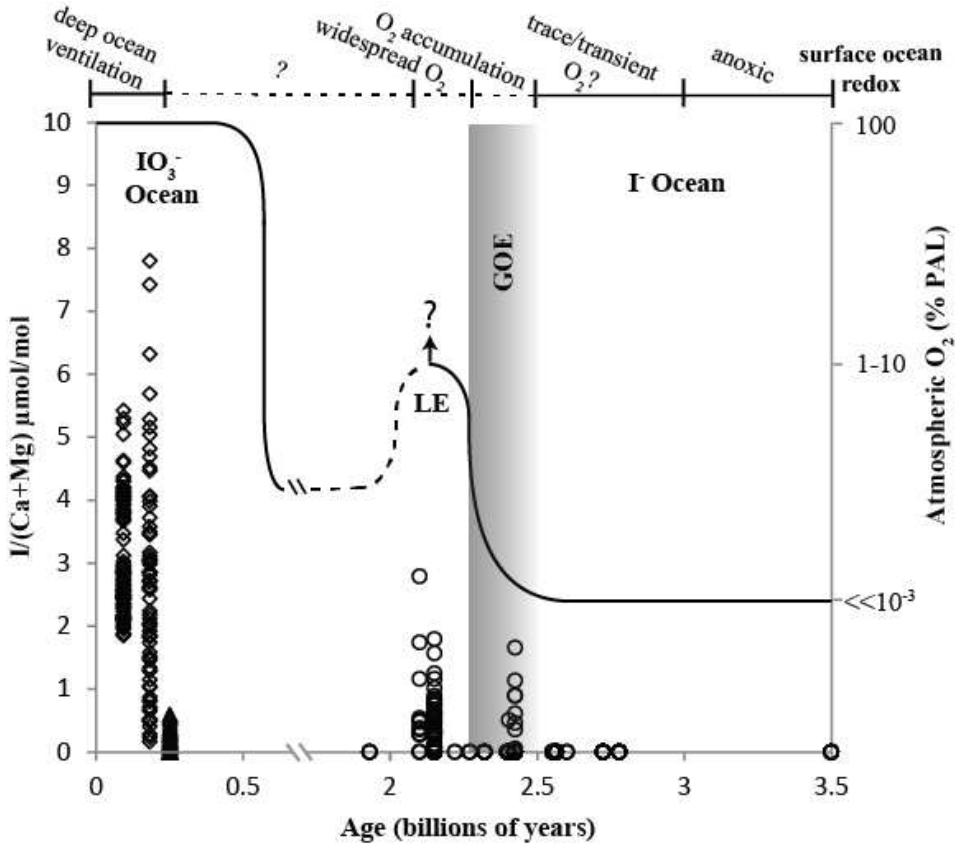

Figure 1. Compilation of all available I/(Ca+Mg) ratios through time. All ages are represented by the midpoint for the ranges presented in Table 1. Data from: Lu et al. 2010 (◇); Loope et al. 2013 (△); this study (○).Values from Lu et al. (2010) do not include Mg concentrations in the ratio as these are for calcites. Oxygen curve generalized from Lyons et al. (2014).

Great Oxidation Event

We find the first convincing evidence for an oxidative marine iodine cycle in the ca. 2.45–2.4 Ga carbonates of the Turee Creek Group of the Hardey and Duck Creek synclines in Western Australia. The studied carbonates in the Hardey Syncline are located above the glacial diamictite of the Meteorite Bore Member (Bekker and others, 2002; Krapez, 1996). The Meteorite Bore Member is correlated to the Ramsay Lake Formation of the Huronian Supergroup, Canada (Swanner and others, 2013), deposited prior to the permanent loss of NMD-S signal at ca. 2.32 Ga (Bekker and others, 2004). An absence of the Meteorite Bore Member in the Duck Creek

Syncline makes the age of these rocks less certain relative to glacial events, but these carbonates are inferred to precede deposition of the Meteorite Bore Member (Krapez, 1996). Though the timing and stratigraphic position of the loss of NMD-S signal in the Turee Creek Group is still unconstrained (Swanner and others, 2013), the correlation to other intervals with multiple sulfur isotope data suggest the potential for aerobic iodine cycling prior to the permanent loss of NMD-S signal. The timing of the increase in I/(Ca+Mg) is generally consistent with increasing enrichments in redox-sensitive trace metals such as Mo and Re in Neoarchean organic-rich shales linked to at least transient oxygen accumulation (Anbar and others, 2007). Surface ocean IO_3^- formation prior to the permanent loss of NMD-S signal could be explained with two scenarios: (1) dissolved O_2 in shallow seawater was sufficiently high, at least locally (perhaps in oxygen oases), for IO_3^- accumulation, while atmospheric O_2 was low enough for continued generation and preservation of the NMD-S signal (Pavlov and Kasting, 2002), or (2) both the atmosphere and surface ocean accumulated significant amounts of O_2, but the NMD-S fractionations found in deposits of this age were inherited from earlier atmospheric conditions through crustal recycling of sulfur (Reinhard and others, 2013). Regardless, the I/(Ca+Mg) record indicates surface ocean IO_3^- formation, implying a switch to more oxidizing surface ocean conditions at 2.45–2.4 Ga, broadly coincident with the beginning of the GOE (Lyons and others, 2014).

Resolving the significance of the observed rise in I/(Ca+Mg) during the GOE demands an understanding of modern iodine cycling. The main controls on $[IO_3^-]$ in surface waters are IO_3^- reduction either microbially or photochemically (Küpper and others, 2011), IO_3^- advection from oxic deep waters, and *in situ* IO_3^- production (Luther III and others, 1995). Independent geochemical evidence suggests a redox-stratified ocean before and after the GOE, with sulfidic anoxic conditions prominent along continental margins and Fe-rich anoxic conditions prevailing in the deeper ocean (Planavsky and others, 2011). A redox-stratified ocean would imply a GOE

iodine cycle conceptually similar to that in the modern Black Sea where advection of iodine from deep waters is in the form of I^- (Luther III and Campbell, 1991; Wong and Brewer, 1977), and with IO_3^- formation and accumulation to ~65 to 100 nM (Luther III and Campbell, 1991; Wong and Brewer, 1977) via oxidation outpacing photochemical and biotic IO_3^- reduction in the surface waters (Truesdale and others, 2001). Oxidation of I^- to IO_3^- is biologically mediated in the modern ocean (Küpper and others, 2011), and oxidants stronger than O_2, such as O_3 and H_2O_2, are considered to be essential to produce IO_3^- abiotically but cannot account for the abundance of IO_3^- in the modern ocean (Luther III and others, 1995). Though the pathways of marine IO_3^- formation are still debated, IO_3^- is exclusively observed in well-oxygenated waters and is completely reduced to I^- with the onset of anoxic conditions (Emerson and others, 1979; Luther III and Campbell, 1991; Wong and Brewer, 1977; Wong and others, 1985). These observations point to O_2 accumulation in the surface ocean and related IO_3^- stabilization as the driver for the first increase in I/(Ca+Mg) ratios during the GOE.

We place a tentative threshold for an aerobic iodine cycle in the surface ocean at 1 μM O_2 during the first rise of I/(Ca+Mg) during the GOE. Observations in the oxygen-minimum zone (OMZ) along the eastern coast of the North Pacific Ocean indicate reduction under oxygen concentrations ranging from ~225 μM near the ocean surface to as low as 1 μM in the core of the OMZ, with IO_3^- quantitatively reduced in the same interval (Rue and others, 1997). Importantly, these oxygen concentrations are not representative of the levels at which IO_3^- could form but rather the minimum at we observe IO_3^- accumulation. Given this threshold of O_2 needed to stabilize IO_3^- in marine systems, the apparent absence of a fully oxic and persistent iodine cycle prior to the GOE does not conflict with other recent evidence for local oxidative processes and oxygenic photosynthesis in the Archean, albeit at still low levels. Recent studies have argued for aerobic N cycling in the surface ocean prior to the GOE (Thomazo and others, 2011) and local

Mn oxidation as early as 3.0 Ga (Crowe and others, 2013; Planavsky and others, 2014), providing early evidence for some surface ocean and even atmospheric O_2 accumulation. The higher pE for IO_3^-/I^- compared to NO_3^-/N_2 and MnO_2/Mn^{+2} (Rue and others, 1997), the generally lower $\Delta G_{rxn}°$ for IO_3^- reduction compared to Mn reduction and denitrification (Farrenkopf and others, 1997), and recent observations indicating modern aerobic Mn and N cycling at O_2 concentrations as low as sub-μM levels (Clement and others, 2009; Thamdrup and others, 2012) allow for the possibility of aerobic N and Mn cycles in the Archean without widespread IO_3^- or O_2 accumulation. In this light, the shallow Archean ocean might have been functionally anoxic, with its redox state lying between that required for coupled nitrification/denitrification and Mn-oxidation and the somewhat higher state required for IO_3^- accumulation. A case consistent with this hypothesis comes from carbonates of the well-preserved 2.7 Ga Tumbiana Fm. analyzed in this study, where previous work using N isotopes has led some workers to infer an aerobic N cycle (Thomazo and others, 2011), yet iodine concentrations are below detection.

Lomagundi Event

The LE spans the ca. 2.22–2.1 Ga period and is marked by the largest and longest-lived positive carbonate carbon isotope ($\delta^{13}C_{carb}$) excursion in Earth history, with $\Delta^{13}C_{carb}$ rising above +10 ‰. This exceptional $\delta^{13}C_{carb}$ trend has traditionally been interpreted to reflect an increase in relative rates of OM production and burial globally, causing the estimated release of 12–22 times the modern atmospheric inventory of O_2 (Karhu and Holland, 1996). Our global record of individual carbonate sections with significant I/(Ca+Mg) ratios deposited during the LE stands in stark contrast to the older data and can be reasonably attributed to a shift to more oxidizing conditions (Table 1; Fig. 1). Other redox proxies, such as marine sulfate evaporites, carbonate-associated sulfate (CAS), and trace metal enrichments recorded in marine sediments indicate increasing atmospheric and marine oxygenation during the same interval when our evidence

points to surface ocean oxygenation (Partin and others, 2013; Planavsky and others, 2012; Schröder and others, 2008).

Starting during the LE, another potential control on I/(Ca+Mg) ratios is the size of the marine iodine reservoir during enhanced OM burial. For example, relatively low I/(Ca+Mg) ratios from carbonate successions deposited during Oceanic Anoxic Events (OAEs), in association with positive $\delta^{13}C_{carb}$ excursions, are interpreted to be the result of a shrinking marine iodine reservoir during the times of enhanced OM burial—in combination with redox shifts and associated IO_3^- reduction (Lu and others, 2010). The Mcheka Fm. shows a negative correlation between $\delta^{13}C$ values and I/(Ca+Mg) ratios during the final stage of the LE (Fig. 2). Similar to the OAE, increasing I/(Ca+Mg) ratios in tandem with a decrease in $\delta^{13}C_{carb}$ could result from an increasing marine iodine reservoir following the decline in OM burial. There is scatter and even blank values within the profile, suggesting currently unconstrained diagenetic controls. Nevertheless, the retention of CAS concentration in the same samples (Planavsky and others, 2012), which is a proxy extremely susceptible to diagenetic loss (Gill and others, 2008), and a lack of correlation between I/(Ca+Mg) and Mg/Ca ratios (Figure DR1) suggest that the overall elevated shift in I/(Ca+Mg) ratios is primary.

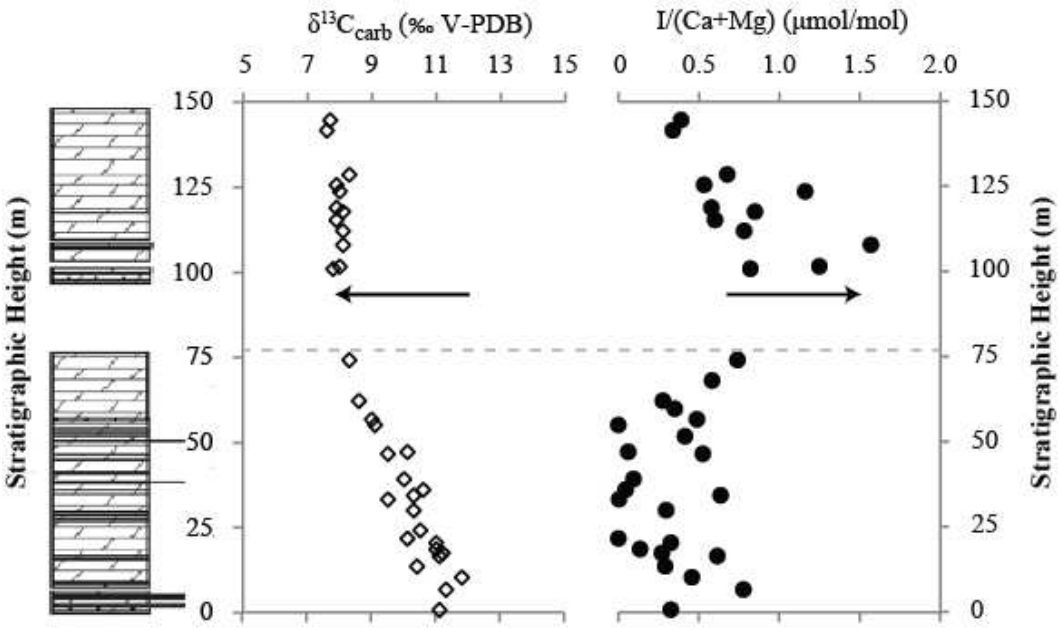

Figure 1.2. $\delta^{13}C_{carb}$ values from Planavsky et al. (2012) and I/(Ca+Mg) ratios from this study for the Mcheka Formation of Zimbabwe (see Table DR2). Note the apparent shift (delineated by arrows) to generally higher I/(Ca+Mg) ratios coincident with the falling limb of the Lomagundi Event. See text for further details.

CONCLUSION

Our results suggest the onset of an oxidative surface ocean iodine cycle during the GOE. Prior to this, redox gradients may have existed in the Archean that allowed for trace and/or transient oxygen levels to support aerobic N and Mn cycles, but the present data suggest an environment dominantly hostile to IO_3^- accumulation and thus one that was mostly anoxic. During the Lomagundi excursion, a general increase in carbonate units with nonzero I/(Ca+Mg) ratios implies widespread IO_3^- stability in the surface ocean related to O_2 concentrations above 1 μM. Although large spatiotemporal gaps still exist for the I/(Ca+Mg) record, our results provide a proof of concept, highlighting the proxy's promise even in very old carbonate rocks with varying degrees of alteration. The importance of this approach is elevated significantly by its relevance to shallow, carbonate-dominated settings, which are not well suited to interrogation by most other paleoredox proxies.

REFERENCES CITED

Anbar, A. D., Duan, Y., Lyons, T. W., Arnold, G. L., Kendall, B., Creaser, R. A., Kaufman, A. J., Gordon, G. W., Scott, C. and Garvin, J., 2007, A whiff of oxygen before the great oxidation event?: Science, v. 317, p. 1903-1906.

Bekker, A., Holland, H., Wang, P.-L., Rumble, D., Stein, H., Hannah, J., Coetzee, L. and Beukes, N., 2004, Dating the rise of atmospheric oxygen: Nature, v. 427, p. 117-120.

Bekker, A., Krapež, B. and Karhu, J., 2002, Preliminary chemostratigraphic data on carbonates from the Paleoproterozoic Turee Creek Supersequence and Wooly Dolomite of Western Australia, 16th Intern: Sed. Congr, v., p. 26-27.

Broecker, W. S., Peng, T.-H. and Beng, Z., 1982, Tracers in the Sea. Lamont-Doherty Geological Observatory, Columbia University.

Clement, B. G., Luther, G. W. and Tebo, B. M., 2009, Rapid, oxygen-dependent microbial Mn (II) oxidation kinetics at sub-micromolar oxygen concentrations in the Black Sea suboxic zone: Geochimica et Cosmochimica Acta, v. 73, p. 1878-1889.

Crowe, S. A., Døssing, L. N., Beukes, N. J., Bau, M., Kruger, S. J., Frei, R. and Canfield, D. E., 2013, Atmospheric oxygenation three billion years ago: Nature, v. 501, p. 535-538.

Emerson, S., Cranston, R. E. and Liss, P. S., 1979, Redox species in a reducing fjord: equilibrium and kinetic considerations: Deep Sea Research Part A. Oceanographic Research Papers, v. 26, p. 859-878.

Farrenkopf, A. M., Dollhopf, M. E., Chadhain, S. N., Luther III, G. W. and Nealson, K. H., 1997, Reduction of iodate in seawater during Arabian Sea shipboard incubations and in laboratory cultures of the marine bacterium< i> Shewanella putrefaciens</i> strain MR-4: Marine Chemistry, v. 57, p. 347-354.

Gill, B. C., Lyons, T. W. and Frank, T. D., 2008, Behavior of carbonate-associated sulfate during meteoric diagenesis and implications for the sulfur isotope paleoproxy: Geochimica et Cosmochimica Acta, v. 72, p. 4699-4711.

Karhu, J. A. and Holland, H. D., 1996, Carbon isotopes and the rise of atmospheric oxygen: Geology, v. 24, p. 867-870.

Krapez, B., 1996, Sequence stratigraphic concepts applied to the identification of basin□filling rhythms in Precambrian successions: Australian Journal of Earth Sciences, v. 43, p. 355-380.

Küpper, F. C., Feiters, M. C., Olofsson, B., Kaiho, T., Yanagida, S., Zimmermann, M. B., Carpenter, L. J., Luther, G. W., Lu, Z. and Jonsson, M., 2011, Commemorating two centuries of iodine research: an interdisciplinary overview of current research: Angewandte Chemie International Edition, v. 50, p. 11598-11620.

Loope, G. R., Kump, L. R. and Arthur, M. A., 2013, Shallow water redox conditions from the Permian–Triassic boundary microbialite: The rare earth element and iodine geochemistry of carbonates from Turkey and South China: Chemical Geology, v. 351, p. 195-208.

Lu, Z., Jenkyns, H. C. and Rickaby, R. E., 2010, Iodine to calcium ratios in marine carbonate as a paleo-redox proxy during oceanic anoxic events: Geology, v. 38, p. 1107-1110.

Luther III, G. W. and Campbell, T., 1991, Iodine speciation in the water column of the Black Sea: Deep Sea Research Part A. Oceanographic Research Papers, v. 38, p. S875-S882.

Luther III, G. W., Wu, J. and Cullen, J. B., 1995, Redox Chemistry of Iodine in Seawater: Frontier Molecular Orbital Theory Considerations: Aquatic chemistry: interfacial and interspecies processes, v. 244, p. 135.

Lyons, T. W., Reinhard, C. T. and Planavsky, N. J., 2014, The rise of oxygen in Earth/'s early ocean and atmosphere: Nature, v. 506, p. 307-315.

Muramatsu, Y. and Hans Wedepohl, K., 1998, The distribution of iodine in the earth's crust: Chemical Geology, v. 147, p. 201-216.

Partin, C., Bekker, A., Planavsky, N., Scott, C., Gill, B., Li, C., Podkovyrov, V., Maslov, A., Konhauser, K. and Lalonde, S., 2013, Large-scale fluctuations in Precambrian atmospheric and oceanic oxygen levels from the record of U in shales: Earth and Planetary Science Letters, v. 369, p. 284-293.

Pavlov, A. and Kasting, J., 2002, Mass-independent fractionation of sulfur isotopes in Archean sediments: strong evidence for an anoxic Archean atmosphere: Astrobiology, v. 2, p. 27-41.

Planavsky, N. J., Asael, D., Hofmann, A., Reinhard, C. T., Lalonde, S. V., Knudsen, A., Wang, X., Ossa, F. O., Pecoits, E. and Smith, A. J., 2014, Evidence for oxygenic photosynthesis half a billion years before the Great Oxidation Event: Nature Geoscience, v. 7, p. 283-286.

Planavsky, N. J., Bekker, A., Hofmann, A., Owens, J. D. and Lyons, T. W., 2012, Sulfur record of rising and falling marine oxygen and sulfate levels during the Lomagundi event: Proceedings of the National Academy of Sciences, v. 109, p. 18300-18305.

Planavsky, N. J., McGoldrick, P., Scott, C. T., Li, C., Reinhard, C. T., Kelly, A. E., Chu, X., Bekker, A., Love, G. D. and Lyons, T. W., 2011, Widespread iron-rich conditions in the mid-Proterozoic ocean: Nature, v. 477, p. 448-451.

Reinhard, C. T., Planavsky, N. J. and Lyons, T. W., 2013, Long-term sedimentary recycling of rare sulphur isotope anomalies: Nature, v. 497, p. 100-103.

Rue, E. L., Smith, G. J., Cutter, G. A. and Bruland, K. W., 1997, The response of trace element redox couples to suboxic conditions in the water column: Deep Sea Research Part I: Oceanographic Research Papers, v. 44, p. 113-134.

Schröder, S., Bekker, A., Beukes, N., Strauss, H. and Van Niekerk, H., 2008, Rise in seawater sulphate concentration associated with the Paleoproterozoic positive carbon isotope

excursion: evidence from sulphate evaporites in the 2.2–2.1 Gyr shallow-marine Lucknow Formation, South Africa: Terra Nova, v. 20, p. 108-117.

Sharp, Z. and Draper, D., 2013, The chlorine abundance of Earth: Implications for a habitable planet: Earth and Planetary Science Letters, v. 369, p. 71-77.

Swanner, E. D., Bekker, A., Pecoits, E., Konhauser, K. O., Cates, N. L. and Mojzsis, S. J., 2013, Geochemistry of pyrite from diamictites of the Boolgeeda Iron Formation, Western Australia with implications for the GOE and Paleoproterozoic ice ages: Chemical Geology, v. 362, p. 131-142.

Thamdrup, B., Dalsgaard, T. and Revsbech, N. P., 2012, Widespread functional anoxia in the oxygen minimum zone of the Eastern South Pacific: Deep Sea Research Part I: Oceanographic Research Papers, v. 65, p. 36-45.

Thomazo, C., Ader, M. and Philippot, P., 2011, Extreme 15N-enrichments in 2.72-Gyr-old sediments: evidence for a turning point in the nitrogen cycle: Geobiology, v. 9, p. 107-120.

Truesdale, V. W., Watts, S. F. and Rendell, A., 2001, On the possibility of iodide oxidation in the near-surface of the Black Sea and its implications to iodine in the general ocean: Deep Sea Research Part I: Oceanographic Research Papers, v. 48, p. 2397-2412.

Tucker, M. E., 1982, Precambrian dolomites: petrographic and isotopic evidence that they differ from Phanerozoic dolomites: Geology, v. 10, p. 7-12.

Wong, G. T. and Brewer, P. G., 1977, The marine chemistry of iodine in anoxic basins: Geochimica et Cosmochimica Acta, v. 41, p. 151-159.

Wong, G. T., Takayanagi, K. and Todd, J. F., 1985, Dissolved iodine in waters overlying and in the Orca Basin, Gulf of Mexico: Marine Chemistry, v. 17, p. 177-183.

SUPPLEMENTAL MATERIALS

Table S1.1. Ages and related references for geologic context for carbonates analyzed in this study.

Stratigraphic unit and location	Age (Ga)	Reference for age estimates
Dresser Fm., Warrawoona Group, Western Australia	ca. 3.500	(Van Kranendonk and others, 2006)
Steep Rock Group, Ontario, Canada	2.801-2.757	(Stone, 2010)
Tumbiana Fm., Fortescue Group, Western Austrailia	2.729-2.719	(Blake and others, 2004)
Cheshire Fm., Ngezi Group, Zimbabwe	2.650-2.552	(Bolhar and others, 2002)
Wittenoom Fm., Hamersley Group, Western Australia	2.59-2.54	(Krapež and others, 2003; Rasmussen and others, 2005)
Campbellrand Subgroup, South Africa	2.563-2.541	(Barton and others, 1994)
Tongwane Fm., Chunniespoort Group, South Africa	2.486-2.368	(Bekker and others, 2001)
Duitschland Fm., Pretoria Group, South Africa	2.486-2.368	(Bekker and others, 2001)
Espanola Fm., Huronian Supergroup, Ontario Canada	2.475-2.32	(Bekker and others, 2005; Rasmussen and others, 2013)
Carbonates of the Turee Creek Group, Western Australia	2.450-2.400	(Bekker and others, 2002; Krapez, 1996; Takehara and others, 2010)
Cercadinho Fm., Minas Supergroup, Brazil	ca. 2.22	(Babinski and others, 1995; Bekker and others, 2003b)
Gandarela Fm., Minas Supergroup, Brazil	ca. 2.42	(Babinski and others, 1995; Bekker and others, 2003b)
Gordon Lake Fm., Huronian Supergroup, Ontario, Canada	2.32	(Bekker and others, 2006; Rasmussen and others, 2013)
Bad River Dolomite, Chocolay Group, Lake Superior, USA	2.32-2.22	(Bekker and others, 2003a)
Saunders Fm., Chocolay Group, Lake Superior, USA	2.32-2.22	(Bekker and others, 2003a)
Lucknow Fm., Olifantshoek Group, South Africa	2.15	(Schröder and others, 2008)
Mcheka Fm., Lomagundi Group, Zimbabwe	2.15	(Master and others, 2010)
Lower Albanel Fm., Mistassini Group, Quebec, Canada	2.10	(Mirota and Veizer, 1994)
Nash Fork Fm., Snowy Pass Supergroup, Wyoming, USA	2.15-2.10	(Bekker and others, 2003a)
Aquas Claras Fm., Serra Pelada Sequence, Brazil	ca. 2.1	(Mougeot and others, 1996)
Aluminium River Fm., Amer Group, Nunavut, Canada	1.95-1.91	(Rainbird and others, 2010)

Table S2.2. Iodine to calcium plus magnesium ratios measured in this study. Sources for geologic context, age, and prior geochemical analysis performed on given samples are displayed in Table DR1. Samples from the Mcheka, Espanola, Lucknow, and Lower Albanel formations are described in Planavsky et al. (2012). Those from the Dresser and Tumbiana formations are from the Pilbara Drilling Project (PDP1; e.g. (Thomazo and others, 2011)). Samples from the Wittenoom Dolomite were taken from the ABDP-9 core from the Hamersley Province of Western Austrailia (e.g., (Reinhard and others, 2009)). Also included below are results from the Nash Fork Formation, which were not included in the compilation in the main text due to higher grade metamorphic alterations.

Geologic Unit	**sample**	**I/(Mg+Ca) (µmol/mol)**
Aluminum River Formation, Amer Group	AB-49	0.00
Aluminum River Formation, Amer Group	AB57	0.00
Aluminum River Formation, Amer Group	AB-48	0.00
Aluminum River Formation, Amer Group	AB-47	0.00
Aquas Claras Fm., Serra Pelada Sequence	F67 300.10	0.54
Aquas Clara Fm., Serra Pelada Sequence	FD-67 314.53	0.28
Aquas Clara Fm., Serra Pelada Sequence	FD-67 303.85	0.51
Aquas Clara Fm., Serra Pelada Sequence	FD-214 142.75	0.39
Aquas Claras Fm., Serra Pelada Sequence	SL-1246 325.95	0.00
Aquas Claras Fm., Serra Pelada Sequence	SL-2286 328.28	0.00
Aquas Claras Fm., Serra Pelada Sequence	SL-1246 305.29	0.00
Aquas Claras Fm., Serra Pelada Sequence	SL-1246 328.37	0.00
Nash Fork Fm., Snowy Pass Supergroup	BM-2	0.05
Nash Fork Fm., Snowy Pass Supergroup	BM-17	0.00
Nash Fork Fm., Snowy Pass Supergroup	BM-4 AB110	0.00
Nash Fork Fm., Snowy Pass Supergroup	BM-7 AB123	0.00
Nash Fork Fm., Snowy Pass Supergroup	BM-3 AB107	0.00
Nash Fork Fm., Snowy Pass Supergroup	BM-14	0.00
Nash Fork Fm., Snowy Pass Supergroup	BM10 AB 11	0.00
Nash Fork Fm., Snowy Pass Supergroup	BM-18	0.00
Nash Fork Fm., Snowy Pass Supergroup	BM-9 AB105	0.00
Nash Fork Fm., Snowy Pass Supergroup	BM-13	0.00
Nash Fork Fm., Snowy Pass Supergroup	BM-12 AB-116	0.00
Nash Fork Fm., Snowy Pass Supergroup	BM-6 AB-112	0.00
Nash Fork Fm., Snowy Pass Supergroup	BM-1 AB113	0.00
Nash Fork Fm., Snowy Pass Supergroup	BM-11 AB106	0.00
Nash Fork Fm., Snowy Pass Supergroup	BM-5 AB117	0.00
Nash Fork Fm., Snowy Pass Supergroup	BM15	0.00
Nash Fork Fm., Snowy Pass Supergroup	BM-16	0.00
Nash Fork Fm., Snowy Pass Supergroup	2000_9/1	0.00

Geologic Unit	sample	I/(Mg+Ca) (µmol/mol)
Nash Fork Fm., Snowy Pass Supergroup	97-9-2	0.00
Lower Albanel Fm., Mistassini Group	LAF-F3	2.79
Lower Albanel Fm., Mistassini Group	UAF-2	0.28
Lower Albanel Fm., Mistassini Group	UAF-1	1.16
Lower Albanel Fm., Mistassini Group	LA-E4	0.36
Lower Albanel Fm., Mistassini Group	LA-D5	0.47
Lower Albanel Fm., Mistassini Group	LAF-D2	0.29
Lower Albanel Fm., Mistassini Group	LAF-C1	1.74
Lower Albanel Fm., Mistassini Group	MI-H-66 AB7	0.00
Lower Albanel Fm., Mistassini Group	MI-13-1 AB4	0.01
Lower Albanel Fm., Mistassini Group	MI-16-2 AB9	0.00
Mcheka Fm., Lomagundi Group	ZA-1	0.33
Mcheka Fm., Lomagundi Group	ZA-4	0.78
Mcheka Fm., Lomagundi Group	ZA-6	0.46
Mcheka Fm., Lomagundi Group	ZA-7	0.29
Mcheka Fm., Lomagundi Group	ZA-8	0.61
Mcheka Fm., Lomagundi Group	ZA-9	0.27
Mcheka Fm., Lomagundi Group	ZA-10	0.13
Mcheka Fm., Lomagundi Group	ZA-11	0.32
Mcheka Fm., Lomagundi Group	ZA-12	0.00
Mcheka Fm., Lomagundi Group	ZA-13	1.65
Mcheka Fm., Lomagundi Group	ZA-16	0.30
Mcheka Fm., Lomagundi Group	ZA-18	0.00
Mcheka Fm., Lomagundi Group	ZA-19	0.63
Mcheka Fm., Lomagundi Group	ZA-20	0.04
Mcheka Fm., Lomagundi Group	ZA-22	0.09
Mcheka Fm., Lomagundi Group	ZA-26	0.53
Mcheka Fm., Lomagundi Group	ZA-27	0.06
Mcheka Fm., Lomagundi Group	ZA 29	0.41
Mcheka Fm., Lomagundi Group	ZA-30	0.00
Mcheka Fm., Lomagundi Group	ZA-31	0.49
Mcheka Fm., Lomagundi Group	ZA 32	0.35
Mcheka Fm., Lomagundi Group	ZA-33	0.28
Mcheka Fm., Lomagundi Group	ZA-35	0.58
Mcheka Fm., Lomagundi Group	ZA-35	0.89
Mcheka Fm., Lomagundi Group	ZA-37	0.74
Mcheka Fm., Lomagundi Group	Z-2	0.82

Geologic Unit	sample	I/(Mg+Ca) (µmol/mol)
Mcheka Fm., Lomagundi Group	Z-3	1.25
Mcheka Fm., Lomagundi Group	Z8	1.57
Mcheka Fm., Lomagundi Group	Z-11	0.78
Mcheka Fm., Lomagundi Group	Z-13	0.60
Mcheka Fm., Lomagundi Group	Z-15	0.85
Mcheka Fm., Lomagundi Group	Z-16	0.58
Mcheka Fm., Lomagundi Group	Z19	1.16
Mcheka Fm., Lomagundi Group	Z-20	0.53
Mcheka Fm., Lomagundi Group	Z-21	0.68
Mcheka Fm., Lomagundi Group	Z-25	0.34
Mcheka Fm., Lomagundi Group	Z-26	0.39
Lucknow Fm., Olifantshoek Group	LK-9 AB38	1.02
Lucknow Fm., Olifantshoek Group	LK-1	0.09
Lucknow Fm., Olifantshoek Group	LK-4	0.47
Lucknow Fm., Olifantshoek Group	AB-41, LK-2	1.79
Lucknow Fm., Olifantshoek Group	LO-3	0.00
Gordon Lake Fm., Huronian Supergroup	PL-4	0.00
Gordon Lake Fm., Huronian Supergroup	PL-5	0.00
Gordon Lake Fm., Huronian Supergroup	JT-98-2	0.00
Gordon Lake Fm., Huronian Supergroup	JT-98-3	0.00
Gordon Lake Fm., Huronian Supergroup	FE-3	0.00
Gordon Lake Fm., Huronian Supergroup	PL-3	0.00
Gordon Lake Fm., Huronian Supergroup	JT-98-1-2	0.00
Gordon Lake Fm., Huronian Supergroup	PL-2	0.00
Gordon Lake Fm., Huronian Supergroup	PL-6	0.00
Bad River Dolomite, Chocolay Group	BD-96-3	0.00
Bad River Dolomite, Chocolay Group	AB147	0.00
Saunders Fm., Chocolay Group	AB158	0.00
Gandarela Fm., Minas Supergroup	GA20/1	0.00
Gandarela Fm., Minas Supergroup	GA-5	0.00
Gandarela Fm., Minas Supergroup	GQ-2	0.00
Cercadinho Fm., Minas Supergroup	CE-20-1	0.00
Cercadinho Fm., Minas Supergroup	CE-20-2	0.00
Carbonates of the Turee Creek Group, Duck Creek Syncline	DC-00-1	0.89
Carbonates of the Turee Creek Group, Duck Creek Syncline	DC-00-2	0.36
Carbonates of the Turee Creek Group, Duck	DC-00-4	0.05

Geologic Unit	sample	I/(Mg+Ca) (µmol/mol)
Creek Syncline		
Carbonates of the Turee Creek Group, Duck Creek Syncline	TC -4/+16 AB 171	0.46
Carbonates of the Turee Creek Group, Duck Creek Syncline	TC-4/+20 AB 164	0.00
Carbonates of the Turee Creek Group, Duck Creek Syncline	TC-3 AB172	0.00
Carbonates of the Turee Creek Group, Duck Creek Syncline	TC-9	0.00
Carbonates of the Turee Creek Group, Duck Creek Syncline	TC 3	0.00
Carbonates of the Turee Creek Group, Duck Creek Syncline	TC 4-4	0.00
Carbonates of the Turee Creek Group, Duck Creek Syncline	TC 6	0.00
Carbonates of the Turee Creek Group, Hardey Syncline	HS-2 AB-169	0.00
Carbonates of the Turee Creek Group, Hardey Syncline	HS-7 AB 170	1.66
Carbonates of the Turee Creek Group, Hardey Syncline	HS-9 AB-167	0.61
Carbonates of the Turee Creek Group, Hardey Syncline	TC-2	0.00
Carbonates of the Turee Creek Group, Hardey Syncline	HS-1	0.00
Carbonates of the Turee Creek Group, Hardey Syncline	TC-1	0.00
Carbonates of the Turee Creek Group, Hardey Syncline	TC-10	0.00
Carbonates of the Turee Creek Group, Hardey Syncline	TC-5	0.00
Carbonates of the Turee Creek Group, Duck Creek Syncline	DC-00-3	0.00
Carbonates of the Turee Creek Group, Hardey Syncline	HS-6	0.00
Carbonates of the Turee Creek Group, Hardey Syncline	TC-8	0.00
Carbonates of the Turee Creek Group, Hardey Syncline	TC-11	0.00
Carbonates of the Turee Creek Group, Hardey Syncline	TC-4	0.00
Carbonates of the Turee Creek Group, Hardey Syncline	HS-4	0.00
Carbonates of the Turee Creek Group, Hardey Syncline	HS-8	0.00

Geologic Unit	sample	I/(Mg+Ca) (µmol/mol)
Carbonates of the Turee Creek Group, Hardey Syncline	TC-7	0.00
Carbonates of the Turee Creek Group, Hardey Syncline	HS-3	0.00
Carbonates of the Turee Creek Group, Hardey Syncline	HS-10	0.00
Carbonates of the Turee Creek Group, Hardey Syncline	HS-5	0.00
Duitschland Fm., Pretoria Group	BH2-8.2	0.00
Duitschland Fm., Pretoria Group	BH2-9.5	0.00
Tongwane Fm., Chunniespoort Group	TON-3	0.00
Tongwane Fm., Chunniespoort Group	TON-2	0.00
Tongwane Fm., Chunniespoort Group	TON-6	0.00
Tongwane Fm., Chunniespoort Group	AB-123	0.00
Tongwane Fm., Chunniespoort Group	AB-126 TON-5	0.51
Espanola Formation, Huronian Supergroup	El-2	0.00
Espanola Formation, Huronian Supergroup	El-4	0.00
Espanola Formation, Huronian Supergroup	EL35A	0.00
Espanola Formation, Huronian Supergroup	EL-56	0.00
Espanola Formation, Huronian Supergroup	EL-1	0.00
Espanola Formation, Huronian Supergroup	EL-13	0.00
Espanola Formation, Huronian Supergroup	EL-18	0.00
Espanola Formation, Huronian Supergroup	AB31	0.00
Wittenoom Fm., Hamersley Group	abdp-9 330.29	0.00
Wittenoom Fm., Hamersley Group	abdp-9 331.98	0.00
Wittenoom Fm., Hamersley Group	abdp-9 332.61	0.00
Wittenoom Fm., Hamersley Group	adbp-9 418.33	0.00
Wittenoom Fm., Hamersley Group	adbp-9 421.7	0.00
Wittenoom Fm., Hamersley Group	adbp-9 423.31	0.00
Wittenoom Fm., Hamersley Group	adbp-9 427.58	0.00
Wittenoom Fm., Hamersley Group	adbp-9 429.27	0.00
Wittenoom Fm., Hamersley Group	adbp-9 432.36	0.00
Wittenoom Fm., Hamersley Group	adbp-9 435.3	0.00
Wittenoom Fm., Hamersley Group	adbp-9 439.54	0.00
Wittenoom Fm., Hamersley Group	adbp-9 442.48	0.00
Wittenoom Fm., Hamersley Group	adbp-9 446.21	0.00
Wittenoom Fm., Hamersley Group	adbp-9 449.4	0.00
Wittenoom Fm., Hamersley Group	adbp-9 451.1	0.00
Wittenoom Fm., Hamersley Group	adbp-9 453.3	0.00

Geologic Unit	sample	I/(Mg+Ca) (µmol/mol)
Campbellrand Subgroup	CR-1	0.00
Campbellrand Subgroup	CR-2	0.00
Campbellrand Subgroup	CR-3	0.00
Campbellrand Subgroup	CR-4	0.00
Campbellrand Subgroup	CR-5	0.00
Campbellrand Subgroup	CR-6	0.00
Cheshire Fm., Ngezi Group	CH-1	0.00
Cheshire Fm., Ngezi Group	CF-16	0.00
Cheshire Fm., Ngezi Group	Cheshire	0.00
Tumbiana Fm., Fortescue Group	P1 37.4	0.00
Tumbiana Fm., Fortescue Group	P1 44.5	0.00
Tumbiana Fm., Fortescue Group	P1 47.0A	0.00
Tumbiana Fm., Fortescue Group	P1 68	0.00
Tumbiana Fm., Fortescue Group	P1 69.2	0.00
Tumbiana Fm., Fortescue Group	P1 70.4C	0.00
Tumbiana Fm., Fortescue Group	P1 72.4	0.00
Tumbiana Fm., Fortescue Group	P1 73.5	0.00
Tumbiana Fm., Fortescue Group	P1 75.1	0.00
Tumbiana Fm., Fortescue Group	P1 77.1	0.00
Tumbiana Fm., Fortescue Group	P1 80.6A	0.00
Tumbiana Fm., Fortescue Group	P1 83.2B	0.00
Tumbiana Fm., Fortescue Group	P1 84.8	0.00
Tumbiana Fm., Fortescue Group	P1 85.7B	0.00
Tumbiana Fm., Fortescue Group	P1 87.5	0.00
Tumbiana Fm., Fortescue Group	P1 88.2	0.00
Tumbiana Fm., Fortescue Group	P1 89.5	0.00
Tumbiana Fm., Fortescue Group	P1 90.4	0.00
Steep Rock Group	SR S4-1	0.00
Steep Rock Group	SR-3	0.00
Steep Rock Group	SMALL STREAM SR7	0.00
Steep Rock Group	SMALL STREAM SR-4	0.00
Steep Rock Group	STEEP ROCK STOP 4	0.00
Steep Rock Group	SR-54	0.00
Steep Rock Group	STOP 1	0.00
Steep Rock Group	SR-56	0.00

Geologic Unit	sample	I/(Mg+Ca) (µmol/mol)
Steep Rock Group	SR10-2	0.00
Steep Rock Group	SR10 SMALL STREAM	0.00
Steep Rock Group	Steep Rock	0.00
Steep Rock Group	SR 10-1	0.00
Steep Rock Group	SR 11	0.00
Steep Rock Group	SR 11-2	0.00
Dresser Fm., Warrawoona Group	P2c-92.9	0.00
Dresser Fm., Warrawoona Group	P2c-93.45	0.00
Dresser Fm., Warrawoona Group	P2c-93.5a BC	0.00
Dresser Fm., Warrawoona Group	P2c-94.1	0.00
Dresser Fm., Warrawoona Group	P2c-94.2	0.00
Dresser Fm., Warrawoona Group	P2c-95.5a ba	0.00
Dresser Fm., Warrawoona Group	P2b-84.6a	0.00
Dresser Fm., Warrawoona Group	P2b-87.39b	0.00

Turee Creek

The presence of high I/(Ca+Mg) ratios in carbonates of the Turee Creek Group in the Duck Creek Syncline presents an interesting and a special case where high iodine concentrations could be linked to post-depositional processes rather than to oxygen accumulation and IO_3^- formation in the water column during primary carbonate precipitation. The carbonate unit expressing significantly higher than blank I/(Ca+Mg) ratios are directly below an uncomformity with a paleosol developed at 2.1-2.0 Ga. A combination of this stratigraphic position and carbonate carbon isotope values near -5 ‰ in the carbonate unit (Table DR3) point to the potential for subaerial exposure of the carbonate and caliche formation after the GOE and LE, when higher atmospheric oxygen concentrations during the period of subaerial exposure could have allowed for IO_3^- formation in meteoric fluids. This would permit IO_3^- incorporation into carbonate during meteoric alteration of carbonate leading to caliche development. The concentrations of total iodine in modern meteoric fluids are low (< 0.02 μmol; (Truesdalea and Jones, 1996)) and approach the detection limit for I/(Ca+Mg) (see main text), but the slightly acidic pH values of meteoric fluids and groundwaters allow the possibility of I^- oxidation to IO_3^- mediated by Mn-oxides (Fox and others, 2009). Regardless of this uncertainty, stratigraphic position and carbon and oxygen isotope values from iodine-containing carbonates of the Turee Creek Group in the Hardey Syncline provide an additional support for an aerobic iodine cycle in the aftermath of the oldest Paleoproterozoic glaciation.

Table S1.3. Carbon and oxygen isotope values for the Turee Creek Group carbonates that contain iodine.

Sample	Syncline	$\delta^{13}C_{carb}$	$\delta^{18}O_{carb}$
DC-00-1	Duck Creek	-5.16	-5.48
DC-00-2	Duck Creek	-5.62	-5.5
DC-00-3	Duck Creek	-5.1	-6.19
DC-00-4	Duck Creek	-5.9	-5.9
TC-4/+16	Duck Creek	1.8	-10.0
HS-2	Hardey	0.8	-15.6
HS-7	Hardey	0.1	-8.9
HS-9	Hardey	0.9	-7.6

Mcheka Formation

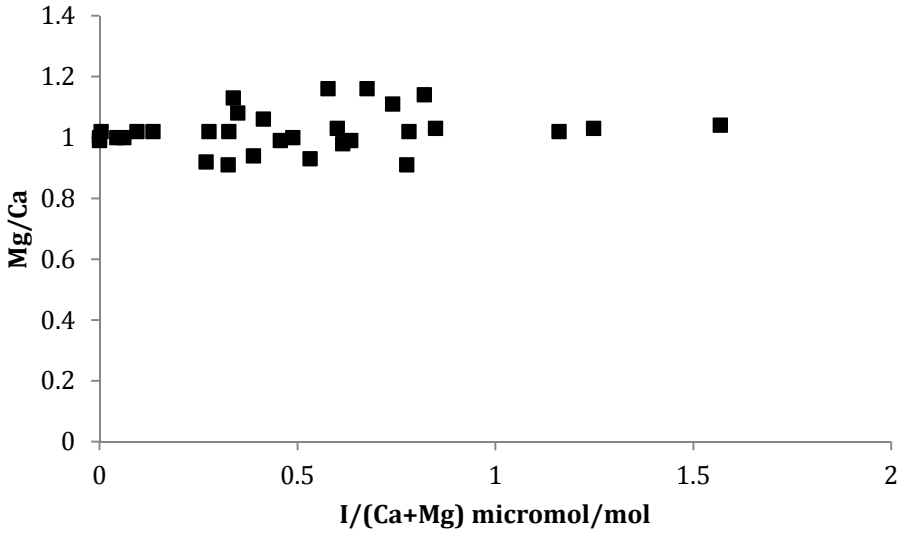

Figure S1.1. Mg/Ca versus I/(Ca+Mg) ratios in the Mcheka Formation carbonate show little variation in the degree of dolomitization. From this we expect no significant partial shift in I/(Ca+Mg) ratios related to dolomitization.

SUPPLEMENTARY REFERENCES

Babinski, M., Chemale, F. and Van Schmus, W. R., 1995, The PB/PB age of the minas supergroup carbonate rocks, quadrilatero FERRIFERO, BRAZIL: Precambrian Research, v. 72, p. 235-245.

Barton, E., Altermann, W., Williams, I. and Smith, C., 1994, U-Pb zircon age for a tuff in the Campbell Group, Griqualand West Sequence, South Africa: implications for Early Proterozoic rock accumulation rates: Geology, v. 22, p. 343-346.

Bekker, A., Karhu, J., Eriksson, K. and Kaufman, A., 2003a, Chemostratigraphy of Paleoproterozoic carbonate successions of the Wyoming Craton: tectonic forcing of biogeochemical change?: Precambrian Research, v. 120, p. 279-325.

Bekker, A., Karhu, J. and Kaufman, A., 2006, Carbon isotope record for the onset of the Lomagundi carbon isotope excursion in the Great Lakes area, North America: Precambrian Research, v. 148, p. 145-180.

Bekker, A., Kaufman, A., Karhu, J. and Eriksson, K., 2005, Evidence for Paleoproterozoic cap carbonates in North America: Precambrian Research, v. 137, p. 167-206.

Bekker, A., Kaufman, A. J., Karhu, J. A., Beukes, N. J., Swart, Q. D., Coetzee, L. L. and Eriksson, K. A., 2001, Chemostratigraphy of the Paleoproterozoic Duitschland Formation, South Africa: implications for coupled climate change and carbon cycling: American Journal of Science, v. 301, p. 261-285.

Bekker, A., Krapež, B. and Karhu, J., 2002, Preliminary chemostratigraphic data on carbonates from the Paleoproterozoic Turee Creek Supersequence and Wooly Dolomite of Western Australia, 16th Intern: Sed. Congr, v., p. 26-27.

Bekker, A., Sial, A., Karhu, J., Ferreira, V., Noce, C., Kaufman, A., Romano, A. and Pimentel, M., 2003b, Chemostratigraphy of carbonates from the Minas Supergroup, Quadrilátero Ferryífero (Iron Quadrangle), Brazil: A stratigraphic record of early proterozoic atmospheric, biogeochemical and climactic change: American Journal of Science, v. 303, p. 865-904.

Blake, T., Buick, R., Brown, S. and Barley, M., 2004, Geochronology of a Late Archaean flood basalt province in the Pilbara Craton, Australia: constraints on basin evolution, volcanic and sedimentary accumulation, and continental drift rates: Precambrian Research, v. 133, p. 143-173.

Bolhar, R., Hofmann, A., Woodhead, J., Hergt, J. and Dirks, P., 2002, Pb-and Nd-isotope systematics of stromatolitic limestones from the 2.7 Ga Ngezi Group of the Belingwe Greenstone Belt: constraints on timing of deposition and provenance: Precambrian Research, v. 114, p. 277-294.

Fox, P. M., Davis, J. A. and Luther, G. W., 2009, The kinetics of iodide oxidation by the manganese oxide mineral birnessite: Geochimica et Cosmochimica Acta, v. 73, p. 2850-2861.

Krapez, B., 1996, Sequence stratigraphic concepts applied to the identification of basin□filling rhythms in Precambrian successions: Australian Journal of Earth Sciences, v. 43, p. 355-380.

Krapež, B., Barley, M. E. and Pickard, A. L., 2003, Hydrothermal and resedimented origins of the precursor sediments to banded iron formation: sedimentological evidence from the Early Palaeoproterozoic Brockman Supersequence of Western Australia: Sedimentology, v. 50, p. 979-1011.

Master, S., Bekker, A. and Hofmann, A., 2010, A review of the stratigraphy and geological setting of the Palaeoproterozoic Magondi Supergroup, Zimbabwe–Type locality for the Lomagundi carbon isotope excursion: Precambrian Research, v. 182, p. 254-273.

Mirota, M. D. and Veizer, J., 1994, Geochemistry of precambrian carbonates: VI. Aphebian albanel formations, Quebec, Canada: Geochimica et Cosmochimica Acta, v. 58, p. 1735-1745.

Mougeot, R., Respaut, J., Briqueu, L., Ledru, P., Milesi, J., Lerouge, C., Marcoux, E., Huhn, S. and Macambira, M. (1996) Isotope geochemistry constraints for Cu, Au mineralizations and evolution of the Carajás Province (Para, Brazil), Congresso Brasileiro de Geologia, pp. 321-324.

Rainbird, R., Davis, W., Pehrsson, S., Wodicka, N., Rayner, N. and Skulski, T., 2010, Early Paleoproterozoic supracrustal assemblages of the Rae domain, Nunavut, Canada: intracratonic basin development during supercontinent break-up and assembly: Precambrian Research, v. 181, p. 167-186.

Rasmussen, B., Bekker, A. and Fletcher, I. R., 2013, Correlation of Paleoproterozoic glaciations based on U–Pb zircon ages for tuff beds in the Transvaal and Huronian Supergroups: Earth and Planetary Science Letters, v. 382, p. 173-180.

Rasmussen, B., Blake, T. S. and Fletcher, I. R., 2005, U-Pb zircon age constraints on the Hamersley spherule beds: Evidence for a single 2.63 Ga Jeerinah-Carawine impact ejecta layer: Geology, v. 33, p. 725-728.

Reinhard, C. T., Raiswell, R., Scott, C., Anbar, A. D. and Lyons, T. W., 2009, A late Archean sulfidic sea stimulated by early oxidative weathering of the continents: Science, v. 326, p. 713-716.

Schröder, S., Bekker, A., Beukes, N., Strauss, H. and Van Niekerk, H., 2008, Rise in seawater sulphate concentration associated with the Paleoproterozoic positive carbon isotope excursion: evidence from sulphate evaporites in the 2.2–2.1 Gyr shallow marine Lucknow Formation, South Africa: Terra Nova, v. 20, p. 108-117.

Stone, D., 2010, Precambrian geology of the central Wabigoon Subprovince area, northwestern Ontario. Ontario Geological Survey.

Takehara, M., Komure, M., Kiyokawa, S., Horie, K. and Yokoyama, K. (2010) Detrital zircon SHRIMP U–Pb age of 2.3 Ga diamictites of the Meteorite Bore Member in the south Pilbara, Western Australia, 5th International Archean Symposium, Abstracts Volume: Geological Survey of Western Australia, Record, pp. 223-224.

Thomazo, C., Ader, M. and Philippot, P., 2011, Extreme 15N enrichments in 2.72 Gyr old sediments: evidence for a turning point in the nitrogen cycle: Geobiology, v. 9, p. 107-120.

Truesdalea, V. and Jones, S., 1996, The variation of iodate and total iodine in some UK rainwaters during 1980–1981: Journal of hydrology, v. 179, p. 67-86.

Van Kranendonk, M. J., Philippot, P. and Lepot, K., 2006, The Pilbara Drilling Project: c. 2.72 Ga Tumbiana Formation and c. 3.49 Ga Dresser Formation Pilbara Craton, Western Australia. Geological Survey of Western Australia.

CHAPTER 2

Iodine constraints on Proterozoic shallow ocean redox and their biological implications

ABSTRACT

Surface ocean oxygen levels during the Proterozoic Eon — the location and interval hosting the emergence and initial diversification of eukaryotes — were lower than today's, although how much lower is debated. Here, we use concentrations of iodate (the oxidized iodine species) in shallow-marine carbonate rocks (limestones and dolostones) — sensitive to both local oxygen availability and the position of the oxycline (Glock and others, 2014; Hardisty and others, 2014; Lu and others, 2016; Lu and others, 2010; Zhou and others, 2015; Zhou and others, 2014) — to generate the first comprehensive record of Proterozoic near-surface marine redox conditions. The oxycline is the typically sharp transition between anoxic deep waters and O_2-containing surface waters. To assess the validity of our approach, Neogene-Quaternary carbonates are used to demonstrate that diagenesis only decreases carbonate-iodine contents. Despite the potential for diagenetic loss, maximum Proterozoic carbonate iodine levels are elevated relative to the O_2-poor Archean, particularly during the Lomagundi and Shuram carbonate carbon isotope excursions of the Paleo- and Neoproterozoic, respectively. The predominantly low iodine levels from the Proterozoic are most parsimoniously linked to a shallow oxycline whereby O_2 concentrations in surface waters were at least intermittently above the threshold levels required to support complex life. However, the diagnostically low iodine data from mid-Proterozoic shallow-water carbonates point to a particularly shallow and dynamic oxycline across which anoxic waters mixed into shallow surface waters (Gilleaudeau and Kah, 2015; Guilbaud and others, 2015; Sperling and others, 2015). This redox instability may have challenged early eukaryotic diversification and expansion, creating an evolutionary landscape unfavorable for the emergence of animals (Johnston and others, 2012; Johnston and others, 2009).

INTRODUCTION

The shallow oceans of the Proterozoic were the host to both oxygen production and the sequential radiations of eukaryotes and animals (Knoll, 2014). Nevertheless, the current conversation about biospheric oxygenation, the first appearances and diversification of the earliest eukaryotes and animals, and their associated oxygen demands (Mills and others, 2014; Sperling and others, 2013) has often focused instead on conditions in the atmosphere (Planavsky and others, 2014) and sub-photic deep-marine waters (Sperling and others, 2015). Such comparisons are indirect, since *in situ* oxygenic photosynthesis in the shallow photic zone provides the potential for elevated shallow-ocean oxygen at micromolar (μM) levels even under an anoxic atmosphere (Christopher T. Reinhard, 2016; Olson and others, 2013). This disconnect reflects a shortage of temporally expansive paleoredox records specific to the shallow ocean. The need to fill this knowledge gap is particularly critical through the mid-Proterozoic (ca. 1.8 to 0.8 billion years ago or Ga), which precedes the evolution of the earliest metazoans (Knoll, 2014).

Chromium isotope data have recently yielded estimates for atmospheric O_2 during the mid-Proterozoic as low as < 0.1-1% of present atmospheric levels (PAL), in contrast to previous estimates of >1-40% of PAL (Cole and others, 2016; Crowe and others, 2013; Gilleaudeau and others, 2016; Planavsky and others, 2014). If these low estimates are correct, the predicted nanomolar (nM) to low μM equilibrium-driven levels of dissolved O_2 in the surface ocean would challenge most complex life (Planavsky and others, 2014). Generally consistent with low atmospheric pO_2 through portions of the Proterozoic, accumulations of redox-sensitive metals (Mo, Cr, U, and Fe) in basinal black shale specifically fingerprint an anoxic deeper ocean dominated by a combination of ferruginous and sulfidic (euxinic) waters (Gilleaudeau and Kah, 2015; Guilbaud and others, 2015; Reinhard and others, 2013; Sperling and others, 2015).

Carbon isotope compositions of shallow carbonates ($\delta^{13}C_{carb}$) have been used as a roadmap to the redox evolution of the Proterozoic biosphere. In particular, the Proterozoic hosts the largest positive and negative $\delta^{13}C_{carb}$ excursions in Earth history — the Paleoproterozoic Lomagundi and Ediacaran Shuram anomalies, respectively. Both have been interpreted as large-scale Proterozoic oxidation events bracketing the discussed mid-Proterozoic low oxygen atmosphere (Fike and others, 2006; Karhu and Holland, 1996). Export of organic carbon from primary producers in the photic zone and its subsequent burial in sediments is the primary driver of biospheric oxygenation through Earth's history. Patterns and perturbations of carbon cycling reflected in the $\delta^{13}C$ values of marine dissolved inorganic carbon (DIC) are captured in carbonate rocks. However, these records are at best only indirect measures of redox conditions in the surface ocean, and their relationships to the broader workings of the carbon cycle as manifest in marine water column signals can be lost or overprinted during diagenesis by pore fluid chemistry (Schrag and others, 2013; Swart and Kennedy, 2012).

Ratios of iodine-to-calcium-magnesium (I/[Ca+Mg]) in shallow-marine carbonates can track the presence or absence of O_2 in the shallow ocean (Hardisty and others, 2014) and the position of the oxic-anoxic interface in the water column (oxycline) relative to the site of carbonate precipitation (Lu and others, 2016). The oxidized and reduced iodine species, iodate (IO_3^-) and iodide (I^-), respectively, constitute the bulk of total dissolved iodine in seawater (Chance and others, 2014; Emerson and others, 1979; Farrenkopf and Luther Iii, 2002; Rue and others, 1997; Wong and Brewer, 1977). Concentrations of total dissolved iodine in modern seawater, near 450-500 nM (Chance and others, 2014), are globally uniform and have a residence time (~300 kyrs) that is orders of magnitude longer than the mixing time of the ocean. Importantly, IO_3^- exists exclusively in oxic waters, with IO_3^- reduction occurring in weakly oxic waters prior to the onset of iron and sulfate reduction (Emerson and others, 1979; Kennedy and

Elderfield, 1987a; Kennedy and Elderfield, 1987b; Luther III and Campbell, 1991; Wong and Brewer, 1977). Quantitative IO_3^- reduction is observed directly below the oxycline of oxygen minimum zones (OMZs; (Farrenkopf and Luther Iii, 2002; Rue and others, 1997)), within anoxic basins (Emerson and others, 1979; Luther III and Campbell, 1991; Wong and Brewer, 1977), and in reducing pore waters (Kennedy and Elderfield, 1987a; Kennedy and Elderfield, 1987b). Iodine's described redox behavior can be traced from ancient oceans as iodate is the sole iodine species that co-precipitates with carbonate rocks (Lu and others, 2010). Thus, carbonate minerals formed in these anoxic waters — where I^- is the predominant dissolved iodine species — are not expected to precipitate with iodine, as demonstrated in calcite synthesis experiments (Lu and others, 2010). This expectation is consistent with previous reports noting a lack of iodine in carbonate rocks prior to the Great Oxidation Event (GOE) (Hardisty and others, 2014).

Although quantitative reduction of IO_3^- occurs within hours in low-oxygen and anoxic waters (Farrenkopf and others, 1997), I^- oxidation can be a slower process, with rate estimates ranging from weeks to years (Campos and others, 1996; Chance and others, 2014; Luther III and others, 1995). Due to this redox asymmetry, the lowest non-zero marine IO_3^- concentrations occur within the oxycline of waters directly overlying OMZs or within anoxic basins (Farrenkopf and Luther Iii, 2002; Rue and others, 1997). In this zone, *ex situ* input of the relatively slow oxidizing I^- — transported from underlying anoxic IO_3^--free waters — results in steep $[IO_3^-]$ gradients (Farrenkopf and Luther Iii, 2002; Lu and others, 2016; Luther III and Campbell, 1991; Rue and others, 1997; Wong and Brewer, 1977). Modern seawater non-zero $[IO_3^-]$ values of <250 nM are nearly exclusively found in such settings (Chance and others, 2014; Lu and others, 2016). This seawater $[IO_3^-]$ range would be recorded as I/[Ca+Mg] ratios of < ~2.6 μmol/mol, as observed in both laboratory calcite-precipitation experiments (Lu and others, 2010) and direct measurements of carbonate from low oxygen settings (Glock and others, 2014; Lu and others, 2016). Analogous

to the oxyclines that overlie modern OMZs, ancient carbonate with non-zero I/(Ca+Mg) of less than ~2.6 μmol/mol are interpreted to reflect precipitation within waters with local O_2 levels above that necessary to sustain IO_3^- accumulation but which are also characterized by, or in frequent exchange with, waters hosting active IO_3^- reduction (Lu and others, 2016).

Here we provide the first comprehensive record of Proterozoic surface ocean redox through a compilation of I/(Ca+Mg) ratios from carbonate rocks (limestones and dolostones). Using our Proterozoic I/(Ca+Mg) record and the context gleaned from pristine modern carbonates from modern, well-oxygenated and low oxygen settings as well as diagenetic carbonates from Neogene-Quaternary settings, we suggest that surface ocean oxygenation following the GOE could have sustained eukaryotic life. However, we further recommend that the low ratios typical of the mid-Proterozoic are a reflection of carbonate precipitation in waters with overall low and unstable oxygen levels in close spatial proximity to anoxic waters.

MATERIALS

We measured I/(Ca+Mg) ratios of carbonate rocks (n=518) from 20 sedimentary successions spanning the late Paleoproterozoic to late Neoproterozoic and combined these with existing published data (Glock and others, 2014; Hardisty and others, 2014; Loope and others, 2013; Lu and others, 2016; Lu and others, 2010; Zhou and others, 2015; Zhou and others, 2014). Details regarding age, stratigraphy, and complementary geochemistry for the individual sections are included in the Supplementary Materials. This data set also includes samples from four previously studied carbonate sections that capture the Ediacaran Shuram negative $\delta^{13}C_{carb}$ anomaly: the Khufai Formation of the Sultanate of Oman (Osburn and others, 2015); the Doushantuo Formation of South China; the Johnnie Formation of Death Valley, USA; and the Clemente Formation of northern Mexico (Loyd and others, 2012b). For this and the previously published Precambrian iodine data (Hardisty and others, 2014), emphasis was placed on

carbonate successions with independent sedimentological evidence for shallow-marine deposition, and units with clear indications of secondary alteration, such as veins and metamorphism above greenschist grade, were avoided.

Samples chosen for comparative evaluation of the effects of diagenesis on I/(Ca+Mg) were collected from short bank-top cores of the modern Great Bahama Bank, coral heads from the Pleistocene Key Largo Limestone in South Florida, the Neogene-Quaternary Clino and Unda cores from Great Bahama Bank , and carbonate concretions of the Miocene Monterey Formation in California ([n=310]; Fig. S1). Together, these settings contain a range of primary and diagenetic carbonate: (a) primary aragonite and high-Mg calcite (HMC) (Fig. S2; Table S1); (b) neomorphic, low-Mg calcite (LMC) that formed via the interaction of meteoric fluids with aragonite (Gill and others, 2008); (c) LMC and dolomite formed during the interaction of aragonite with meteoric and marine pore fluids (e.g., (Swart and Kennedy, 2012; Swart and Melim, 2000)) (Fig. S4); and (d) dolomite concretions that formed largely within anoxic pore fluids (Loyd and others, 2012a). Details regarding the site-specific depositional settings and additional geochemical data are provided in the Supplementary Materials. With the exception of the Monterey Formation, the water columns during primary carbonate deposition were persistently oxygenated and far removed from anoxic waters, meaning that low values and dramatic variations in I/(Ca+Mg) are likely to reflect diagenetic overprinting rather than water column redox dynamics.

RESULTS

The I/(Ca+Mg) variations in our Neogene and younger samples are most prominently linked with carbonate mineralogy (Fig. 2), specifically the degree to which the minerals present are primary (aragonite and HMC) versus diagenetic phases (LMC and dolomite). The highest I/(Ca+Mg) values, up to 11.6 μmol/mol, are found in dominantly aragonite and HMC samples

from bank-top cores from the well-oxygenated Great Bahama Bank (Fig. 1A; Fig. S2). Aragonite-to-LMC neomorphism has the potential to preserve I/(Ca+Mg) typical of well-oxygenated water columns (Fig. 1A), particularly during meteoric alteration (Fig. S3). In most cases, however, I/(Ca+Mg) in diagenetic LMC are low and in the range of values we would expect to find in carbonate precipitated from low-oxygen depositional settings (Fig. 1A; Fig. S4). Diagenetic dolomite from the Bahamas and Monterey yield the lowest I/(Ca+Mg) ratios, with values of <0.46 µmol/mol when dolomite is present at >40 wt.% and below detection in most cases (Fig. 1B). *We emphasize that there is no example of an increase in I/(Ca+Mg) associated with post-depositional diagenesis* (Fig. 1; Fig. S2, S3,and S4).

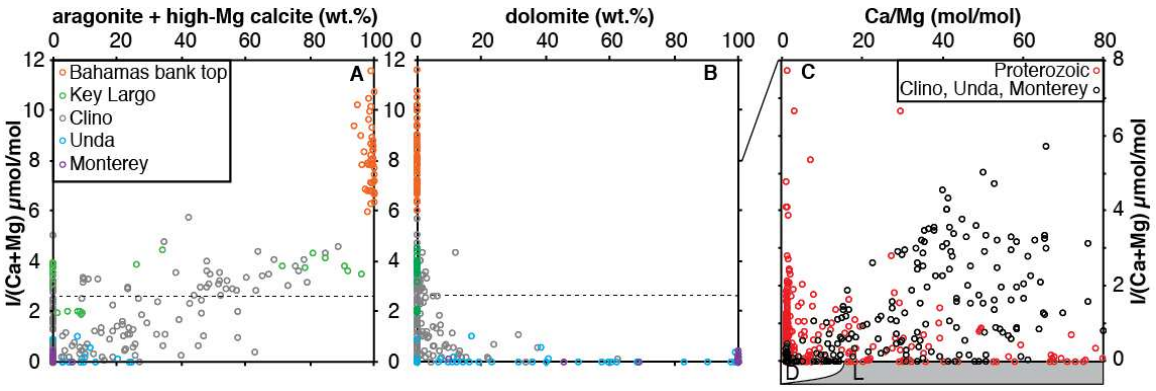

Figure 1. The composition of (A) primary aragonite and high-Mg calcite and (B) diagenetic dolomite relative to I/(Ca+Mg) ratios for the diagenetic sample set described in the main text and shown in the key. The horizontal yellow dashed line is at an I/(Ca+Mg) of 2.6 µmol/mol, the threshold below which, as discussed in the text, is characteristic of reducing marine settings (Glock and others, 2014; Lu and others, 2016). (C) Comparison of I/(Ca+Mg) to Ca/Mg for the recent diagenetic dolomite-bearing sample sets relative to the Proterozoic sample set from this and previous studies (Hardisty and others, 2014). The upper panel shows the relative proportion of limestone versus dolomite for varying Ca/Mg ratios, which is justified through a comparison of Ca/Mg versus dolomite weight percent in our diagenetic sample set (Fig. S6). Ca/Mg ratios >80 are present in the sample sets, but not shown in order to emphasize the relevant trends.

Comparison of the Proterozoic and recent sample sets reveals that Proterozoic I/(Ca+Mg) ratios from dolomite have the potential to be elevated beyond, and in some cases well beyond, the ≤0.46 μmol/mol values observed in recent diagenetic dolomite. Consistent with these observations, the highest Proterozoic values are in most cases found in dolomite (Fig. 1C). The Proterozoic data reveal, in stark contrast to the lack of iodine in carbonates deposited prior to the GOE (Hardisty and others, 2014), that appreciable iodine is present in some of the samples from nearly all the units evaluated (Fig. 2). Proterozoic I/(Ca+Mg) ratios from carbonates older than the late Ediacaran Shuram anomaly are ≤2.8 μmol/mol and are often much less — notably within the range observed in primary carbonate from modern low oxygen settings (yellow squares, Fig. 2). There is a drop in maximum I/(Ca+Mg) to ≤0.8 μmol/mol around ~2.0 Ga following the Lomagundi positive carbon isotope excursion (LE; ~2.2-2.1 Ga). In the following interval, from 2.0 to 1.0 Ga, maximum values of ≤0.8 μmol/mol are found in 13 of the 14 studied units with the only exception being the Tieling Formation of North China, where maximum I/(Ca+Mg) ratios are similar to those characterizing the LE and Neoproterozoic (Fig. 2; Fig. S5). Starting at roughly 1.0 Ga, maximum values are more frequently elevated relative to the mid-Proterozoic. Lastly, all four of the Ediacaran, Shuram-age sections analyzed here show a marked increase in I/(Ca+Mg) in phase with the dramatic decrease in $\delta^{13}C_{carb}$ (Fig. 3).

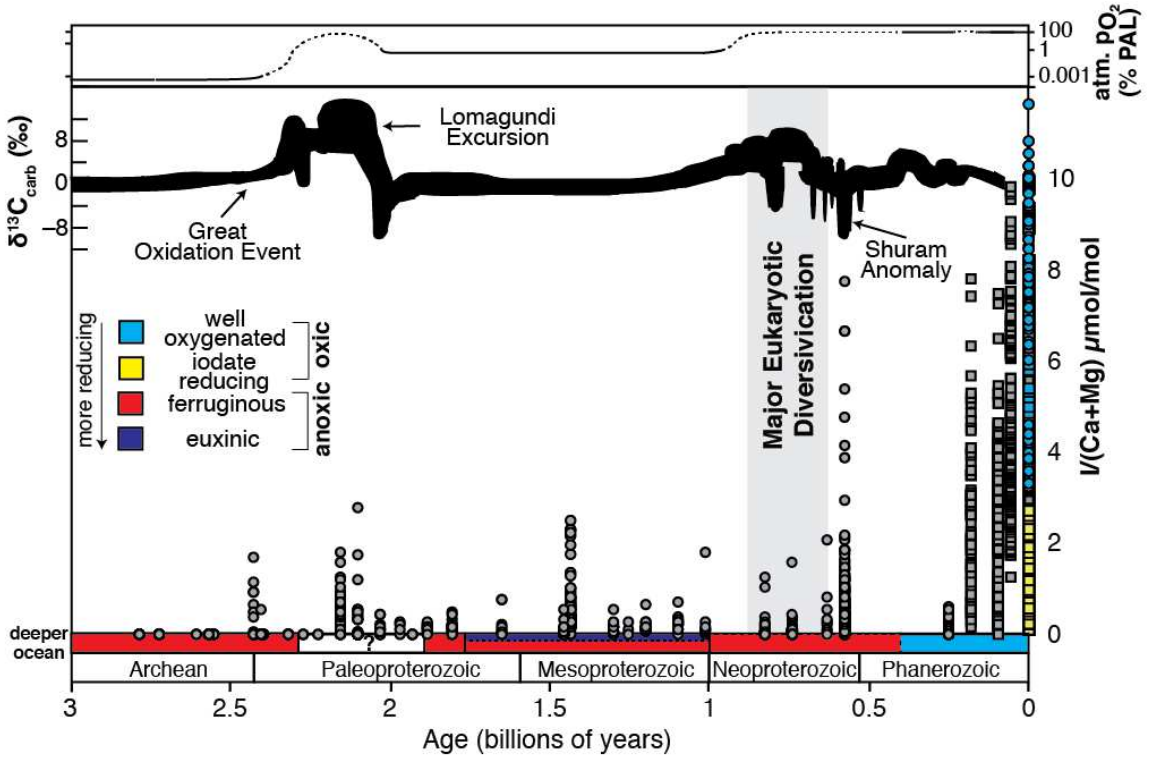

Figure 2. The secular trends in atmospheric oxygen (Lyons and others, 2014; Planavsky and others, 2014), $\delta^{13}C_{carb}$, and I/(Ca+Mg) (Glock and others, 2014; Hardisty and others, 2014; Loope and others, 2013; Lu and others, 2016; Lu and others, 2010; Zhou and others, 2015; Zhou and others, 2014) representing surface ocean oxygen, and deep ocean redox (Sperling and others, 2015). Events specified in the text are labeled, including the period marked by the first known major eukaryotic diversification (vertical gray bar (Knoll, 2014)). Square symbols indicate data representing I/Ca from calcitic foraminifers, equivalent to I/(Ca+Mg) in the case of calcite. Blue symbols come from modern to recent settings with independent evidence for well-oxygenated water columns and lacking indicators of diagenetic overprinting (Lu and others, 2016), aragonitic coral heads of the Key Largo Limestone (Fig. 1A) and aragonite to HMC-dominated bulk carbonate from the modern Great Bahama Bank (Fig. 1A). Yellow symbols correspond to modern foraminifers from within the oxycline of reducing settings (Glock and others, 2014; Lu and others, 2016) and where iodate reduction and mixing between anoxic and oxic waters is occurring. Red represents ferruginous and purple euxinic deep-marine waters (Sperling and others, 2015). Dashed lines in upper panel represent uncertainty due to a lack of quantitative constraints.

DISCUSSION

Neogene-Quaternary perspectives on Proterozoic carbonate diagenesis

Our proxy validation efforts with the Neogene-Quaternary samples indicate that I/(Ca+Mg) would not increase after deposition during diagenesis in reducing pore fluids (Loyd and others, 2012a; McClain and others, 1992; Schrag and others, 2013). As such, the simple presence of iodine in carbonate is an ideal proxy for oxic conditions, and 'false positives' are not anticipated and have not been observed in young sediments. Iodine's redox relationship distinguishes it from other common paleoredox proxies (e.g., Fe speciation, S isotopes and concentrations, and Mo and U concentrations), which fingerprint local anoxic water columns but that are most commonly applied to deeper basinal shale. Beyond the simple presence-absence of surface ocean O_2, detailed comparison of Proterozoic I/(Ca+Mg) trends to Neogene-Quaternary diagenetic carbonate and dolomite support that Proterozoic temporal trends may reflect seawater redox evolution, including relative changes in oxycline depth, when interpreted with the appropriate caution. For instance, there are no known temporal variations in diagenesis that would cause the observed patterns through the Precambrian and preferentially favor the diagnostic persistence of low maximum values during the Archean and mid-Proterozoic.

A case study in our effort to distinguish seawater versus pore water origins of Proterozoic I/(Ca+Mg) signals comes from comparison between the I/(Ca+Mg) trends spanning the Shuram negative $\delta^{13}C_{carb}$ anomaly (Fig. 3) and our sample set recording Neogene-Quaternary diagenesis (Fig. 1). Meteoric and marine diagenesis have been invoked to explain the extremely negative $\delta^{13}C_{carb}$ of the Shuram excursion (Schrag and others, 2013; Swart and Kennedy, 2012), with values tracking from +5 to -12‰ (Fig. 3). If diagenetic, the $\delta^{13}C_{carb}$ would most likely reflect post-depositional mineralogical transformations and the associated low $\delta^{13}C$ of dissolved inorganic carbon of pore fluids resulting from organic matter remineralization under anoxic or

reducing subsurface conditions (Schrag and others, 2013). Our data from Neogene-Quaternary diagenetic sediments show that I/(Ca+Mg) values do not increase during diagenesis (Fig. 1; Fig. S3 and S4) as IO_3^- is quantitatively reduced under the anoxic conditions typical of diagenetic carbonate precipitation (Kennedy and Elderfield, 1987a; Kennedy and Elderfield, 1987b). In contrast, however, I/(Ca+Mg) ratios across the Shuram excursion, in each of four paleogeographic localities, *increase* in parallel with *decreasing* $\delta^{13}C_{carb}$ and consistently do so despite variable mineralogy and sedimentary facies (Fig. 3; Fig, S7). This relationship is opposite to that expected from diagenesis (Fig. 1) and hence supports the likelihood that the Shuram anomaly at least partially reflects the local seawater availability of IO_3^- and associated, likely global, trends in $\delta^{13}C_{carb}$. A primary contribution to the Shuram anomaly is further braced by records of carbonate-associated sulfate (Kaufman and others, 2007; Loyd and others, 2013; Osburn and others, 2015), U concentrations (Zhao and others, 2016), and compound-specific $\delta^{13}C$ of organic carbon (Lee and others, 2015), all which show trends counter to those expected from diagenetic alteration.

Lastly, dolomitization in Proterozoic samples is not necessarily an indication of false secular trends or severally altered samples. Instead, previous workers have argued from a combination of sedimentological fabric retention (Fairchild and others, 1991; Kah, 2000; Tucker, 1982) and geochemical (Kah, 2000; Tucker, 1982; Wilson and others, 2010) and petrographic (Tucker, 1982; van Smeerdijk Hood and Wallace, 2012; van Smeerdijk Hood and others, 2011) evidence that Precambrian dolomite may have been primary or formed earlier during diagenesis relative to those of the Phanerozoic, in open exchange with seawater and in some cases occurring at the sediment-water interface. The implication is that Proterozoic dolomite could be a strong and even preferred geochemical archive of ancient marine conditions relative to stratigraphically associated limestone. A comparison of data from our Neogene diagenetic dolomite from the

Bahamas and Monterey to Proterozoic samples further reinforces the potential occurrence and benefit of early Proterozoic dolomite and hence processes regulating I/(Ca+Mg) other than dolomitization (Fig. 1C). Specifically, the highest I/(Ca+Mg) ratios from our Proterozoic carbonate (most notably the Shuram) are found most often in dolomite — the opposite trend to that seen in our Neogene samples — and maximum Proterozoic values in dolostones, including those from the mid-Proterozoic, exceed values seen in our Neogene diagenetic dolomite sample set (Fig. 1C). Given the early redox sensitivity of IO_3^- reduction with declining [O_2] (Kennedy and Elderfield, 1987a; Kennedy and Elderfield, 1987b; Rue and others, 1997), our data reinforce that in some cases Proterozoic dolomite precipitation likely occurred near or at the sediment-water interface and hence should record at least partial seawater signals (Fairchild and others, 1991; Kah, 2000; Tucker, 1982; van Smeerdijk Hood and Wallace, 2012; van Smeerdijk Hood and others, 2011; Wilson and others, 2010). As such, first-order temporal trends in maximum I/(Ca+Mg) ratios are cautiously interpreted in discussions below as primary records of shallow ocean redox evolution, emphasizing the maximum I/(Ca+Mg) from a given section as a minimum estimate of local seawater IO_3^- availability.

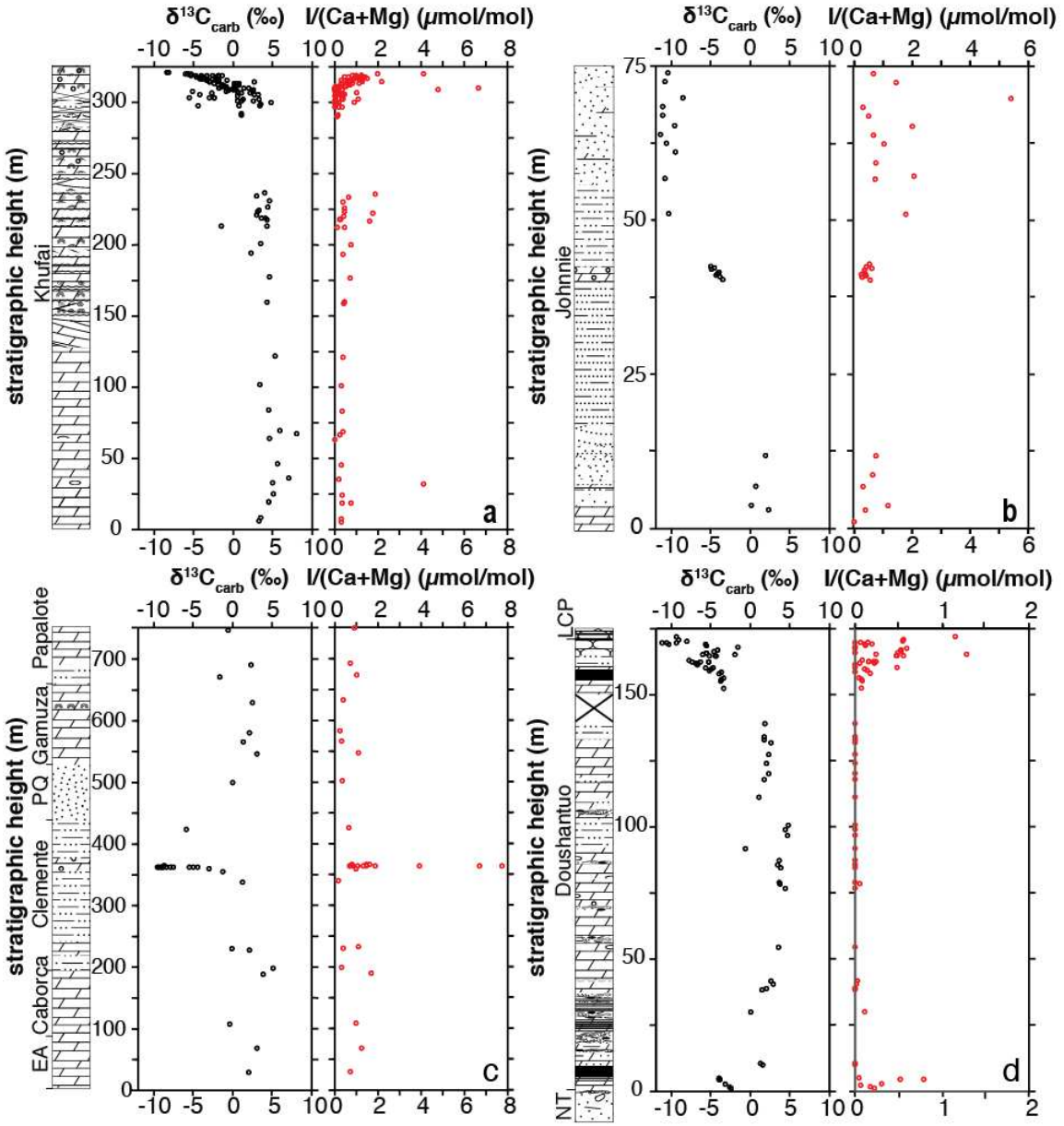

Figure 3. Carbonate carbon isotope ($\delta^{13}C_{carb}$) and iodine to calcium and magnesium (I/(Ca+Mg)) ratios and stratigraphic profiles for Ediacaran, Shuram-age sedimentary successions (A) Khufai Formation, Oman ($\delta^{13}C_{carb}$ from (Osburn and others, 2015)), (B) the Johnnie Formation, Death Valley, USA, (C) Clemente Formation, Northern Mexico ($\delta^{13}C_{carb}$ from (Loyd and others, 2012b)), and (D) Doushantuo Formation, Siduping of South China. 1σ for I/(Ca+Mg) is equal to 0.2 μmol/mol (see Methods), twice the width of the data points in the figure. The stratigraphic key and paleogeographic localities of the individual sections are shown in Figure S7.

Proterozoic surface ocean redox

In light of our study of diagenetic effects in recent carbonates, the simple presence of iodine in most of the Proterozoic carbonate units we analyzed provides strong evidence for surface ocean [O_2] above the low threshold required for IO_3^- accumulation. Previous studies have argued for an [O_2] requirement of at least 1-3 μM for marine IO_3^- accumulation and hence the presence of carbonate-bound iodine (Hardisty and others, 2014). Further support for Proterozoic surface ocean [O_2] at or above low μM levels comes from the presence of eukaryotic microfossils during the mid-Proterozoic (Knoll, 2014), as well as from modeling efforts indicating the potential for single digit μM surface ocean O_2 concentrations from *in situ* oxygenic photosynthesis under even a completely anoxic atmosphere (Christopher T. Reinhard, 2016; Olson and others, 2013). Importantly, the >1-3 μM surface ocean O_2 levels observed for modern oxidative marine iodine cycling are above those predicted from the very low mid-Proterozoic atmospheric pO_2 suggested recently by Cr isotope measurements (Cole and others, 2016; Gilleaudeau and others, 2016; Planavsky and others, 2014) (Fig. 2), Collectively, the two proxies may provide evidence for a disequilibrium between the atmosphere and surface ocean favored by *in situ* marine oxygen production (Christopher T. Reinhard, 2016; Olson and others, 2013). Alternatively, the apparent discrepancy could reflect the uncertainties in our current understanding of modern iodine (Luther III and others, 1995) and chromium cycling (see (Gilleaudeau and others, 2016) vs (Cole and others, 2016; Planavsky and others, 2014)).

Proterozoic records for I/(Ca+Mg) and $\delta^{13}C_{carb}$ show similar temporal trends (Fig. 2 and 3), a relationship not expected if either or both result from diagenesis (Fig. 1; Fig. S3 and S4). Importantly, however, I/(Ca+Mg) provides new constraints, including the degree of mixing with adjacent anoxic waters as related to shallow positions of the oxycline (Lu and others, 2016). Given the relatively low I/(Ca+Mg) ratios observed through most of the Proterozoic (Fig. 2), we

suggest that the iodine record most strongly supports a shallow oxycline near or within the surface ocean for most of the Proterozoic, with surface ocean redox analogous to the oxycline of modern anoxic basins and OMZs. These settings — where oxygen is locally present but IO_3^- reduction is active in resident and/or adjacent exchanging water masses — equate to diagnostically low marine IO_3^- concentrations with corresponding I/(Ca+Mg) ratios in the range observed through the Proterozoic (yellow squares, Fig. 2). That pattern manifests in a predominance of low I/(Ca+Mg) ratios during the Proterozoic interrupted only episodically by largely subtle increases (Fig. 2) during some intervals previously described as oxygenation events, such as at the GOE (Lyons and others, 2014), the Lomagundi (Karhu and Holland, 1996), at 1.4 Ga (Mukherjee and Large, 2016), the Neoproterozoic (Cole and others, 2016; Planavsky and others, 2014), and the Shuram (Fike and others, 2006). Collectively, these trends delineate a history of protracted and dynamic oxygenation within a largely anoxic ocean (Reinhard and others, 2013; Sperling and others, 2015) through the Proterozoic — rather than a unidirectional rise (Sahoo and others, 2016).

We specifically link the generally low but non-zero mid-Proterozoic iodine values to an extremely shallow oxycline that facilitated direct advective exchange between weakly oxic surface waters and underlying or adjacent waters that were dominantly anoxic (Reinhard and others, 2013). In such a setting, it is likely that both upward and lateral mixing of O_2-free waters frequently perturbed and intruded into already poorly oxygenated shallow ocean waters. Reinforcing this interpretation, Phanerozoic iodine ratios are lowest during times of widespread anoxia (Fig. 2; (Loope and others, 2013; Lu and others, 2010; Zhou and others, 2015; Zhou and others, 2014)), and records of chromium isotopes (Cole and others, 2016; Planavsky and others, 2014), rare earth elements (Tang and others, 2016), Zn/Fe ratios (Liu and others, 2016), and carbonate-associated sulfate (Hurtgen and others, 2004; Kah and others, 2001; Kah and others,

2004) all indicate limited mid-Proterozoic oxygenation. Together with independent evidence for mid-depth euxinia throughout the mid-Proterozoic based on iron analysis of shale (Fig. 2), the upward and lateral mixing of anoxic waters into weakly oxygenated surface waters may also have resulted in frequent episodic incursions of hydrogen sulfide into particularly shallow settings.

Summary and implications for Proterozoic life

The Proterozoic iodine record provides a comprehensive window to oxygen dynamics that may have dominated ancient, marginal shallow-marine settings — the ecological hot spots that likely hosted the emergence and diversification of eukaryotes, including animals (Jablonski and others, 1983; Knoll, 2014). The overarching trends in our dataset are difficult to link to diagenetic processes, and there is strong support for a primary origin of iodine records across the heavily discussed Shuram excursion. Previous debate regarding the potential for redox controls on the timing of early animal evolution has focused on experimental and ecological analyses of animal physiology (Mills and others, 2014; Sperling and others, 2013) as related to indirect estimates of atmospheric pO_2 (Planavsky and others, 2014). The iodine data provide a more direct perspective, suggesting the possibility of a Proterozoic surface ocean that was at least intermittently hospitable to eukaryotes and that may have been at, near, or above the lower limits of oxygen required for small, simple (but not large and energetic) animals (Mills and others, 2014; Sperling and others, 2013). Critically, however, our data also support the likelihood that the marginal shelf settings in which early protistan and, later, animal fossils are found were characterized by low and variable O_2 conditions (Gilleaudeau and Kah, 2015) most analogous to those within the oxyclines directly overlying modern OMZs and within anoxic basins. We argue that these conditions were particularly common through the mid-Proterozoic, with shallow waters impacted frequently if not persistently by upward and lateral intrusion of abundant anoxic waters (Reinhard and others, 2013) across a shallow oxycline. Despite maximum shallow ocean [O_2] that

was likely near the proposed thresholds for simple, early animals, such dynamic conditions would have challenged eukaryotic and, later, animal emergence and diversification during the mid-Proterozoic for at least a billion years (Johnston and others, 2012; Johnston and others, 2009).

METHODS

Iodine-to-calcium-magnesium ratios and calcium-to-magnesium ratios were measured at Syracuse University using a Bruker M90 quadrupole inductively-coupled-plasma mass spectrometer (ICP-MS) and at the University of California, Riverside, using a Agilent 7900c ICP-MS, according to standard methods (Hardisty and others, 2014; Lu and others, 2016; Lu and others, 2010; Zhou and others, 2015; Zhou and others, 2014). All samples from the Clino, Unda, Monterey, and Tieling formations were measured at UC Riverside and the remainder at Syracuse University. Approximately 3-5 mg of powdered carbonate was used for each analysis. Weighed samples were initially put through a rinse step intended for dissolution and removal of iodine-containing salts. Samples were sonicated in 1 mL DI water that was then centrifuged and decanted. Following this, 3% HNO_3 was added to each sample allowing for complete dissolution of all carbonate, and these were similarly sonicated for ~10 minutes and centrifuged. The supernatant was diluted in a matrix with combinations of nitric acid and an iodine-stabilizing solution (tertiary amine or tetramethyl ammonium hydroxide) to obtain Ca concentrations of approximately 50 ppm. Calibration standards were made fresh each day from powdered KIO_3 in a similar matrix with the addition of 50 ppm Ca. The coral standard JCP-1 was analyzed intermittently with average values at Syracuse University and UC Riverside identical within error.

The mineralogical determinations for Clino, Unda, Monterey, Key Largo, and Bahamas Bank top cores were performed at the University of Miami using a Panalytical X-Pert Pro, using the method published previously (Swart and others, 2002). The associated error is ± 2 wt. %.

Carbon isotope values for the Johnnie Formation, Clino, Unda, and portions of the Bahamas Bank top cores were measured at the University of California, Riverside, using a GasBench II interface coupled, via continuous flow, to a Delta V Thermo Advantage IRMS (Isotope Ratio Mass Spectrometer). Carbon isotope values for the C1, C4, C6, and C7 Bahamas Bank top cores were analyzed at The Center for Stable Isotope Biogeochemistry at UC, Berkeley, using a MultiCarb system connected with a GV IsoPrime mass spectrometer in dual inlet mode. Carbon isotopes for the Doushantuo Formation were measured at the University of Nevada, Las Vegas, using a Kiel IV carbonate device connected to a Finnigan Delta V Plus mass spectrometer in dual inlet mode. All values are presented in the standard delta notation as per mil (‰) deviation from Vienna Pee Dee Belemnite (V-PDB) with replicate analyses of NBS-19 and internal standards yielding a standard deviation better than 0.10 ‰ for C.

REFERENCES CITED

Campos, M., Farrenkopf, A., Jickells, T. and Luther, G., 1996, A comparison of dissolved iodine cycling at the Bermuda Atlantic Time-series Station and Hawaii Ocean Time-series Station: Deep Sea Research Part II: Topical Studies in Oceanography, v. 43, p. 455-466.

Chance, R., Baker, A. R., Carpenter, L. and Jickells, T. D., 2014, The distribution of iodide at the sea surface: Environmental Science: Processes & Impacts, v., p.

Christopher T. Reinhard, N. J. P., Stephanie L. Olson, Timothy W. Lyons, Douglas H. Erwin, 2016, Earth's oxygen cycle and the evolution of metazoan life: Proceedings of the National Academy of Sciences, v., p.

Cole, D. B., Reinhard, C. T., Wang, X., Gueguen, B., Halverson, G. P., Gibson, T., Hodgskiss, M. S., McKenzie, N. R., Lyons, T. W. and Planavsky, N. J., 2016, A shale-hosted Cr isotope record of low atmospheric oxygen during the Proterozoic: Geology, v., p. G37787. 37781.

Crowe, S. A., Døssing, L. N., Beukes, N. J., Bau, M., Kruger, S. J., Frei, R. and Canfield, D. E., 2013, Atmospheric oxygenation three billion years ago: Nature, v. 501, p. 535-538.

Emerson, S., Cranston, R. E. and Liss, P. S., 1979, Redox species in a reducing fjord: equilibrium and kinetic considerations: Deep Sea Research Part A. Oceanographic Research Papers, v. 26, p. 859-878.

Fairchild, I. J., Knoll, A. H. and Swett, K., 1991, Coastal lithofacies and biofacies associated with syndepositional dolomitization and silicification (Draken Formation, Upper Riphean, Svalbard): Precambrian Research, v. 53, p. 165-197.

Farrenkopf, A. M., Dollhopf, M. E., Chadhain, S. N., Luther III, G. W. and Nealson, K. H., 1997, Reduction of iodate in seawater during Arabian Sea shipboard incubations and in laboratory cultures of the marine bacterium< i> Shewanella putrefaciens</i> strain MR-4: Marine Chemistry, v. 57, p. 347-354.

Farrenkopf, A. M. and Luther Iii, G. W., 2002, Iodine chemistry reflects productivity and denitrification in the Arabian Sea: evidence for flux of dissolved species from sediments of western India into the OMZ: Deep Sea Research Part II: Topical Studies in Oceanography, v. 49, p. 2303-2318.

Fike, D. A., Grotzinger, J. P., Pratt, L. M. and Summons, R. E., 2006, Oxidation of the Ediacaran ocean: Nature, v. 444, p. 744-747.

Gill, B. C., Lyons, T. W. and Frank, T. D., 2008, Behavior of carbonate-associated sulfate during meteoric diagenesis and implications for the sulfur isotope paleoproxy: Geochimica et Cosmochimica Acta, v. 72, p. 4699-4711.

Gilleaudeau, G., Frei, R., Kaufman, A., Kah, L., Azmy, K., Bartley, J., Chernyavskiy, P. and Knoll, A., 2016, Oxygenation of the mid-Proterozoic atmosphere: clues from chromium isotopes in carbonates, v., p.

Gilleaudeau, G. J. and Kah, L. C., 2015, Heterogeneous redox conditions and a shallow chemocline in the Mesoproterozoic ocean: evidence from carbon–sulfur–iron relationships: Precambrian Research, v. 257, p. 94-108.

Glock, N., Liebetrau, V. and Eisenhauer, A., 2014, I/Ca ratios in benthic foraminifera from the Peruvian oxygen minimum zone: analytical methodology and evaluation as proxy for redox conditions: Biogeosciences Discussions, v. 11, p. 11635-11670.

Guilbaud, R., Poulton, S. W., Butterfield, N. J., Zhu, M. and Shields-Zhou, G. A., 2015, A global transition to ferruginous conditions in the early Neoproterozoic oceans: Nature Geoscience, v., p.

Hardisty, D. S., Lu, Z., Planavsky, N. J., Bekker, A., Philippot, P., Zhou, X. and Lyons, T. W., 2014, An iodine record of Paleoproterozoic surface ocean oxygenation: Geology, v. 42, p. 619-622.

Hurtgen, M. T., Arthur, M. A. and Prave, A. R., 2004, The sulfur isotope composition of carbonate-associated sulfate in Mesoproterozoic to Neoproterozoic carbonates from Death Valley, California: Geological Society of America Special Papers, v. 379, p. 177-194.

Jablonski, D., Sepkoski, J. J., Bottjer, D. J. and Sheehan, P. M., 1983, Onshore-offshore patterns in the evolution of Phanerozoic shelf communities: Science, v. 222, p. 1123-1125.

Johnston, D., Poulton, S., Goldberg, T., Sergeev, V., Podkovyrov, V., Vorob'eva, N., Bekker, A. and Knoll, A., 2012, Late Ediacaran redox stability and metazoan evolution: Earth and Planetary Science Letters, v. 335, p. 25-35.

Johnston, D. T., Wolfe-Simon, F., Pearson, A. and Knoll, A. H., 2009, Anoxygenic photosynthesis modulated Proterozoic oxygen and sustained Earth's middle age: Proceedings of the National Academy of Sciences, v. 106, p. 16925-16929.

Kah, L. C., 2000, Depositional δ18O signatures in Proterozoic dolostones: constraints on seawater chemistry and early diagenesis, v., p.

Kah, L. C., Lyons, T. W. and Chesley, J. T., 2001, Geochemistry of a 1.2 Ga carbonate-evaporite succession, northern Baffin and Bylot Islands: implications for Mesoproterozoic marine evolution: Precambrian Research, v. 111, p. 203-234.

Kah, L. C., Lyons, T. W. and Frank, T. D., 2004, Low marine sulphate and protracted oxygenation of the Proterozoic biosphere: Nature, v. 431, p. 834-838.

Karhu, J. A. and Holland, H. D., 1996, Carbon isotopes and the rise of atmospheric oxygen: Geology, v. 24, p. 867-870.

Kaufman, A. J., Corsetti, F. A. and Varni, M. A., 2007, The effect of rising atmospheric oxygen on carbon and sulfur isotope anomalies in the Neoproterozoic Johnnie Formation, Death Valley, USA: Chemical Geology, v. 237, p. 47-63.

Kennedy, H. and Elderfield, H., 1987a, Iodine diagenesis in non-pelagic deep-sea sediments: Geochimica et Cosmochimica Acta, v. 51, p. 2505-2514.

Kennedy, H. A. and Elderfield, H., 1987b, Iodine diagenesis in pelagic deep-sea sediments: Geochimica et Cosmochimica Acta, v. 51, p. 2489-2504.

Knoll, A. H., 2014, Paleobiological perspectives on early eukaryotic evolution: Cold Spring Harbor perspectives in biology, v. 6, p. a016121.

Lee, C., Love, G. D., Fischer, W. W., Grotzinger, J. P. and Halverson, G. P., 2015, Marine organic matter cycling during the Ediacaran Shuram excursion: Geology, v. 43, p. 1103-1106.

Liu, X., Kah, L., Knoll, A., Cui, H., Kaufman, A., Shahar, A. and Hazen, R., 2016, Tracing Earth's O2 evolution using Zn/Fe ratios in marine carbonates: Geochemical Perspectives Letters, v. 2, p. 24-34.

Loope, G. R., Kump, L. R. and Arthur, M. A., 2013, Shallow water redox conditions from the Permian–Triassic boundary microbialite: The rare earth element and iodine geochemistry of carbonates from Turkey and South China: Chemical Geology, v. 351, p. 195-208.

Loyd, S. J., Berelson, W. M., Lyons, T. W., Hammond, D. E. and Corsetti, F. A., 2012a, Constraining pathways of microbial mediation for carbonate concretions of the Miocene Monterey Formation using carbonate-associated sulfate: Geochimica et Cosmochimica Acta, v. 78, p. 77-98.

Loyd, S. J., Marenco, P. J., Hagadorn, J. W., Lyons, T. W., Kaufman, A. J., Sour-Tovar, F. and Corsetti, F. A., 2012b, Sustained low marine sulfate concentrations from the Neoproterozoic to the Cambrian: Insights from carbonates of northwestern Mexico and eastern California: Earth and Planetary Science Letters, v. 339, p. 79-94.

Loyd, S. J., Marenco, P. J., Hagadorn, J. W., Lyons, T. W., Kaufman, A. J., Sour-Tovar, F. and Corsetti, F. A., 2013, Local $\delta^{34}S$ variability in 580Ma carbonates of northwestern Mexico and the Neoproterozoic marine sulfate reservoir: Precambrian Research, v. 224, p. 551-569.

Lu, Z., Hoogakker, B. A., Hillenbrand, C.-D., Zhou, X., Thomas, E., Gutchess, K. M., Lu, W., Jones, L. and Rickaby, R. E., 2016, Oxygen depletion recorded in upper waters of the glacial Southern Ocean: Nature communications, v. 7, p.

Lu, Z., Jenkyns, H. C. and Rickaby, R. E., 2010, Iodine to calcium ratios in marine carbonate as a paleo-redox proxy during oceanic anoxic events: Geology, v. 38, p. 1107-1110.

Luther III, G. W. and Campbell, T., 1991, Iodine speciation in the water column of the Black Sea: Deep Sea Research Part A. Oceanographic Research Papers, v. 38, p. S875-S882.

Luther III, G. W., Wu, J. and Cullen, J. B., 1995, Redox Chemistry of Iodine in Seawater: Frontier Molecular Orbital Theory Considerations: Aquatic chemistry: interfacial and interspecies processes, v. 244, p. 135.

Lyons, T. W., Reinhard, C. T. and Planavsky, N. J., 2014, The rise of oxygen in Earth/'s early ocean and atmosphere: Nature, v. 506, p. 307-315.

McClain, M. E., Swart, P. K. and Vacher, H. L., 1992, The hydrogeochemistry of early meteoric diagenesis in a Holocene deposit of biogenic carbonates: Journal of Sedimentary Research, v. 62, p.

Mills, D. B., Ward, L. M., Jones, C., Sweeten, B., Forth, M., Treusch, A. H. and Canfield, D. E., 2014, Oxygen requirements of the earliest animals: Proceedings of the National Academy of Sciences, v. 111, p. 4168-4172.

Mukherjee, I. and Large, R. R., 2016, Pyrite trace element chemistry of the Velkerri Formation, Roper Group, McArthur Basin: Evidence for atmospheric oxygenation during the Boring Billion: Precambrian Research, v., p.

Olson, S. L., Kump, L. R. and Kasting, J. F., 2013, Quantifying the areal extent and dissolved oxygen concentrations of Archean oxygen oases: Chemical Geology, v. 362, p. 35-43.

Osburn, M. R., Owens, J., Bergmann, K. D., Lyons, T. W. and Grotzinger, J. P., 2015, Dynamic changes in sulfate sulfur isotopes preceding the Ediacaran Shuram Excursion: Geochimica et Cosmochimica Acta, v. 170, p. 204-224.

Planavsky, N. J., Reinhard, C. T., Wang, X., Thomson, D., McGoldrick, P., Rainbird, R. H., Johnson, T., Fischer, W. W. and Lyons, T. W., 2014, Low Mid-Proterozoic atmospheric oxygen levels and the delayed rise of animals: science, v. 346, p. 635-638.

Reinhard, C. T., Planavsky, N. J., Robbins, L. J., Partin, C. A., Gill, B. C., Lalonde, S. V., Bekker, A., Konhauser, K. O. and Lyons, T. W., 2013, Proterozoic ocean redox and biogeochemical stasis: Proceedings of the National Academy of Sciences, v. 110, p. 5357-5362.

Rue, E. L., Smith, G. J., Cutter, G. A. and Bruland, K. W., 1997, The response of trace element redox couples to suboxic conditions in the water column: Deep Sea Research Part I: Oceanographic Research Papers, v. 44, p. 113-134.

Sahoo, S., Planavsky, N., Jiang, G., Kendall, B., Owens, J., Wang, X., Shi, X., Anbar, A. and Lyons, T., 2016, Oceanic oxygenation events in the anoxic Ediacaran ocean: Geobiology, v., p.

Schrag, D. P., Higgins, J. A., Macdonald, F. A. and Johnston, D. T., 2013, Authigenic carbonate and the history of the global carbon cycle: Science, v. 339, p. 540-543.

Sperling, E. A., Halverson, G. P., Knoll, A. H., Macdonald, F. A. and Johnston, D. T., 2013, A basin redox transect at the dawn of animal life: Earth and Planetary Science Letters, v. 371, p. 143-155.

Sperling, E. A., Wolock, C. J., Morgan, A. S., Gill, B. C., Kunzmann, M., Halverson, G. P., Macdonald, F. A., Knoll, A. H. and Johnston, D. T., 2015, Statistical analysis of iron geochemical data suggests limited late Proterozoic oxygenation: Nature, v. 523, p. 451-454.

Swart, P. K., James, N. P., Mallinson, D., Malone, M. J., Matsuda, H. and Simo, T., 2002, 10. Data Report: Carbonate Mineralogy of Sites Drilled during Leg 182, v., p.

Swart, P. K. and Kennedy, M. J., 2012, Does the global stratigraphic reproducibility of $\delta^{13}C$ in Neoproterozoic carbonates require a marine origin? A Pliocene–Pleistocene comparison: Geology, v. 40, p. 87-90.

Swart, P. K. and Melim, L. A., 2000, The origin of dolomites in Tertiary sediments from the margin of Great Bahama Bank: Journal of Sedimentary Research, v. 70, p. 738-748.

Tang, D., Shi, X., Wang, X. and Jiang, G., 2016, Extremely low oxygen concentration in mid-Proterozoic shallow seawaters: Precambrian Research, v., p.

Tucker, M. E., 1982, Precambrian dolomites: petrographic and isotopic evidence that they differ from Phanerozoic dolomites: Geology, v. 10, p. 7-12.

van Smeerdijk Hood, A. and Wallace, M. W., 2012, Synsedimentary diagenesis in a Cryogenian reef complex: Ubiquitous marine dolomite precipitation: Sedimentary Geology, v. 255, p. 56-71.

van Smeerdijk Hood, A., Wallace, M. W. and Drysdale, R. N., 2011, Neoproterozoic aragonite-dolomite seas? Widespread marine dolomite precipitation in Cryogenian reef complexes: Geology, v. 39, p. 871-874.

Wilson, J. P., Fischer, W. W., Johnston, D. T., Knoll, A. H., Grotzinger, J. P., Walter, M. R., McNaughton, N. J., Simon, M., Abelson, J. and Schrag, D. P., 2010, Geobiology of the late Paleoproterozoic Duck Creek Formation, Western Australia: Precambrian Research, v. 179, p. 135-149.

Wong, G. T. and Brewer, P. G., 1977, The marine chemistry of iodine in anoxic basins: Geochimica et Cosmochimica Acta, v. 41, p. 151-159.

Zhao, M.-Y., Zheng, Y.-F. and Zhao, Y.-Y., 2016, Seeking a geochemical identifier for authigenic carbonate: Nature communications, v. 7, p.

Zhou, X., Jenkyns, H. C., Owens, J. D., Junium, C. K., Zheng, X. Y., Sageman, B. B., Hardisty, D. S., Lyons, T. W., Ridgwell, A. and Lu, Z., 2015, Upper ocean oxygenation dynamics from I/Ca ratios during the Cenomanian–Turonian OAE 2: Paleoceanography, v., p.

Zhou, X., Thomas, E., Rickaby, R. E., Winguth, A. M. and Lu, Z., 2014, I/Ca evidence for upper ocean deoxygenation during the PETM: Paleoceanography, v. 29, p. 964-975.

SUPPLEMENTAL MATERIALS

Geologic background and Site-specific Data Descriptions and Interpretations

Neogene-Quaternary Carbonate

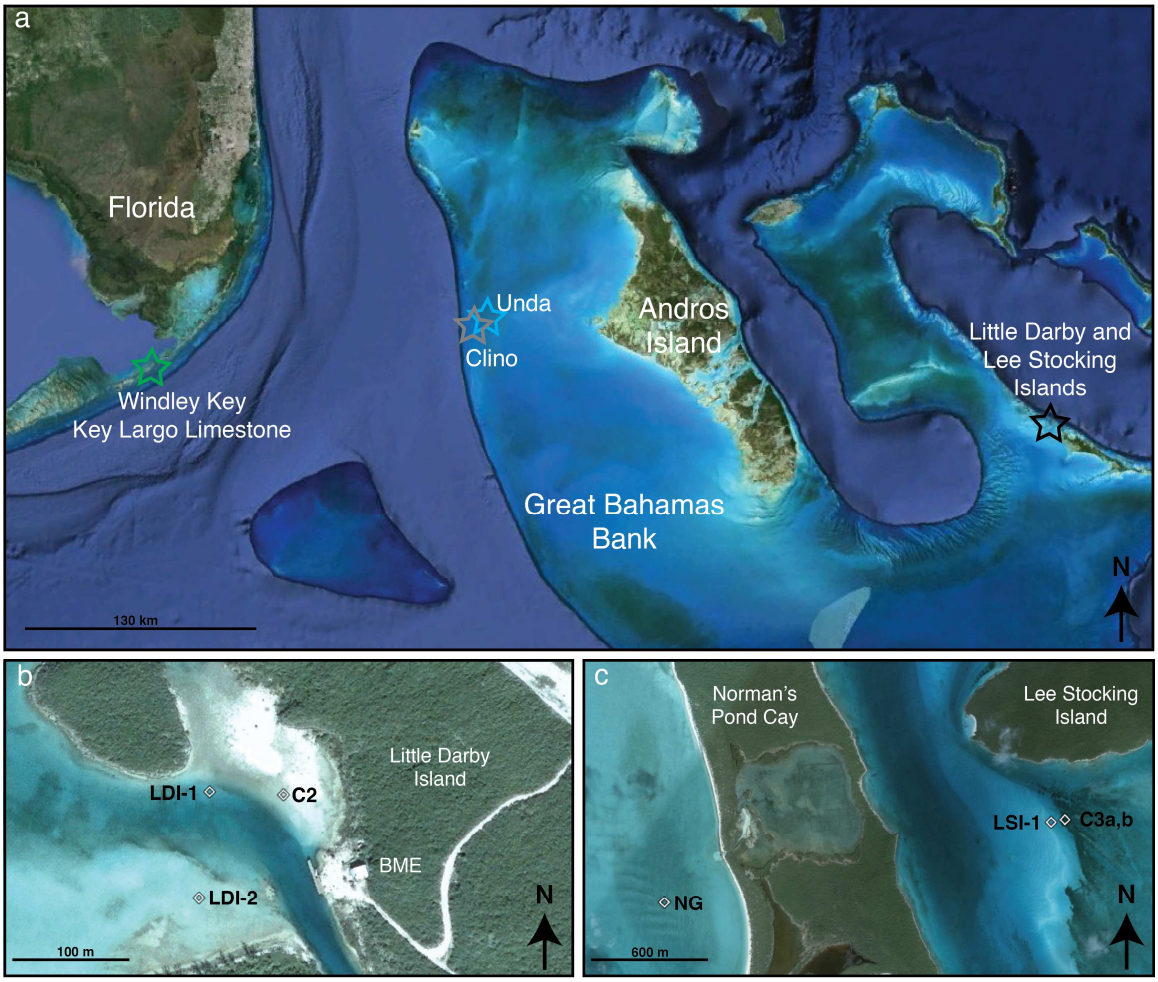

Figure S1. (a) A map showing Bahamas and Florida sampling locations. (b) Inset of sampling localities near Little Darby Island, Bahamas. (c) Inset of sampling localities near Lee Stocking Island, Bahamas. Notice the variation in scale between a, b, and c. The distance between Little Darby Island and Lee Stocking Island sites is ~14.8 km. Core NG (Norman's Grapestones) is the same sampling location for the NG core in a previous study of carbonate diagenesis (Burdige and Zimmerman, 2002) where many cores were collected in the LSI area at locations near our study sites (Burdige and Zimmerman, 2002; Hu and Burdige, 2007). Cores 3a, 3b, and 2 are the same locations as that from another previous study of carbonate diagenesis in the LDI and LSI areas (Romaniello and others, 2013).

Modern Little Darby and Lee Stocking Islands

The Great Bahamas Bank short cores were collected near Little Darby (LDI) and Lee Stocking Islands (LSI), Bahamas (Supplementary Figure 1; Supplementary Table 1). The core locations were explicitly selected as they track previous studies at LDI (Romaniello and others, 2013) and LSI (Burdige and Zimmerman, 2002; Hu and Burdige, 2007) where details regarding carbonate geochemical characterization and diagenesis are provided. Core NG (Norman's Grapestone's) is approximately the same sampling location for the NG profile in a previous study of carbonate diagenesis (Burdige and Zimmerman, 2002) where many cores were collected in the LSI area at locations near our study sites (Burdige and Zimmerman, 2002; Hu and Burdige, 2007). Cores 3a, 3b, and LSI-1 are approximately the same locations as that from another previous work evaluating carbonate diagenesis in the LDI and LSI areas (Romaniello and others, 2013). Together, this context, as well as the results obtained as part of this study, imply that our down core profiles most effectively constrain the primary I/(Ca+Mg) of aragonite-HMC dominated sediments from a variety of well-oxygenated carbonate depositional environments and more minimally the potential effects of initial burial and early sediment diagenesis. Basic characterization of the sampling localities is given in Supplementary Table 1.

Table S1. Coordinates, water depth, and key features for cores from near Little Darby and Lee Stocking Islands, Bahamas, shown in Supplementary Figure 1.

Core	Coordinates	Water Depth (m)	Key Features
C1	23°51'24.59"N 76°13'30.85"W	<1	intertidal
LDI-1	23°51'24.68"N 76°13'33.25"W	<5	subtidal/*Thalassia testudinum* bed
Core 3a	23°46'11.21"N 76° 6'48.92"W	<10	subtidal/*Thalassia testudinum* bed
NG	23°45'57.18"N 76° 8'3.00"W	<10	subtidal/ooid aggregates or grapestones
Core 3b	23°46'11.21"N 76° 6'48.92"W	<10	subtidal/*Thalassia testudinum* bed
LSI-1	23°46'10.78"N 76° 6'51.48"W	<10	subtidal/ooid aggregates or grapestones
LDI-2	23°51'21.55"N 76°13'33.52"W	<2	subtidal/ooid aggregates or grapestones

Push cores were collected during December 2012 using polyethylene tubing hammered into the sediment via a rubber mallet; with the core tubes sealed using rubber stoppers. In many cases, we were able to simply wade to the site of core collection during low tide, but cores NG, LSI-1, and Cores 3a,b were retrieved via diver due to a greater water depth (<10 m). Cores were kept vertical prior to and during sediment removal. Sediment was retrieved from the core barrel simply by pushing the sediment from the bottom up using a plastic plunging device and then slicing sediment into 0.5-3 cm intervals as the sediment became exposed at the top of the core barrel. Pore waters were removed via ceramic rhizon samplers (Seeberg‐Elverfeldt and others, 2005) and any residual water was evaporated in a muffle furnace at 60°C. Samples were powdered and homogenized using mortar and pestle. Data collection for I/(Ca+Mg) ratios, $\delta^{13}C$, and mineralogy are described in the Supplemental Methods. Data are shown in Supplementary Figure 2 and Supplementary Data Table 2. As with our Precambrian carbonate, bulk carbonate was measured. The inoculation of pore water splits from select cores with zinc acetate precipitated pore water dissolved sulfide from the pore waters as ZnS, which was quantified via spectrophotometry (Cline, 1969). In each case low dissolved sulfide was detected indicating active sulfate reduction and hence the likelihood that pore water iodine is represented as iodide (I^-), the reduced iodine species that does not precipitate with carbonate (Lu and others, 2010).

LSI and LDI carbonate reveal slightly positive $\delta^{13}C_{carb}$ (Supplementary Table 2), that expected for largely aragonitic carbonate (Swart and Eberli, 2005). This is due to a slight positive $\delta^{13}C$ fractionation from marine dissolved inorganic carbon (DIC) during aragonite precipitation as well as photosynthetic-driven local positive $\delta^{13}C$ of DIC along carbonate ramps relative to that of global DIC (Swart and Eberli, 2005). As discussed in the main text, our results indicate that the highest I/(Ca+Mg) values from our carbonate survey are found in the LSI and LDI samples and

that this is largely a function of these samples consisting dominantly of primary aragonite and high-Mg calcite (HMC).

Interestingly, the range of I/(Ca+Mg) values in LSI and LDI samples is in itself quite large, from 5.80 to 11.61 μmol/mol (Supplementary Figure 2), which could be derived from differing iodate (IO_3^-) availability at the local sites, differences in iodine contents in HMC versus aragonite, or recrystallization in anoxic pore fluids. Evaluation of the individual cores indicate that the range of core top values is much smaller and elevated, 7.46-11.61 μmol/mol, relative to the combined LDI and LSI sample set and that I/(Ca+Mg) values, if anything, decrease going down core (Supplementary Figure 2). This observation could indicate recrystallization in anoxic pore fluids, as indicated by the presence of dissolved sulfide in the pore waters at LDI and LSI, is diluting primary I/(Ca+Mg) ratios. Indeed, there are small amounts of low-Mg calcite (LMC) in most of the samples, which likely represents recrystallized carbonate (Burdige and Zimmerman, 2002; Hu and Burdige, 2007). However, no internal trend for combined LSI and LDI samples (or the individual cores) of decreasing I/(Ca+Mg) with increasing weight percent LMC is present, suggesting recrystallization to LMC is, if anything, not completely responsible for the lower I/(Ca+Mg) values. We also note that we were unsuccessful in assigning particular I/(Ca+Mg) values to each aragonite and HMC and using mass balance based purely on differences in the abundance in primarily mineralogy to explain the LSI and LDI observations. Also, I/(Ca+Mg) does not systematically vary based on depositional setting (e.g. ooids, intertidal, subtidal, sea grass, sea grass free; Supplementary Table 1; Supplementary Figure 2). Together, these results indicate a combination of factors as responsible for the observed I/(Ca+Mg) range in LSI and LDI carbonate.

Importantly, however, our results clearly reveal I/(Ca+Mg) associated with primary aragonite and HMC as higher than secondary LMC and dolomite and a lack of diagenetic

increases. Also, the I/(Ca+Mg) range from well-oxygenated LSI and LDI settings, 5.51 to 11.6 μmol/mol (Glock and others, 2014; Hardisty and others, 2014; Lu and others, 2010; Zhou and others, 2015; Zhou and others, 2014), is easily distinguished from the <2.6 μmol/mol observed in carbonate from low oxygen waters near the oxycline of oxygen minimum zones and other hypoxic settings ((Glock and others, 2014; Lu and others, 2016); (red squares, Figure 2) and is comparable to the I/(Ca+Mg) range from calcite foraminifers from well-oxygenated settings (Lu and others, 2016). We also point out that the LSI and LDI I/(Ca+Mg) values are similar to the highest I/(Ca+Mg) found in carbonate capturing the Shuram and the highest Phanerozoic values (Figure 2, 3).

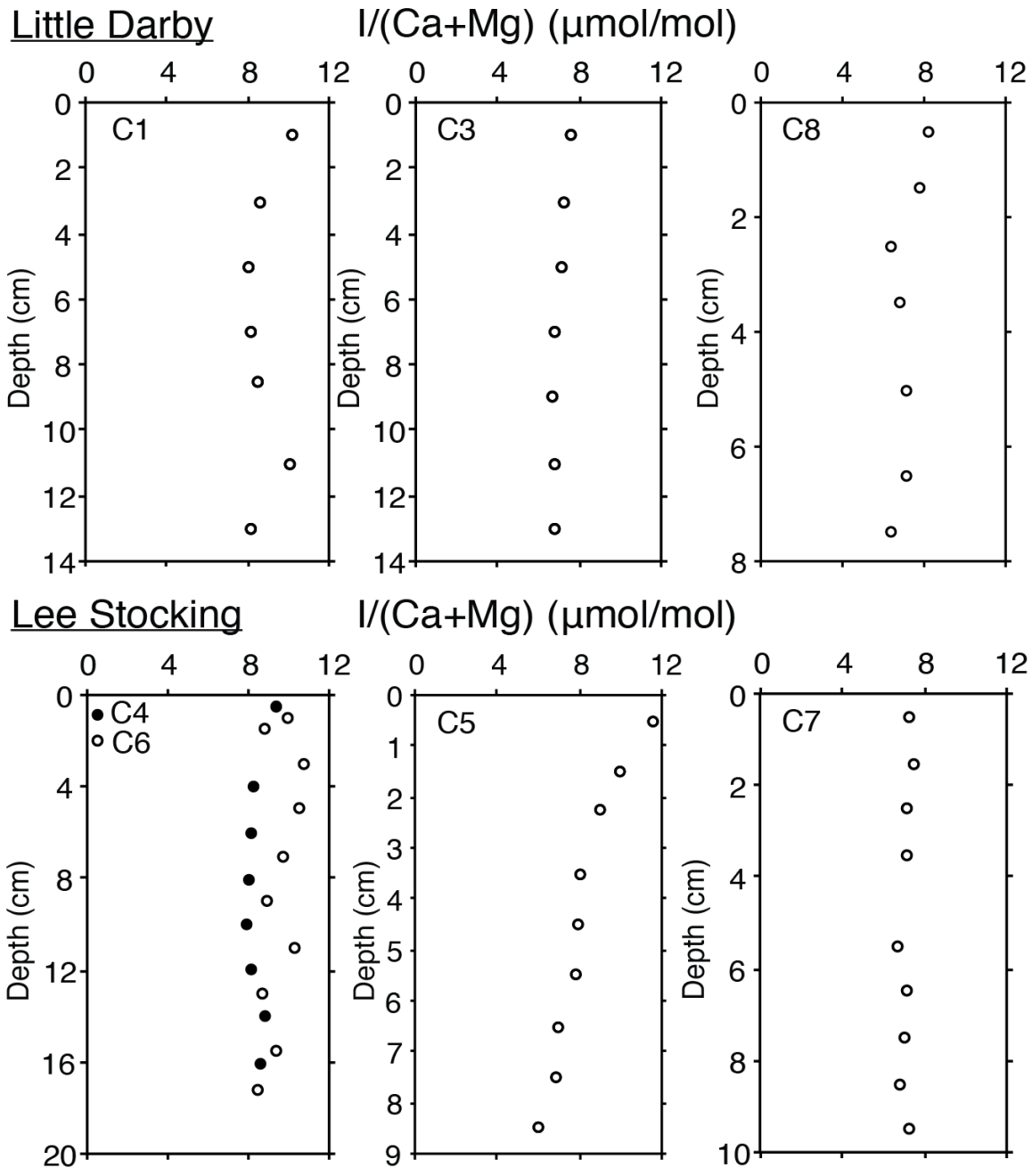

Figure S2. I/(Ca+Mg) ratios for seven different cores collected near Little Darby and Lee Stocking Islands. Note the variable depth scales on the y-axes. The coring locations are shown in Supplementary Figure 1 and details are given in Supplementary Table 1.

Pleistocene Key Largo Limestone

Aragonite dissolution and re-precipitation as LMC can occur when each aragonite and HMC are exposed to meteoric fluids (McClain and others, 1992). This process is common when sea level regression or tectonic uplift exposes aragonitic carbonate facies. Depending on atmospheric redox, organic matter content in sediments, and the degree of isolation, diagenesis under these conditions has the potential to be poised at an oxygenated state, meaning that IO_3^- is potentially available in the pore fluids, compromising primary I/(Ca+Mg) ratios from seawater. However, importantly, previous studies evaluating meteoric alterations in the Bahamas found that such alterations were distinctly limited to the the vadose and upper phreatic surface where active sulfate reduction was occurring (McClain and others, 1992). If conditions are anoxic during recrystallization, primary iodine is anticipated to be overprinted, as only IO_3^- is precipitated with carbonate, which requires at least slightly oxic conditions (Lu and others, 2010).

In order to elucidate the effects of this type of meteoric diagenesis on I/(Ca+Mg) ratios, we measured I/(Ca+Mg) ratios across three aragonite-to-calcite transitions driven by meteoric fluids in *Montastrea annularis* coral heads from the Pleistocene Key Largo Limestone of South Florida (Gill and others, 2008) (Supplementary Figures 1 and 3). The transects analyzed for I/(Ca+Mg) are exactly the same as those used in a more detailed study by Gill et al. (Gill and others, 2008), who assessed the response of carbonate-associated sulfate, or CAS, under the same conditions, providing mineralogical and geochemical (such as $\delta^{18}O$, $\delta^{13}C$, [CAS], $\delta^{34}S_{CAS}$, and the elemental concentrations of Sr, Mg, Na, and K) context for each sample. The presence of the *M. annularis* coral has not to our knowledge been documented in anoxic or low oxygen settings and its simple presence represents an indicator of well-oxygenated water column conditions during primary carbonate precipitation. Some support for this comes from the sulfide stress associated with black band disease causing fatality in *M. annularis* (Carlton and Richardson, 1995).

I/(Ca+Mg) changes little across the negative $\delta^{13}C$ excursion and aragonite-LMC transitions of the Key Largo Limestone (Figure 1; Supplementary Figure 3). Only one of the three transections, KL-11, shows an I/(Ca+Mg) decrease across this boundary, and even in this case the decrease is only sustained in some LMC samples. Importantly, we point out that I/(Ca+Mg) from the largely aragonitic portions of the coral heads is lower relative to that from LSI and LDI samples. This could represent minor recrystallization to LMC in the aragonite portions of the transects (Figure 1) or unconstrained vital effects associated with *M. annularis*. Vital effects are not relevant to our Precambrian carbonate.

As discussed in the text, this case study provides preliminary evidence that I/(Ca+Mg) ratios can be preserved during meteoric alterations, but that decreases are possible during recrystallization. We speculate that such preservation of primary I/(Ca+Mg) ratios during recrystallization provides evidence of sustained oxic conditions during aragonite-to-LMC recrystallization. Further, the I/(Ca+Mg) ratios from the aragonitic portions of the corals are shown in the main text (blue squares, Figure 4) as representing I/(Ca+Mg) values from primary carbonate from a well-oxygenated setting. This is consistent with the I/(Ca+Mg) range in *M. annularis* as elevated relative to that of the low oxygen settings near the chemocline of the Peruvian OMZ (Glock and others, 2014) and other hypoxic settings (Lu and others, 2016) and being similar to that from calcitic forams from well-oxygenated settings (Lu and others, 2016).

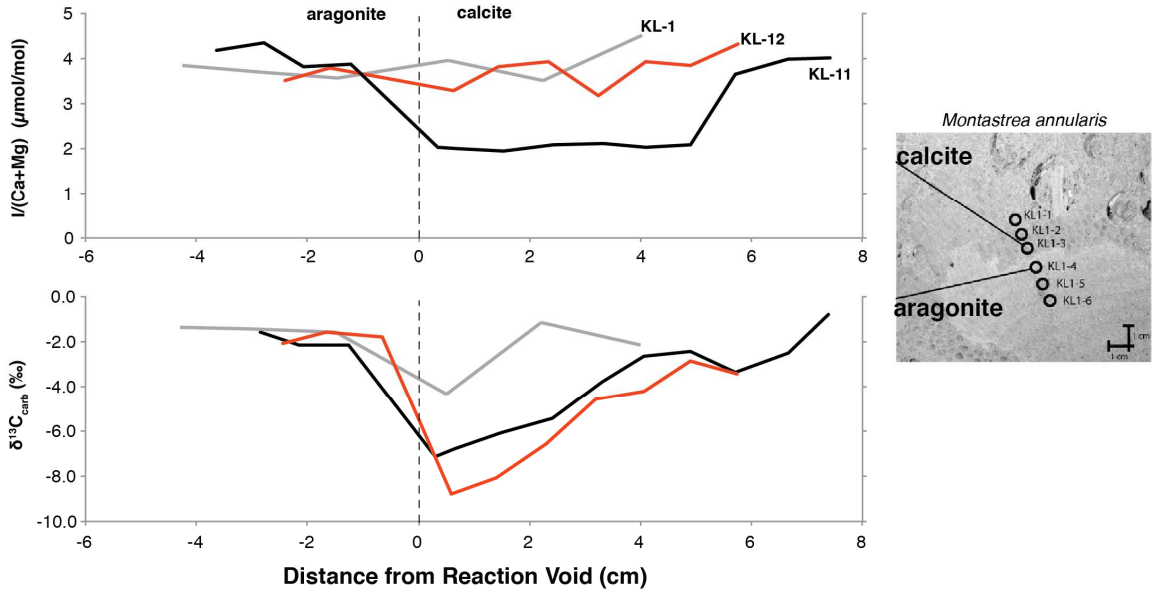

Figure S3. (a) I/(Ca+Mg) and (b) δ13Ccarb for transects from three aragonite-dominated to calcite-dominated portions of (c) Montastrea annularis coral heads of the Pleistocene Key Largo Limestone of south Florida. The mineralogical transition is driven by carbonate subaerial exposure, dissolution of primary aragonite, and recrystallization of secondary calcite in meteoric fluids. The samples and transects are the exact same as those use in Gill et al. (ref (Gill and others, 2008)).

Miocene-recent Clino and Unda

The Clino and Unda cores of the Bahamas Bank Drilling Project (1991) are extremely well characterized with respect to diagenesis (Melim, 1996, 2001; Melim and others, 2004; Melim and others, 1995; Swart, 2001a, b; Swart and Eberli, 2005; Swart and Melim, 2000), mineralogy (Melim and others, 1995), and sedimentology (Kenter, 2001; Manfrino, 2001). Important aspects are highlighted below, but readers are referred to these comprehensive previous works for detailed background information. The Clino and Unda cores capture a prograding carbonate ramp along the slope of the Great Bahamas Bank (GBB) from the late Miocene until late Pleistocene (Supplementary Figure 1; Supplementary Figure 4). The presence of reefs and other organisms indicate that water column conditions were well oxygenated throughout deposition, which is not disputed by any previous studies, meaning changes in I/(Ca+Mg) are

most likely to represent diagenetic alterations, mineralogical variation, and changes in depositional setting, not water column redox dynamics.

In the case of Clino (Supplementary Figure 4), sediments below ~150 m represent a former slope setting on the margin of the GBB originally composed largely of bank-top derived aragonite along with more minor pelagic LMC coccolithophores and foraminifera. The core captures multiple periods of sea level transgression and regression and records multiple phases of associated subareal exposure (Swart and Eberli, 2005). Bank top-derived aragonite is highest during high stands (Swart and Eberli, 2005). Now, following extensive recrystallization to more stable carbonate phases, paleo-slope carbonate consists of various combinations of each aragonite, LMC, and dolomite, with diagenetic recrystallization of primary aragonite and HMC occurring exclusively in marine pore fluids.

Above 150 m, Clino carbonate was deposited on a platform setting primarily as aragonite and HMC. The near absence of primary aragonite and HMC minerals (Melim and others, 1995), the presence of multiple exposure horizons (Manfrino, 2001; Melim, 2001; Melim and others, 1995), and the presence of a negative $\delta^{13}C$ excursion (Melim and others, 1995) unrelated to the $\delta^{13}C$ of DIC of overlying or global seawater together indicate multiple periods of subaerial exposure during sea level variations and subsequent recrystallization of primary aragonite and HMC to LMC in meteoric fluids. Clino dolomite is inferred from previous work as precipitating in association with either non-depositional surfaces or in geochemically evolved pore fluids (Swart, 2001b; Swart and Melim, 2000). Samples for this study were collected that capture variable combinations of primary versus diagenetic carbonate minerals, variable styles of dolomitization, the distinct diagenetic zones (meteoric vs. marine pore fluids), the $\delta^{13}C_{carb}$ excursion, and variable sedimentology.

Unda was not sampled in as high of resolution as Clino, but instead specific intervals were targeted. Unda deposition occurred entirely on the platform near the margin of the Great Bahamas Bank (Kenter, 2001; Manfrino, 2001). Similar to Clino, the upper portion of Unda (above ~106 m) has experienced meteoric aragonite-HMC alterations while carbonate below ~106 m has experienced diagenesis exclusively in marine pore fluids (Melim, 2001; Melim and others, 1995). Samples were collected that capture the meteoric-marine burial diagenetic transition as well as specific intervals below this transition where dolomite is particularly abundant. Unda dolomite is inferred, with limited exceptions, as having precipitated at some time long after deposition but in seawater-like fluids, as constrained by the $^{87}Sr/^{86}Sr$ ratios of dolomite yielding ages significantly younger than the host sediment (Swart, 2001a) and un-evolved pore water profiles gradients with a similar composition to seawater (Swart, 2001b; Swart and Melim, 2000).

For Clino, I/(Ca+Mg) values are all <5.71 μmol/mol (Supplementary Figure 4). A detailed evaluation of the down core trends indicates that I/(Ca+Mg) ratios are elevated in the aragonite-dominated portions of the core, with these values being similar to that expected for well-oxygenated water columns (Figure 2 main text). Importantly, we also point out that the changes in I/(Ca+Mg) are decoupled from the negative carbon isotope excursion in Clino, which is derived from meteoric alteration of aragonite and HMC to LMC. Instead, the I/(Ca+Mg) values are systematically overprinted to lower values during progressive recrystallization of primary aragonite and HMC to secondary carbonate minerals. The changes in I/(Ca+Mg) going down core do not track the paleo-environment, sedimentology, carbon isotopes, or diagenetic style, but instead mineralogy and associated Ca/Mg ratio (Figure 1; Supplementary Figure 4). The $\delta^{13}C$ and mineralogy found for this study are similar to that of previous works for other samples of the same cores (Melim and others, 1995).

For Unda, the I/(Ca+Mg) values are uniformly low, with all values <1.01 μmol/mol and values not exceeding 0.4 μmol/mol at dolomite >40 weight % (Figure 2b main text) and decreases in I/(Ca+Mg) with associated decreases in Ca/Mg, reflecting dolomite. The $\delta^{13}C$ and mineralogy found for this study are similar to that of previous works evaluating different samples from the same core (Melim and others, 1995).

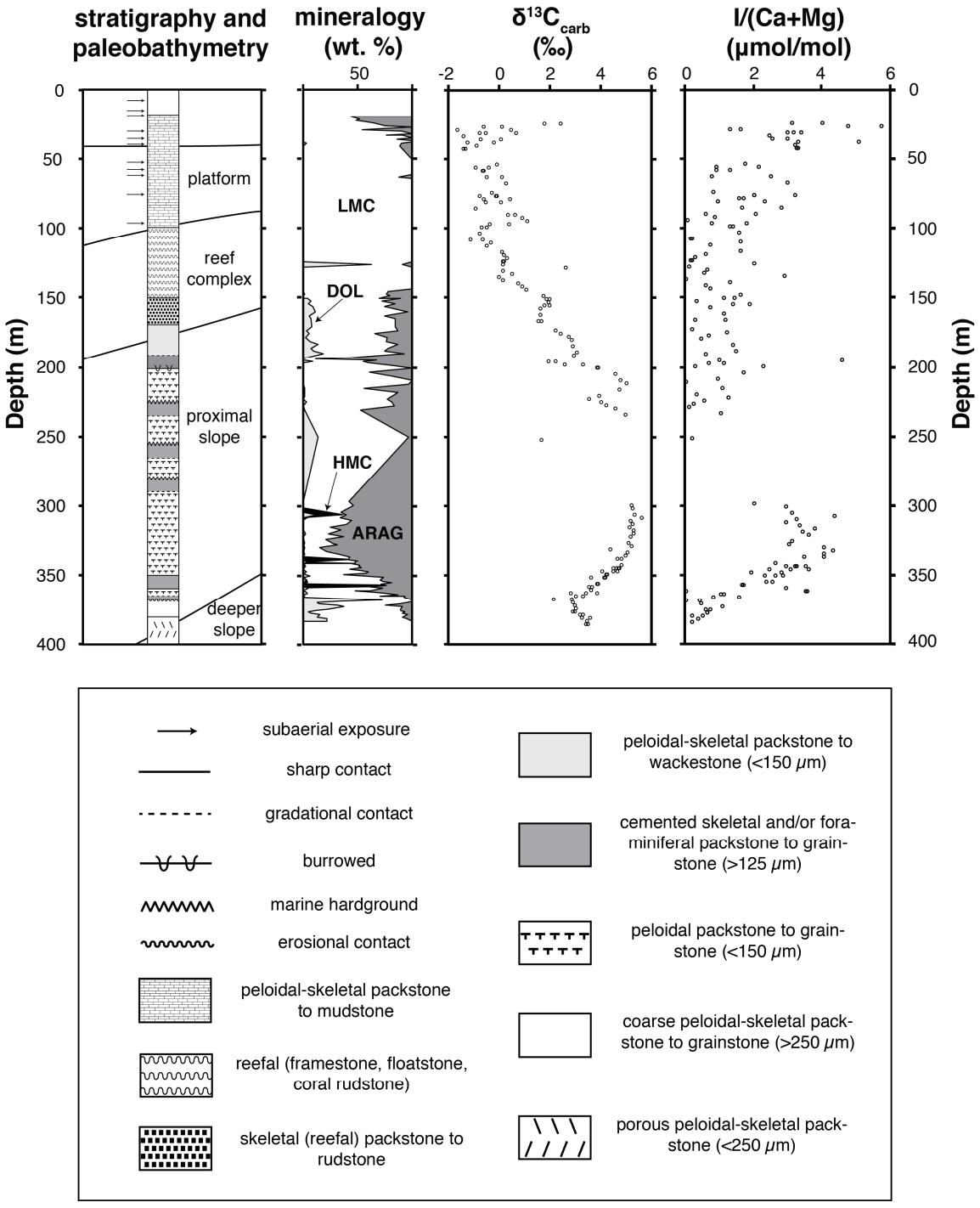

Figure S4. The (a) paleobathymetry, (b) carbonate mineralogy, (c) $\delta^{13}C_{carb}$, and (d) I/(Ca+Mg) ratios for core Clino of the Great Bahama Bank. The lithological descriptions come from references (Kenter, 2001; Manfrino, 2001).

Miocene Monterey Formation

We analyzed samples from largely dolomite concretions of the Monterey Formation of Central California that are the exact same as those used in Loyd et al. (ref (Loyd and others, 2012a)). In this previous work and others, it was determined that the dolomite concretions formed largely in anoxic pore fluids characterized by iron reduction, sulfate reduction, or methanogenesis and closed to exchange with seawater (Blättler and others, 2015; Loyd and others, 2012a). As these electron acceptors are well constrained as being utilized following quantitative IO_3^- reduction (Farrenkopf and others, 1997; Kennedy and Elderfield, 1987a; Kennedy and Elderfield, 1987b; Rue and others, 1997), iodine speciation in the pore fluids hosting the bulk of concretion formation is expected to be quantitatively I^-. Since I^- does not precipitate with carbonate (Lu and others, 2010), these dolomite are expected to have little-to-no iodine, similar to pre-GOE carbonate (Hardisty and others, 2014).

The Monterey sample set is largely dolomite and I/(Ca+Mg) ratios do not exceed 0.46 μmol/mol (Figure 1). This value is low relative to even the middle Proterozoic range but is still elevated relative to that anticipated from anoxic pore fluids. We suggest that this data may imply, building results from Loyd et al. (ref (Loyd and others, 2012a)), that the concretions began formation earlier during diagenesis in at least weakly oxidizing fluids, but formed in mainly in anoxic pore fluids. Other possible iodine sources include dolomitization of iodine-containing calcitic foraminifers (found only rarely in these concretions) or other primary carbonate containing iodine derived from the overlying water column.

Proterozoic Carbonate

~2.03 Ga Wooly Dolomite

The Wooly Dolomite of the Wyloo Group in the Horseshoe rift basin of Western Australia contains platform carbonate deposited directly after the Lomagundi carbon isotope excursion. Samples of the Wooly Dolomite for this study come from the NMOD-3 drill core from the Mount Olympus area and are exactly those used in ref (Bekker and others, 2016), which includes associated $\delta^{13}C_{carb}$ and $\delta^{18}O_{carb}$ data for the same samples. Details regarding age (Müller and others, 2005), sedimentology, stratigraphy, and geochemistry (Bekker and others, 2016) are all available from previous studies but are described briefly below.

Age constraints for the Wooly Dolomite come from a SHRIMP U-Pb zircon age of 2.031±0.006 Ga from volcaniclastic siltstones and sandstones within the Wooly Dolomite (Müller and others, 2005). The Wooly Dolomite at the Mount Olympus area consists of platform carbonate with interbedded dolomite and siltstone, with dolostone lithofacies containing stromatolitic breccia and cross-bedding along with clastic fragments with oncolitic overgrowths (Bekker and others, 2016). Importantly, the $\delta^{13}C_{carb}$ values from dolomite used in this study from the Mount Olympus Area vary greatly from those observed at other Wooly Dolomite localities, with negative $\delta^{13}C_{carb}$ values observed in most of the samples, indicating extensive diagenetic recrystallization in association with organic matter-rich lithologies (Bekker and others, 2016).

Eleven samples were measured for I/(Ca+Mg) ratios from the Wooly Dolomite (Supplementary Table 3) with values ranging from below blank levels to 0.42 μmol/mol. Given the negative $\delta^{13}C_{carb}$ values for these samples, indicating diagenetic recrystallization and organic matter remineralization, it is difficult in this case to distinguish if extremely low I/(Ca+Mg) ratios are the result of a locally anoxic water column or diagenetic overprinting in exchange with anoxic pore fluids, but we do note that the range of I/(Ca+Mg) ratios is consistent with all other

Mesoproterozoic and post-Lomagundi Paleoproterozoic samples represented in this study. Due to extensive faulting observed in the drill core from the Mt. Olympus area, a stratigraphic context is not available (Krapež, in revision), but we do note, that similarly to other Mesoproterozoic and post-Lomagundi Paleoproterozoic carbonate from this study, there is no correlation of I/(Ca+Mg) ratios with either $\delta^{13}C_{carb}$ or $\delta^{18}O_{carb}$ values, which is not surprising given the extremely low ratios.

~1.97 Ga Snare Group, Basler Lake and Mattberry Lakes, Slave craton, Canada

The greenschist facies Snare Group is developed east of the Wopmay fault zone and includes quartz arenite and stromatolitic and clastic dolomite unconformably overlying the Slave craton and considered correlative with the ~1969 Ma passive margin sequence (Epworth Group) in the northern part of the Wopmay Orogen (Bowring and Grotzinger, 1992; Hoffman and others, 1970; Jackson and others, 2013; McGlynn and others, 1972). It is divided into two members at Mattberry Lake: lower siliciclastic member that contains conglomerate, arenite, siltstone, and mudstone and upper carbonate member that contains dolostone and calc-arenite with rare stromatolites, intraformational breccia, imbricated clasts, and ripple marks (Jackson, 2008; Lord, 1963; Saylor and Grotzinger, 1992). The siliciclastic member (up to 700 m thick) was deposited on a shallow-marine shelf as indicated by trough and hummocky cross-bedding, wavy and flaser bedding, mud cracks, wave ripples, rip-up clasts, graded beds, and load structures (Jackson, 2008; Saylor and Grotzinger, 1992). The carbonate member is a upward-shallowing sequence of rhythmite, stromatolotic bioherms, and irregularly laminated, cherty dolomite with tepee structures deposited in carbonate shelf and slope setting (Saylor and Grotzinger, 1992). A karstic breccia is developed between the upper and lower members.

Only 4 samples were measured for I/(Ca+Mg) from the Snare Group with only 2 > blank levels but < 0.3 μmol/mol (Supplementary Table 3). This observation is consistent with low

I/(Ca+Mg) ratios in the temporally surrounding Wooly Dolomite and Pethei Group and generally consistent with the range observed for most carbonate from ~2-1 Ga.

~1.88 Ga Taltheilei Formation, Pethei Group, East Arm of Slave Lake, Slave craton, Canada

The 130 to 200 m thick Taltheilei Formation of the Pethei Group was deposited along the southeastern margin of the Slave craton and belongs to the platform facies. It contains shallow-water, marine stromatolitic dolomite of two facies: 1) laterally-continuous, stromatolitic, laminated, and massive dolomite with oncolites, edgewise conglomerates, and desiccation cracks of back-reef, intertidal lagoonal setting, and 2) stromatolitic bioherms consisting of branching stromatolites with elliptical plain view surrounded by coarse-grained, clastic carbonate of barrier-reef setting (Hoffman, 1968; Hoffman, 1974). Recent and ongoing geochronologic studies bracket this unit between ~1.88-1.85 Ga in age (Kjarsgaard, 2013; van Breemen and Aspler, 2013).

Fourteen samples from the Taltheilei Formation were measured for I/(Ca+Mg) ratios (Supplementary Table 3). Seven of the samples were > blank iodine levels and all samples were <0.3 μmol/mol.

~1.8 Ga Duck Creek Formation

The Paleoproterozoic Duck Creek formation spans ~1000 m of the Ashburton Basin in Northwestern Australia. Samples from this study come directly from those used in Wilson et al. (ref.(Wilson and others, 2010)), where additional details regarding age, depositional setting, paleobiology, diagenetic history, and geochemistry can be found.

The Duck Creek Formation age is constrained at ~1.8 Ga by a U-Pb date of 1.795±0.007 Ga from zircons within an ashbed near the top of the formation (Wilson and others, 2010), a date

consistent with previous studies (Evans and others, 2003; Sircombe, 2003). The Duck Creek Formation was deposited along a marginal setting with two distinct sedimentary sequences that record deepening above peritidal carbonate successions (Wilson and others, 2010). In this study, we focused on shallow facies, as evidenced by imbricated clasts, ripples, hummocky cross-stratification, low relief stromatolites truncated by beach rock, and frequent grainstone (Wilson and others, 2010).

The I/(Ca+Mg) ratios in the Duck Creek Formation are within the range of all other Late Paleoproterozoic and Mesoproterozoic carbonate measured in this study, with values ranging from below blank values to 0.48 μmol/mol (Supplementary Table 3). Twenty three samples were measured in total from the Duck Creek Formation, with 11 at blank values and most <0.2 μmol/mol. Fe-rich carbonate are abundant within the shallow carbonate settings, indicating ferruginous bottom waters and providing evidence for redox stratification in the near surface (Wilson and others, 2010). Our iodine data show no relationship to sequence stratigraphy, mineralogy, or $\delta^{13}C_{carb}$ or $\delta^{18}O_{carb}$, but they are generally consistent with independent evidence for a shallow chemocline (Wilson and others, 2010).

~1.65 Ga Paradise Creek Formation

The Mesoproteozoic Paradise Creek formation is within the McNamara group of Northern Australia, part of the Lawn Hill Platform which covers an area of ~20,000 km^2 with thicknesses between 2.5 and 8.5 km. Paradise Creek samples from this study are taken from the Oxide Creek section and are directly those used in Gellatly and Lyons (2005) for determination of [CAS] and $\delta^{34}S_{CAS}$. Details on age constraints (Idnurm, 2000; Page and others, 2000), sedimentology (Sami, 2000), and geochemistry (Gellatly and Lyons, 2005) of the Paradise Creek formation are available from previous studies, but briefly described below.

The ~1.65 Ga age of the Paradise Creek formation is constrained via a U-Pb SHRIMP

date of 1.658±0.003 Ga within a thin pink tuffaceous bed within the Paradise Creek Formation (Idnurm, 2000) which is further supported by ages of 1.678±0.002 and 1.595±0.006 Ga from overlying rhyolites and underlying tuffs, respectively (Page and others, 2000). The Paradise Creek is interpreted to record multiple shallowing and deepening sequences, with storm lag deposits, ooid grainstones, cross-stratification, some evaporate pseudomorphs, desiccation features, scour surfaces, and stromatolites, all indicating dominantly shallow water platform to ramp deposition (Sami, 2000). In general, the predominance of peloidal silt and silt-sized grains and storm lag deposits opposed to carbonate muds has been used to infer that McNamara Group deposition was dominated by detrital opposed to chemically precipitated carbonate (Sami, 2000).

I/(Ca+Mg) ratios from the Paradise Creek formation (Supplementary Table 3) at Oxide Creek show no stratigraphic trends or apparent relationship with CAS (Gellatly and Lyons, 2005). The data set is sparse relative to some other sections measured, making it difficult to assess stratigraphic trends, but the range in I/(Ca+Mg) is similar to that of all other Mesoproterozoic and Late Paleoproterozoic carbonates measured. Values are generally near or blank values at < 0.1 μmol/mol, but two high values near 0.75 μmol/mol are present. The data are however similar to [CAS] in that maximum absolute values are low relative to their Neo- and Paleoproterozoic counterparts (Hardisty and others, 2014; Planavsky and others, 2012).

~1.45 Ga Helena Formation

The Helena Formation is part of the Middle Belt carbonate of the Belt Supergroup, which is exposed across approximately 130,000 km^2 of Montana and Idaho, USA (Winston, 1990), and ranges from 5 to 16 km in thickness. Samples from the Helena formation at Ousel Creek are those used from Gellatley and Lyons (2006), a study of Mesoproterozoic sulfate concentration. Details regarding Helena age constraints (Aleinikoff and others, 1996; Evans and others, 2003), $\delta^{34}S_{CAS}$ and [CAS] (Gellatly and Lyons, 2005) and other geochemical data (Frank and others, 1997), and

associated stratigraphic and sedimentological descriptions (Winston and Lyons, 1993) and diagenetic interpretations(Frank and Lyons, 1998; Pollock and others, 2006) are available from previous studies, but are summarized briefly below.

The ~1.45 Ga Helena age is constrained by U-Pb ages of 1.449±0.010 Ga from a tuff bed in the upper Helena at Logan Pass and 1.443±0.005 in the overlying Purcell Lava at the base of the directly overlying Missoula Group (Aleinikoff and others, 1996; Evans and others, 2003). The lower Helena formation contains ~10 m thick cyclic intervals of siliciclastic to carbonate rocks representing shallowing and deepening sequences and transitions to stromatolitic and oolitic facies in the middle and upper portion of the formation. Each is captured in detail in this study. Evidences for shallow deposition include mudcracks and other dessication features, stromatolites, storm lag deposits, and crossbedding (Winston and Lyons, 1993). We point out that ref. (Winston and Lyons, 1993) used the sedimentology to infer a landlocked basin similar to the modern Caspian Sea while, however, more recent interpretations support marine deposition for most of the Helena Formation (Gellatly and Lyons, 2005; Luepke and Lyons, 2001; Lyons and others, 2000). We further point out that potential diagenetic features, molar tooth structures in particular (Frank and Lyons, 1998; Pollock and others, 2006), are found throughout the Helena (Winston and Lyons, 1993), but these features were not a focus of this study and in general I/(Ca+Mg) ratios in bulk rock analysis containing and not containing molar tooth structures varied little (Supplementary Table 3).

The I/(Ca+Mg) ratios throughout the Helena deposition (Supplementary Table 3) are similar to most other Mesoproterozoic and Late Paleoprtoerozoic sections in this study, with values <0.5 μmol/mol. Intriguingly however, there is a possible trend of increasing values going up section, a trait not observed in any other Mesoproterozoic section. As has been noted for other Proterozoic sections with associated [CAS] values, the Paleoproterozoic Mcheka carbonate

specifically (Hardisty and others, 2014; Planavsky and others, 2012), the trend generally correlates with increasing [CAS] values, suggesting locally increased SO_4^{-2} and IO_3^- abundance going up section. Gellatly and Lyons (2005) suggest local controls on salinity resulting from a switch to a more restricted setting, suggesting the observed trend, if anything, is local. The data are further similar to [CAS] in that maximum absolute values are low relative to their Neo and Paleoproterozoic counterparts (Hardisty and others, 2014; Planavsky and others, 2012). We do comment however that the coupled trend is a general stratigraphic observation and not supported by crossplots of I/(Ca+Mg) versus [CAS], likely due to both low data resolution and differing diagenetic sensitivities between [CAS] and I/(Ca+Mg).

~1.437 Ga Tieling Formation

The Tieling Formation is at the top of the Jixian Group of North China. Samples for this study came from a JQ2 drill core from Kuangcheng County in a suburb 250 kilometers northeast away from Beijing. The Tieling Formation is dated at 1.437±0.021 Ga using SHRIMP U-Pb zircon ages from a K-bentonite bed within the Tieling Formation itself (Su and others, 2010). The Tieling has a lower member (Daizhuangzi) comprised of manganiferous dolomite and an upper member (Laohuding) composed of stromatolitic limestone with dolomite in the upper and lower portions (Mingxiang and others, 2008). The lower dolomitic member is interpreted as having been deposited largely within the intertidal zone, while the upper member was deposited from shallow subtidal to intertidal environments. In general, the dolomite occurs most commonly from portions interpreted as intertidal (Mingxiang and others, 2008).

The I/(Ca+Mg) ratios from the Tieling Formation are the highest observed in the middle Proterozoic (up to 2.72 μmol/mol) and are also elevated relative to the rest of the Proterozoic, outside of the Shuram (Supplementary Figure 5). Importantly, unlike the Shuram, the I/(Ca+Mg)

range from the Tieling is still similar to that of modern low oxygen water columns (Glock and others, 2014; Lu and others, 2016) (Figure 2). We point out that the highest I/(Ca+Mg) ratios from the Tieling Formation are observed specifically from portions containing dolomite, which is discerned by Ca/Mg values of ~1-20 mol/mol (Supplementary Figure 5; Supplementary Figure 6). This may reflect a mineralogical bias, with the dolomite best capturing seawater IO_3^-, as discussed in the main text. Alternatively, as the dolomite is interpreted as having been deposited in very shallow settings, the elevated I/(Ca+Mg) may represent better-oxygenated waters relatively more distal from the chemocline. Regardless, the high I/(Ca+Mg) ratios from the Tieling represent local redox conditions, but we also point out that I/(Ca+Mg) ratios from the syndepositional Kaltasy Formation (discussed below), though not elevated, show an abundance of non-blank iodine values relative to the rest of the Proterozoic sample sets. Together, this may suggest a period of chemocline deepening and associated redox stability in shallow water near ~1.43 Ga relative to surrounding time periods. So called "Ocean Oxygenation Events" have been proposed for the Ediacaran (Sahoo and others, 2016), represented by temporally restricted oxic indications in an otherwise largely anoxic ocean. Such a scenario may describe the water column during Tieling deposition, which warrants further investigation.

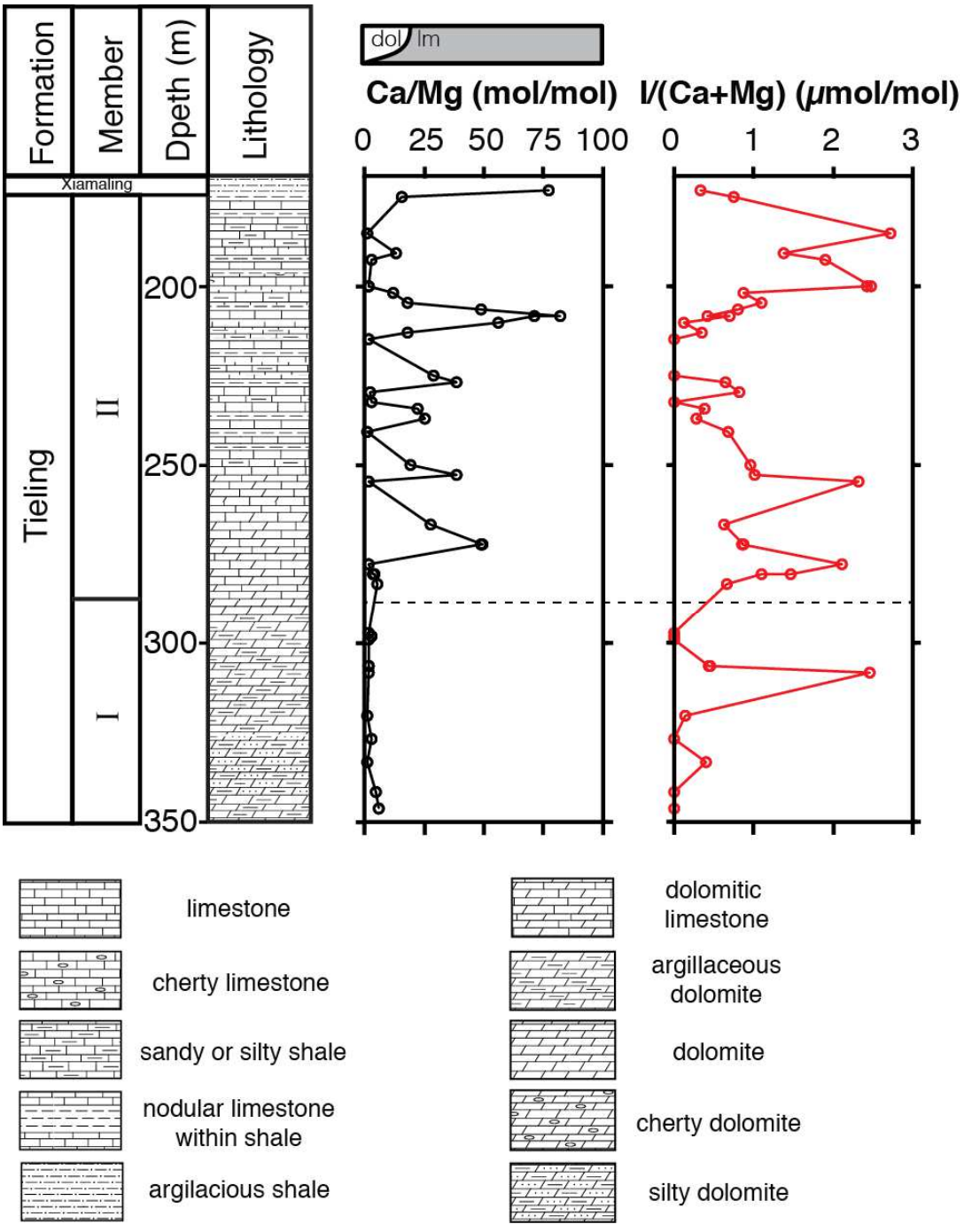

Figure S5. The stratigraphic column and key, Ca/Mg ratios and I/(Ca+Mg) ratios from the Tieling Formation. The upper box is a qualitative representation of dolomite versus limestone abundance as a function of Ca/Mg ratios, which is justified in Supplementary Figure 6. The horizontal dashed line represents the upper and lower members, as described in the supplementary text for the Tieling Formation.

~1.43 Ga Kaltasy Formation

The Kaltasy Formation is part of the Kyrpy Group of the Kama-Belaya aulacogen within the broader Eastern European Platform. Kaltasy carbonate samples from this study come from drill core (borehole 203) of the Bedryazh area, which captures up to 2400 m of the Kaltasy Formation. Samples for this study were previously examined by Kah et al. (ref. (Kah and others, 2007)), and are thus well constrained with respect to $\delta^{13}C_{carb}$, $\delta^{18}O_{carb}$, $^{87}Sr/^{86}Sr$, and elemental concentration (Ca, Mg, Fe, Mn, Sr). A distinct sample set from the same drill core were used in a separate study of age, paleobiology, and redox geochemistry as defined by Fe speciation and trace metal abundances of the underlying Arlan member (Sperling and others, 2014). Details regarding age, sedimentological and stratigraphical descriptions, geochemistry, and paleobiology can be found in ref (Kah and others, 2007) and ref (Sperling and others, 2014); we describe them briefly below.

Re-Os dates from shale of the lower Kaltasy Formation (Arlan member) yield depositional ages of 1.414±0.040 and 1.427±0.043 Ga, constraining Kaltasy age to ~1.43 Ga (Sperling and others, 2014). Carbonate strata of the Ashit member are composed largely of shallow water dolomicrite, and record grain size variation and episodic limestone and marl deposition relating to shallowing and deepening cycles within a generally shallow-marine carbonate platform (Kah and others, 2007).

I/(Ca+Mg) ratios from the Kaltasy Formation (Supplementary Table 3) fall within the typical range found for all late Paleoproterozoic-Mesoproterozoic carbonate in this study, with values from 0.16 to 0.50 μmol/mol. Importantly, although the maximum values are within the observed range for most of the Mesoproterozoic, the Kaltasy can be distinguished from other carbonate strata in that all samples measured yielded I/(Ca+Mg) ratios above blank levels. This is in excellent agreement with a recent geochemical and paleobiological study of the Kaltasy

formation where detailed Fe speciation and trace metal concentrations as well as the presence of abundant eukaryotic microfossils indicated dominantly oxic water masses (Sperling and others, 2014). The simple presence of carbonate-bound iodine in all samples yields a similar interpretation, suggesting oxic conditions were more stable, at least locally, during Kaltasy formation with respect to other Proterozoic carbonate successions analyzed in this study. Alternatively, all iodine above blank levels may reflect exceptional preservation relative to other studied carbonate strata. Similar to most other studied formations, I/(Ca+Mg) shows no stratigraphic trend and no relationship between associated isotopic and trace metal abundances from the same samples.

~1.3 Dismal Lakes Group

The Dismal Lakes Group consists of >1500 m of siliciclastic and carbonate rocks exposed within the Coppermine Homocline of Northwest Canada. Samples for this study come from Dismal Lake and September Lake areas, and were previously analyzed by ref. (Frank and others, 2003; Kah and others, 2004), who measured $\delta^{13}C_{carb}$, $\delta^{18}O_{carb}$, Mg/Ca, Fe, Mn, Sr, $\delta^{34}S_{CAS}$, and [CAS]. Details regarding age constraints (Frank and others, 2003), sedimentology and stratigraphy (Frank and others, 2003), and geochemistry (Frank and others, 2003; Kah and others, 2004) of the Dismal Lakes Group are available from previous studies, but summarized briefly below.

A combination of U-Pb dates of 1.270±0.004 and 1.267±.002 Ga from overlying flood basalts (LeCheminant and Heaman, 1989) and ultramafic intrusions (Irvine, 1970) of the Coppermine River Group, respectively, and $\delta^{13}C_{carb}$ chemostratigraphy (Frank and others, 2003) indicate deposition between 1.27 and approximately 1.30 Ga (Frank and others, 2003). Samples from this study come from the upper Kendall River, Sulky, and Greenhorn Formations, which comprise the upper ~2/3 of the >1500 m thick Dismal Lakes Group. The upper Kendall River

Formation is dominated by oolitic, intraclastic, and microbially laminated carbonate strata that marks initial development of the Dismal Lakes carbonate platform(Frank and others, 2003). Carbonate strata of the overlying Sulky formation transition from laminated dolostone with interbedded shale, to reef-forming conical stromatolites likely growing below storm wave base, to domal and columnar stromatolites that suggest gradual shallowing (Kerans and Donaldson, 1988). The overlying Greenhorn Formation marks a return to peritidal deposition, and consists predominantly of microbially laminated dolomite. There is a transition to oolitic and stromatolitic facies toward the top suggesting development of higher energy, intertidal to shallow subtidal condition (Kerans and others, 1981).

I/(Ca+Mg) ratios within the Dismal Lakes group (Supplementary Table 3) are comparable to most of the other late Paleoproterozoic and Mesoproterozoic carbonate measured in this study, with all samples <0.52 μmol/mol, all but 2 samples <0.2 μmol/mol, and most samples near or below blank values of 0.1 μmol/mol. Similar to most other Mesoproterozoic sections, no stratigraphic trend is obvious despite known shifts in $\delta^{13}C_{carb}$ (Frank and others, 2003), a proxy for organic carbon cycling. I/(Ca+Mg) ratios show no correlation to isotope or concentration proxies measured in other studies or to mineralogy or carbonate lithology. Though only a few samples presented in this study have previously published CAS data, the I/(Ca+Mg) ratios for the Dismal Lakes group is generally similar to [CAS] in that both are low relative to their late Paleoproterozoic and Neoproterozoic counterparts.

~1.26 Ga Mescal Formation

The Mesoproterozoic Mescal Formation is within the Apache group of Northern Arizona and has a maximum thickness of ~490 meters (Wrucke, 1989). Samples from the Mescal formation in this study come from the Algal Member at the Roosevelt Dam section and are directly those used in Gellatley and Lyons (Gellatly and Lyons, 2005) where additional data on

[CAS] and $\delta^{34}S_{CAS}$ are available. Details regarding age (Stewart and others, 2001), depositional setting (Wrucke, 1989), and geochemistry (Gellatly and Lyons, 2005) are available from previous studies, but are summarized briefly below.

The ~1.26 Ga age of the Mescal Formation is constrained via Pb-Pb dating of detrital zircons of the overlying Troy Quartzite at 1.256 Ga and underlying Dripping Springs Quartzite at 1.264 Ga (Stewart and others, 2001). The Algal Member of the Mescal Formation is mostly dolomite with some chert, but only rare limestone (Wrucke, 1989). The Algal Member is interpreted as having been deposited in a shallow marine setting as reflected by transitions from up to 1 m tall domal and laterally extensive (up to 60 km) stromatolites biostromes, indicating subtidal to intertidal depoitional environments to discrete hemispheroid stromatolite colonies indicating intertidal zones (Wrucke, 1989).

The I/(Ca+Mg) dataset from the Mescal Limestone (Supplementary Table 3) is the relatively, with only four samples, but the range of values is consistent with all other Late Paleoproterozoic and Mesoproterozoic I/(Ca+Mg) ratios observed, with two values at blank levels and one at each 0.10 and 0.25 μmol/mol. The low resolution data set clearly prohibits recognition of stratigraphic trends or comparisons to CAS data, but combined, the relatively low [CAS] (Gellatly and Lyons, 2005) and I/(Ca+Mg) ratios from the Mescal Formation is similar that found for most of the late Paleoproterozoic and Mesoproterozoic (Hardisty and others, 2014; Planavsky and others, 2012), emphasizing both lower marine SO_4^{-2} and IO_3^- availability.

~1.2-1.1 Ga Angmaat Formation

The Angmaat Formation (formerly Society Cliffs Formation (Lavoie and Turner, 2009)) is located within the Bylot Supergroup, a >6 km thick package preserved in the Borden basins of NE Arctic Canada. Samples from this study were collected from a measured section on Bylot Island, and were studied extensively in previous studies (Kah and others, 2001; Kah and others,

2004), where associated data regarding $\delta^{13}C_{carb}$, $\delta^{18}O_{carb}$, $\delta^{34}S_{CAS}$, [CAS], and elemental composition (Ca, Mg, Mn, Fe, Sr) are available. Details regarding age constraints (Kah and others, 2001; Kah and others, 2004), sedimentology and stratigraphy (Kah and others, 2001), and geochemistry (Kah and others, 2001; Kah and others, 2004) of the Society Cliffs formation are available from previous studies, but are summarized briefly below.

The age of the ~1.2 Ga Angmaat Formation is constrained via Pb-Pb dates from sedimentary carbonates within the Angmaat Formation of 1.199±0.024 and 1.204±0.022 Ga (Kah and others, 2001), as well as a U-Th-Pb whole rock age of 1092+6-59 Ma for black shale of the underlying Arctic Bay Formation. These dates are supported by paleontological and isotopic geochemical correlations to better dated successions elsewhere (summarized by ref. (Knoll and others, 2013)). The Angmaat Formation consists of approximately 740 m of carbonate with minor siliciclastic input. Strata consist predominantly of shallowing upward cycles of microbial carbonate and seafloor precipitates. On Bylot Island, the bottom 300 meters of section consist of cycles that are frequently capped with gypsum that is interbedded with either carbonate seafloor precipitate structures or shale (commonly containing halite hoppers).

I/(Ca+Mg) ratios from Society Cliffs samples (Supplementary Table 3) range from blank levels to 0.60 μmol/mol, but with all but one sample <0.30 μmol/mol. There is no apparent stratigraphic trend, but it should be noted that values all fall within the low range bracketing most of the Mesoproterozoic and Late Paleoproterozoic. Like the other sections analyzed, there is no clear relationship with available $\delta^{13}C_{carb}$, $\delta^{18}O_{carb}$, Mg/Ca, Fe, Mn, Sr, $\delta^{34}S_{CAS}$, or CAS (Kah and others, 2001; Kah and others, 2004), likely reflecting a small sample set and I/(Ca+Mg) oscillations below an extreme low threshold level.

~1.1 Ga Atar and El Mreiti groups

The Mesoproterozoic Atar and El Mreiti groups are exposed within the Taoudeni Basin, which spans 1,750,000 km^2 of the Western African craton, exposing >2 km of Proterozoic strata. Samples for this study come from the Atar and Tawaz formations of the Atar Group, and the Touirist and Tenoumer formations of the El Mreiti Group. The Atar and Touirist formations represent time-equivalent facies within distinct environmental regimes within the basin. Samples measured for I/(Ca+Mg) were previously examined (Kah and others, 2012), where complimentary $\delta^{13}C_{carb}$, $\delta^{18}O_{carb}$, Mg/Ca, Sr, Mn, Fe are available. Samples were collected at Lekhleigate (ATL) and Serize (ATS) in the Atar region as well as the interdune region, north of Char (South Interdune) (Jones and others, 2010). Details regarding age constraints (Rooney and others, 2010), stratigraphy and sedimentology (Kah and others, 2012), diagenesis (Kah and others, 2012), and geochemistry (Gilleaudeau and Kah, 2015; Kah and others, 2012) of the Atar group are available from previous studies, but are briefly outlined below.

The Atar group is constrained at ~1.1 Ga by three Re-Os dates at 1105±37, 1107±12, 1109±22 from dolerite sills in the Touirist and En Nesoar Formations (El Mreiti Group) (Rooney and others, 2010). In general, the Atar group (the Touirist and Atar formations specifically) represents craton-wide flooding and shallow marine deposition (Bertrand-Sarfati and Moussine-Pouchkine, 1988). After a clear drop in sea level and exposure of large parts of the platform, the Tawaz (Atar Group) and time-equivalent Tenoumer (El Mreiti Group) formations represent a return to open marine limestone deposition. Widespread columnar and branching stromatolites interbedded with clastic carbonate deposits, as well as widespread molar-tooth structures (Bishop and others, 2006; James and others, 1998; Kah and others, 2004; Pollock and others, 2006) indicate shallow subtidal to intertidal marine environments (Kah and others, 2012).

The Atar group contains a range of I/(Ca+Mg) below a low threshold, with values ranging from blank levels to 0.68 μmol/mol, but with most values between 0.18 and 0.28 μmol/mol (Supplementary Table 3). As with most other Mesoproterozoic carbonates analyzed, no stratigraphic trend is observed. Further, a comparison to $\delta^{13}C_{carb}$, $\delta^{18}O_{carb}$, Mg/Ca, Fe, Mn, and Sr (from ref. (Kah and others, 2012)) reveals no obvious relationships. This is surprising, as elevated Fe and Mn in the Atar have previously been interpreted to reflect proximity to a local anoxic water column during carbonate precipitation (Kah and others, 2012), which is consistent with our interpretation for the Atar and most of other middle Proterozoic carbonate from this study. Redox conditions allowing dissolved Fe and Mn accumulation are expected to cause complete reduction of IO_3^- to I^- (Rue and others, 1997), thus reducing carbonate-bound iodine. Our interpretation of Mesoproterozoic low oxygen surface ocean and a shallow and highly variable chemocline is consistent with independent interpretations of Fe speciation from interbedded shale through the Atar and El Mreiti groups of a shallow and sometimes highly variable chemocline (Gilleaudeau and Kah, 2015).

~1.04 Ga Sukhaya Tunguska Formation

The upper Mesoproterozoic to lower Neoproterozoic Sukhaya Tunguska, Turkhansk, Miroyedika, and Burovya Formations are part of the Turukhansk Uplift located near the northwestern margin of the Siberian Platform. Only 9 samples are represented here from the Turukhansk Uplift, with 5 coming from the Sukhaya Tunguska Formation. All samples from this study come from ref. (Bartley and Kah, 2004), where additional data including $\delta^{13}C_{carb}$, $\delta^{18}O_{carb}$, and trace metals are available. Details regarding the age (Ovchinnikova and others, 1995), depositional environment (Bartley and others, 2001), and geochemistry (Bartley and others, 2001) have been published previously but are briefly summarized below.

The age of the Sukhaya Tunguska Formation is constrained via carbonate Pb-Pb dating of

1.035±0.060 Ga in the same formation and supported by micro-paleontological and isotopic correlations to other uppermost Mesoproterozoic successions (Ovchinnikova and others, 1995). Overlying formations are broadly constrained to be early Neoproterozoic in age. The Sukhaya Tunguska Formation is interpreted to have been deposited in a subtidal to intertidal setting (Bartley and others, 2001). Both dolomite and limestone occur among our samples; the sample with elevated I/Ca+Mg is a nodular limestone within a shallow water silt-rich succession.

The maximum I/(Ca+Mg) value of 1.74 μmol/mol for Sukhaya Tunguska is found in limestone from the Sukhaya Tunguska Formation (Supplementary Table 3). No stratigraphic trends or correlations with $\delta^{13}C_{carb}$ or $\delta^{18}O_{carb}$, or trace metals could be elucidated. The maximum I/(Ca+Mg) ratio of 1.74 μmol/mol is significant in that it is elevated relative to most of the middle Proterozoic range and represents a transition to higher absolute I/(Ca+Mg) rations starting in the Neoproterozoic. We recognize the potential for shallow anoxic conditions during Tunguska deposition along with likely diagenetic iodine loss as accounting for the mostly low values, similar to our interpretations for the remainder of the previous Proterozoic. However, we emphasize that the increase in maximum I/(Ca+Mg) ratios relative to the late Paleoproterozoic and Mesoproterozoic is consistent with observations for carbonates from the following Neoproterozoic. This general increase in maximum values suggests at least the potential for increased surface ocean oxygen and deepened chemoclines, but we suspect that near surface marine IO_3^- (and, probably O_2) was highly dynamic.

~0.85 Ga Shaler Group, Wynniatt and Minto Inlet formations

The Wynniatt (590 m thick) and Minto Inlet (210 m thick) formations are found in the ~4000 m thick Shaler Group, northwestern Canada. The samples used in this study represent a portion used in ref. (Asmerom and others, 1991) where $\delta^{87}Sr$, $\delta^{13}C_{carb}$ or $\delta^{18}O_{carb}$, and trace metal abundances are available. Details regarding age (van Acken and others, 2013), sedimentology

and stratigraphy (Asmerom and others, 1991; Jones and others, 2010), and geochemistry (Asmerom and others, 1991; Jones and others, 2010) are all available from previous studies but are described briefly below.

The ~0.85 Ga age of the Wynniatt and Minto Inlet Formations is constrained via a Re-Os date of 0.849±0.048 Ga from an organic-rich black shale near the base of the Wynniatt Formation, which directly overlies the Minto Inlet Formation (van Acken and others, 2013). The Minto Inlet Formation consists of interbedded sulfate evaporates and carbonate and represents a period of variably high salinity in an intermittently closed basin (Asmerom and others, 1991; Jones and others, 2010). The Wynniatt Formation represents a return to shallow marine conditions with normal salinity, with dolomite containing molar tooth structures, ribbonites, dolosiltites, oolitess, and stromatolites along with evaporate beds representing brief returns to conditions similar to Minto Inlet deposition (Asmerom and others, 1991; Jones and others, 2010).

I/(Ca+Mg) ratios in the Wynniatt and Minto Inlet Formations are generally low (Supplementary Table 3). We however stress that the one sample containing iodine has 1.02 μmol/mol, a value above most of the late Paleoproterozoic and Mesoproterozoic. We recognize the potential for shallow anoxic conditions during Wynniatt and Minto Inlet deposition along with likely diagenetic iodine loss, similar to our interpretations for the remainder of the previous Proterozoic. We however emphasize that the increase in maximum I/(Ca+Mg) ratios relative to the late Paleoproterozoic and Mesoproterozoic is consistent with observations for other carbonates from the Neoproterozoic. This general increase in maximum values suggests at least the potential for increased surface ocean oxygen and deepened chemoclines, but we recommend that near surface marine IO_3^- was highly dynamic. Notably, the elevated maximum I/(Ca+Mg) ratio within the Wynniatt Formation is consistent with the increase in Cr concentrations and $\delta^{53}Cr$ values within the upper Wynniatt Formation indicating a switch to O_2>0.1% PAL(Planavsky and

others, 2014). We also note that the increase in maximum I/(Ca+Mg) ratios above that characterizing the Mesoproterozoic and late Paleoproterozoic is consistent with similar general increases in maximum values observed in the Neoproterozoic and ~1.04 Ga Sukhaya Tunguska Formation.

~ 0.825 Ga Akademikerbreen Group and Limestone-Dolomite Series

The Akademikerbeen Group, Svalbard, and the Limestone-Dolomite Series in central East Greenland are two parts of a tectonically dissected Neoproterozoic carbonate platform. Direct radiometric constraints on Akademikerbeen carbonate accumulation are limited, but the >1000 succession lies beneath Sturtian glaciogenic rocks (ca. 716 Ma) and is correlated by both fossils and chemostratigraphic methods to 800-730 Ma successions elsewhere (Halverson and others, 2005; Strauss and others, 2014). A few samples also represent carbonate units in the underlying, earlier Neoproterozoic Veteranen Group.

The Akademikerbreen succession consists of shallow marine carbonate that range from peritidal microbialites to micritic beds deposited below fair weather wave base (Knoll and Swett, 1989). Most samples in our data set come from peritidal carbonates of the Draken Formation (Knoll and others, 1991) and cross-bedded oolites and pisolites of the overlying Backlundtoppen Formation (Knoll and others, 1989) and its East Greenland equivalents (Bed 18). The two samples that show high I/Ca+Mg values (Supplementary Table 3) are a Draken flake conglomerate deposited in a coastal lagoon and a micirite from Bed 13 in East Greenland (equivalent to beds of the Svanbergfjellet Formation in Svalbard). Similar to other successions, IO_3^- content shows little relationship to lithology, facies or isotopic chemistry.

~0.750 Ga Beck Springs Dolomite

The Neoproterozoic Beck Spring Dolomite lies between the Horse Thief Springs and Kingston Peak Formations within the Pahrump Group in Death Valley, USA. Samples collected here came from the top of the Beck Spring Dolomite at Saratoga Springs, southern Ibex Hills and were collected specifically for this study. Details regarding the age (Karlstrom and others, 2000; Mahon and others, 2014), depositional setting (Hurtgen and others, 2004), and geochemistry (Hurtgen and others, 2004) of the Beck Springs Dolomite have been published previously, but are summarized below.

The Beck Springs Dolomite age is constrained at ~0.750 Ga by a 0.787 ± 0.011 from U-Pb dates of detrital zircons in the underlying Horse Thief Springs Formation (Mahon and others, 2014) and a lithologic correlation of the top of the Beck Springs (Dehler and others, 2001) to a radiometrically dated ash layer at ca. 742 at the top of the Chuar Group in Grand Canyon, USA (Karlstrom and others, 2000). The Beck Spring dolomite contains multiple shallowing upward sequences expressed as alternating 1-2 m thick siltstones and up to 2 m dolomite with varying thin and massive bedding. At the top of the Beck Springs is a massive dolomite containing large ooids found in discrete lag deposits and massive bedding.

Of the 20 samples measured for I/(Ca+Mg) ratios measured from the Beck Springs Dolomite, only 6 were above blank levels (Supplementary Table 3). The maximum values observed for the Beck Springs Dolomite are more similar to that observed for the late Paleoproterozoic and Mesoproterozoic than the Neoproterozoic, with all other Neoproterozoic sections having values >1.0 μmol/mol. However, the Beck Springs Dolomite is similar to each Neoproterozoic, Mesoprtoerozoic, and Late Neoproterozoic sections in that it contains many I/(Ca+Mg) values near blank levels. The extreme low I/(Ca+Mg) ratios prohibit recognition of any stratigraphic trends. Like I/(Ca+Mg), previous studies have analyzed [CAS] from the Beck

Springs Dolomite, though not from these same samples, and found values <150 ppm and mostly <100 ppm, more similar to Mesoproterozoic [CAS] records than that found in the Ediacaran of the late Neoproterozoic (Hurtgen and others, 2004).

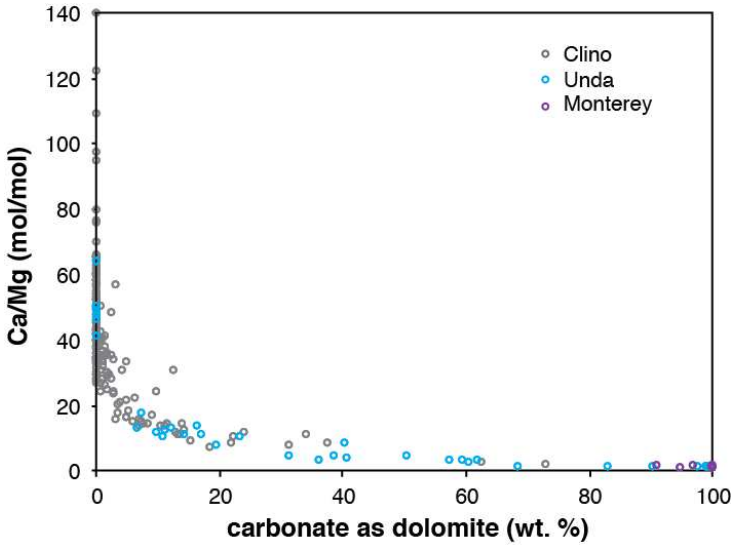

Figure S6. The relationship of Ca/Mg versus dolomite abundance from dolomite-containing cores from the diagenetic sample set (Monterey, Unda, Clino) discussed in the main and supplementary text.

~0.580 Ga Khufai Formation, Sultanate of Oman

Results and stratigraphy from the Khufai Formation are shown in Figure 3a. Sediments from the Khufai Fm. consist of a compilation from across the Huqf region in the Sultanate of Oman, representing a broad array of shallow to mid-ramp facies ranging from stromatolites, ooids, cross-stratified grainstones, and microbialites (Osburn, 2013). Importantly, all carbonate are pervasively dolomitized, but most retain their primary structures (Osburn, 2013), potentially indicating dolomitization before or during lithification (Tucker, 1982). The stratigraphic column shown in the main text represents a generalized compilation with carbon isotopes used to

stratigraphically correlate the sections. Readers are referred to Osburn et al., (Osburn, 2013; Osburn and others, 2014; Osburn and others, 2015) for detailed geologic descriptions and further geochemical data. Of importance to note is that [CAS] increase in parallel with I/(Ca+Mg) ratios, though scatter in both data sets prevents a direct relationship. I/(Ca+Mg) ratios and descriptors identifying sample location (matching that of (Osburn, 2013; Osburn and others, 2015)) are given in Supplementary Table 3.

$\delta^{13}C_{carb}$ values remain positive, with scatter between 3.25 to 7.97 ‰, for the lower 290 meters of the Khufai Formation (Figure 3a). At 290 meters, $\delta^{13}C_{carb}$ values decrease systematically to ~-8.6 ‰, capturing the onset of the Shuram carbon isotope excursion (Osburn, 2013).

Outside of 4 outlier values, ranging from 4.12 µmol/mol at ~32.9 meters and 1.60-1.86 µmol/mol at ~ 217-236 meters, I/(Ca+Mg) ratios in the lower 290 meters of the measured section (35 of the 130 measured samples from the Khufai) are below 0.75 µmol/mol, with most below 0.5 µmol/mol (Figure 5a). The outlier values are not associated with a particular change in mineralogy or sedimentary facies or shift in $\delta^{13}C_{carb}$, but are affiliated with one particular measured section, KDS, which represents the majority of the pre-Shuram stratigraphy in this compilation. At 290 meters, there is a systematic increase in I/(Ca+Mg) ratios with the general trend increasing to 1.40 µmol/mol, but with 5 data points extending beyond this up to 6.66 µmol/mol. The highest values are comparable to late Phanerozoic values from well-oxygenated waters from modern-recent localities (Figure 2, 3). Again, the stratigraphic height of increase in I/(Ca+Mg) ratios corresponds directly to the decrease in $\delta^{13}C_{carb}$ toward negative values.

~0.580 Ga Johnnie Formation, Death Valley, USA

The measured section from the Johnnie Formation was collected from Saddle Peak Hills, Death Valley, USA (N 35° 45.439’ W 116° 20.936’) and captures the Shuram carbon isotope

excursion, with an assigned age, through correlation with other Shuram carbonates, between 580 and 551 Ma, as discussed in detail above. A detailed sedimentological description is given below (Figure 3b). At the bottom of the section is ~2 m of massive grey dolomite. Above this is a series of alternating sandstone/siltstone beds with dolomite cement until the Johnnie Oolite at ~ 40 meters, which marks the bottom of the Rainstorm Member. The Johnnie Oolite is a tan-colored dolomite and represents the onset of the $\delta^{13}C_{carb}$ excursion. The oolite is a pervasive marker bed throughout the Death Valley Region, with parallel sedimentology and geochemistry noted at several locations and contains up to approximately 30% cement (Corsetti and Kaufman, 2003). The Johnnie Oolite in Death Valley has also been tentatively correlated to an oolite marker bed from the Clemente Formation in Northern Mexico which captures the onset of the Shuram carbon isotope excursion (Loyd and others, 2013) and is represented in this study. The Johnnie Oolite at Salt Spring Hills is ~2.5 meters thick. Above the oolite, the sedimentology sharply transitions to sandstone with dolomite cement until the top of the section. The sandstone consists of abundant hummocky cross-stratification, multiple lag deposits containing rip-up clasts and ooids, and several interbedded carbonate grainstones. At other localities in the nearby Nopah Range, aragonite fans have been noted (Pruss and others, 2008), but none were observed during our sampling and description of the Rainstorm Member at Saddle Peak Hills.

The $\delta^{13}C_{carb}$ values range from 3.12 to -0.16 ‰ within the sampled units below the Johnnie Oolite. Within the Johnnie Oolite, $\delta^{13}C_{carb}$ values begin a sharp decrease, ranging from -3.58 to -4.95 ‰ from the base to the top of the oolite, indicating the onset of the Shuram excursion (Figure 3b). Above the oolite, $\delta^{13}C_{carb}$ values express a trend decreasing from -10.47 ‰ at 51.2 meters to a nadir of -11.47 ‰ at 61.4 meters, before dropping to -8.16 ‰ by the top of the section.

Below the Johnnie Oolite, I/(Ca+Mg) ratios are less than 1.2 μmol/mol, but the majority of the values are less than 0.80 μmol/mol (Figure 5b). The I/(Ca+Mg) excursion begins directly above the oolite in mixed sandstone dolomite facies that extends to the top of the section. The Johnnie Formation is the only section capturing the Shuram in our study where the increase in I/(Ca+Mg) ratios does not correlate directly with the onset of the decrease in $\delta^{13}C_{carb}$. Previous publication of geochemistry and mineralogy of the Johnnie Oolite from Winters Pass, near Death Valley, showed an increase in [CAS] also beginning directly above the Johnnie Oolite, a result credited to the degree of pervasive secondary cements and the susceptibility of [CAS] to diagenetic alteration (Corsetti and Kaufman, 2003). Considering the susceptibility of I/(Ca+Mg) ratios to diagenetic alteration discussed in the main text, we give a parallel explanation to that of [CAS], though this does not explain the increase in [CAS] and I/(Ca+Mg) ratios noted in the oolite of the Clemente. Above the Johnnie Oolite, I/(Ca+Mg) ratios show a pulsed increase to values ranging from ~2 to 5.4 μmol/mol to the top of the section. The highest values are comparable to late Phanerozoic values from well-oxygenated waters following Oceanic Anoxic Event 2 (Lu and others, 2010) and following the PETM (Zhou and others, 2014) and are triple that recorded in a data set spanning the Paleoproterozoic (Hardisty and others, 2014).

~0.580 Ga Clemente Formation, Northern Mexico

The Clemente Formation of Sonora, Mexico, expresses a $\delta^{13}C_{carb}$ excursion (Loyd and others, 2012b, 2013) correlated to the Shuram $\delta^{13}C_{carb}$ excursion (Condon and others, 2005). Carbon isotope values shown in the main text are from ref. (Loyd and others, 2013), with the same samples used for iodine analysis in this study. Detailed sedimentological descriptions and other complimentary geochemical data ([CAS], $\delta^{34}S_{CAS}$, Mn, Mg/Ca, Sr) are available from previous studies (Loyd and others, 2012b, 2013). Of importance to note is that the Clemente Formation contains an oolite member that has been tentatively correlated to the Johnnie Oolite.

The oolite is dolomite and the formerly aragonite fan-bearing beds above the oolite are a mixture of dolomite and calcite. Carbonate beds overlying the oolite facies are the only units from this study with significant calcite, though the section is predominantly dolomite. Like the Johnnie Formations, the Clemente Formation also records an increase in [CAS] associated with the Shuram carbon isotope excursion. The sedimentary and geochemical relationship between the Clemente Formation and Johnnie Formation are discussed in detail in ref. (Loyd and others, 2012b, 2013). Correlation based on the presence of the Shuram carbon isotope excursion puts the Clemente age between 580 and 551 Ma (580 Ma used in Figure 4) (Loyd and others, 2013).

The $\delta^{13}C_{carb}$ values show scatter between -0.4 and 5.1 ‰ from the bottom of the section until the base of the oolite, corresponding to dolomite facies (Figure 3c). Beginning at the base of the oolite, 356.5 meters, $\delta^{13}C_{carb}$ values decrease systematically to a nadir of -8.9 ‰ at ~364 meters and then increase to values >0 ‰ ~500 meters up-section. Importantly, the carbon isotope excursion includes a mineralogical switch from dolomite to limestone, starting at ~362 meters, and the mineralogy transitions back to dolomite by 423.5 meters. Above 500 meters, $\delta^{13}C_{carb}$ remains <5 ‰, with some scatter to negative values.

I/(Ca+Mg) ratios scatter below 1.6 μmol/mol until ~ 364 meters, but with values generally less than 1 μmol/mol (Figure 3c). At 364 meters there is a sharp increase in I/(Ca+Mg) ratios, again paralleling the carbon isotope excursion, with values increasing to as high as 7.74 μmol/mol. The increase in I/(Ca+Mg) ratios includes the limestone interval. Importantly, however, the increase in I/(C+Mg) is not exclusive to the limestone interval, with the highest two values recorded occurring within dolomite (Supplementary Table 3). Beginning at 423.5 meters, I/(Ca+Mg) ratios again decrease, with values <1.02 μmol/mol to the top of the section.

0.635-0.551 Ga Doushantuo Formation, Siduping, South China

The Neoproterozoic Doushantuo Formation at Siduping of South China captures both the cap carbonate and associated $\delta^{13}C_{carb}$ excursion following the Marinoan glaciation and the Shuram $\delta^{13}C_{carb}$ excursion (Figure 3d). Our I/(Ca+Mg) data spans both of these $\delta^{13}C_{carb}$ excursions. U-Pb zircon dates from volcanic ash beds at the base and top of the Doushantuo Formation in the Yangtze Gorges area constrain its age between 0.635 and 0.551 Ga (Condon and others, 2005). The middle Doushantuo negative $\delta^{13}C_{carb}$ anomaly (N2) is less well constrained but likely around 580 Ma (Jiang and others, 2007; Jiang and others, 2011). Using the Doushantuo cap carbonate at the base and the organic-rich black shales at the top as marker beds (Jiang and others, 2011), in combination with physical surfaces and $\delta^{13}C_{carb}$ chemostratigraphy, the Doushantuo Formation at the Siduping section can be correlated with that of the Yangtze Gorges area (Jiang and others, 2011; Wang and others, 2016). With available data, we place a 0.635 Ga age for the cap carbonate and 0.580 Ga age for the Shuram (upper Doushantuo) $\delta^{13}C_{carb}$ excursion, which represent maximum ages.

Results from the Doushantuo at Siduping are shown in Figure 3d. The Siduping section has been interpreted as deposited in the middle-upper slope of the Ediacaran Yangtze platform (Jiang and others, 2011). Evidence for the paleogeographic reconstruction comes from the regional stratigraphic patterns and intermittent, but consistent, appearance of olistostrome carbonate and a lack of shallow-water indicators such as microbial laminae, ooids, cross-stratification, ripples, and stromatolites. The Siduping section is well suited for testing the redox variations at moderate water depth in marginal settings.

The Doushantuo Formation of the Siduping section is about 170 m thick. The base of the Doushantuo Formation is characterized by a 5-m-thick cap carbonate that directly overlies the Nantuo glacial diamictite. The cap carbonate is overlain by an approximately 5-m-thick black

shale, followed by 10-m-thick dolomitic siltstone and silty dolostone. The majority of the Doushantuo Formation afterwards is composed of micritic or microcrystalline dolostone with minor shaly partings or thin shaly beds. Abundant slumping blocks and olistostrome breccias are found throughout this interval. The top of the Doushantuo Formation is marked by a 10-m-thick black shale interval with lenticular limestone and dolostone beds, which transit upwards into bedded cherts and silicified shales of the Liuchapo Formation.

At the base of the Doushantuo formation, within the cap carbonate, $\delta^{13}C_{carb}$ values are as low as -4.1 ‰ (Figure 5d). Directly above the cap carbonate, $\delta^{13}C_{carb}$ values rise from near 2 ‰ to ~ 5 ‰ between 40 and 100 meters (Supplementary Table 3). Above this, $\delta^{13}C_{carb}$ drops to stable values near 2 ‰ until ~ 140 meters. Above 140 meters, $\delta^{13}C_{carb}$ drops down to -10.5 ‰ at the top of the profile, representing the Shuram carbon isotope excursion (Wang and others, 2016).

There is significant iodine in the lower 10 meters within and directly above the cap carbonate, with I/(Ca+Mg) ratios as high as 2 μmol/mol (Figure 3d). I/(Ca+Mg) ratios above this are near or at blank levels until ~150 meters. Above this, values increase to ~ 1.3 μmol/mol, but generally < 0.6 μmol/mol. These maximum values are muted relative to the other measured Shuram sections. The shift to negative $\delta^{13}C_{carb}$ values and the increase in I/(Ca+Mg) ratios is not associated with any known shifts in primary mineralogy or sedimentary facies that are not also represented elsewhere in the section (Figure 3; Supplementary Table 3). The shift in I/(Ca+Mg) ratios begins at the same position as the decrease in $\delta^{13}C_{carb}$ representing the Shuram carbon isotope excursion.

The binary shift from absence to presence of carbonate-associated iodine associated with the Shuram, which is not observed at any of the other measured sections, and the relatively muted peak values compared to the other sections may reflect the persistence of a particularly shallow

chemocline even during the Shuram. Siduping represents a deeper water section compared to other Shuram sections from this study, so the site of carbonate deposition may be relatively closer to the chemocline. This is supported by previous studies showing a stratified ocean model with a euxinic OMZ-like wedge along the margin represented by the Doushantuo (Li and others, 2010). The switch from absence to presence of carbonate-bound iodine could record a switch from locally oxygen-poor/anoxic conditions at very shallow depth to a relatively more oxic state (Hardisty and others, 2014), but with a sustained significant contribution from upwardly mixing of anoxic, IO_3^--depleted, water masses sourced from the enhanced persistence of a comparatively shallow local chemocline. Alternatively, this switch from absence to presence of iodine in carbonate may be the result of diagenesis overprinting or diluting already very low pre-Shuram signals. Regardless, the increase of I/(Ca+Mg) during the Shuram remains evident.

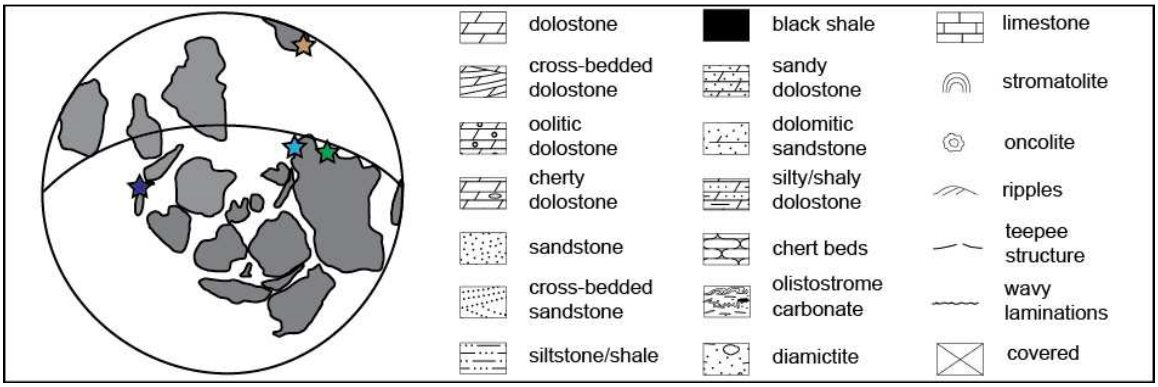

Figure S7. Stratigraphic key and paleogeography corresponding to Figure 5 of the main text. Ediacaran (600 million years ago) paleogeographic locations (modified from (Pisarevsky and others, 2008)) of sampled sections correspond to the Johnnie Formation (green), Clemente Formation (blue), Douhantuo Formation (brown), and Khufai Formation (purple).

Table S2. The I/(Ca+Mg) ratios, $\delta^{13}C_{carb}$, and carbonate mineralogy for samples from the diagenetic sample set. Sample depth is given when relevant. Ca/Mg ratios are given for dolomite containing sample sets. The sample set includes short cores from the Great Bahamas Bank, Key Largo Limestone, Clino and Unda cores of the Great Bahamas Bank, and Monterey concretions, as described in the main text and supplementary materials. Data for $\delta^{13}C_{carb}$ from the Monterey concretions and Key Largo Limestone are from references (Loyd and others, 2012a) and (Gill and others, 2008), respectively.

Sample or Locality	Depth (m)	Arag (wt.%)	HMC (wt.%)	LMC (wt.%)	Dolo (wt.%)	I/(Ca+Mg) (µmol/mol)	$\delta^{13}C_{carb}$ (‰)	Ca/Mg (mol/mol)
Great Bahamas Bank core tops								
C1 0-2	0.01	75.96	22.79	1.25	0.00	10.22	4.78	
C1 2-4	0.03	92.86	6.61	0.53	0.00	8.60	4.66	
C1 4-6	0.05	91.23	8.45	0.32	0.00	8.07	4.62	
C1 6-8	0.07	82.71	16.71	0.58	0.00	8.15	4.41	
C1 8-10	0.09	87.70	12.04	0.26	0.00	8.46	4.16	
C1 10-12	0.11	83.26	17.12	0.00	0.00	10.02	4.57	
C1 12-14	0.13	77.60	23.02	0.00	0.00	8.12	4.71	
LDI-1 0-2	0.01	81.46	18.72	0.00	0.00	7.58		
LDI-1 2-4	0.03	74.41	25.57	0.02	0.00	7.20		
LDI-1 4-6	0.05	81.48	18.86	0.00	0.00	7.12		
LDI-1 6-8	0.07	79.76	21.21	0.00	0.00	6.81		
LDI-1 8-10	0.09	84.77	15.16	0.07	0.00	6.68		
LDI-1 10-12	0.11	88.96	10.80	0.23	0.00	6.78		
LDI-1 12-14	0.13	79.91	19.17	0.91	0.00	6.82		
C3a 0-1	0.005	78.33	22.46	0	0.00	9.99	3.20	
C3a 1-2	0.015	85.73	13.67	0.60	0.00	8.86	3.79	
C3a 2-4	0.03	75.68	24.15	0.16	0.00	10.75	3.72	
C3a 4-6	0.05	68.14	30.15	1.72	0.00	10.54	3.61	
C3a 6-8	0.07	81.54	16.61	1.85	0.00	9.66	3.70	
C3a 8-10	0.09	82.42	16.74	0.84	0.00	8.95	3.29	
C3a 10-12	0.11	63.98	30.65	5.36	0.00	10.23	3.80	
C3a 12-14	0.13	67.69	31.31	1.00	0.00	8.70	3.30	
C3a 14-17	0.155	68.70	30.56	0.75	0.00	9.36	3.82	
C3a 17-20	0.185	74.75	24.81	0.44	0.00	8.43	3.86	
NG 0-1	0.005	92.59	6.18	1.24	0.00	11.61		
NG 1-2	0.015	91.36	7.10	1.54	0.00	9.99		
NG 1.5-3	0.0225	86.89	8.79	4.32	0.00	9.04		
NG 3-4	0.035	89.65	9.34	1.02	0.00	8.04	4.81	
NG 4-5	0.05	90.98	6.76	2.25	0.00	7.90		
NG 5-6	0.06	91.44	6.84	1.73	0.00	7.86		
NG 6-7	0.065	90.27	7.02	2.71	0.00	6.92	4.68	
NG 7-8	0.075	93.90	4.69	1.41	0.00	6.81		
NG 8-9	0.085	91.76	6.22	2.03	0.00	5.99		

Sample or Locality	Depth (m)	Arag (wt.%)	HMC (wt.%)	LMC (wt.%)	Dolo (wt.%)	I/(Ca+Mg) (µmol/mol)	$\delta^{13}C_{carb}$ (‰)	Ca/Mg (mol/mol)
C3b 0-1	0.005	67.03	26.49	6.48	0.00	9.43	4.11	
C3b 3-5	0.04	82.90	17.24	0.00	0.00	8.00	4.65	
C3b 5-7	0.06	88.51	10.25	1.24	0.00	7.88	4.35	
C3b 7-9	0.08	83.07	17.28	0.00	0.00	7.83	4.52	
C3b 9-11	0.1	84.87	14.98	0.14	0.00	7.71	4.55	
C3b 11-13	0.12	76.90	19.02	4.08	0.00	7.87	4.40	
C3b 13-15	0.14	91.46	8.13	0.42	0.00	8.61	4.11	
C3b 15-17	0.16	75.55	21.29	3.17	0.00	8.40	4.31	
LSI-1 0-1	0.005	94.27	5.85	0.00	0.00	7.24	4.74	
LSI-1 1-2	0.015	90.35	9.63	0.02	0.00	7.46	4.83	
LSI-1 2-3	0.025	93.73	6.35	0.00	0.00	7.17	4.88	
LSI-1 3-4	0.035	94.20	5.26	0.53	0.00	7.18	4.89	
LSI-1 5-6	0.055	90.09	9.84	0.07	0.00	6.72	4.86	
LSI-1 6-7	0.065	92.11	8.11	0.00	0.00	7.09	4.86	
LSI-1 7-8	0.075	93.70	6.38	0.00	0.00	7.00	4.90	
LSI-1 8-9	0.085	88.64	10.28	1.07	0.00	6.83	4.81	
LSI-1 9-10	0.095	95.59	4.31	0.10	0.00	7.23	4.79	
LDI-2 0-1	0.005	89.25	9.45	1.30	0.00	8.24		
LDI-2 1-2	0.015	89.67	9.96	0.37	0.00	7.83		
LDI-2 2-3	0.025	75.88	24.08	0.04	0.00	6.41		
LDI-2 3-4	0.035	88.83	8.81	2.35	0.00	6.84		
LDI-2 4-6	0.05	85.16	13.78	1.07	0.00	7.15		
LDI-2 6-7	0.065	80.63	18.37	1.01	0.00	7.14		
LDI-2 7-8	0.075	87.93	10.92	1.15	0.00	6.34		
Key Largo								
KL 1-1	0.04	34.14	0.00	65.86	0.00	4.55	-2.2	
KL 1-2	0.022	0.00	0.00	100.00	0.00	3.53	-1.2	
KL 1-3	0.005	25.84	0.00	74.16	0.00	4.00	-4.4	
KL 1-4	-0.015	95.85	0.00	4.15	0.00	3.59	-1.6	
KL 1-5	-0.03	91.67	0.00	8.33	0.00	3.73	-1.5	
KL 1-6	-0.043	90.66	0.00	9.34	0.00	3.88	-1.4	
KL 11-1	0.074	0.00	0.00	100.00	0.00	4.03	-0.8	
KL 11-2	0.0665	0.00	0.00	100.00	0.00	4.01	-2.5	
KL 11-3	0.057	0.00	0.00	100.00	0.00	3.67	-3.4	
KL 11-4	0.049	4.48	0.00	95.52	0.00	2.09	-2.5	
KL 11-5	0.0405	9.12	0.00	90.88	0.00	2.03	-2.7	
KL 11-6	0.033	8.37	0.00	91.63	0.00	2.12	-3.8	
KL 11-7	0.024	7.65	0.00	92.35	0.00	2.11	-5.5	
KL 11-8	0.015	8.74	0.00	91.26	0.00	1.96	-6.1	
KL 11-9	0.0065	1.29	0.00	98.71	0.00	2.01	-6.8	
KL 11-10	0.003	71.33	0.00	28.67	0.00	2.04	-2.15	
KL 11-11	-0.0125	78.45	0.00	21.55	0.00	3.89	-2.13	

Sample or Locality	Depth (m)	Arag (wt.%)	HMC (wt.%)	LMC (wt.%)	Dolo (wt.%)	I/(Ca+Mg) (µmol/mol)	$\delta^{13}C_{carb}$ (‰)	Ca/Mg (mol/mol)
KL 11-12	-0.0215					3.86		
KL 11-13	-0.0285	80.62	0.00	19.38	0.00	4.39	-1.62	
KL 11-14	-0.037	84.57	0.00	15.43	0.00	4.21		
KL 12-1	0.0575					4.35		
KL 12-2	0.049	0.00	0.00	100.00	0.00	3.86	-2.87	
KL 12-3	0.0405					3.95		
KL 12-4	0.032	0.00	0.00	100.00	0.00	3.20	-4.57	
KL 12-5	0.023	0.00	0.00	100.00	0.00	3.97	-6.6	
KL 12-6	0.014	0.00	0.00	100.00	0.00	3.85	-8.1	
KL 12-7	0.006					3.30		
KL 12-8	-0.0065					3.60		
KL 12-9	-0.0165					3.82		
KL 12-10	-0.0245					3.52		
Monterey								
mmc8-lb		0	0.00	0.00	100.00	0.23	15.90	1.07
mmc2-2		0	0.00	0.00	100.00	0.16	15.10	1.08
mmc1-2		0	0.00	0.00	100.00	0.00	11.40	1.16
mmc4-1la		0	0.00	0.00	100.00	0.15	14.90	1.11
mmc1-5		0	0.00	0.00	100.00	0.00	10.00	1.20
mmc8-ra		0	0.00	0.00	100.00	0.32	16.10	1.03
mmc8-m		0	0.00	0.00	100.00	0.24	11.00	1.26
msc1-1		0	0.00	3.09	96.91	0.00	4.60	1.25
mmc4-10a		0	0.00	0.00	100.00	0.08	11.00	1.10
mmc1-1		0	5.77	0.00	94.55	0.01	13.20	1.13
mmc2-5		0	0.00	0.00	100.00	0.08	13.20	1.13
mmc5-1r		0	0.00	0.00	100.00	0.46	14.00	1.19
mmc4-1lb		0	0.00	0.00	100.00	0.00	12.40	1.13
mmc2-t		0	0.00	0.00	100.00	0.00	16.10	1.04
mmc2-m		0	0.00	0.00	100.00	0.00	15.60	1.04
mmc4-1rb		0	0.00	0.00	100.00	0.00	14.10	1.15
msc1-3		0	0.00	0.00	100.00	0.06	-6.20	1.24
mmc8-la		0	0.00	0.00	100.00	0.21	15.90	1.09
mmc2-b		0	0.00	0.00	100.00	0.00		1.13
mnc1-2		0	0.00	9.03	90.97	0.14	5.00	1.79
mmc3-1		0	0.00	0.00	100.00	0.11	12.70	1.11
mmc4-1ra		0	0.00	0.00	100.00	0.20	13.60	1.14
mmc1-4		0	0.00	0.00	100.00	0.00	13.30	1.13
mmc2-3		0.00	0.00	0.00	100.00	0.00	15.20	1.07
Clino								

Sample or Locality	Depth (m)	Arag (wt.%)	HMC (wt.%)	LMC (wt.%)	Dolo (wt.%)	I/(Ca+Mg) (µmol/mol)	$\delta^{13}C_{carb}$ (‰)	Ca/Mg (mol/mol)
Clino	22.96	47.68	0.00	52.32	0.00	3.99	2.41	109.19
Clino	24.23	51.26	0.00	48.74	0.00	3.08	1.79	139.80
Clino	25.30	42.07	0.00	57.93	0.00	5.71	-0.60	65.76
Clino	25.91	34.42	0.00	65.58	0.00	4.74	0.11	52.78
Clino	27.43	24.89	0.00	75.11	0.00	1.27	-1.65	70.10
Clino	28.35	0.00	0.00	100.00	0.00	1.58	0.47	76.41
Clino	30.48	45.84	0.00	54.16	0.00	2.95	0.65	97.43
Clino	31.55	9.13	0.00	90.87	0.00	3.15	-0.78	76.18
Clino	31.70	9.10	0.00	90.90	0.00	3.36	-0.53	65.51
Clino	33.68	0.00	0.00	100.00	0.00	2.45	-1.40	41.71
Clino	34.19	23.06	0.00	76.94	0.00	2.98	0.07	56.94
Clino	34.65	8.86	0.00	91.14	0.00	2.52	-0.74	46.94
Clino	37.62	13.78	0.00	86.22	0.00	3.29	-0.23	45.85
Clino	38.35	0.00	0.00	100.00	0.00	5.05	-1.26	50.01
Clino	39.62	0.00	0.00	100.00	0.00	3.21	-0.88	63.08
Clino	40.54	9.52	0.00	87.53	2.94	3.30	-1.42	57.21
Clino	42.67	10.85	0.00	89.15	0.00	3.26	-1.34	65.41
Clino	52.22	0.00	0.00	100.00	0.00	1.72	-0.09	95.08
Clino	55.47	0.00	0.00	100.00	0.00	0.86	-0.42	58.60
Clino	55.65	0.00	0.00	100.00	0.00	2.11	-0.93	64.48
Clino	56.92	0.00	0.00	100.00	0.00	1.26	-0.64	65.59
Clino	58.70	0.00	0.00	100.00	0.00	0.87	-0.62	53.35
Clino	61.34	0.00	0.00	100.00	0.00	0.75	-0.49	54.90
Clino	63.14	0.00	0.00	100.00	0.00	2.49	0.11	53.44
Clino	66.14	0.00	0.00	100.00	0.00	2.99	0.26	65.64
Clino	73.15	0.00	0.00	100.00	0.00	0.79	-0.27	79.95
Clino	75.79	0.00	0.00	100.00	0.00	3.18	-0.76	58.41
Clino	76.61	0.00	0.00	100.00	0.00	1.98	-0.11	54.68
Clino	76.86	0.00	0.00	100.00	0.00	1.99	-0.11	58.32
Clino	78.69	0.00	0.00	100.00	0.00	1.54	0.43	50.14
Clino	78.92	0.00	0.00	100.00	0.00	1.68	-0.63	60.37
Clino	79.43	0.00	0.00	100.00	0.00	2.28	-0.54	62.08
Clino	80.09	0.00	0.00	100.00	0.00	0.91	0.05	58.61
Clino	84.61	0.00	0.00	100.00	0.00	1.62	-0.94	57.02
Clino	85.47	0.00	0.00	100.00	0.00	2.78		61.41
Clino	88.39	0.00	0.00	100.00	0.00	0.58	0.35	56.94
Clino	89.74	0.00	0.00	100.00	0.00	2.05	0.64	60.17
Clino	92.05	0.00	0.00	100.00	0.00	0.85	0.91	54.13
Clino	94.67	0.00	0.00	100.00	0.00	0.03	1.08	61.10
Clino	95.89	0.00	0.00	100.00	0.00	0.76	0.37	50.49
Clino	96.93	0.00	0.00	100.00	0.00	1.76	-0.37	48.96
Clino	98.22	0.00	0.00	100.00	0.00	1.36	-0.68	52.77

Sample or Locality	Depth (m)	Arag (wt.%)	HMC (wt.%)	LMC (wt.%)	Dolo (wt.%)	I/(Ca+Mg) (µmol/mol)	$\delta^{13}C_{carb}$ (‰)	Ca/Mg (mol/mol)
Clino	98.25	0.00	0.00	100.00	0.00	1.29	-0.51	65.11
Clino	103.78	0.00	0.00	100.00	0.00	1.53	-0.78	47.03
Clino	106.73	0.00	0.00	100.00	0.00	0.14	-1.13	59.60
Clino	107.47	0.00	0.00	100.00	0.00	0.15	-0.64	50.86
Clino	110.03	0.00	0.00	100.00	0.00	1.61	-0.32	52.86
Clino	111.56	0.00	0.00	100.00	0.00	0.68	-0.48	56.43
Clino	116.05	0.00	0.00	100.00	0.00	1.60	0.09	43.43
Clino	117.96	0.00	0.00	100.00	0.00	0.55	0.17	45.41
Clino	120.09	0.00	0.00	100.00	0.00	0.24	0.32	37.29
Clino	122.22	0.00	0.00	100.00	0.00	0.15	0.16	44.25
Clino	123.88	0.00	0.00	100.00	0.00	0.13	0.18	39.32
Clino	126.19	0.00	0.00	100.00	0.00	1.99	0.14	36.19
Clino	127.84	8.79	0.00	28.91	62.30	0.09	2.62	2.67
Clino	129.41	0.00	0.00	100.00	0.00	0.60	0.15	33.01
Clino	131.67	0.00	0.00	100.00	0.00	0.54	0.51	34.29
Clino	134.37	0.00	0.00	100.00	0.00	2.89	0.00	35.02
Clino	136.19	0.00	0.00	100.00	0.00	0.00	0.15	33.75
Clino	138.86	0.00	0.00	100.00	0.00	1.28	0.76	30.60
Clino	140.82	0.00	0.00	100.00	0.00	0.55	0.91	29.95
Clino	142.65	0.00	0.00	100.00	0.00	0.71	1.07	28.35
Clino	147.37	21.34	0.00	78.66	0.00	1.57	1.74	27.28
Clino	149.30	23.26	0.00	75.69	1.06	1.09	1.87	28.63
Clino	150.27	19.78	0.00	80.22	0.00	1.43	2.00	27.56
Clino	152.40	9.84	0.00	86.79	3.37	0.32	1.95	18.05
Clino	153.52	27.54	0.00	65.47	6.99	1.87	1.96	16.12
Clino	155.55	14.96	0.00	80.21	4.82	1.37	1.79	16.75
Clino	157.73	25.31	0.00	65.78	8.91	0.72	1.62	17.23
Clino	162.15	3.97	0.00	85.15	10.89	1.12	1.60	13.67
Clino	164.90	25.32	0.00	69.74	4.93	0.25	1.56	21.54
Clino	166.50	14.76	0.00	77.92	7.32	1.16	1.64	15.05
Clino	172.85	15.28	0.00	77.24	7.48	0.18	2.23	14.57
Clino	175.34	12.91	0.00	84.07	3.02	1.19	2.40	16.01
Clino	177.65	34.09	0.00	60.88	5.03	0.64	2.72	18.48
Clino	180.04	22.19	0.00	75.62	2.20	0.45	2.87	28.46
Clino	182.93	23.46	0.00	70.74	5.80	1.37	2.89	15.28
Clino	187.73	21.47	0.00	71.20	7.32	1.46	3.04	15.14
Clino	189.94	24.87	0.00	65.64	9.50	0.57	2.95	24.10
Clino	194.67	57.20	0.00	39.53	3.27	0.95	2.23	20.16
Clino	195.80	88.51	0.00	11.49	0.00	4.55	1.93	39.95
Clino	196.62	32.03	0.00	67.48	0.48	1.12	2.56	27.08
Clino	197.64	45.03	0.00	46.60	8.36	0.66	3.28	14.58
Clino	198.98	39.68	0.00	59.58	0.73	0.28	3.87	31.05

Sample or Locality	Depth (m)	Arag (wt.%)	HMC (wt.%)	LMC (wt.%)	Dolo (wt.%)	I/(Ca+Mg) (µmol/mol)	$\delta^{13}C_{carb}$ (‰)	Ca/Mg (mol/mol)
Clino	200.33	18.35	0.00	81.65	0.00	2.28	3.83	38.13
Clino	205.23	39.11	0.00	60.89	0.00	1.68	4.55	43.48
Clino	208.56	17.44	0.00	82.56	0.00	0.91	4.78	43.55
Clino	211.43	0.00	0.00	100.00	0.00	0.00	4.99	43.15
Clino	214.27	2.74	0.00	97.26	0.00	1.05	4.74	41.84
Clino	219.66	12.45	0.00	86.31	1.24	0.30	3.93	26.04
Clino	222.53	18.56	0.00	79.90	1.55	1.22	3.53	24.75
Clino	224.36	22.31	0.00	77.69	0.00	0.52	4.00	29.56
Clino	226.82	18.48	0.00	78.99	2.53	0.20	4.22	24.60
Clino	229.15	15.85	0.00	84.15	0.00	0.06	4.56	34.99
Clino	232.96	46.80	0.00	51.65	1.55	0.99	4.96	35.90
Clino	252.40	2.55	0.00	83.65	13.80	0.17	1.66	14.36
Clino	299.01	57.40	0.00	42.60	0.00	2.00	5.18	46.22
Clino	301.29	53.65	0.00	46.35	0.00	2.91	5.25	50.58
Clino	306.45	65.43	36.60	-2.02	0.00	3.08	5.31	46.61
Clino	308.20	60.17	3.35	24.78	11.70	4.35	5.61	17.82
Clino	310.44	0.00	0.00	33.82	0.00	3.22	5.16	53.77
Clino	312.52	55.59	0.00	44.41	0.00	2.90	5.26	42.16
Clino	314.83	59.98	0.00	39.56	0.46	3.34	5.11	50.66
Clino	316.97	75.14	0.00	24.86	0.00	3.79	5.27	45.03
Clino	319.02	64.98	0.00	35.02	0.00	3.40	5.28	42.64
Clino	321.77	76.41	0.00	21.19	2.40	3.59	5.14	48.32
Clino	367.54	62.65	0.00	37.35	0.00	0.39		33.93
Clino	325.98	78.81	0.00	20.96	0.23	3.12	5.10	41.05
Clino	328.57	72.83	0.00	26.22	0.96	3.00	5.19	33.50
Clino	329.29	68.57	0.00	30.62	0.81	4.05	4.37	41.05
Clino	331.60	84.50	0.00	14.08	1.42	4.33	5.04	41.42
Clino	334.09	78.07	0.00	21.21	0.72	4.05	4.95	41.04
Clino	336.68	66.99	0.00	31.71	1.30	3.46	4.79	38.04
Clino	338.07	57.32	44.96	-2.28	0.00	4.03	4.66	37.19
Clino	341.07	52.16	0.00	42.99	4.85	2.61	4.80	33.67
Clino	343.10	51.81	0.00	47.62	0.57	3.24	4.62	34.72
Clino	343.31	54.06	0.00	45.09	0.86	3.19	4.70	35.32
Clino	344.53	47.81	0.00	50.61	1.58	2.95	4.50	30.48
Clino	344.83	48.85	0.00	49.45	1.69	3.49	4.72	35.40
Clino	345.47	48.31	0.00	51.08	0.61	3.06	4.50	39.83
Clino	345.97	45.92	0.00	53.22	0.86	2.43	4.04	33.70
Clino	346.58	47.54	0.00	52.46	0.00	3.58	4.66	41.74
Clino	347.22	56.93	0.00	42.57	0.50	2.80	4.26	42.49
Clino	348.39	45.94	0.00	53.17	0.88	1.91	4.21	32.24
Clino	349.66	42.45	0.00	56.81	0.74	2.29	4.15	40.16
Clino	350.82	62.99	0.00	34.91	2.10	2.84	4.11	29.81

Sample or Locality	Depth (m)	Arag (wt.%)	HMC (wt.%)	LMC (wt.%)	Dolo (wt.%)	I/(Ca+Mg) (µmol/mol)	$\delta^{13}C_{carb}$ (‰)	Ca/Mg (mol/mol)
Clino	351.54	43.69	0.00	50.23	6.09	2.61	3.60	22.60
Clino	354.48	28.82	3.73	65.54	1.90	2.36	3.85	31.55
Clino	355.85	26.57	0.00	71.05	2.38	2.53	3.87	35.20
Clino	356.92	18.35	85.70	0.00	0.00	1.68	3.55	53.77
Clino	357.84	28.03	74.07	*0.00*	0.00	1.65	3.66	27.69
Clino	358.83	23.24	0.00	75.09	1.67	2.91	3.60	28.98
Clino	361.16	26.93	0.00	68.85	4.21	0.00	3.84	31.06
Clino	362.19	38.10	0.00	61.90	0.00	3.54	3.39	38.04
Clino	362.51	51.68	0.00	48.32	0.00	3.53	2.83	36.34
Clino	363.39	34.69	0.00	62.64	2.67	1.10	3.30	24.00
Clino	364.54	21.73	0.00	74.60	3.68	1.00	3.03	21.30
Clino	366.24	29.09	0.00	69.80	1.11	1.56	2.85	34.42
Clino	366.37	6.54	0.00	93.46	0.00	0.78	2.15	33.65
Clino	370.28	0.00	0.00	66.13	33.87	0.00	2.88	11.03
Clino	371.07	3.41	0.00	83.59	13.00	0.46	2.98	11.22
Clino	373.51	23.82	0.00	44.88	31.30	1.06	3.01	8.05
Clino	374.75	8.27	0.00	54.35	37.38	0.55	2.88	8.94
Clino	375.84	10.49	0.00	65.80	23.71	0.72	2.97	11.81
Clino	377.09	9.95	0.00	78.79	11.27	0.60	3.28	14.93
Clino	378.26	5.79	0.00	89.31	4.90	0.60	3.18	16.58
Clino	379.55	8.98	0.00	84.13	6.89	0.47	3.26	13.78
Clino	380.57	3.30	0.00	81.46	15.24	0.17	3.58	9.53
Clino	381.81	8.32	0.00	78.82	12.86	0.33	3.44	12.27
Clino	383.26	4.87	0.00	73.25	21.88	0.19	3.41	8.77
Clino	384.76	0.00	0.00	78.03	21.97	0.14	3.49	10.55
Unda								
Unda	94.31	0.00	0.00	100.00	0.00	0.87	-0.29	49.19
Unda	95.40	0.00	0.00	100.00	0.00	0.00	-0.20	48.14
Unda	97.97	0.00	0.00	100.00	0.00	0.00	1.66	46.70
Unda	104.67	0.00	0.00	100.00	0.00	0.15	0.20	50.70
Unda	106.83	0.00	0.00	100.00	0.00	0.00	0.48	41.24
Unda	109.47	0.00	0.00	16.94	83.06	0.00	2.50	1.69
Unda	109.73	0.00	0.00	59.32	40.68	0.00	1.70	3.99
Unda	112.50	0.00	0.00	93.52	6.48	0.13	1.75	13.61
Unda	114.96	8.62	0.00	51.31	40.07	0.00	1.85	8.59
Unda	117.68	11.52	0.00	50.01	38.47	0.00	1.63	5.04
Unda	120.85	24.34	0.00	44.32	31.33	0.56	2.51	5.09
Unda	123.01	23.70	0.00	57.10	19.20	0.00	2.67	8.05
Unda	125.37	0.00	0.00	49.88	50.12	0.00		4.98
Unda	130.71	12.99	0.00	76.25	10.76	0.00	2.53	10.94
Unda	132.23	20.04	0.00	72.65	7.31	0.00	2.47	17.81
Unda	134.75	4.92	0.00	78.94	16.14	0.13	2.67	14.18

Sample or Locality	Depth (m)	Arag (wt.%)	HMC (wt.%)	LMC (wt.%)	Dolo (wt.%)	I/(Ca+Mg) (µmol/mol)	$\delta^{13}C_{carb}$ (‰)	Ca/Mg (mol/mol)
Unda	137.31	0.00	0.00	87.80	12.20	0.00	2.77	13.22
Unda	139.80	9.78	0.00	79.04	11.19	0.00	2.85	12.72
Unda	142.29	9.32	0.00	67.61	23.07	0.18	2.77	10.47
Unda	145.19	7.62	0.00	75.47	16.91	0.00	2.78	11.11
Unda	148.03	2.86	0.00	87.59	9.55	1.01	2.85	11.68
Unda	150.32	2.70	0.00	83.11	14.19	0.00	-0.27	11.36
Unda	274.62	0.00	0.00	38.11	61.89	0.00	1.73	3.24
Unda	275.64	0.00	0.00	64.10	35.90	0.00	1.71	3.72
Unda	277.37	0.00	0.00	40.70	59.30	0.00	1.83	3.58
Unda	279.15	0.00	0.00	39.70	60.30	0.00	1.82	2.99
Unda	280.42	0.00	0.00	42.76	57.24	0.00	1.73	3.73
Unda	281.99	0.00	0.00	0.65	99.35	0.00	1.60	1.38
Unda	283.90	0.00	0.00	0.44	99.56	0.00	2.00	1.36
Unda	285.52	0.00	0.00	0.55	99.45	0.00	2.09	1.37
Unda	286.82	0.00	0.00	9.89	90.11	0.00	1.84	1.45
Unda	287.93	0.00	0.00	31.69	68.31	0.00	1.98	1.78
Unda	289.61	0.00	0.00	0.51	99.49	0.00	2.01	1.37
Unda	291.13	0.00	0.00	0.60	99.40	0.00	2.21	1.36
Unda	292.61	0.00	0.00	0.66	99.34	0.00	2.31	1.36
Unda	293.07	0.00	0.00	0.00	100.00	0.00	2.85	1.39
Unda	293.75	0.00	0.00	0.00	100.00	0.00	3.44	1.37
Unda	294.36	0.00	0.00	1.11	98.89	0.00	2.91	1.36
Unda	295.91	0.00	0.00	1.10	98.90	0.00	2.60	1.34
Unda	297.46	0.00	0.00	0.00	100.00	0.40	2.68	1.35
Unda	298.75	0.00	0.00	1.03	98.97	0.00	2.88	1.29
Unda	299.26	0.00	0.00	0.00	100.00	0.00	2.76	1.31
Unda	299.75	0.00	0.00	0.00	100.00	0.00	2.74	1.34
Unda	301.02	0.00	0.00	0.00	100.00	0.00	2.67	1.29
Unda	301.83	0.00	0.00	1.06	98.94	0.00	2.72	1.33
Unda	302.56	0.00	0.00	0.00	100.00	0.00	2.46	1.30
Unda	303.17	0.00	0.00	0.00	100.00	0.00	2.80	1.31
Unda	304.80	0.00	0.00	0.00	100.00	0.00	2.66	1.30
Unda	306.48	0.00	0.00	0.00	100.00	0.00	2.48	1.35

Table S3. The I/(Ca+Mg) and Ca/Mg ratios for all Proterozoic samples. Sample height, sample description, and $\delta^{13}C_{carb}$ are given when available, with references given in the supplementary text for each individual section.

Formation	Mineralogy/ sedimentology	Height (m)	I/(Ca+Mg) (µmol/mol)	$\delta^{13}C_{carb}$ (‰)	Ca/Mg (mol/mol)
Wooly Dolomite	dolomite		0.11	-5.9	1.45
Wooly Dolomite	dolomite		0.41	-4.5	1.84
Wooly Dolomite	dolomite		0.17	-9.4	1.67
Wooly Dolomite	dolomite		0.09	-4.9	1.53
Wooly Dolomite	dolomite		0.07	-3.7	1.50
Wooly Dolomite	dolomite		0.00	-5.4	1.54
Wooly Dolomite	dolomite		0.15	-2.5	1.47
Wooly Dolomite	dolomite		0.42	-6	1.50
Wooly Dolomite	dolomite		0.00	-0.6	1.15
Wooly Dolomite	dolomite		0.00	-6.6	1.50
Wooly Dolomite	dolomite		0.05	-0.8	31.47
Basler Lake	dolomite		0.27	2.7	1.09
Basler Lake	dolomite		0.22	2.5	1.10
Basler Lake	dolomite		0.00	2.2	1.08
Basler Lake	dolomite		0.07	2.6	1.08
Taltheilei	dolomite		0.16	1.3	1.09
Taltheilei	dolomite		0.20	0.8	1.18
Taltheilei	dolomite		0.08	1.2	1.12
Taltheilei	dolomite		0.08	1.4	1.14
Taltheilei	dolomite		0.05	1.2	1.14
Taltheilei	dolomite		0.20	1.3	1.13
Taltheilei	dolomite		0.22	1	1.14
Taltheilei	dolomite		0.26	1.2	1.14
Taltheilei	dolomite		0.12	1.4	1.15
Taltheilei	dolomite		0.15	1.3	1.17
Taltheilei	dolomite		0.00	1	1.13
Taltheilei	dolomite		0.05	1	1.11
Taltheilei	dolomite		0.09	1.3	1.11
Taltheilei	dolomite		0.00	1.4	1.13
Duck Creek Formation	dolomite	20	0.04	1.21	1.08
Duck Creek Formation	dolomite	42	0.04	1.18	1.07
Duck Creek Formation	dolomite	187	0.00	0.3	1.12
Duck Creek Formation	dolomite	238	0.01	1.71	1.32
Duck Creek Formation	dolomite		0.00		1.08
Duck Creek Formation	dolomite		0.14		1.06
Duck Creek Formation	dolomite	334	0.22	1.06	1.09
Duck Creek Formation	dolomite	378	0.08	1.14	1.09
Duck Creek Formation	dolomite	428	0.09	1.14	1.12
Duck Creek	dolomite		0.15		1.14

Formation	Mineralogy/ sedimentology	Height (m)	I/(Ca+Mg) (µmol/mol)	$\delta^{13}C_{carb}$ (‰)	Ca/Mg (mol/mol)
Formation					
Duck Creek Formation	dolomite		0.32		1.19
Duck Creek Formation	dolomite	570	0.15	1.41	1.07
Duck Creek Formation	dolomite	838	0.14	0.52	1.33
Duck Creek Formation	dolomite	832	0.11	0.66	1.29
Duck Creek Formation	dolomite		0.00		1.24
Duck Creek Formation	dolomite		0.00		1.24
Duck Creek Formation	dolomite		0.00		1.41
Duck Creek Formation	dolomite		0.19		1.03
Duck Creek Formation	dolomite		0.22		1.28
Duck Creek Formation	dolomite		0.48		1.04
Duck Creek Formation	dolomite		0.43		1.32
Duck Creek Formation	dolomite		0.17		1.05
Paradise Creek	dolomite	368.3	0.00		1.19
Paradise Creek	dolomite	420	0.04		1.16
Paradise Creek	dolomite	430.5	0.07		1.22
Paradise Creek	dolomite	450	0.18		1.22
Paradise Creek	dolomite	502.5	0.16		1.17
Paradise Creek	dolomite	420	0.00		1.15
Paradise Creek	dolomite	373.5	0.03		1.18
Paradise Creek	dolomite	399	0.76		1.18
Paradise Creek	dolomite	379.5	0.72		1.64
Paradise Creek	dolomite	507	0.00		1.15
Helena (Ousel Creek)	Dolomite with molar tooth ribbons	189	0.13		8.99
Helena (Ousel Creek)	Dolomite with molar tooth ribbons ribbons	140.2	0.04		29.95
Helena (Ousel Creek)	Dolomite with molar tooth ribbons	85.3	0.00		39.86
Helena (Ousel Creek)	Dolomite with mudcracks	399.3	0.50		1.33
Helena (Ousel Creek)	baicalia	50	0.00		67.11
Helena (Ousel Creek)	Dolomite with baicalia	317	0.11		10.63
Helena (Ousel Creek)	columnar ,stromatolites, microlaminae	68.8	0.01		5.05
Helena (Ousel Creek)	Intraclasts dolomite	335.3	0.30		7.85
Helena (Ousel	silicicalstic, pinch and	228.6	0.13		6.95

Formation	Mineralogy/ sedimentology	Height (m)	I/(Ca+Mg) (µmol/mol)	$\delta^{13}C_{carb}$ (‰)	Ca/Mg (mol/mol)
Creek)	swell, couples in dolomite				
Tieling		172.55	0.33		77.40
Tieling		174.51	0.75		15.45
Tieling		184.66	2.72		1.44
Tieling		190.148	1.37		13.30
Tieling		192.15	1.90		2.70
Tieling		199.5	2.47		1.67
Tieling		199.5	2.42		1.67
Tieling		201.81	0.87		11.88
Tieling		203.91	1.09		18.02
Tieling		206.36	0.79		48.59
Tieling		208.11	0.41		81.92
Tieling		208.25	0.69		71.23
Tieling		210	0.12		55.88
Tieling		212.73	0.34		18.30
Tieling		214.97	0.00		1.86
Tieling		224.35	0.00		29.00
Tieling		226.87	0.64		38.85
Tieling		229.46	0.82		2.35
Tieling		232.12	0.00		3.02
Tieling		234.5	0.38		22.49
Tieling		237.3	0.28		25.49
Tieling		240.8	0.68		1.39
Tieling		249.97	0.95		19.14
Tieling		252.63	1.01		38.66
Tieling		254.59	2.32		1.90
Tieling		266.63	0.63		27.90
Tieling		272.58	0.87		49.19
Tieling		272.58	0.85		48.93
Tieling		277.48	2.12		1.74
Tieling		280.875	1.47		3.86
Tieling		280.875	1.09		3.92
Tieling		283.08	0.67		5.52
Tieling		297.15	0.00		2.03
Tieling		298.06	0.00		3.00
Tieling		299.18	0.00		1.84
Tieling		306.67	0.43		1.59
Tieling		306.67	0.45		1.59
Tieling		308.7	2.46		1.67
Tieling		320.53	0.14		1.24
Tieling		327.18	0.00		3.10
Tieling		333.34	0.40		1.19
Tieling		341.53	0.00		4.56
Tieling		346.36	0.00		6.24
Tieling			0.00		1.34
Tieling			0.00		3.95
Kaltasy	microspar	2341	0.16		1.15
Kaltasy	micrite	3256.8	0.27	-0.4	1.10
Kaltasy	micrite	3582	0.23	-1.6	17.34

Formation	Mineralogy/ sedimentology	Height (m)	I/(Ca+Mg) (µmol/mol)	$\delta^{13}C_{carb}$ (‰)	Ca/Mg (mol/mol)
Kaltasy	microspar	2557.6	0.18	-0.8	1.15
Kaltasy	microspar	3506.3	0.29	1.9	29.28
Kaltasy	microspar	4106	0.27	-1.9	1.07
Kaltasy	micrite	2340	0.36	-1	1.10
Kaltasy	micrite	3752.6	0.24	-1.6	35.00
Kaltasy	micrite	3056.7	0.40	-3.4	36.07
Kaltasy	microspar	2751.5	0.28	-0.9	1.07
Kaltasy	microspar	2353	0.25	-0.8	1.07
Kaltasy	precipitate	3350.5	0.50	-1	2.38
Greenhorn	microspar	318	0.00	1	1.10
Greenhorn	synsedimentary precipitate	26.3	0.12	-0.7	1.09
Greenhorn	microspar	351	0.05	1.5	1.09
Greenhorn	micrite	364	0.52	1.7	1.10
Greenhorn	microlaminated precipitates	324	0.13	1.1	1.07
Greenhorn	microlaminated precipitates	324	0.25	1.1	1.06
Kendal	microbreccia	21	0.00	0.3	1.11
Kendal	synsedimentary precipitate	9	0.00	0.7	1.11
Kendall	ooid	3	0.19	0.5	1.10
Sulkly	microspar	168	0.01	2.1	1.08
Sulky	micrite	76	0.04	1.3	1.09
Sulky	micrite	48	0.00	0.8	1.11
Sulky	micrite	43.5	0.13	0.2	1.10
Sulky	microspar	240	0.00	2	1.07
Sulky	micrite	67	0.13	1.6	1.09
Sulky	microbial microspar	214	0.05	2.1	1.08
Mescal	dolomite	13	0.10		1.10
Mescal	dolomite	27	0.00		1.02
Mescal	dolomite	34	0.00		1.06
Mescal	dolomite	13	0.25		1.14
Society Cliffs	precipitate	184	0.08	3.4	1.08
Society Cliffs	microspar	431.2	0.17	2.4	1.12
Society Cliffs	precipitate	587.4	0.12	2.3	1.10
Society Cliffs	precipitate	127	0.09	3.4	1.07
Society Cliffs	precipitate	486.6	0.13	2.3	1.08
Society Cliffs	precipitate	184	0.04	3.4	1.09
Society Cliffs	precipitate	223	0.20	3.3	1.07
Society Cliffs	microspar	557.9	0.62	2.6	1.09
Society Cliffs	microspar	403	0.10	0.8	1.09
Society Cliffs	microspar	268.3	0.09	0.1	1.05
Society Cliffs	micrite intraclast	738.2	0.09	1.9	1.09
Society Cliffs	microspar	626.9	0.24	1.5	1.05
Victor Bay	micrite	862.5	0.27	2.2	1.09
Society Cliffs	microspar	304.4	0.10	0.4	1.09
Society Cliffs	micritic intraclast	691.5	0.06	1.8	1.07
Victor Bay	micrite	837.6	0.11	2.2	1.09
Victor Bay	micrite	837.6	0.14	2.2	1.10

Formation	Mineralogy/ sedimentology	Height (m)	I/(Ca+Mg) (µmol/mol)	$\delta^{13}C_{carb}$ (‰)	Ca/Mg (mol/mol)
Atar	HB cement	167.5	0.17	2.19	66.33
Atar	MT microspar	134	0.20	1.43	101.90
Atar	Microspar	98	0.68	1.21	101.16
Atar	Microspar	98	0.33	1.21	106.16
Atar	HB cement	103	0.30	0.04	104.91
Atar	microbial lamina	140	0.27	1.67	95.02
Atar	HB cement	160.5	0.26	1.88	6.67
Atar	HB cement	160.5	0.17	1.88	6.44
Tawaz	Microspar	318	0.25	2.04	1.38
Tawaz	MT microspar	307	0.26	0.82	16.68
Tawaz	microspar	335	0.07	0.61	5.52
Tawaz	microbial lamina	300	0.06	-0.35	20.98
Tenoumer	microspar	232.1	0.38	3.2	300.33
Tenoumer	microspar	250.5	0.00	3.6	325.29
Tourist	microspar	23.7	0.00	1.9	112.25
Burovya	limestone	997	0.07	2.4	66.57
Burovya	limestone	997	0.15	2.4	67.20
Sukhaya Tunguska	limestone	281	0.00	1.2	74.23
Sukhaya Tunguska	limestone	300	0.08	1.6	79.03
Sukhaya Tunguska	Nodular limestone	332	1.79	1.5	7.67
Sukhaya Tunguska	limestone	361	0.08	1.1	21.70
Sukhaya Tunguska	limestone	361	0.02	1.1	21.38
Miroyedikha	dolostone	20	0.00	1.5	1.08
Turukhansk	dolostone	65	0.24	2.6	1.10
Minto Inlet			0.04		210.50
Minto Inlet			0.00		1.15
Minto Inlet			0.00		1.42
Minto Inlet			0.00		1.42
Wynniatt	laminated micrite (dol)	2373	0.00	4.9	1.05
Wynniatt			0.23		17.47
Wynniatt			0.00		17.01
Wynniatt	microspar (1st)	2513	0.00	5.8	57.46
Wynniatt			0.00		19.92
Wynniatt	microspar (1st); poorly laminated synerisis	2406	0.00	4.5	84.00
Wynniatt	oosparite (1st)	2530	0.00	4.5	16.17
Wynniatt	flake conclomerate (1st); micrite clasts	2629	1.02	3.1	12.16
Wynniatt	laminated microspar (1st); styolites, interbedded cherts	2754	0.00	5	95.29
Wynniatt			0.00		165.69
Wynniatt	cryptalgal microspar (1st)	2854	0.00	6	9.79
Wynniatt	laminated microspar (1st)	2879	0.00	5.7	52.00
Wynniatt			0.22		2.02
Draken	Lms, pisolite		0.07		1.10
Draken	Dol., flake		1.24		1.05

Formation	Mineralogy/ sedimentology	Height (m)	I/(Ca+Mg) (µmol/mol)	$\delta^{13}C_{carb}$ (‰)	Ca/Mg (mol/mol)
	conglomerate				
Draken	Dol., flake conglomerate		0.00		1.06
Draken	Dol., micrite		0.00		1.83
Draken	Dol., micrite		0.10		1.95
Cavendishryggen	Lms, oolite		0.00		1.12
Draken	Lms. calcisilite		0.05		1.26
Draken	Dolarenite		0.14		2.07
Draken	Dol., pisolite		0.04		1.06
Draken	Dol., pisolite		0.00		1.05
Draken	Lms. calcisitite		0.04		140.26
Backlundtoppen	Lms. oolite		0.00		95.76
Oxfordbreen	Lms., oolite		0.05		74.91
Grusdievbreen	Lms., calarenite		0.01		72.41
Grusdievbreen	Lms. micrite		0.00		43.36
Gursdievbreen	Lms. Flake conglomerate		0.00		65.98
Svanbergfjellet	Dol., stromatolite		0.33		1.15
Svanbergfjellet	Lms., calcisilite		0.05		3.58
Draken	Dol., oolite		0.00		1.06
Draken	Dolarenite		0.03		6.56
Draken	Dolarenite		0.17		3.30
Draken	Dol., flake conglomerate		0.17		1.04
Draken	Dol., flake conglomerate		0.01		1.02
Bed 17	Dol.		0.02		5.81
Bed 18	Lms, oolite		0.07		192.45
Bed 13	Lms., micrite		1.55		4.60
Bed 13	Lms, micrite		0.07		1.26
Bed 14	Dol., arenite		0.00		7.22
Bed 18	Lms, oolite		0.05		106.90
Bed 18	Lms., oolite		0.05		100.13
Bed 18	Dol, pisolite		0.00		89.53
Bed 18	Lms, arenite		0.40		2.30
Bed 18	Lms. pisolite		0.07		68.70
Bed 18	Lms. pisolite		0.05		105.95
Bed 18	Lms. pisolite		0.08		87.42
Bed 18	Lms, oolite		0.00		186.82
Beck Springs	Dolomite		0.12		1.10
Beck Springs	Dolomite		0.21		1.13
Beck Springs	Dolomite		0.31		1.29
Beck Springs	Dolomite		0.28		1.09
Beck Springs	Dolomite		0.00		1.12
Beck Springs	Dolomite		0.00		1.10
Beck Springs	Dolomite		0.00		1.08
Beck Springs	Dolomite		0.00		1.11
Beck Springs	Dolomite		0.11		1.09
Beck Springs	Dolomite		0.37		1.07
Beck Springs	Dolomite		0.00		1.09

Formation	Mineralogy/ sedimentology	Height (m)	I/(Ca+Mg) (µmol/mol)	$\delta^{13}C_{carb}$ (‰)	Ca/Mg (mol/mol)
Beck Springs	Dolomite		0.00		1.07
Beck Springs	Dolomite		0.00		1.10
Beck Springs	Dolomite		0.00		7.25
Beck Springs	Dolomite		0.00		1.24
Beck Springs	Dolomite		0.00		1.09
Beck Springs	Dolomite		0.00		1.09
Beck Springs	Dolomite		0.00		1.42
Beck Springs	Dolomite		0.00		1.09
Beck Springs	Dolomite		0.00		1.14
Khufai	incw	5.93	0.29	3.25	0.98
Khufai	incw	24.54	0.31	5.03	1.16
Khufai	incw	63.95	0.01	4.55	1.04
Khufai	grst	212.60	0.42	-1.60	58.86
Khufai	oolite	302.22	1.06	-2.52	1.04
Khufai	incw	8.02	0.30	3.44	1.06
Khufai	incw	19.81	0.32	4.44	1.10
Khufai	incw	19.81	0.74	4.44	1.11
Khufai		316.50	1.18	-4.75	1.11
Khufai	incw	32.85	4.12	4.91	1.03
Khufai	lammud	45.37	0.29	5.51	1.13
Khufai	lammud	68.74	0.35	5.81	1.09
Khufai	grst	83.94	0.33	4.45	1.03
Khufai	mixgrst	158.82	0.41	4.21	0.98
Khufai	mixgrst	176.64	0.70	4.52	1.04
Khufai	strom	200.55	0.73	3.36	1.02
Khufai	mic	212.90	0.09	4.25	1.02
Khufai	mic	216.74	1.60	4.27	1.02
Khufai	irreg	217.95	0.22	3.54	0.97
Khufai	mic	218.21	0.25	4.02	0.99
Khufai	mic	219.93	0.40	2.89	1.02
Khufai			0.44		0.97
Khufai	tepee	222.88	1.75	3.01	0.96
Khufai	irreg	223.14	0.46	3.17	0.99
Khufai	mixgrst	226.06	0.44	4.30	0.94
Khufai	inccong	229.82	0.36	4.56	0.95
Khufai	dolomic	233.92	0.63	2.89	0.96
Khufai	ooids	236.01	1.86	3.88	0.96
Khufai	dolosilt	306.30	0.14	0.45	0.95
Khufai	fenmud	307.39	0.19	-0.78	1.06
Khufai	mixgrst	308.48	0.34	0.20	1.07
Khufai	irreg	309.89	0.13	-1.29	1.00
Khufai	ooids	313.18	1.12	-3.13	1.25
Khufai	incdol	316.14	1.22	-4.07	1.09
Khufai	incdol	319.09	1.22	-5.44	1.06
Khufai	dolosilt	302.47	0.37	-3.13	1.14
Khufai	dolosilt	304.93	0.34	-4.29	1.06
Khufai	dolosilt	307.40	0.06	-0.01	1.02
Khufai	fenmud	307.95	0.11	-0.53	1.05
Khufai	fenmud	309.04	0.06	-0.05	1.07

Formation	Mineralogy/ sedimentology	Height (m)	I/(Ca+Mg) (µmol/mol)	$\delta^{13}C_{carb}$ (‰)	Ca/Mg (mol/mol)
Khufai	irreg	309.86	0.00	-0.97	1.04
Khufai	incdol	315.23	0.73	-2.01	1.05
Khufai	incdol	315.68	0.62	-3.70	1.07
Khufai	incdol	319.09	1.22	-5.89	1.04
Khufai	mixgrst	310.23	0.11	0.15	1.08
Khufai	ooids	310.45	0.09	0.05	1.07
Khufai	ooids	311.14	0.49	0.66	1.08
Khufai	ooids	312.27	0.64	0.09	1.09
Khufai	ooids	314.32	1.24	-1.92	1.13
Khufai	incdol	315.25	0.56	-4.31	1.12
Khufai	incdol	317.75	1.39	-5.42	1.11
Khufai	incdol	319.00	0.81	-6.16	1.10
Khufai	incdol	320.00	4.10	-8.56	1.16
Khufai	mixgrst	309.26	0.11	1.27	1.10
Khufai	irreg	309.72	0.09	0.10	1.06
Khufai	ooids	310.68	0.16	0.37	1.04
Khufai	ooids	311.82	0.65	0.68	1.07
Khufai	ooids	312.16	0.70	0.28	1.06
Khufai	ooids	314.00	0.58	-0.85	1.07
Khufai	mstrom	313.30	0.30	2.61	2.91
Khufai	ooids	315.00	0.72	-1.97	1.07
Khufai	ooids	315.20	0.67	-2.22	1.11
Khufai	ooids	316.00	0.83	-2.66	1.10
Khufai	incdol	316.60	0.89	-4.21	1.10
Khufai	incdol	317.00	1.47	-3.94	1.12
Khufai	irreg	296.40	0.19	-4.50	1.08
Khufai	mixgrst	297.10	0.00	3.31	29.88
Khufai	mixgrst	297.43	0.01	3.38	1.76
Khufai	stroms	299.25	0.00	4.75	1.15
Khufai	lamdols	303.96	0.00	2.64	0.93
Khufai	lamdols	304.93	0.06	3.07	1.14
Khufai	lamdols	305.30	0.43	2.13	1.00
Khufai	lamdols	306.19	1.01	-5.26	1.05
Khufai	lamdols	307.10	0.02	2.44	0.98
Khufai	mixgrst	307.69	0.00	2.47	0.97
Khufai	stroms	308.43	0.00	1.90	1.13
Khufai	lamdols	309.63	0.00	0.29	1.14
Khufai	stroms	310.37	0.00	-1.03	1.07
Khufai	oolite	311.67	0.30	-1.95	1.22
Khufai	oolite	313.52	0.32	-2.97	1.12
Khufai	oolite	315.00	0.58	-3.37	1.26
Khufai	oolite	316.00	0.30	-3.99	1.09
Khufai	incdol	317.80	0.96	-4.87	1.07
Khufai	incdol	319.40	0.95	-5.89	16.41
Khufai	silt	320.00	1.96	-8.32	1.10
Khufai	oolite	315.00	2.16	-3.45	1.17
Khufai	irreg	311.18	0.51	-1.38	1.07
Khufai	tepee	309.74	6.66	-1.55	29.04
Khufai	dolosilt	306.19	0.20	-0.99	1.36

Formation	Mineralogy/ sedimentology	Height (m)	I/(Ca+Mg) (µmol/mol)	$\delta^{13}C_{carb}$ (‰)	Ca/Mg (mol/mol)
Khufai	dolosilt	305.93	0.27	0.52	1.12
Khufai	dolosilt	305.24	0.40	0.94	1.03
Khufai	dolosilt	305.19	0.39	-2.79	1.06
Khufai	mixgrst	300.13	0.89	2.53	1.05
Khufai	mixgrst	297.24	0.32	0.68	1.01
Khufai	oolite	291.38	0.12	0.93	0.97
Khufai	irreg	289.66	0.12	0.97	0.99
Khufai		317.69	0.64	-4.15	1.14
Khufai		316.54	0.91	-2.31	1.12
Khufai		315.77	1.16	-3.45	1.16
Khufai		311.92	0.62	-2.47	1.17
Khufai		317.31	1.29	-2.69	1.11
Khufai		317.77	1.16	-1.87	1.13
Khufai		317.92	0.98	-1.44	1.11
Khufai		318.08	1.02	-2.03	1.16
Khufai		318.08	0.44	-3.42	1.16
Khufai		300.00	0.17	0.42	1.12
Khufai		300.48	0.05	0.93	1.11
Khufai		300.95	0.01	1.18	1.12
Khufai		301.33	0.04	3.18	1.18
Khufai		301.90	0.32	-5.62	3.00
Khufai		302.48	0.34	-2.49	2.34
Khufai		303.81	0.04	0.43	1.10
Khufai		308.67	0.16	0.19	12.65
Khufai		309.05	4.77	-1.91	1.09
Khufai		311.54	0.02	-1.53	1.09
Khufai		313.08	0.81	-1.87	1.84
Khufai	thwkstn	193.40	0.35	2.20	27.10
Khufai	incw	121.10	0.38	5.29	32.01
Khufai	incw	36.02	0.20	6.94	146.76
Khufai	incp	66.86	0.23	7.97	151.83
Khufai	incp	101.59	0.30	3.28	14.80
Khufai	sgrst	160.12	0.44	-12.20	113.40
Johnnie	dolomite	1.2	0.07		1.06
Johnnie	dolomite	3.2	0.44	2.24	1.17
Johnnie	sandstone with dolomite cement	3.9	1.21	0.09	2.02
Johnnie	sandstone with dolomite cement	7	0.37	0.62	1.18
Johnnie	sandstone with dolomite cement	8.8	0.68		1.12
Johnnie	sandstone with dolomite cement	12	0.80	1.86	1.13
Johnnie	oolitic dolomite	40.6	0.62	-3.58	1.33
Johnnie	oolitic dolomite	40.9	0.33	-3.96	1.12
Johnnie	oolitic dolomite	41.2	0.46	-4.41	1.10
Johnnie	oolitic dolomite	41.5	0.45	-4.2	1.11
Johnnie	oolitic dolomite	41.5	0.32		1.11
Johnnie	oolitic dolomite	41.8	0.43	-4.04	1.08
Johnnie	oolitic dolomite	42.1	0.43	-4.95	1.11

Formation	Mineralogy/ sedimentology	Height (m)	I/(Ca+Mg) (µmol/mol)	$\delta^{13}C_{carb}$ (‰)	Ca/Mg (mol/mol)
Johnnie	oolitic dolomite	42.4	0.67	-4.65	1.08
Johnnie	oolitic dolomite	42.7	0.48	-5.06	1.08
Johnnie	oolitic dolomite	43.1	0.59		1.11
Johnnie	sandstone with dolomite cement	51.2	1.81	-10.47	1.16
Johnnie	sandstone with dolomite cement	56.9	0.77	-10.89	1.21
Johnnie	sandstone with dolomite cement	57.3	2.09		1.17
Johnnie	sandstone with dolomite cement	59.6	0.79		5.35
Johnnie	sandstone with dolomite cement	61.1	2.82	-9.55	26.98
Johnnie	sandstone with dolomite cement	62.6	1.08	-10.76	5.40
Johnnie	sandstone with dolomite cement	64.1	0.72	-11.47	9.05
Johnnie	sandstone with dolomite cement	65.6	2.03	-9.64	4.94
Johnnie	sandstone with dolomite cement	67.1	0.56	-11.23	7.74
Johnnie	sandstone with dolomite cement	68.6	0.37	-11.19	9.16
Johnnie	sandstone with dolomite cement	70.1	5.37	-8.65	6.95
Johnnie	sandstone with dolomite cement	72.6	1.49	-10.96	7.40
Johnnie	sandstone with dolomite cement	74.1	0.72	-10.56	4.73
Johnnie	sandstone with dolomite cement		0.51	-8.85	1.05
Clemente	dol	747.5	0.85	-0.6	1.08
Clemente	dol	690.5	0.65	2.3	0.91
Clemente	dol	672.5	0.97	-1.6	1.16
Clemente	dol	630.5	0.31	2.5	0.96
Clemente	dol	580.5	0.18	2.1	7.23
Clemente	dol	565.5	0.26	1.3	1.17
Clemente	dol	545.5	1.02	3	1.11
Clemente	dol	500.5	0.28	0	1.07
Clemente	sandy dol	423.5	0.60	-5.9	0.89
Clemente	lime	364.2	1.43	-8.6	38.90
Clemente	lime	364.05	0.73	-8.7	34.81
Clemente	lime	363.6	1.57	-8.3	28.80
Clemente	lime	363.15	1.84	-8.9	27.63
Clemente	lime/dol	363.2	6.67	-7.5	3.03
Clemente	lime/dol	362.85	0.63	-9.5	29.95
Clemente	lime/dol	362.7	0.65	-7.9	1.42
Clemente	lime/dol	362.4	3.88	-9.3	1.46
Clemente	lime/dol	362.25	1.28	-9	1.32
Clemente	dol	361.95	0.99	-5.5	1.12
Clemente	dol	361.8	7.75	-5	1.19
Clemente	dol	361.65	0.77	-4.4	1.21

Formation	Mineralogy/ sedimentology	Height (m)	I/(Ca+Mg) (µmol/mol)	$\delta^{13}C_{carb}$ (‰)	Ca/Mg (mol/mol)
Clemente	dol	361.5	1.42	-3	1.24
Clemente	dol	356.5	0.94	-1.3	1.24
Clemente	dol	338.5	0.09	1.2	1.23
Clemente	sandy dol	231.5	1.03	-0.1	1.39
Clemente	dol	228.5	0.32	2.1	1.18
Clemente	dol	198.5	0.24	5.1	16.35
Clemente	dol	188.5	1.64	3.8	16.35
Clemente	dol	108.5	0.92	-0.4	9.90
Clemente	dol	68.5	1.20	3	1.22
Clemente	dol	28.5	0.65	2	1.00
Doushantuo	dark-gray dolostone	1.5	0.22	-2.49	1.10
Doushantuo	gray dolostone	1.9	0.18	-2.73	1.13
Doushantuo	dark-gray dolostone	2.7	0.06		1.14
Doushantuo	dark-gray shaly dolostone	3	0.31	-3.28	1.10
Doushantuo	dark-gray shaly dolostone	4.4	0.52	-4.07	1.15
Doushantuo	gray dolostone	4.5	0.79	-3.92	1.18
Doushantuo	dark shaly dolostone	5.4	0.04	-4.01	1.09
Doushantuo	dark silty dolostone	10	0.00	1.54	0.93
Doushantuo	dark silty dolostone	10.8	2.07		1.50
Doushantuo	dark silty dolostone	11	0.00	1.23	0.16
Doushantuo	dark dolostone	30	0.11	-0.01	1.06
Doushantuo	dark dolostone	38.4	0.00	1.4	1.24
Doushantuo	dark dolostone	39.2	0.00	1.96	1.16
Doushantuo	dark dolostone	40.5	0.02	2.81	1.12
Doushantuo	dark dolostone	41.7	0.03	2.55	1.14
Doushantuo	dark dolostone	54.8	0.00	3.55	1.07
Doushantuo	dark cherty dolostone	76.6	0.00	4.35	1.09
Doushantuo	dark cherty dolostone	78.3	0.05	3.75	1.08
Doushantuo	dark cherty dolostone	79	0.00	3.6	1.06
Doushantuo	dark shaly dolostone	84.6	0.00	3.86	1.11
Doushantuo	dark shaly dolostone	85.4	0.00	3.46	1.11
Doushantuo	dark dolostone	87.6	0.00	3.61	1.06
Doushantuo	dark cherty dolostone	91.6	0.00	-0.72	1.11
Doushantuo	dark gray shaly dolostone	96.5	0.00	4.63	1.06
Doushantuo	dark gray shaly dolostone	99.2	0.00	4.38	0.92
Doushantuo	dark gray shaly dolostone	100.7	0.00	4.8	1.06
Doushantuo	dark gray shaly dolostone	111	0.00	1	0.94
Doushantuo	dark gray shaly dolostone	118	0.00	1.67	0.94
Doushantuo	dark gray shaly dolostone	120	0.00	2.28	1.07
Doushantuo	dark gray shaly dolostone	124	0.00	2.01	0.95
Doushantuo	dark gray shaly dolostone	127.3	0.00	2.27	0.88

Formation	Mineralogy/ sedimentology	Height (m)	I/(Ca+Mg) (μmol/mol)	$\delta^{13}C_{carb}$ (‰)	Ca/Mg (mol/mol)
Doushantuo	dark gray shaly dolostone	131.5	0.00	2.61	0.99
Doushantuo	dark gray shaly dolostone	133	0.00	1.73	0.94
Doushantuo	dark gray shaly dolostone	134	0.00	1.74	0.96
Doushantuo	gray shaly dolostone	139.2	0.00	1.79	0.97
Doushantuo	dark gray shaly dolostone	152	0.07	-3.46	0.98
Doushantuo	dark dolostone	155	0.08	-3.86	0.97
Doushantuo	dark dolostone	155.5	0.07	-3.74	0.97
Doushantuo	dark dolostone	156	0.04	-3.49	0.96
Doushantuo	dark dolostone	158	0.18	-4.07	0.95
Doushantuo	dark dolostone	158.5	0.00	-3.73	0.95
Doushantuo	dark dolostone	159	0.14	-5.25	0.97
Doushantuo	dark dolostone	159.5	0.11	-5.09	0.96
Doushantuo	dark dolostone	160	0.48	-4.8	1.00
Doushantuo	gray dolostone	160.2	0.00	-5.8	0.98
Doushantuo	dark dolostone	161	0.00	-6.79	0.99
Doushantuo	dark dolostone	161.7	0.05	-6.82	0.97
Doushantuo	dark dolostone	161.8	0.22	-6.97	0.98
Doushantuo	dark dolostone	162	0.21	-7.52	0.99
Doushantuo	dark shaly dolostone	162.2	0.24	-5.35	0.97
Doushantuo	dark shaly dolostone	162.3	0.16	-6.43	0.98
Doushantuo	dark shaly dolostone	162.5	0.16	-5.37	0.97
Doushantuo	dark shaly dolostone	162.9	0.08	-7.9	0.99
Doushantuo	dark dolostone	164.2	0.47	-4.38	0.97
Doushantuo	dark dolostone	164.4	0.48	-4.49	0.96
Doushantuo	dark dolostone	164.7	0.56	-5.28	0.96
Doushantuo	dark dolostone	164.9	1.29	-2.04	0.97
Doushantuo	dark dolostone	165	0.24	-6.19	0.96
Doushantuo	dark shaly dolostone	165.4	0.00	-5.62	0.94
Doushantuo	dark shaly dolostone	165.8	0.49	-5.62	0.94
Doushantuo	dark shaly dolostone	166	0.53	-4.7	0.95
Doushantuo	dark shaly dolostone	166.5	0.53	-4.25	0.94
Doushantuo	black shale	167	0.60		1.13
Doushantuo	black shale	167.5	0.00		1.30
Doushantuo	dark shaly dolostone	168	0.00	-1.6	0.92
Doushantuo	dark shaly dolostone	168.5	0.12	-5.65	0.94
Doushantuo	dark shaly dolostone	168.7	0.19	-5.76	0.93
Doushantuo	dark shaly dolostone	169	0.11	-10.47	0.93
Doushantuo	dark shaly dolostone	169.3	0.15	-11.33	0.94
Doushantuo	dark shaly dolostone	169.4	0.00	-10.7	0.93
Doushantuo	cherty dolostone	169.5	0.06	-9.45	0.93
Doushantuo	cherty dolostone	170	0.55	-8.19	0.93
Doushantuo	cherty dolostone	170.5	0.56	-9.21	0.93
Doushantuo	cherty dolostone	171.5	1.16	-9.53	0.92

SUPPLEMENTAL REFERENCES CITED

Aleinikoff, J., Evans, K., Fanning, C., Obradovich, J., Ruppel, E., Zieg, J. and Steinmetz, J. (1996) SHRIMP U–Pb ages of felsic igneous rocks, Belt Supergroup, western Montana, Geological Society of America, Abstracts with Programs.

Asmerom, Y., Jacobsen, S. B., Knoll, A. H., Butterfield, N. J. and Swett, K., 1991, Strontium isotopic variations of Neoproterozoic seawater: implications for crustal evolution: Geochimica et Cosmochimica Acta, v. 55, p. 2883-2894.

Bartley, J. K. and Kah, L. C., 2004, Marine carbon reservoir, Corg-Ccarb coupling, and the evolution of the Proterozoic carbon cycle: Geology, v. 32, p. 129-132.

Bartley, J. K., Semikhatov, M. A., Kaufman, A. J., Knoll, A. H., Pope, M. C. and Jacobsen, S. B., 2001, Global events across the Mesoproterozoic–Neoproterozoic boundary: C and Sr isotopic evidence from Siberia: Precambrian Research, v. 111, p. 165-202.

Bekker, A., Krapež, B., Müller, S. G. and Karhu, J. A., 2016, A short-term, post-Lomagundi positive C isotope excursion at c. 2.03 Ga recorded by the Wooly Dolomite, Western Australia: Journal of the Geological Society, v., p. jgs2015-2152.

Bertrand-Sarfati, J. and Moussine-Pouchkine, A., 1988, Is cratonic sedimentation consistent with available models? An example from the Upper Proterozoic of the West African craton: Sedimentary Geology, v. 58, p. 255-276.

Bishop, J. W., Sumner, D. Y. and Huerta, N. J., 2006, Molar tooth structures of the Neoarchean Monteville Formation, Transvaal Supergroup, South Africa. II: A wave□induced fluid flow model: Sedimentology, v. 53, p. 1069-1082.

Blättler, C. L., Miller, N. R. and Higgins, J. A., 2015, Mg and Ca isotope signatures of authigenic dolomite in siliceous deep-sea sediments: Earth and Planetary Science Letters, v. 419, p. 32-42.

Bowring, S. A. and Grotzinger, J. P., 1992, Implications of new chronostratigraphy for tectonic evolution of Wopmay Orogen, northwest Canadian Shield: American Journal of Science, v. 292, p. 1-20.

Burdige, D. J. and Zimmerman, R. C., 2002, Impact of sea grass density on carbonate dissolution in Bahamian sediments: Limnology and Oceanography, v. 47, p. 1751-1763.

Carlton, R. G. and Richardson, L. L., 1995, Oxygen and sulfide dynamics in a horizontally migrating cyanobacterial mat: black band disease of corals: FEMS Microbiology Ecology, v. 18, p. 155-162.

Cline, J. D., 1969, Spectrophotometric determination of hydrogen sulfide in natural waters: Limnology and Oceanography, v. 14, p. 454-458.

Condon, D., Zhu, M., Bowring, S., Wang, W., Yang, A. and Jin, Y., 2005, U-Pb ages from the neoproterozoic Doushantuo Formation, China: science, v. 308, p. 95-98.

Corsetti, F. A. and Kaufman, A. J., 2003, Stratigraphic investigations of carbon isotope anomalies and Neoproterozoic ice ages in Death Valley, California: Geological Society of America Bulletin, v. 115, p. 916-932.

Dehler, C. M., Elrick, M., Karlstrom, K. E., Smith, G. A., Crossey, L. J. and Timmons, J. M., 2001, Neoproterozoic Chuar Group (800–742Ma), Grand Canyon: a record of cyclic marine deposition during global cooling and supercontinent rifting: Sedimentary Geology, v. 141, p. 465-499.

Evans, D. A., Sircombe, K., Wingate, M. T., Doyle, M., McCarthy, M., Pidgeon, R. T. and Van Niekerk, H. S., 2003, Revised geochronology of magmatism in the western Capricorn Orogen at 1805–1785 Ma: diachroneity of the Pilbara–Yilgarn collision: Australian Journal of Earth Sciences, v. 50, p. 853-864.

Farrenkopf, A. M., Dollhopf, M. E., Chadhain, S. N., Luther III, G. W. and Nealson, K. H., 1997, Reduction of iodate in seawater during Arabian Sea shipboard incubations and in laboratory cultures of the marine bacterium< i> Shewanella putrefaciens</i> strain MR-4: Marine Chemistry, v. 57, p. 347-354.

Frank, T., Kah, L. and Lyons, T., 2003, Changes in organic matter production and accumulation as a mechanism for isotopic evolution in the Mesoproterozoic ocean: Geological Magazine, v. 140, p. 397-420.

Frank, T. D. and Lyons, T. W., 1998, “Molar-tooth” structures: A geochemical perspective on a Proterozoic enigma: Geology, v. 26, p. 683-686.

Frank, T. D., Lyons, T. W. and Lohmann, K. C., 1997, Isotopic evidence for the paleoenvironmental evolution of the Mesoproterozoic Helena Formation, Belt Supergroup, Montana, USA: Geochimica et Cosmochimica Acta, v. 61, p. 5023-5041.

Gellatly, A. M. and Lyons, T. W., 2005, Trace sulfate in mid-Proterozoic carbonates and the sulfur isotope record of biospheric evolution: Geochimica et Cosmochimica Acta, v. 69, p. 3813-3829.

Gill, B. C., Lyons, T. W. and Frank, T. D., 2008, Behavior of carbonate-associated sulfate during meteoric diagenesis and implications for the sulfur isotope paleoproxy: Geochimica et Cosmochimica Acta, v. 72, p. 4699-4711.

Gilleaudeau, G. J. and Kah, L. C., 2015, Heterogeneous redox conditions and a shallow chemocline in the Mesoproterozoic ocean: evidence from carbon–sulfur–iron relationships: Precambrian Research, v. 257, p. 94-108.

Glock, N., Liebetrau, V. and Eisenhauer, A., 2014, I/Ca ratios in benthic foraminifera from the Peruvian oxygen minimum zone: analytical methodology and evaluation as proxy for redox conditions: Biogeosciences Discussions, v. 11, p. 11635-11670.

Halverson, G. P., Hoffman, P. F., Schrag, D. P., Maloof, A. C. and Rice, A. H. N., 2005, Toward a Neoproterozoic composite carbon-isotope record: Geological Society of America Bulletin, v. 117, p. 1181-1207.

Hardisty, D. S., Lu, Z., Planavsky, N. J., Bekker, A., Philippot, P., Zhou, X. and Lyons, T. W., 2014, An iodine record of Paleoproterozoic surface ocean oxygenation: Geology, v. 42, p. 619-622.

Hoffman, P., 1968, Stratigraphy of the Lower Proterozoic (Aphebian), Great Slave Supergroup, East Arm of Great Slave Lake, District of Mackenzie. Department of Energy, Mines and Resources.

Hoffman, P., 1974, Shallow and Deepwater Stromatolites in Lower Proterozoic Platform--to--Basin Facies Change, Great Slave Lake, Canada: AAPG Bulletin, v. 58, p. 856-867.

Hoffman, P., Fraser, J. and McGlynn, J. (1970) The Coronation geosyncline of Aphebian age, district of Mackenzie, Symposium on Basins and Geosynclines of the Canadian Shield: Geological Survey of Canada, Paper, pp. 70-40.

Hu, X. and Burdige, D. J., 2007, Enriched stable carbon isotopes in the pore waters of carbonate sediments dominated by seagrasses: Evidence for coupled carbonate dissolution and reprecipitation: Geochimica et Cosmochimica Acta, v. 71, p. 129-144.

Hurtgen, M. T., Arthur, M. A. and Prave, A. R., 2004, The sulfur isotope composition of carbonate-associated sulfate in Mesoproterozoic to Neoproterozoic carbonates from Death Valley, California: Geological Society of America Special Papers, v. 379, p. 177-194.

Idnurm, M., 2000, Towards a high resolution Late Palaeoproterozoic–earliest Mesoproterozoic apparent polar wander path for northern Australia: Australian Journal of Earth Sciences, v. 47, p. 405-429.

Irvine, T., 1970, Crystallization sequences in the Muskox intrusion and other layered intrusions. I. Olivine-pyroxene-plagioclase relations: Geol. Soc. S. Afr. Spec. Publ., v. 1, p. 441-476.

Jackson, V., 2008, Preliminary geologic map of part of the southern Wopmay Orogen (parts of NTS 86B and 86C; 2007 updates); descriptive notes to accompany 1: 100,000 scale map: NWT Geosci Office, NWT Open Rep, v. 7, p.

Jackson, V., van Breemen, O., Ootes, L., Bleeker, W., Bennett, V., Davis, W., Ketchum, J., Smar, L. and McFarlane, C., 2013, U–Pb zircon ages and field relationships of Archean basement and Proterozoic intrusions, south-central Wopmay Orogen, NWT: implications for tectonic assignments 1, 2: Canadian Journal of Earth Sciences, v. 50, p. 979-1006.

James, N. P., Narbonne, G. M. and Sherman, A. G., 1998, Molar-tooth carbonates: shallow subtidal facies of the Mid-to Late Proterozoic: Journal of Sedimentary Research, v. 68, p.

Jiang, G., Kaufman, A. J., Christie-Blick, N., Zhang, S. and Wu, H., 2007, Carbon isotope variability across the Ediacaran Yangtze platform in South China: Implications for a large surface-to-deep ocean [delta]13C gradient: Earth and Planetary Science Letters, v. 261, p. 303-320.

Jiang, G., Shi, X., Zhang, S., Wang, Y. and Xiao, S., 2011, Stratigraphy and paleogeography of the Ediacaran Doushantuo Formation (ca. 635-551 Ma) in South China: Gondwana Research, v. 19, p. 831-849.

Jones, D., Maloof, A., Hurtgen, M., Rainbird, R. and Schrag, D., 2010, Regional and global chemostratigraphic correlation of the early Neoproterozoic Shaler Supergroup, Victoria Island, northwestern Canada: Precambrian Research, v. 181, p. 43-63.

Kah, L., Crawford, D., Bartley, J., Kozlov, V., Sergeeva, N. and Puchkov, V., 2007, C-and Sr-isotope chemostratigraphy as a tool for verifying age of Riphean deposits in the Kama-Belaya aulacogen, the east European platform: Stratigraphy and Geological Correlation, v. 15, p. 12-29.

Kah, L. C., Bartley, J. K. and Teal, D. A., 2012, Chemostratigraphy of the Late Mesoproterozoic Atar Group, Taoudeni Basin, Mauritania: Muted isotopic variability, facies correlation, and global isotopic trends: Precambrian Research, v. 200, p. 82-103.

Kah, L. C., Lyons, T. W. and Chesley, J. T., 2001, Geochemistry of a 1.2 Ga carbonate-evaporite succession, northern Baffin and Bylot Islands: implications for Mesoproterozoic marine evolution: Precambrian Research, v. 111, p. 203-234.

Kah, L. C., Lyons, T. W. and Frank, T. D., 2004, Low marine sulphate and protracted oxygenation of the Proterozoic biosphere: Nature, v. 431, p. 834-838.

Karlstrom, K. E., Bowring, S. A., Dehler, C. M., Knoll, A. H., Porter, S. M., Des Marais, D. J., Weil, A. B., Sharp, Z. D., Geissman, J. W. and Elrick, M. B., 2000, Chuar Group of the Grand Canyon: Record of breakup of Rodinia, associated change in the global carbon cycle, and ecosystem expansion by 740 Ma: Geology, v. 28, p. 619-622.

Kennedy, H. and Elderfield, H., 1987a, Iodine diagenesis in non-pelagic deep-sea sediments: Geochimica et Cosmochimica Acta, v. 51, p. 2505-2514.

Kennedy, H. A. and Elderfield, H., 1987b, Iodine diagenesis in pelagic deep-sea sediments: Geochimica et Cosmochimica Acta, v. 51, p. 2489-2504.

Kenter, J. A., Ginsburg, Robert, N., Troelstra, Simon, R., 2001, Sea-level-driven sedimentation patterns on the slope and margin, v., p.

Kerans, C. and Donaldson, J., 1988, Deepwater conical stromatolite reef, Sulky Formation (Dismal Lakes Group), Middle Proterozoic, NWT, v., p.

Kerans, C., Ross, G., Donaldson, J. and Geldsetzer, H., 1981, Tectonism and depositional history of the Helikian Hornby Bay and Dismal Lakes groups, District of Mackenzie: Proterozoic basins of Canada. Edited by FHA Campbell. Geological Survey of Canada, Paper, v., p. 81-10.

Kjarsgaard, B. A., Pearson, D.G., DuFrane, A., and Heaman, L., 2013, Proterozoic geology of the East Arm Basin with emphasis on Paleoproterozoic magmatic rocks, Thaidene Nene MERA study area: Chapter 3 in Mineral and Energy Resource Assessment for the

Proposed Thaidene Nene National Park Reserve in the Area of the East Arm of Great Slave Lake, Northwest Territories, (eds.) D.F. Wright, E.J. Ambrose, D. Lemkow, and G.F. Bonham-Carte; Geological Survey of Canada, v. Open File 7196, p. 77-117.

Knoll, A. and Swett, K., 1989, Carbonate deposition during the late Proterozoic Era: an example from Spitsbergen: American Journal of Science, v. 290, p. 104-132.

Knoll, A., Swett, K. and Mark, J., 1991, The Draken Conglomerate formation: Paleobiology of a Proterozoic tidal flat complex: J. Paleontol, v. 65, p. 531-569.

Knoll, A. H., Swett, K. and Burkhardt, E., 1989, Paleoenvironmental distribution of microfossils and stromatolites in the Upper Proterozoic Backlundtoppen Formation, Spitsbergen: Journal of Paleontology, v., p. 129-145.

Knoll, A. H., Wörndle, S. and Kah, L. C., 2013, Covariance of microfossil assemblages and microbialite textures across an upper Mesoproterozoic carbonate platform: Palaios, v. 28, p. 453-470.

Krapež, B., Müller, S.G., Karhu, J.A., Bekker, A., in revision, Stratigraphy of the Late Palaeoproterozoic (~2.03 Ga) Wooly Dolomite, Ashburton Province, Western Australia: a syn-rift carbonate sequence with positive δ13C values: Precambrian Research, v., p.

Lavoie, D. and Turner, E. C., 2009, Mesoproterozoic carbonate systems in the Borden Basin, Nunavut: Canadian Journal of Earth Sciences, v. 46, p. 915-938.

LeCheminant, A. and Heaman, L., 1989, Mackenzie igneous events, Canada: Middle Proterozoic hotspot magmatism associated with ocean opening: Earth and Planetary Science Letters, v. 96, p. 38-48.

Li, C., Love, G. D., Lyons, T. W., Fike, D. A., Sessions, A. L. and Chu, X., 2010, A stratified redox model for the Ediacaran ocean: Science, v. 328, p. 80-83.

Lord, C. S., 1963, Snare River and Ingray Lake map-areas, Northwest Territories. R. Duhamel, Queen's Printer and Controller of Stationery.

Loyd, S. J., Berelson, W. M., Lyons, T. W., Hammond, D. E. and Corsetti, F. A., 2012a, Constraining pathways of microbial mediation for carbonate concretions of the Miocene Monterey Formation using carbonate-associated sulfate: Geochimica et Cosmochimica Acta, v. 78, p. 77-98.

Loyd, S. J., Marenco, P. J., Hagadorn, J. W., Lyons, T. W., Kaufman, A. J., Sour-Tovar, F. and Corsetti, F. A., 2012b, Sustained low marine sulfate concentrations from the Neoproterozoic to the Cambrian: Insights from carbonates of northwestern Mexico and eastern California: Earth and Planetary Science Letters, v. 339, p. 79-94.

Loyd, S. J., Marenco, P. J., Hagadorn, J. W., Lyons, T. W., Kaufman, A. J., Sour-Tovar, F. and Corsetti, F. A., 2013, Local $\delta^{34}S$ variability in 580Ma carbonates of northwestern Mexico and the Neoproterozoic marine sulfate reservoir: Precambrian Research, v. 224, p. 551-569.

Lu, Z., Hoogakker, B. A., Hillenbrand, C.-D., Zhou, X., Thomas, E., Gutchess, K. M., Lu, W., Jones, L. and Rickaby, R. E., 2016, Oxygen depletion recorded in upper waters of the glacial Southern Ocean: Nature communications, v. 7, p.

Lu, Z., Jenkyns, H. C. and Rickaby, R. E., 2010, Iodine to calcium ratios in marine carbonate as a paleo-redox proxy during oceanic anoxic events: Geology, v. 38, p. 1107-1110.

Luepke, J. J. and Lyons, T. W., 2001, Pre-Rodinian (Mesoproterozoic) supercontinental rifting along the western margin of Laurentia: geochemical evidence from the Belt-Purcell Supergroup: Precambrian Research, v. 111, p. 79-90.

Lyons, T. W., Luepke, J. J., Schreiber, M. E. and Zieg, G. A., 2000, Sulfur geochemical constraints on Mesoproterozoic restricted marine deposition: lower Belt Supergroup, northwestern United States: Geochimica et Cosmochimica Acta, v. 64, p. 427-437.

Mahon, R. C., Dehler, C. M., Link, P. K., Karlstrom, K. E. and Gehrels, G. E., 2014, Geochronologic and stratigraphic constraints on the Mesoproterozoic and Neoproterozoic Pahrump Group, Death Valley, California: A record of the assembly, stability, and breakup of Rodinia: Geological Society of America Bulletin, v. 126, p. 652-664.

Manfrino, C., Ginsburg, Robert N., 2001, Pliocene to Pleistocene deposition history of the upper platform margin, v., p.

McClain, M. E., Swart, P. K. and Vacher, H. L., 1992, The hydrogeochemistry of early meteoric diagenesis in a Holocene deposit of biogenic carbonates: Journal of Sedimentary Research, v. 62, p.

McGlynn, J., Glass, D. J. and Fraser, J. A. (1972) Archean and Proterozoic Geology of the Yellowknife and Great Bear Areas, Northwest Territories: Excursion A27. 24th International Geological Congress.

Melim, L. A., 1996, Limitations on lowstand meteoric diagenesis in the Pliocene-Pleistocene of Florida and Great Bahama Bank: Implications for eustatic sea-level models: Geology, v. 24, p. 893-896.

Melim, L. A., Swart, P. K. and Eberli, G. P., 2004, Mixing-zone diagenesis in the subsurface of Florida and the Bahamas: Journal of Sedimentary Research, v. 74, p. 904-913.

Melim, L. A., Swart, P. K. and Maliva, R. G., 1995, Meteoric-like fabrics forming in marine waters: implications for the use of petrography to identify diagenetic environments: Geology, v. 23, p. 755-758.

Melim, L. A., Swart, Peter K., Maliva, Robert G., 2001, Meteoric and marine-burial diagenesis in the subsurface of Great Bahama Bank, v., p.

Mingxiang, M., Fengjie, Y., Jinhan, G. and Qingfen, M., 2008, Glauconites formed in the high-energy shallow-marine environment of the Late Mesoproterozoic: case study from Tieling Formation at Jixian Section in Tianjin, North China: Earth Science Frontiers, v. 15, p. 146-158.

Müller, S. G., Krapež, B., Barley, M. E. and Fletcher, I. R., 2005, Giant iron-ore deposits of the Hamersley province related to the breakup of Paleoproterozoic Australia: New insights from in situ SHRIMP dating of baddeleyite from mafic intrusions: Geology, v. 33, p. 577-580.

Osburn, M. R. (2013) Isotopic proxies for microbial and environmental change: insights hydrogen isotopes and the Ediacaran Khufai Formation. California Institute of Technology.

Osburn, M. R., Grotzinger, J. P. and Bergmann, K., 2014, Facies, stratigraphy, and evolution of a middle Ediacaran carbonate ramp: Khufai Formation, Sultanate of Oman: AAPG Bulletin, v. 98, p. 1631-1667.

Osburn, M. R., Owens, J., Bergmann, K. D., Lyons, T. W. and Grotzinger, J. P., 2015, Dynamic changes in sulfate sulfur isotopes preceding the Ediacaran Shuram Excursion: Geochimica et Cosmochimica Acta, v. 170, p. 204-224.

Ovchinnikova, G., Gorokhov, I. and Belyatskii, B., 1995, U-Pb systematics of Pre-Cambrian carbonates: the Riphean Sukhaya Tunguska Formation in the Turukhansk Uplift, Siberia: Lithology and Mineral Resources, v. 30, p.

Page, R., Jackson, M. and Krassay, A., 2000, Constraining sequence stratigraphy in north Australian basins: SHRIMP U–Pb zircon geochronology between Mt Isa and McArthur River*: Australian Journal of Earth Sciences, v. 47, p. 431-459.

Pisarevsky, S. A., Murphy, J. B., Cawood, P. A. and Collins, A. S., 2008, Late Neoproterozoic and Early Cambrian palaeogeography: models and problems: Geological Society, London, Special Publications, v. 294, p. 9-31.

Planavsky, N. J., Bekker, A., Hofmann, A., Owens, J. D. and Lyons, T. W., 2012, Sulfur record of rising and falling marine oxygen and sulfate levels during the Lomagundi event: Proceedings of the National Academy of Sciences, v. 109, p. 18300-18305.

Planavsky, N. J., Reinhard, C. T., Wang, X., Thomson, D., McGoldrick, P., Rainbird, R. H., Johnson, T., Fischer, W. W. and Lyons, T. W., 2014, Low Mid-Proterozoic atmospheric oxygen levels and the delayed rise of animals: science, v. 346, p. 635-638.

Pollock, M. D., Kah, L. C. and Bartley, J. K., 2006, Morphology of molar-tooth structures in Precambrian carbonates: influence of substrate rheology and implications for genesis: Journal of Sedimentary Research, v. 76, p. 310-323.

Pruss, S. B., Corsetti, F. A. and Fischer, W. W., 2008, Seafloor-precipitated carbonate fans in the Neoproterozoic Rainstorm Member, Johnnie Formation, Death Valley Region, USA: Sedimentary Geology, v. 207, p. 34-40.

Romaniello, S. J., Herrmann, A. D. and Anbar, A. D., 2013, Uranium concentrations and 238 U/235 U isotope ratios in modern carbonates from the Bahamas: Assessing a novel paleoredox proxy: Chemical Geology, v. 362, p. 305-316.

Rooney, A. D., Selby, D., Houzay, J.-P. and Renne, P. R., 2010, Re–Os geochronology of a Mesoproterozoic sedimentary succession, Taoudeni basin, Mauritania: implications for basin-wide correlations and Re–Os organic-rich sediments systematics: Earth and Planetary Science Letters, v. 289, p. 486-496.

Rue, E. L., Smith, G. J., Cutter, G. A. and Bruland, K. W., 1997, The response of trace element redox couples to suboxic conditions in the water column: Deep Sea Research Part I: Oceanographic Research Papers, v. 44, p. 113-134.

Sahoo, S., Planavsky, N., Jiang, G., Kendall, B., Owens, J., Wang, X., Shi, X., Anbar, A. and Lyons, T., 2016, Oceanic oxygenation events in the anoxic Ediacaran ocean: Geobiology, v., p.

Sami, T. T., 2000, Evolution of late Paleoproterozoic ramp systems, lower McNamara Group, northeastern Australia, v., p.

Saylor, B. and Grotzinger, J., 1992, Reconnaissance of the structure and stratigraphy of the Basler Lake area, southern Wopmay Orogen, Northwest Territories: Current research, part C. Geological Survey of Canada, Paper, v., p. 259-268.

Seeberg□Elverfeldt, J., Schlüter, M., Feseker, T. and Kölling, M., 2005, Rhizon sampling of porewaters near the sediment□water interface of aquatic systems: Limnology and oceanography: Methods, v. 3, p. 361-371.

Sircombe, K., 2003, Age of the Mt Boggola volcanic succession and further geochronological constraint on the Ashburton Basin, Western Australia: Australian Journal of Earth Sciences, v. 50, p. 967-974.

Sperling, E., Rooney, A., Hays, L., Sergeev, V., Vorob'eva, N., Sergeeva, N., Selby, D., Johnston, D. and Knoll, A., 2014, Redox heterogeneity of subsurface waters in the Mesoproterozoic ocean: Geobiology, v. 12, p. 373-386.

Stewart, J. H., Gehrels, G. E., Barth, A. P., Link, P. K., Christie-Blick, N. and Wrucke, C. T., 2001, Detrital zircon provenance of Mesoproterozoic to Cambrian arenites in the western United States and northwestern Mexico: Geological Society of America Bulletin, v. 113, p. 1343-1356.

Strauss, J. V., Rooney, A. D., Macdonald, F. A., Brandon, A. D. and Knoll, A. H., 2014, 740 Ma vase-shaped microfossils from Yukon, Canada: Implications for Neoproterozoic chronology and biostratigraphy: Geology, v. 42, p. 659-662.

Su, W., Li, H., Huff, W., Ettensohn, F., Zhang, S., Zhou, H. and Wan, Y., 2010, SHRIMP U-Pb dating for a K-bentonite bed in the Tieling Formation, North China: Chinese Science Bulletin, v. 55, p. 3312-3323.

Swart, P. K. and Eberli, G., 2005, The nature of the δ 13 C of periplatform sediments: implications for stratigraphy and the global carbon cycle: Sedimentary Geology, v. 175, p. 115-129.

Swart, P. K., Elderfield, H., Beets, Kay, 2001a, The 87Sr/86Sr ratios of carbonates, phosphorites, and fluids collected during the Bahamas drilling project cores Clino and Unda: implications for dating and diagenesis, v., p.

Swart, P. K., Elderfiled, H., Ostlund, G., 2001b, The geochemistry of pore fluids from bore holes in the Great Bahama Bank, v., p.

Swart, P. K. and Melim, L. A., 2000, The origin of dolomites in Tertiary sediments from the margin of Great Bahama Bank: Journal of Sedimentary Research, v. 70, p. 738-748.

Tucker, M. E., 1982, Precambrian dolomites: petrographic and isotopic evidence that they differ from Phanerozoic dolomites: Geology, v. 10, p. 7-12.

van Acken, D., Thomson, D., Rainbird, R. H. and Creaser, R. A., 2013, Constraining the depositional history of the Neoproterozoic Shaler Supergroup, Amundsen Basin, NW Canada: Rhenium-osmium dating of black shales from the Wynniatt and Boot Inlet Formations: Precambrian Research, v. 236, p. 124-131.

van Breemen, O., Kjarsgaard, B.A., Tella, S., Lemkow, D., and and Aspler, L., 2013, U-Pb detrital zircon geochronology of clastic sedimentary rocks of the Paleoproterozoic Nonacho and East Arm basins, Thaidene Nene MERA study area: Chapter 4 in Mineral and Energy Resource Assessment for the Proposed Thaidene Nene National Park Reserve in the Area of the East Arm of Great Slave Lake, Northwest Territories, (eds.) D.F. Wright, E.J. Ambrose, D. Lemkow, and G.F. Bonham-Carter; Geological Survey of Canada, v. Open File 7196, p. 119-143.

Wang, X., Jiang, G., Shi, X. and Xiao, S., 2016, Paired carbonate and organic carbon isotope variations of the Ediacaran Doushantuo Formation from an upper slope section at Siduping, South China: Precambrian Research, v. 273, p. 53-66.

Wilson, J. P., Fischer, W. W., Johnston, D. T., Knoll, A. H., Grotzinger, J. P., Walter, M. R., McNaughton, N. J., Simon, M., Abelson, J. and Schrag, D. P., 2010, Geobiology of the late Paleoproterozoic Duck Creek Formation, Western Australia: Precambrian Research, v. 179, p. 135-149.

Winston, D. (1990) Evidence for intracratonic, fluvial and lacustrine settings of Middle to Late Proterozoic basins of western USA, Mid-Proterozoic Laurentia-Baltica. Geol. Assoc. Canada Spec. Paper, p. 535-564.

Winston, D. and Lyons, T. (1993) Sedimentary cycles in the St. Regis, Empire and Helena formations of the Middle Proterozoic Belt Supergroup, northwestern Montana, Geologic Guidebook to the Belt-Purcell Supergroup, Glacier National Park and vicinity, Montana and adjacent Canada: Belt Symposium III Field Trip Guidebook, Belt Association, c/o PK Link, Dept. of Geology, Idaho State University, Pocatello, ID, pp. 21-51.

Wrucke, C. T., 1989, The middle Proterozoic Apache Group, Troy quartzite, and associated diabase of Arizona: Geologic evolution of Arizona: Arizona Geological Society Digest, v. 17, p. 239-258.

Zhou, X., Jenkyns, H. C., Owens, J. D., Junium, C. K., Zheng, X. Y., Sageman, B. B., Hardisty, D. S., Lyons, T. W., Ridgwell, A. and Lu, Z., 2015, Upper ocean oxygenation dynamics from I/Ca ratios during the Cenomanian–Turonian OAE 2: Paleoceanography, v., p.

Zhou, X., Thomas, E., Rickaby, R. E., Winguth, A. M. and Lu, Z., 2014, I/Ca evidence for upper ocean deoxygenation during the PETM: Paleoceanography, v. 29, p. 964-975

CHAPTER 3

Insights from the FOAM site, Long Island Sound, U.S.A: Calibrating Fe and Mo geochemistry for sedimentary paleoredox determinations

ABSTRACT

Iron speciation and trace metal proxies are commonly applied in studies spanning the geologic record for estimating water column redox conditions, including the presence of free sulfide in the water column. Building from classic past work at the FOAM (Friends of Anoxic Mud) site in Long Island Sound, USA, we extend the utility of these methods specifically toward a refined view of the Fe and Mo signatures of pore waters containing H_2S beneath O_2-containing bottom waters. Refined recognition of these conditions has important implications for the evolution of the marine sulfate reservoir and interpretation of benthic infaunal communities through time, more specifically the possibility of thiotrophy and associated symbiotic relationships among combined micro-/macrofaunal communities. For this purpose we compare data for iron speciation and Mo concentrations in FOAM sediments marked by pore water sulfide accumulation of up to 3 mM. For the operationally defined Fe speciation scheme, 'highly reactive' Fe (Fe_{HR}) is the sum of pyritized Fe (Fe_{py}) and Fe dominantly present in oxide phases that is available to react with pore water sulfide to form pyrite on early diagenetic time scales. For systems lacking H_2S in the water column, Fe_{HR}/Fe_T ratios are typically less than 0.38 (where Fe_T is the total amount of iron), and Fe_T/Al ratios lie near the value of average continental crust (~0.5). Results from FOAM fall within this range, consistent with the oxic bottom waters. At the same time, high Fe_{py}/Fe_{HR} ratios greater than 0.8 fingerprint sulfide-dominated pore fluids wherein the majority of the reactive iron minerals are converted to pyrite.

Molybdenum data in similar continental margin sediments show muted authigenic Mo enrichments (2-25 ppm) relative to concentrations of up to hundreds of ppm seen in sulfidic (euxinic) water columns. Results from FOAM, however, deviate from these values, with sedimentary Mo concentrations of 1-2 ppm over 50 cm depth. These values are typical of average continental crust, despite pore water Mo concentrations indicative of enhanced Mo delivery to the

sediments via adsorption to Mn or Fe oxides and high associated levels of dissolved sulfide. Simple calculations of the authigenic Mo flux indicate that FOAM sediments do receive authigenic enrichments, but bioturbation promoting sediment reoxidation and high sedimentation rates may prevent accumulation beyond those typical of detrital crustal material.

Together, dual application of Mo concentrations and Fe speciation allows us to delineate sediments in the geologic record likely to have been characterized by high sedimentation rates, perhaps repeated oxidation, and appreciable pore water dissolved sulfide, with implications for ecological relationships among micro- and macro-organisms.

INTRODUCTION

Iron speciation and molybdenum concentrations have been well-calibrated in shales for the determination of end-member ferruginous (iron-rich) or euxinic (sulfidic) water column redox conditions (Berner 1970; Raiswell and others, 1988; Canfield and others, 1992; Raiswell and Canfield, 1996; Raiswell and Canfield, 1998; Poulton and Canfield, 2005; Lyons and Severmann, 2006; Algeo and Lyons, 2006; Goldberg and others, 2009; Poulton and Canfield, 2011). This past research has resulted in extensive application of these proxies toward an understanding of water column redox dynamics through time, including Phanerozoic ocean anoxic events (März et al. 2008; Gill and others, 2011), the Proterozoic (Scott and others, 2008; Poulton and others, 2004; Canfield and others, 2007; Li et al. 2010; Johnston et al. 2012), and the Archean (Reinhard and others, 2009; Kendall and others, 2010; Scott and others, 2011). Here, we present Fe-speciation and Mo concentration data from sediments at the FOAM (Friends of Anoxic Mud) site in Long Island Sound, USA, with the end goal of improving the ability of the Fe-Mo proxies to track pore water sulfide availability in sediments deposited beneath an oxic water column. Research at FOAM has served as a cornerstone in the development of sedimentary Fe redox proxies (e.g.,

Canfield et al, 1992) and is therefore ideal for revisiting these relationships following more than two decades of additional proxy development for Fe and Mo.

BACKGROUND

The Fe Proxies

The utility of the Fe geochemical proxies is built on a foundation of extensive past work on the reactivity of Fe minerals with dissolved sulfide in sedimentary environments (Berner, 1970; Canfield and others, 1992; Raiswell and Canfield, 1988; Canfield, 1989; Raiswell and others, 1994; Raiswell and Canfield, 1996; Poulton and Canfield, 2005) and a well-developed understanding of syngenetic (water column) versus diagenetic pyrite formation (Canfield and others, 1996; Lyons, 1997; Wisjman and others, 2001; Lyons and others, 2003; Anderson and Raiswell, 2004). The current Fe speciation scheme (Poulton and Canfield, 2005) builds on a predecessor proxy, degree of pyritization (DOP), which was defined in part through work on Long Island Sound sediments and the recognition that iron should limit pyrite formation under the H_2S-replete conditions of euxinic settings (Berner 1970). DOP considers the availability of Fe with the potential to react with sulfide and ultimately form pyrite versus the amount of pyrite actually found in the sediments. In a landmark study conducted at FOAM, Canfield et al. (1992) showed that DOP can be successfully applied in some instances to differentiate between sediments deposited beneath an oxic versus euxinic water column (Raiswell and others, 1988). However, the method often overestimates the 'highly reactive' pool with respect to sulfide by extracting some (often silicate-bound) Fe that reacts with sulfide only on long (~10^6-yr) time scales (Raiswell & Canfield; 1996; see Lyons and Severmann, 2006, for review). For this reason, DOP provides a useful indicator of euxinic conditions but is not ideally suited to further differentiate among other redox regimes (e.g, ferruginous and oxic).

Building from the concept of DOP, Raiswell and Canfield (1998) advocated ratios of 'highly reactive' Fe to total Fe (Fe_{HR}/Fe_T) as a way of tracing water column anoxia, with 'highly reactive' Fe represented in this case by the sum of pyritized and dithionite extractable Fe from crystalline Fe oxides (Raiswell and others, 1994). This step was intended, unlike DOP, to estimate Fe phases that are truly reactive on short time scales. As another step forward, the refined sequential extraction scheme of Poulton and Canfield (2005) spans a broader range of highly reactive Fe phases, emphasizing oxide Fe, carbonate-bound Fe, and magnetite Fe, which all react with sulfide to form pyrite on time scales relevant to early diagenesis (Canfield, 1989; Canfield, and others, 1992; Canfield and Raiswell, 1996), which, when summed with pyrite, forms the operationally defined 'highly reactive' Fe (Fe_{HR}) pool. This approach allows application of Fe_{HR}/Fe_T ratios to serve as indicators of anoxic water column conditions. At the same time, Fe_{py}/Fe_{HR} ratios, when viewed in concert, can act as an indicator of the availability of free sulfide versus dissolved Fe in the water column (Poulton and others, 2004; Poulton and Canfield, 2011).

The detrital input of Fe_{HR} into the sediments stimulates the production of pyrite when excess sulfide is available, but typical lithogenic ratios of $Fe_{HR}/Fe_T < 0.38$ and $Fe_T/Al \approx 0.5$ are maintained when euxinic or ferruginous conditions are not present in the water column (Raiswell and Canfield 1998; Lyons and others, 2003; Lyons and Severmann 2006). By contrast, if anoxia persists in the water column, both Fe_{HR}/Fe_T and Fe_T/Al are elevated beyond these crustal baselines, and those enrichments are the telltale fingerprints of ancient anoxia. According to one model, soluble Fe(II) generated during reductive dissolution of Fe-oxides along continental margins diffuses out of sediments, allowing enhanced delivery of Fe_{HR} through an 'Fe shuttle' to the deep basin whether it is captured as syngenetic pyrite (Canfield and others, 1996; Lyons 1997;

Raiswell and Canfield, 1998; Wisjman and others, 2001; Anderson and Raiswell, 2004; Lyons and Severmann, 2006; Severmann and others, 2008; Scholz and others, 2014). This 'extra' Fe is decoupled from the local delivery of silicate phases, including unreactive Fe fractions, with the net result of $Fe_{HR}/Fe_T > 0.38$ (Raiswell and Canfield, 1998) and $Fe_T/Al > 0.5$ (Lyons and others, 2003; Lyons and Severmann 2006). Under euxinic conditions, near complete reaction of the Fe_{HR} to form pyrite causes Fe_{py}/Fe_{HR} to exceed 0.7 to 0.8 (Poulton and others, 2004; März and others, 2008; Poulton and Canfield, 2011). The ability to distinguish with certainty the degree of sulfide versus iron limitation under anoxic conditions separates the sequential Fe extraction techniques from DOP. Sequential Fe extractions have been used widely to differentiate euxinic versus ferruginous (anoxic but Fe-dominated) water column redox conditions throughout the geologic record, but there has been limited application that specifically targets persistent sulfide limited to the pore waters — hence this study.

Mo Geochemistry

Trace metals, particularly Mo, have also become reliable indicators of water column redox (e.g., Algeo and Maynard, 2004) due in part to careful calibration against the Fe proxies in modern sediments with a range of redox conditions (for example, Lyons and others, 2003). Recent studies, like ours, have sought to use Mo to determine the extent of sulfide availability in the sediment column specifically (Scott and Lyons, 2012). Molybdenum is the most abundant transition metal in the modern ocean, with a near uniform concentration of ~104 nM (Broecker and Peng, 1982; Emerson and Huested 1991) and a relatively long residence time of ~450 kyr (Miller and others, 2011). Molybdenum exists almost entirely as MoO_4^{-2} under oxic conditions, delivered primarily from oxidative weathering of sulfide minerals, and has a strong affinity for sorption to Mn and Fe oxides, which is a significant pathway of Mo deposition in the modern,

mostly oxic ocean (Barling and Anbar, 2004; Arnold and others, 2004; Dahl and others, 2010). In the absence of sulfide in the water column and sediments, Mo buried with oxides will often diffuse back to the overlying water column following reductive dissolution of the oxides during sediment diagenesis (Scott and Lyons, 2013), with the possibility of little to no authigenic sediment enrichments and concentrations near those characteristic of average continental crust (~1-2 ppm; Taylor and McLennan, 1995).

Under sulfide-rich conditions, Mo is readily converted from molybdate (MoO_4^{-2}) to particle reactive thiomolybdate ($MoO_{4-x}S_x^{-2}$; Helz and others, 1996; Erickson and Helz, 2000) that is predictably buried in association with organic matter and pyrite (Algeo and Lyons 2006). This relationship has particular importance when considering settings with sulfide restricted to the sediment pore fluids versus euxinic sites with, by definition, free sulfide present in the water column. In either case, if total dissolved sulfide concentrations exceed ~100 μM, quantitative sulfidization of MoO_4^{-2} to MoS_4^{-2} is expected (Helz and others, 1996). Euxinic environments compose <<1 % of today's ocean but were of much greater importance in the geologic past (e.g., Canfield, 1998; Reinhard and others, 2013). Molybdenum enrichments under sulfide conditions typically exceed the average continental crust value of approximately 1-2 ppm (Taylor and McLennan, 1995) by a wide margin, with sediment concentrations of up to hundreds of ppm often seen in association with euxinia (Scott and Lyons, 2012).

In modern sulfidic sediments accumulating beneath an oxic water column, concentrations of Mo rarely exceed 25 ppm, with most of these settings having authigenic enrichments falling below 10 ppm (McManus and others, 2008; Scott and Lyons 2012). Molybdenum delivered to the sediments through oxide burial is retained upon oxide dissolution via reaction with H_2S and sequestration with organic matter and/or pyrite, among other possibilities, in the subsurface

layers, rather than diffusing back to the water column. Scott and Lyons (2012) proposed that, outside of geological time periods characterized by widespread euxinia and associated marine Mo drawdown (e.g., Reinhard and others, 2013; Owens and others, 2016), authigenic Mo enrichments beyond crustal values but less than 25 ppm may be used as indicators of sulfide accumulation within sediments beneath O_2-containing bottom waters. However, there are examples of sulfidic pore water systems, such as the present study, and even euxinic settings that fail to show diagnostic Mo enrichment (e.g., Lyons and Kashgarian, 2005).

The present work is a case study that explores the potential and limitations of Fe speciation and Mo concentrations as fingerprints for the presence of sulfidic pore fluids beneath an oxic water column. Based on reports of appreciable sedimentary sulfide accumulation and DOP values of approximately 0.4 at the FOAM site (Canfield and others, 1992), we began our study predicting Mo enrichments of 2-25 ppm and Fe_T/Al, Fe_{HR}/Fe_T, and Fe_{py}/Fe_{HR} ratios of ~0.5, <0.38, and >0.8, respectively. Deviations from these predictions, as discussed below, point to the possibility of a wider range of environmental controls, including sedimentation rate and temporal patterns of re-oxidation of surface sediments.

FOAM site

The FOAM study site, located in Long Island Sound, USA, is an urban estuary just off the coast of Connecticut near New Haven. FOAM and several nearby locations in Long Island Sound have been the focus of numerous studies on early marine diagenesis and pyrite formation (Canfield and Berner, 1987; Canfield, 1989; Canfield and Raiswell, 1991; Canfield and others, 1992; Raiswell and Canfield, 1998), sulfate reduction (Goldhaber and others, 1977; Westrich, 1983), bioturbation (Berner and Westrich, 1985), and sedimentation rates (Krishnaswami and others, 1984), making background knowledge readily available and the site ideal for proxy

calibrations and comparisons. Sedimentary sulfide concentrations have been reported to range from 2 to 6 mM at FOAM and adjacent study sites characterized by high rates of sulfate reduction (Goldhaber and others, 1977; Westrich, 1983; Canfield, 1989; Canfield and others, 1992).

Sedimentation rates at FOAM and adjacent study sites were evaluated most thoroughly by Krishnaswami and others (1984) using ^{234}Th, ^{7}Be, ^{210}Pb, ^{239,240}Pu, and ^{14}C. Sedimentation rates were found to vary according to sediment depth and were affected by episodic sedimentation and erosion. The sedimentation rate of the upper 15 cm was found to be 0.03 cm/yr and near 0.1 cm/yr. in the depth range of 15-110 cm. Goldhaber and others (1977) reported a higher rate of sedimentation of 0.3 cm/yr, integrating across the upper 20 cm, using the timing of anthropogenic metal inputs, rate of pore water ammonium generation, and maximum concentration of dissolved sulfide. The presence of extensive bioturbation and infaunal irrigation to depths of 8-10 cm (Goldhaber and others, 1977) has left the upper 4 cm of the sediment homogenized (Krishnaswami and others, 1984). The activities of these burrowing organisms have been documented to change on seasonal time scales, thus enhancing infaunal irrigation of sulfate to the sediments in the summer compared to winter and creating distinct differences in the depth of sulfide accumulation from winter to summer. Bioturbation is the dominant transport mechanism in the summer, and diffusion dominates during the winter (Goldhaber and others, 1977). Occasional dredging of portions of the Sound may have caused sediment reworking subsequent to these past studies, but has not been observed in this or past studies.

Outside of variations in sedimentation rate and burrowing activity, Long Island Sound has had documented hypoxic bottom waters (low oxygen but not euxinic or ferruginous conditions) since the 1970s (Lee and Lwiza 2008). The effects of nutrient loading have been evaluated, and inputs have been limited via legislation put forward in 1998. This legislation has

resulted in lower inputs of total phosphorous and nitrogen into the Sound via the Connecticut, Houstatonic, and Thames rivers (USEPA, 1998). Though still-high nutrient loads into Long Island Sound undoubtedly contribute to amplified hypoxia, studies have shown that increased density stratification from weak summer winds and temperature-controlled saturation in the winter months are the most significant regulators of dissolved oxygen concentration (Anderson and Taylor, 2001). A thorough record of dissolved bottom water oxygen concentration in Long Island Sound from 1995 through 2004 clearly shows the seasonal dependence of hypoxia, with dissolved oxygen annually reaching a nadir in the summer months (Lee and Lwiza, 2008). Though these fluctuations are important broadly, data from stations near FOAM indicate that bottom water oxygen depletion during the summer is less severe at this location compared to others in the Sound, and recorded depletions at FOAM do not reach intensities that allow bottom water sulfide accumulation or infaunal asphyxiation (<4.6 mg/L O_2; Vaquer-Sunyer and Duarte, 2008).

Previous studies paint an overall picture of non-steady state diagenetic processes regulating the pore water chemistry of the upper portions of the sediments at FOAM. Despite this, the pore water and sediment chemistry below the maximum depth of active infaunal habitation (8-10 cm) consistently point to steady state conditions (Goldhaber and others, 1977; Westrich and others, 1983; Boudreau and Canfield, 1988).

METHODS

Our FOAM core was collected in the autumn of 2010 using a modified piston-gravity corer. The site is located at 41°14’26.82’’N, 72°44’44.78’’W at a water depth of approximately 10 m. Cored sediments were divided into 1-2 cm intervals within 2 hours of collection, and the sediment was transferred into 50 mL centrifuge tubes. Immediately following division of the

cores, pore waters were extracted within an N_2-flushed glove bag via the rhizon technique (Seeberg-Elverfeldt and others, 2005). Pore water aliquots for measurement of pore water H_2S were dosed with zinc acetate, forcing ZnS precipitation. Pore water splits for metal analysis were acidified with trace metal grade HCl. Following pore water extraction, sediments were sealed and frozen immediately, minimizing oxidation.

Pore water H_2S concentrations were measured using the methylene blue method (Cline, 1969). Sulfate concentrations were determined by suppressed ion chromatography with conductivity detection (ICS-2000, AS11 column; Dionex) using samples pretreated with ZnAc to avoid sulfide oxidation. Pore water concentrations of Mn, Fe, Mo, and U were measured via inductively coupled plasma mass spectrometry (ICP-MS; Agilent 7500ce). Sample replicates yielded standard deviations < 5% for Mn, Fe, Mo, and U.

Homogenized sample was dried overnight at 60° C to remove any remaining moisture. Dried samples were further homogenized and powdered via mortar and pestle after removal of shell material. Sediments were weighed before and after drying for water content determinations.

Dried sediment was used for the determination of total organic carbon (TOC). First, total carbon was measured using an Eltra CS-500 carbon-sulfur analyzer wherein CO_2 produced by combustion of dried sample powder at 1400°C under an O_2 stream was quantified via infrared absorption cells. Total inorganic carbon was determined by measuring CO_2 liberated by addition of 2.5 N HCl. TOC was determined by difference.

Elemental sulfur concentrations, acid volatile sulfur (AVS), and chromium reducible sulfur (CRS) were determined sequentially (modified after Canfield and others, 1986; Zopfi and others, 2004). Briefly, for the removal of elemental S, approximately 2-3 mg of wet, freshly

thawed sample was weighed into centrifuge tubes. Methanol was added (with a sample-to-extractant ratio of ~1/10), and the headspace was filled with N_2 gas. The samples were shaken for 24 hours, bringing elemental sulfur into solution. After shaking, the samples were centrifuged, and the methanol solution was decanted and stored. The sample container with the sediment residue was maintained with a N_2 headspace, and 6 mol l^{-1} HCl was added for approximately 1 hr. The H_2S liberated by AVS digestion was trapped in a 5% zinc acetate solution. An acidified (12 M HCl) solution of reduced chromic chloride was then added while maintaining an N_2 headspace. CRS was liberated as H_2S and precipitated as ZnS with a solution of 3% zinc acetate and 10% ammonium hydroxide. The reaction was allowed to proceed for approximately 2 hours at approximately 200°C. In a separate extraction, concentrations of elemental sulfur were determined by adding a fresh chromous chloride solution to the decanted methanol, with an extraction time of 1 hour with a fresh ZnAc trap solution. Concentrations of sulfur as AVS and elemental sulfur, because of their relatively small amounts, were determined via the methylene blue method (Cline, 1969). CRS was quantified by iodometric titration according to Canfield and others (1986). Recoveries of sulfur for pyrite standards averaged 86 ± 9.2 % of the expected (n=8).

To determine the degree of sulfidization (DOS) or degree of pyritization (DOP), analysis of HCl extractable Fe was performed via the method of Berner (1970) and Raiswell et al. (1988). Briefly, 100 mg of sample was treated with 5 mL of 12 M HCl, then immediately heated to boil for approximately 1 minute. Following heating, a small amount of DI water was added to quench the reaction, and the solution was then transferred quantitatively to a volumetric flask. The volumetric flask was filled with DI water and shaken. After the particles settled, 10 mL of the solution were further diluted to 50 mL using DI H_2O. One hour prior to analysis, 1 mL of a

buffered ferrozine solution was added to allow for full color development. Samples were diluted, and Fe concentrations were measured spectrophotometrically (λ = 562nm). DOS was calculated as follows:

$$DOS = (Fe_{py} + Fe_{AVS})/(Fe_{py} + Fe_{HCl+} Fe_{AVS}), \quad \text{(Equation 1)}$$

where Fe_{HCl} is the Fe fraction soluble after 1 minute in 12 M HCl, and Fe_{py} and Fe_{AVS} represent the CRS and AVS Fe fractions, respectively (Berner 1970; Raiswell and others, 1988). However, in cases where Fe_{AVS} is low, like that documented in this study and those previously at FOAM (see discussion below), DOS can be simplified to DOP, which does not include Fe_{AVS} in the calculation.

Approximately 100 mg of dried sample were weighed for determination of Fe speciation according to the method of Poulton and Canfield (2005). There was, however, one modification of that method: the Na-acetate extraction was replaced with an ascorbate step, which targets ferrihydrite (Ferdelman, 1988; Raiswell and others, 2010). Iron oxides, including ferrihydrite, have been determined through previous studies at FOAM as the most important Fe minerals precursors for diagenetic pyrite formation (Canfield, 1989). Care was taken to ensure that all solutions were bubbled with N_2 gas prior to addition to samples, and sample container headspaces were maintained with N_2 gas to minimize Fe oxidation. The procedure was initiated with the addition of the ascorbate solution at pH 7.5 followed by agitation for 24 hrs. Next, the sample was centrifuged, an aliquot of the supernatant was removed and stored, and the remaining liquid was discarded. A sodium dithionite solution at pH 4.8 was then added to the sample, and the solution was shaken for 2 hrs. The sample was then centrifuged, and aliquots were removed as before. An ammonium oxalate solution at pH 3.2 was then added, and the solution was shaken for 6 hrs. An aliquot of the supernatant was removed following centrifugation. Concentrations of Fe for each

extraction were determined via ICP-MS. The net result is three operationally defined Fe fractions: (1) ascorbate Fe representing amorphous/poorly crystalline (oxyhydr)oxides, herein referred to as Fe_{asc}; (2) sodium dithionite Fe representing crystalline oxides such as goethite and hematite, referred to as Fe_{dith}; and (3) oxalate Fe representing magnetite, referred to as Fe_{mag}. Combined, Fe_{py}, Fe_{AVS}, Fe_{asc}, Fe_{ox}, and Fe_{mag} represent the total 'highly reactive' Fe pool (Fe_{HR}). Replicate samples yielded precisions of <7% for Fe_{asc}, Fe_{dith}, and Fe_{mag}.

Bulk Fe, Mn, Al, Mo, and U concentrations were determined using a total digest procedure. Approximately 100 mg of dried, homogenized powder was weighed into crucibles and heated at 450° C for approximately 12 hrs to remove any combustible carbon and sulfides. The remaining ash was then weighed for determination of loss on ignition (LOI). The remaining sample was put through a multi-acid total digest. Specifically, concentrated trace metal grade HF and HNO_3 were added at a 1:5 v/v ratio and heated overnight at 130°C. Next, the samples were evaporated to dryness. A 1:3 v/v mixture of concentrated trace metal grade HCl and HNO_3 was then added and heated again overnight at 130°C. The solution was then evaporated as before. The remaining material was dissolved in 0.28 M HNO_3 and heated for approximately 1 hr at 80°C. The 0.28 M HNO_3 mixture was then diluted, and concentrations of Fe, Mn, Al, Mo, and U were measured using an Agilent 7500c ICP-MS at the University of California-Riverside, as for the pore water samples and the solid Fe speciation procedure. Repeated analyses of USGS reference material SDO-1 were preformed to assess accuracy, with all elements analyzed in this study falling within the reported ranges. Digestion and analysis of replicate FOAM samples revealed standard deviations < 0.1 wt % for Al, Mn, and Fe and <0.2 ppm for Mo and U.

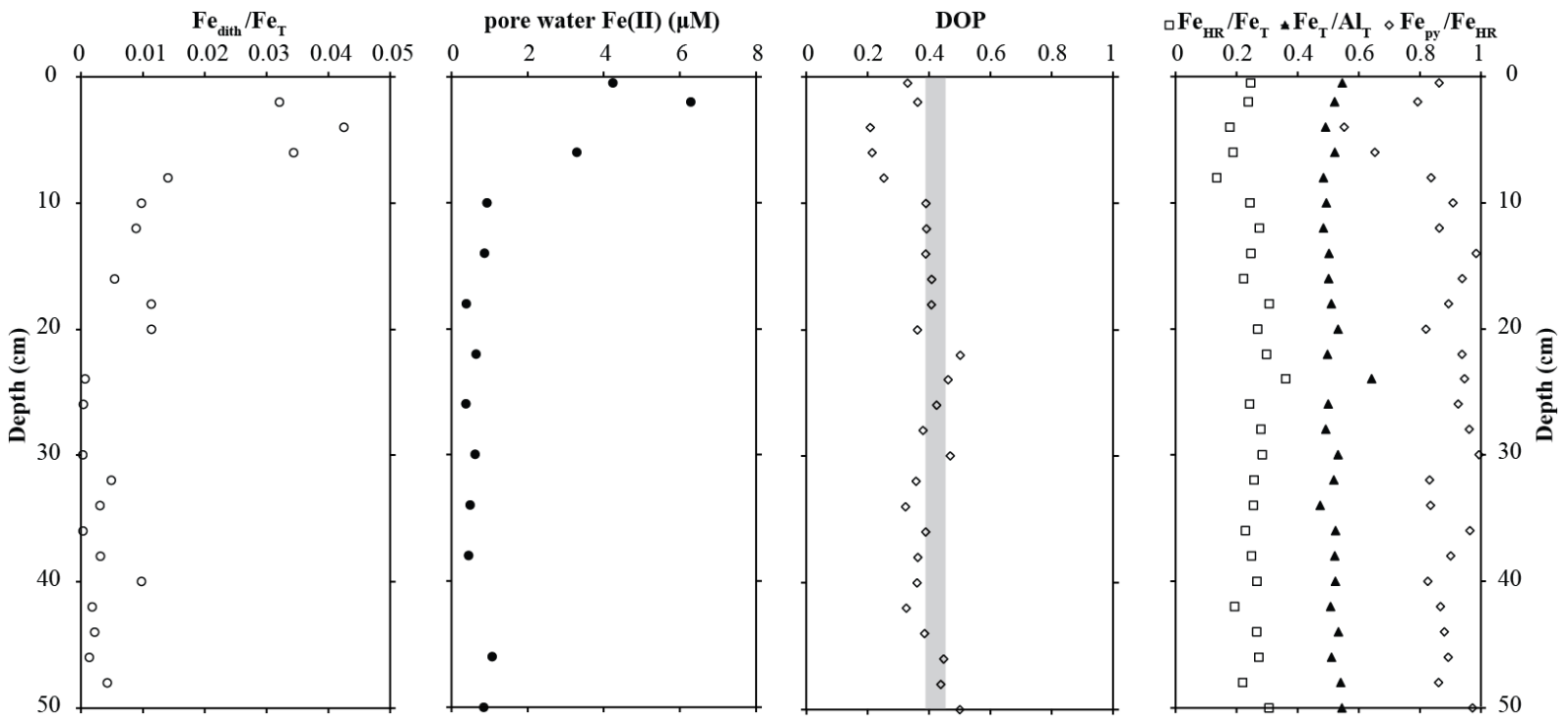

Figure 1. Dithionite Fe to total Fe ratios, dissolved pore water Fe concentrations (Fe^{2+}), degree of pyritization, and ratios of 'highly reactive Fe to total Fe concentrations, total Fe to Al ratios, and pyritized Fe over highly reactive Fe. The vertical bar represents the range of degree of pyritization previously measured at FOAM in a more limited data set from Canfield et al. (1992)

RESULTS

DOP and sequential Fe

Calculated values for DOP are mostly near 0.4, but with values near 0.2 at 4-8 cm, which is similar to previous studies (Fig. 1 and Table S1). At 4-8 cm, sedimentary Fe concentrations decrease, and there is an associated peak in pore water Fe at this depth rising from 4.24 μM at 0.5 cm to 6.29 μM at 2 cm before decreasing to 0.94 μM at 10 cm (Figure 1), suggesting reductive dissolution of Fe oxides. Fe_{dith} for this interval (4-10 cm) shows a marked decrease further suggestive of Fe oxide dissolution (Figure 1). Fe_{dith} is the most abundant highly reactive Fe phase in the upper 10 cm other than pyrite, peaking at 0.14 wt %, but then decreasing to < 0.04 wt % below 10 cm through the remainder of the profile. Once Fe_{dith} decreases, Fe_{mag} comprises the largest non-pyrite fraction of Fe_{HR}. Fe_{mag} shows no trend with depth, but Fe_{asc} displays a peak at 4 cm, just above the depth of sulfide accumulation, before steadily decreasing to the bottom of the core. Below 10 cm, Fe_{dith} and Fe_{asc} represent a similarly negligible fraction of the total Fe.

Pyrite is the dominant Fe fraction of the highly reactive pool, demonstrated by Fe_{py}/Fe_{HR} values close to 0.8 for the majority of the profile (Fig. 1). Values range from 0.6-0.7 wt % in the upper 2 cm to 0.3-0.4 wt % from 4-8 cm and then increase consistently to > 0.5 wt % for the remainder of the profile (Fig. 2). AVS (not shown) represents the lowest fraction of Fe_{HR} and was not significant in this study. Elemental sulfur concentrations remained < 0.2 wt % throughout the core.

The Fe_T/Al ratio is approximately 0.5, and Fe_{HR}/Fe_T remains < 0.38, typical of values observed for a detritally dominated Fe flux to the sediments under an oxic water column (Lyons and Severmann 2006). Ratios of Fe_{py}/Fe_{HR} ratios decline in the upper 5 cm of the core from 0.86 to 0.55 and starting at 8 cm rise to values > 0.8 for the rest of profile. The permanent increase to

values > 0.8 overlaps with the zone in Fe reduction, as is evident by the concomitant decrease in Fe-dithionite concentrations and a subsequent increase in dissolved Fe(II) over the same depth interval. At this Fe_{py}/Fe_{HR} transition, sulfide accumulates, and there is a subsequent increase in the abundance of pyrite to greater than 1.5 wt.% as the soluble Fe is titrated from the pore fluids in parallel with a steady decline in Fe_{dith} concentrations.

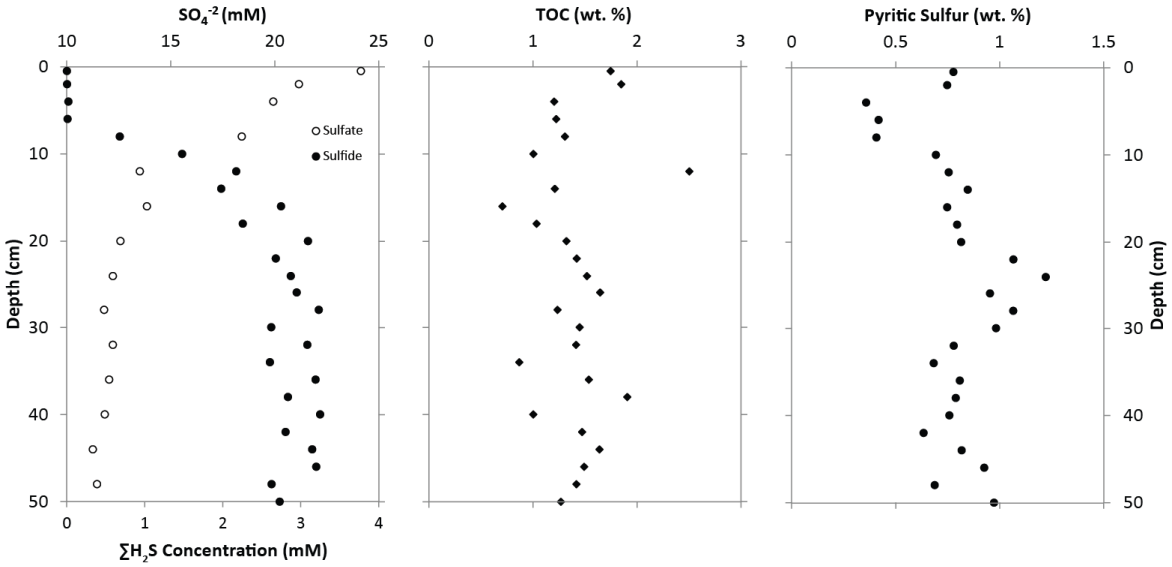

Figure 2. FOAM concentration profiles for pore water sulfate and hydrogen sulfide, total organic carbon (TOC), and weight percent sulfur in pyrite. Profiles reveal a loss of sulfate starting at the sediment water interface, but without significant sulfide concentrations until 8 cm depth. The peak in sulfide concentrations corresponds with an increase in pyritic sulfur.

Redox zonation

Sulfide concentrations peak near 3 mM and therefore are in the range of concentrations of up to 6 mM observed during previous studies (Canfield and others, 1992), with sulfide accumulation limited to depths of approximately 8 cm and greater (Figure 2). The general trend of decreasing organic carbon is consistent with continued remineralization as diagenesis proceeds (Figure 1; Froelich and others, 1979). The pyrite depth profile shows a typical diagenetic trend of sediments having abundant sulfide, with pyrite concentration increasing with depth (Figure 2).

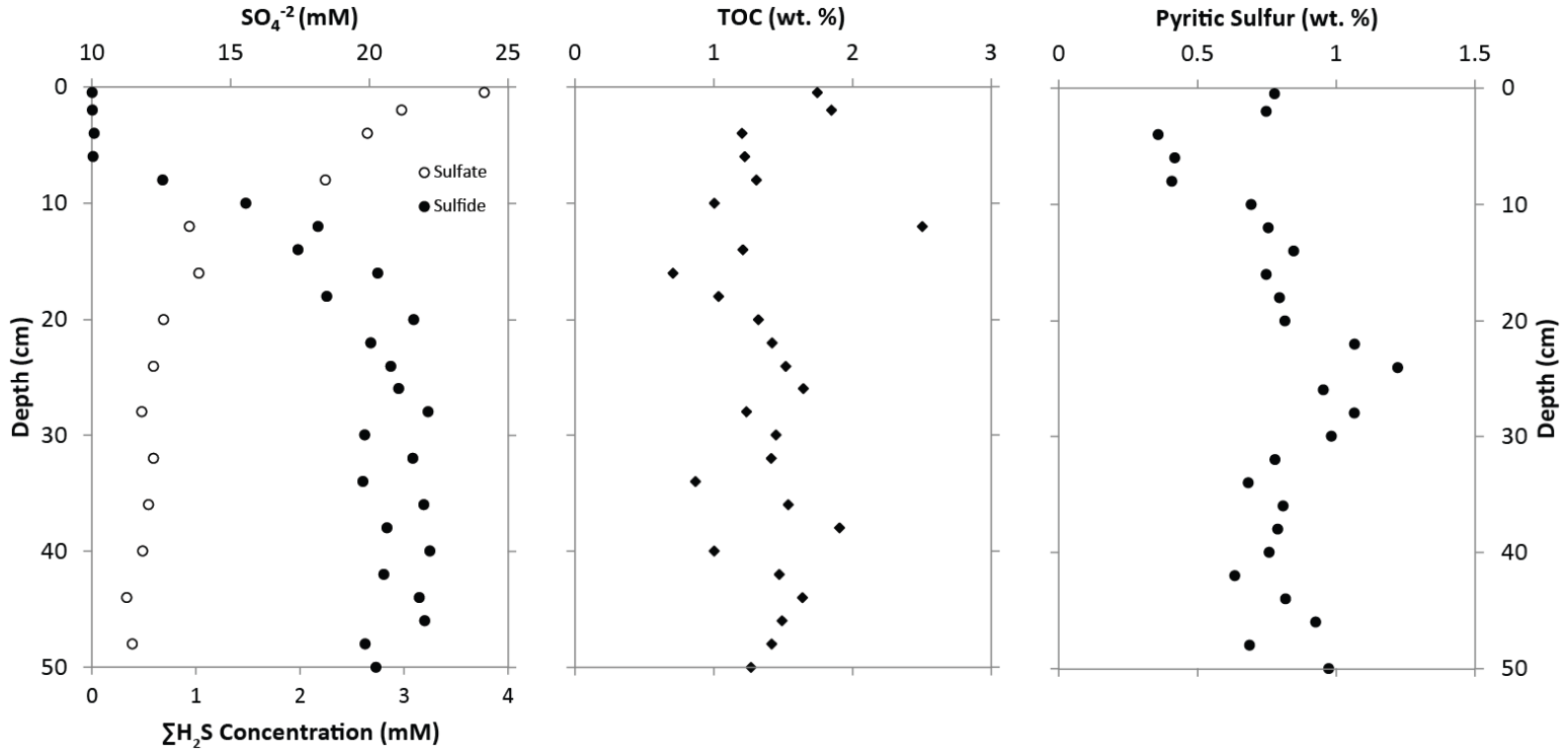

Figure 3. FOAM concentration profiles for pore water sulfate and hydrogen sulfide, total organic carbon (TOC), and weight percent sulfur in pyrite. Profiles reveal a loss of sulfate starting at the sediment water interface, but without significant sulfide concentrations until 8 cm depth. The peak in sulfide concentrations corresponds with an increase in pyritic sulfur.

Pore water profiles indicate Mn and Fe oxide delivery with an accumulation of reduced Mn and Fe in the pore fluids of the upper 6 cm (Figure 1 and 3). This relationship is consistent with results for Fe_{dith}, representing crystalline Fe-oxides, showing a significant decrease from the sediment-water interface to the zone of sulfide accumulation (Figure 1). Pore water Fe and Mn accumulation and directly precedes the depth of initial sulfide accumulation (Figures 1 and 3).

Molybdenum concentrations have not been previously reported at FOAM. The pore water peak in Mo of 200 nM at 5-7 cm is elevated compared to seawater (104 nM) and the over- and underlying pore fluids (Fig. 4; Table S2). This trend is in agreement with other studies measuring pore water Mo in reducing continental margin sediments, with Mo concentrations increasing upon dissolution of Mn and Fe oxides and then dropping to a near-zero concentration as sulfide begins to accumulate (Scott and Lyons, 2012, and references therein). The scavenging of Mo from the pore waters is consistent with conversion of molybdate to thiomolybdates in the presence of sulfide (Helz and others, 1996).

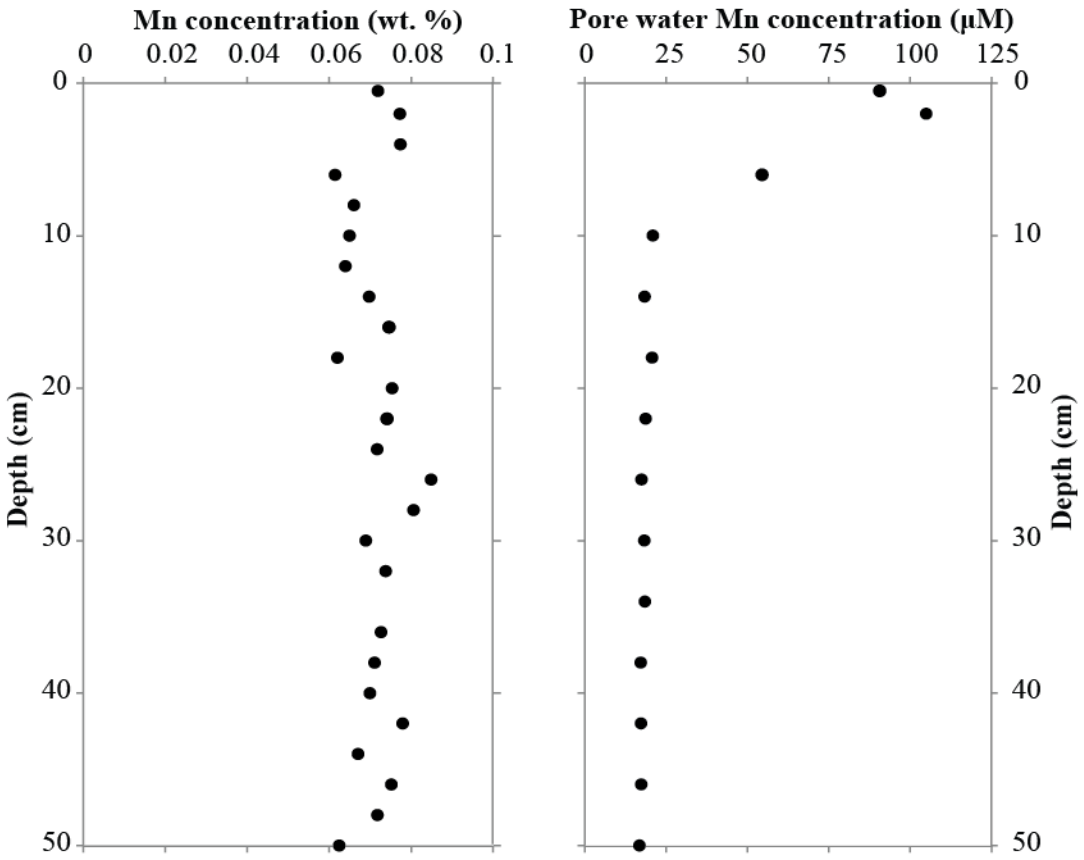

Figure 3. Depth profiles for sedimentary and pore water Mn concentrations.

Surprisingly, sedimentary Mo concentrations at FOAM are near those expected for detrital delivery (average continental crust) — that is, not exceeding 2 ppm despite the highly sulfidic pore fluids that could support significant authigenic enrichment (Figure 4; Table S2). This trend is also observed despite the presence of a subsurface pore water Mo maxima elevated relative to seawater concentrations. The uranium data similarly do not indicate enrichments compared with detrital fluxes (Figure 4), consistent with previous studies at FOAM (Benninger and others, 1979).

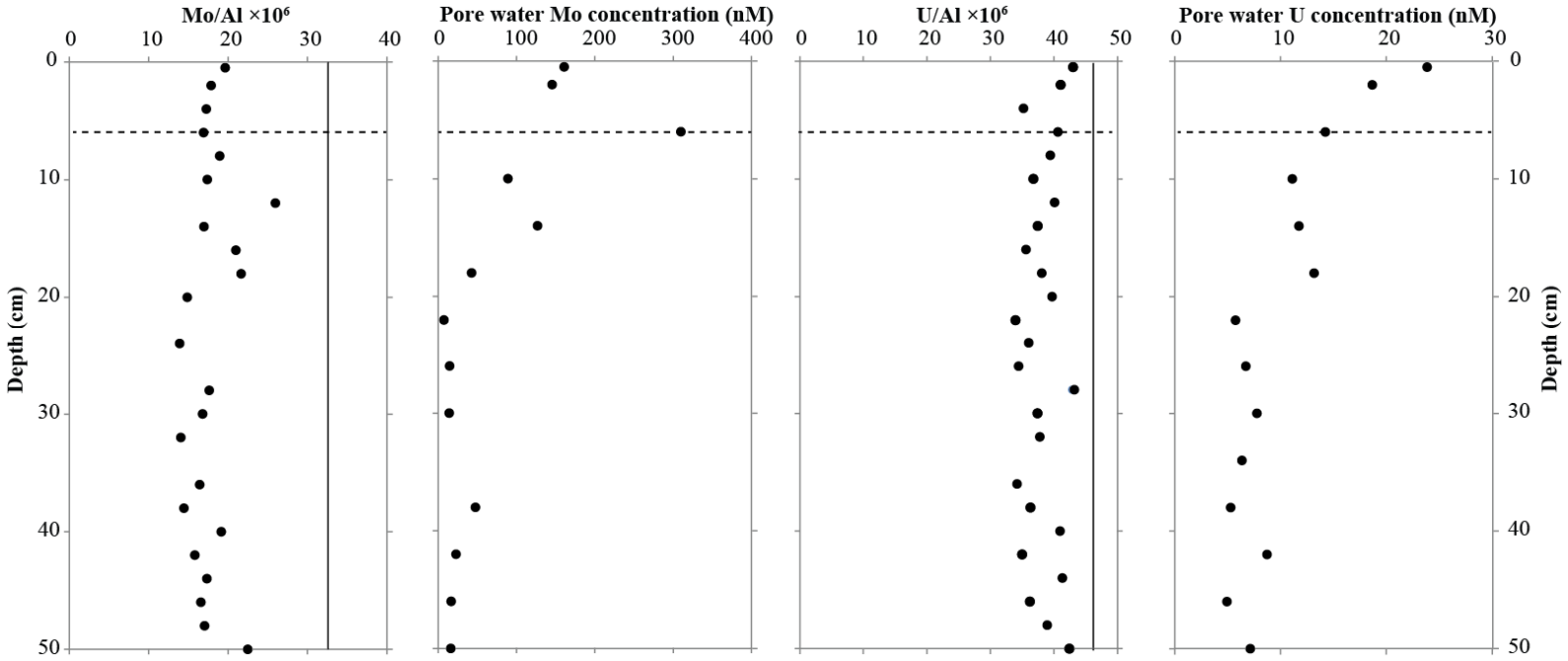

Figure 4. Sedimentary Mo/Al ratios, pore water Mo concentrations, sedimentary U/Al ratios, and pore water U concentrations. Horizontal dashed lines represent the depth of significant sulfide accumulation. Solid vertical lines represent Mo/Al and U/Al average shale values from Turekian and Wedepohl (1961).

DISCUSSION

DOP and sequential Fe

Degree of pyritization was the original Fe-based water column redox proxy (Berner 1970; Raiswell and others, 1988) and has been well studied at the FOAM site. DOP values from FOAM sediments reported in Canfield et al. (1992) and Raiswell and Canfield (1998), as well as this study, display an average near 0.4 (Figure 1). Berner (1970) reported a range from 0.07-0.44 for nearby sites in Long Island Sound also representing well-oxygenated bottom waters. Though DOP is useful for fingerprinting euxinic settings (Raiswell 1988), the boiling HCl step can include Fe silicates that are not reactive toward sulfide on 'short' timescales, thus leading to overestimations of the Fe_{HR} fraction and limiting its utility for identifying free sulfide availability in ancient sediments and water columns (Canfield and others, 1992; reviewed in Lyons and Severmann, 2006). However, while false negatives are possible, high DOP values approaching 1.0 are a robust indicator of past euxinia (e.g., Lyons and Severmann, 2006).

Our Fe_{HR}/Fe_T data, with values <0.38 (Figure 1), are contrary to the enrichments in reactive Fe that typify many modern and ancient anoxic depositional settings and agree well with previous studies of the highly reactive Fe pool in continental margin settings with oxic bottom waters (Raiswell and Canfield 1998; Wijsman and others, 2001; Lyons and others, 2003). Fe_T/Al has been previously measured at FOAM, yielding values similar to our study near 0.5 (Krishnaswami and others, 1984), but ours is the first report of Fe_{HR}/Fe_T data from FOAM using the revised sequential Fe scheme presented by Poulton and Canfield (2005). Nevertheless, comparisons from previous studies are possible since Fe_{dith}, Fe_{py}, and Fe_{AVS} were measured and reported for the upper 12 cm of FOAM in Canfield (1989) and Raiswell and Canfield (1998), yielding values similar to those reported here for Fe_{HR}/Fe_T, 0.2-0.3, as well as Fe_{py}/Fe_{HR} approaching 0.8 at the depths of sulfide accumulation.

The combination of $Fe_{HR}/Fe_T < 0.38$, $Fe_T/Al \approx 0.5$, and $Fe_{py}/Fe_{HR} > 0.8$ is confirmed here to be a reliable paleoredox indicator of sulfide-dominated pore fluids in the absence of water column sulfide or dissolved Fe accumulation. In this case, Fe_{py}/Fe_{HR} points specifically to sulfide accumulation only within the pore fluids of organic-rich sediments. Near complete consumption of Fe_{HR} phases to pyrite below the depth of sulfide accumulation, as indicated by $Fe_{py}/Fe_{HR} > 0.8$ and thus relatively insignificant amounts of Fe_{mag}, Fe_{asc}, and Fe_{dith}, tell us that reactive Fe availability is the limiting factor in sedimentary pyrite formation. *A critical take-home message here is that Fe availability can limit pyrite formation, and thus Fe_{py}/Fe_{HR} can approach 1.0, even under oxic depositional conditions if the pool of labile organic matter and sulfate is sufficient to support continuing sulfide production* (Canfield 1989; Canfield and Raiswell 1991; Canfield and others, 1992). Iron limitation is a condition initially ascribed to pyrite formation in euxinic settings, where it is common (e.g., Lyons and Berner, 1992), but this study confirms the non-uniqueness of that observation (see Canfield and others, 1992).

We also point out that pyrite is found at all depths sampled and that Fe_{py}/Fe_{HR} is > 0.8 in some portions of the interval where pore water sulfide is not accumulating. This does not alter our point, as previous studies at FOAM indicate that sulfate reduction rates are highest at this depth (Goldhaber and others, 1977; Westrich and others, 1984; Canfield 1989; Canfield and others, 1992), but with dissolved sulfide consumed through a combination of pyrite formation, oxidation at the oxic-anoxic interface, and bio-irrigation. In our profile, appreciable H_2S does not begin to accumulate until 8 cm depth, but SO_4^{2-} loss via bacterial reduction starts at 2 cm (Figure 2). Previous FOAM works have shown that during the summer months (when our core was collected) that the depth of bio-irrigation is to 8 cm depth, which prevented sulfide accumulation in this zone (Goldhaber and others, 1977), consistent with the depth of sulfide accumulation in

our core. Starting at the depth of sulfide accumulation, all Fe_{py}/Fe_{HR} values are > 0.8. Together, these observations emphasize the importance of factors controlling pore water sulfide accumulation other than 'highly reactive' Fe availability near the sediment water interface, including bioturbation and oxic sulfur cycling. However, in anoxic sediments beneath the zone of bio-irrigation, sulfide only begins to accumulate when the rate of sulfide production overcomes the decreasing availability of Fe_{HR} (Canfield 1989; Canfield and Raiswell 1991; Canfield and others, 1992)

One important consideration when applying Fe_{py}/Fe_{HR} is the role of Fe_{AVS}. In this study and others at FOAM (Goldhaber and others, 1977; Aller, 1980; Canfield and others, 1992), Fe_{AVS} was a minor contributor to the 'highly reactive' Fe pool, and therefore wasn't considered, with highest concentrations in the upper few centimeters and decreasing down core with increased exposure to pore water sulfide. However, in sediments with significant Fe_{AVS}, it has previously been incorporated into DOP measurements as Degree of Sulfidization (DOS), with Fe_{AVS} both in the numerator and the denominator (for example, Boesen and Postma, 1988; Gagnon and others, 1995; Lyons, 1997; Hurtgen and others, 1999). This is appropriate for euxinic indications, as Fe_{AVS} is commonly formed within and deposited beneath euxinic waters as a primary Fe sulfide (Boesen and Postma, 1988; Lyons, 1997; Hurtgen and others, 1999) and thus should be considered within the budget of 'highly reactive' Fe in the water column. We further suggest that, like DOS, when Fe_T/Al or Fe_{HR}/Fe_T indicate anoxic deposition, that $(Fe_{py}+Fe_{AVS})/Fe_{HR}$ (Kraal and others, 2013) should be used to distinguish between euxinic and ferruginous conditions.

When Fe_{HR}/Fe_T and Fe_T/Al do not provide anoxic indications, we recommend that Fe_{AVS} provides constraints not on sedimentary (pore fluid) sulfide accumulation, but instead it's long-term availability relative to that of pyrite precursors. Berner and others (1979) initially proposed

ratios of AVS-S/py-S as a paleosalinity indicator, as high concentrations of Fe_{AVS} are common in brackish and lacustrine sediments where SO_4^{2-}, and thus H_2S and S intermediates such as elemental S and polysulfide, are limiting. Building on this, we suggest that Fe_{AVS} be viewed as 'partially reacted' Fe when considering sedimentary sulfide accumulation. Although AVS, as a pyrite precursor, is already an iron sink, its persistence in the sediments suggests limitations in pore water H_2S or intermediate S species required for complete reaction to pyrite (Berner and others, 1979; Gagnon and others, 1995). However, availability of H_2S and intermediate species is not the only factors in AVS to FeS_2 transformation. Fe_{AVS} persistent with depth is also expected to be more common in rapidly accumulating sediments, where the time frame of exposure to H_2S and S^0 is limited (Hurtgen and others, 1999) relative to that necessary for complete reaction — which can take up to hundreds of years even in the presence of dissolved sulfide (Boesen and Posta, 1988; Kraal and others, 2013). Such protracted Fe reactivity is also true for some other 'highly reactive' Fe minerals, particularly magnetite (Canfield and Berner, 1987; Canfield and others, 1992). As such, we recommend that Fe_{py}/Fe_{HR} and $(Fe_{py}+Fe_{AVS})/Fe_{HR}$ both be considered in settings where Fe_{AVS} is relevant. In situations with elevated $(Fe_{py}+Fe_{AVS})/Fe_{HR}$ but low Fe_{py}/Fe_{HR}, one can infer likely pore water sulfide accumulation but limited sulfide availability or exposure time. In sediments with insignificant AVS, like FOAM, one can infer 'highly reactive' Fe rather than sulfur limitation. This approach ultimately offers information on paleosalinity as related to sulfate availability (Berner and others, 1979), sedimentation rate, and depth of sedimentary dissolved sulfide depletion.

Results for Fe_{dith}, the second most abundant 'highly reactive' Fe phase other than pyrite at FOAM, show that oxides are lost with depth due to reductive dissolution and reaction with H_2S. This observation is confirmed by the pore water Fe and sedimentary pyrite profiles. Fe_{asc},

amorphous labile Fe oxides, show a similar but less defined trend. Surprisingly, Fe_{asc} and Fe_{dith} represent similar proportions of the Fe_{HR} pool below 10 cm depth, despite the fact that amorphous Fe-oxides are more reactive toward sulfide than crystalline Fe-oxides (Canfield and others, 1992). We cannot completely rule out the possibility that oxidation of pyrite or AVS prior to analysis yielded small amounts of Fe_{asc} and Fe_{dith} or that some amount of Fe is extracted from other phases, such as Fe silicates. Still, as previously described, great care was taken to minimize oxidation, with sample exposure to oxygen at room temperature limited to minutes, and Fe_{AVS} represented a negligible fraction of the 'highly reactive' Fe pool. Regardless, both Fe_{asc} and Fe_{dith} are low (<0.1 wt %) below 10 cm depth and therefore also represent an insignificant fraction of the Fe_{HR} pool at these depths. In general, the persistence of minor Fe_{asc}, Fe_{dith}, and Fe_{mag} at depth — whether because it is still unreacted, because it represents trace products of pyrite oxidation, or through trace dissolution of some silicate-bound Fe — prevents Fe_{py}/Fe_{HR} from becoming 1.0 even below the depth of pore water H_2S accumulation.

The highest value for Fe_{mag} was recorded in the upper 2 cm, but below this there was significant scatter. This distribution was an unexpected result as Canfield and Berner (1987) reported a clear decrease in Fe_{mag} with depth at FOAM. However, the occurrence of the highest value near the top of the profile is consistent with magnetite dissolution and reaction with sulfide deeper in the profile. Canfield and others (1992) reported pyrite growing on magnetite at FOAM, with sulfur isotope values of the pyrite reflecting those of the dissolved hydrogen sulfide in the adjacent pore waters, reportedly tracking addition of new pyrite during burial (Canfield and Berner, 1987). Of the Fe minerals that are reactive toward sulfide, pyrite-coated magnetite reacts five orders of magnitude more slowly than the crystalline Fe oxides that make up the dithionite Fe pool and seven orders of magnitude more slowly than ferrihydrite (Canfield and others, 1992),

meaning that consumption of additional magnetite may be disfavored until the more highly reactive Fe phases are first consumed. Still, the match between S isotope values for pyrite coating magnetite and the proximal pore water sulfide (Canfield and others, 1992) indicates ongoing pyrite formation via reaction of sulfide with magnetite.

Canfield and Berner (1987) showed an absence of uncovered magnetite below 60 cm depth at FOAM, with sampling at 10 cm resolution, and reported a clear decrease in magnetite abundance with depth. Our study was limited to the upper 50 cm with measurements at 2 cm intervals. The scatter in our data could be reflective of higher resolution or that the oxalate Fe extraction does not discern between covered and uncovered magnetite. The oxalate extraction has not been specifically evaluated to determine its effectiveness in extracting pyrite-coated magnetite, which represents the largest magnetite fraction above 50 cm at FOAM (Canfield and Berner 1987). The varied thickness of pyrite coating on magnetite grains, the fact that pyrite is also shed from the magnetite surface as it accumulates, as well as the varied reaction rates with sulfide between coated and uncoated magnetite may further explain the lack of a clear trend in the oxalate Fe data below the upper few centimeters. Regardless, the range of wt % magnetite Fe measured in this study (0.05 to 0.1 wt %) is consistent with previous FOAM studies (Canfield and Berner, 1987) and confirms that magnetite Fe contributes minimally to the Fe_{HR} pool at FOAM.

Figure 5 shows Fe_{HR}/Fe_T versus Fe_{py}/Fe_{HR} for modern sites characterized by a range of different redox states (euxinic, low oxygen but not anoxic water column, oxic water column with sulfidic pore waters, and oxic water column with sulfide-limited pore waters) from a variety of marine depositional environments (continental margin, estuary, deep sea, turbidite, and deltaic). We include Fe_{HR} as defined here — but also Fe_{HR} from studies predating Poulton and Canfield

(2005) where Fe_{HR} is defined as the sum of Fe_{py} and Fe_{dith}. (In general, results from FOAM indicate low contributions of Fe_{mag} and the expected limited contribution from Fe_{carb} confirm this as a good approximation.) The bulk of the data clearly show a distinction between sediments deposited under oxic water columns with and without appreciable pore water sulfide accumulation. The results from FOAM within the zone of sulfide accumulation from this study define a distinctive population expected of sediments deposited under oxic water columns with highly sulfidic pore fluids. FOAM sediments can be contrasted with other studies of sediments beneath oxic water columns. For example, Goldberg and others (2012) presented data from Gullmar Fjord north of Gothenburg, Sweden, showing pore water sulfide concentrations at or below the detection limit of <1 μM. Sequential Fe-speciation results for these sediments show Fe_T/Al approximately 0.5 and Fe_{HR}/Fe_T <0.38 throughout the entirety of the measured interval, similar to our results from FOAM. In contrast, however, results from Gullmar Fjord reveal Fe_{py}/Fe_{HR} values < 0.1, indicating a lack of appreciable sulfide accumulation and clearly contrasting with the values of > 0.8 from the FOAM site where sulfide concentrations exceed 3 mM. In this particular case, residual Fe_{HR} is dominated by crystalline Fe oxides, goethite, and hematite.

Though these results demonstrate that oxic water columns with and without pore water sulfide accumulation are generally discernible, there are three obvious complications observed in Figure 5, all which have been previously discussed in the literature. First, an observation previously made in Raiswell and Canfield (1998) is that low oxygen but not anoxic environments are not discernible from oxic environments. Second, of the modern euxinic environments evaluated with Fe speciation, only Cariaco Basin, Black Sea, and Framvaren Fjord show euxinic signals (Raiswell and Canfield, 1998). By contrast, other euxinic basins, such as Orca Basin of

the Gulf of Mexico and Kau Basin, Indonesia, show Fe_{HR}/Fe_T <0.38 (Raiswell and Canfield, 1998). Interestingly, these basins also exhibit some Fe_{py}/Fe_{HR} significantly less than 0.8. Finally, sediments deposited beneath an oxic water column but with a high input of glacially derived or deltaic material have the potential to appear ferruginous. In this latter case, we refer the reader to the filled squares in Figure 5 along the x-axis and the grey squares, all with $Fe_{HR}/Fe_T > 0.38$ and $Fe_{py}/Fe_{HR} < 0.8$, with data from März and others (2012) and based on the ferruginous intervals as defined in Canfield and others (2008) and Poulton and Canfield (2011).

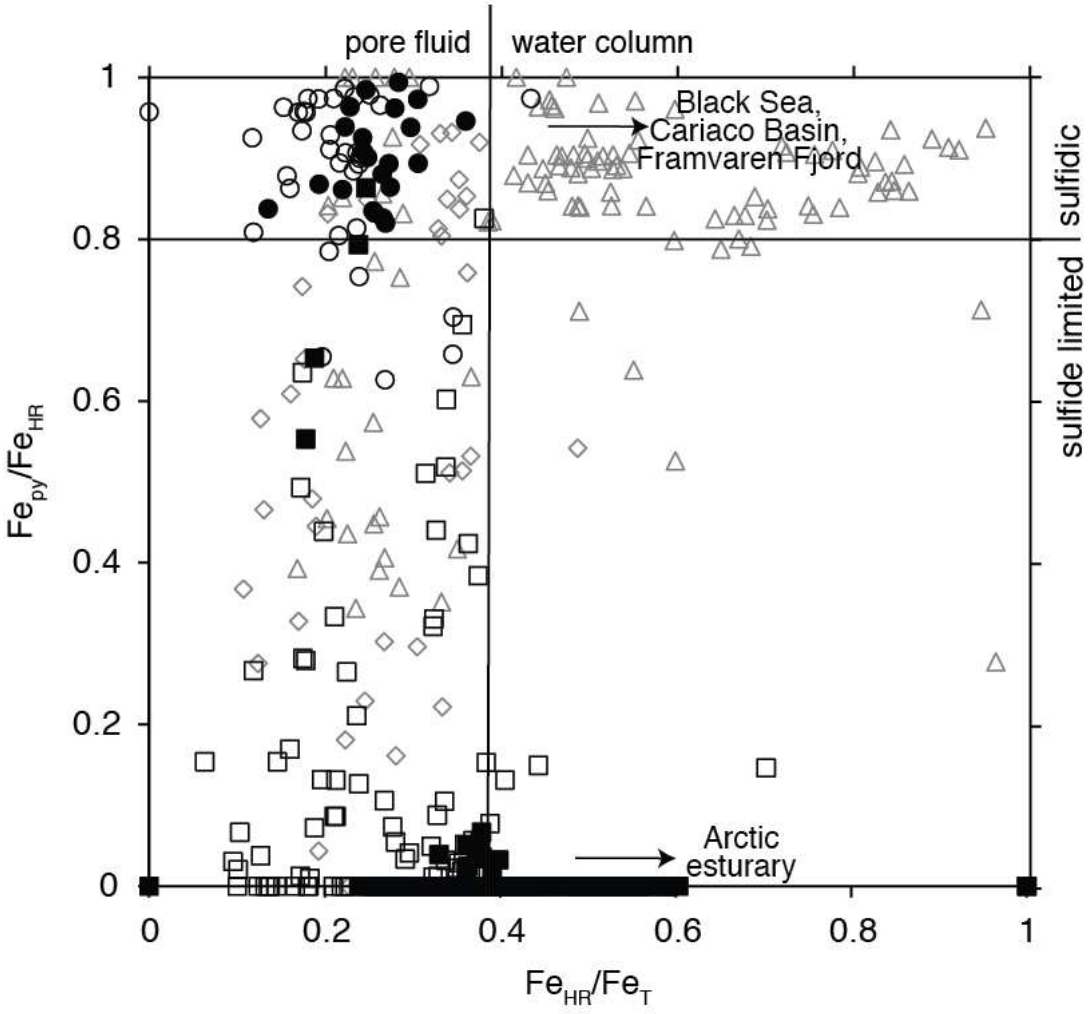

Figure 5. Compilation of modern sediment ratios for pyritized Fe (Fe_{py}) to highly reactive Fe (Fe_{HR}) and Fe_{HR} to total Fe (Fe_T) for: sulfidic sediments beneath an oxic water column (○), sulfide-limited sediments beneath an oxic water column (□), euxinic water column (△), and dysoxic water column (◇). The cross plot compares the availability of sulfide in the water column and pore waters for modern sediments to the operationally defined sedimentary Fe proxies commonly used to infer redox in the geologic record. Filled shapes represent studies utilizing variations of the operationally defined sequential Fe extraction from Poulton and Canfield (2005) for highly reactive Fe (Canfield, 1989; März et al., 2012; Goldberg et al., 2012; this study). Unfilled shapes represent studies where highly reactive Fe is represented by the sums of dithionite Fe (Fe_{ox}) and Fe_{py} only (Raiswell and Canfield 1998; Wisjman et al., 2001; Lyons et al., 2003). The vertical line represents the Fe_{py}/Fe_{HR} boundary for indication of sulfide accumulation presented in Canfield et al., (2008) of 0.8 (derived from Anderson and Raiswell, 2004). The horizontal line represents the boundary for water column oxic conditions for modern sediments, 0.38 (Canfield and Raiswell, 1998). Outside of the FOAM core for this study, data for the top 10 centimeters of cores with sulfide accumulation were omitted in order to generally account for variability in depths of sulfide accumulation if the sulfide depth profiles were not available.

Mo Concentrations

Contrary to our expectations, Mo concentrations at FOAM were not found to be elevated compared to typical continental crust, despite high sulfide concentrations of up to 3 mM. These high sulfide levels are well above the 100 μM 'action point' for total dissolved sulfide concentration that favors the complete transformation of molybdate to tetrathiomolybdate, which can then be efficiently, often quantitatively scavenged under sulfidic reducing conditions (Helz and others, 1996). Past studies of both sulfide-poor and sulfide-rich sediments beneath oxic waters typically report a peak of solid-phase Mo concentrations near the sediment-water interface resulting from sorption to and delivery with Mn and Fe-oxides, followed by a decrease in sedimentary Mo and an increase in pore water Mo with depth as Mn and Fe oxide dissolution proceeds (Bertine and Turekian, 1973; Huerta-Diaz and Morse, 1992; Crusius and others, 1996; Helz and others, 1996; Erickson and Helz, 2000; Bostick and others, 2003; Vorlicek and Helz, 2002; Vorlicek and others, 2004; Algeo and Lyons, 2006; Beck and others, 2008; Helz and others, 2011; Dahl and others, 2013). In sulfidic sediments, following Mn and Fe oxide dissolution, near-complete authigenic Mo removal from pore waters typically occurs at the zone of sulfide accumulation, forming a second solid-phase Mo peak. Neither of these two peaks is observed at FOAM despite pore water Mo levels greater than those of the overlying seawater and a clear indication of subsurface Mn and Fe oxide reduction seen in both pore water and sediment data — suggesting other factors may be controlling the Mo concentrations.

First, we can use estimates of the lithogenic Mo (Mo_{lith}) input relative to the observed bulk Mo concentrations (Mo_{bulk}) to determine the contribution, if any, from authigenic Mo (Mo_{auth}):

$$Mo_{bulk} = Mo_{lith} + Mo_{auth} \qquad \text{(Equation 2)}$$

Although constraints on the lithogenic input of Mo to sediments in Long Island Sound are lacking, we can estimate this component using a bulk average value of Mo/Al for granite- and sandstone-derived lithogenic material 6-19x10^{-6} (Turekian and Wedepohl 1961; Poulson Brucker and others, 2009). Both rock types are common regionally near FOAM. Considering an average sedimentary Al concentration of 6.0 wt % from FOAM (Table S1), we can calculate a lithologic Mo input of 0.36-1.4 ppm. This range is negligible for sediments with large authigenic Mo enrichments, but considering an average Mo concentration for FOAM sediments of 1.02 ppm, Mo_{lith} has the potential to make up anywhere from 35-100% of the bulk Mo concentrations. Given the low Mo/Al ratios for detrital inputs in the FOAM area relative to typical crust (Figure 4), it is clear that the lithogenic input is relatively low but also, importantly, that authigenic Mo is accumulating, albeit at low levels. Other studies evaluating Mo concentrations in sulfidic continental margin settings have suggested that sedimentation rates and bioturbation can be important in controlling the degree of enrichment beyond crustal values (Morford and others, 1999, 2007, 2009; Wang and others, 2011). We consider each of these briefly below.

FOAM and nearby sediments have previously been shown to experience variable but high rates of sedimentation, with estimates ranging from 0.03 to 0.3 cm/yr (Krishnaswami and others, 1984; Goldhaber and others, 1977). When ambient sulfide concentrations are greater than the 100 μM 'action point', as in FOAM pore waters, quantitative conversion of molybdate to tetrathiomolybdate can favor quantitative Mo removal from the pore fluids (Helz and others, 1996). Under such conditions, the sedimentation rate and flux of Mo across the sulfide interface can be used to calculate the authigenic Mo enrichment (Equ. 3) using Fick's First Law (Equ. 4). Equations 3 and 4 are used to calculate Mo_{auth} from the flux (J) of pore water Mo across the sulfide interface:

$$Mo_{auth} = \frac{J}{\omega\rho} \quad \text{(Equation 3)}$$

$$J = -\varphi\frac{\Delta C}{\Delta z} \quad \text{(Equation 4)}$$

where $\boldsymbol{\varphi}$ = diffusion coefficient, with a value of 5.2×10^{-6} cm^2/sec for MoO_4^{-2} used in our calculation (Chappaz and others, 2008); $\boldsymbol{\Delta C}$ = change in pore water concentration across sulfide interface ; $\boldsymbol{\Delta z}$ = depth interval from which ΔC is measured ; $\boldsymbol{\omega}$ = sedimentation rate (cm/sec); and $\boldsymbol{\rho}$ = sediment density (g/cm^3).

For the Mo concentration gradient ($\frac{\Delta C}{\Delta z}$), the sediment depth range was chosen where the peak in pore water Mo is observed to decline to near-zero values, which occurs along the interface of pore water sulfide accumulation (6-10 cm). Using a range of sedimentation rates measured at FOAM (0.3, 0.1, and 0.03 cm/yr) authigenic Mo concentrations of 1.2, 3.5, and 11.6 ppm, were calculated, respectively. These estimates suggest that high sedimentation rates close to 0.3 cm/yr may act to mute authigenic enrichments at marginal settings such as FOAM. It is similarly clear that in the absence of non-steady state processes, such as seasonality and intermittent sedimentation, the lower sedimentation rate of 0.03 would have produced an authigenic enrichment far exceeding the measured Mo concentrations. Rapid sedimentation has been recorded previously at FOAM for particular intervals. For example, Krishnaswami et al. (1984) reported laminated sediments from 20-30 cm, presumably from sediment scouring and rapid redeposition during a large storm event. However, though rapid sedimentation rates may act to prevent *large* enrichments in authigenic Mo in some intervals and throughout the core more generally, sedimentation rates from Krishnaswami et al. (1984), estimated at 0.09 cm/yr, are more representative and are generally accepted for FOAM (e.g., Canfield and others, 1992), suggesting

that other factors may be at play in keeping the enrichments even below the low levels our model predicts.

Uranium, which is also delivered to sediments via Mn and Fe cycling and is enriched authigenically in reducing conditions, shows patterns similar to Mo at FOAM. Increases in pore water uranium concentrations are associated with increases in pore water Mn and Fe, reflecting Mn and Fe oxide dissolution and associated release of sorbed trace metals (Morford and others, 2007). However, similar to Mo, sediment profiles do not show a surface oxide-associated peak or deeper authigenic enrichment Secondary uranium enrichment requires only anoxic conditions and not sulfide accumulation for authigenic enrichment, unlike Mo, and is thought to be driven by microbial reduction of soluble U(VI) to insoluble U(IV) (e.g., McManus and others, 2006). Previous studies have suggested that bioturbation can mix sediments containing authigenic U toward the sediment water interface, where remineralization under more oxic conditions can cause U remobilization and loss to the overlying water column (Zheng and others, 2002). This mechanism is analogous to early work showing that bioturbation can transport solid phase sulfides from reducing to oxidizing portions of the sediment pile, causing sulfide oxidation and sulfate production (Aller, 1980a,b; Berner and Westrich, 1985; Aller and Rude, 1988). Re-oxidation of reduced sediments resulting from sediment mixing during bioturbation together with seasonal variations in the depths of oxidant penetration, likely contribute to the muted Mo enrichments observed at FOAM.

Additionally, seasonal variability in oxidant levels in the actively bioturbated zone may play a key role in controlling the degree of authigenic Mo enrichments. Seasonal variations in sedimentary oxidant penetration depths can be driven by bioturbation and environmental controls, such as temperature, varying seasonal. At FOAM, these relationships are expressed through

temperature-controlled enhanced rates of organic matter remineralization in the upper few centimeters during the later spring and summer, resulting in pore water maxima in organic matter degradation products during this period and sharper gradients for oxidants like SO_4^{2-} (Goldhaber and others, 1977; Aller, 1980a). During the late summer and fall, biogenic reworking and irrigation results in enhanced exchange of pore water solutes with the water column. The net result is a lowering of the products of degradation and increases in pore water concentrations of oxidants, particularly SO_4^{2-}, which are depleted during the earlier summer but are abundant in the overlying bottom waters (Aller, 1980a). In general, biological activity decreases during the winter, and solutes in the bioturbated zone are dominated by physical processes (Goldhaber and others, 1977; Aller, 1980a). For instance, infaunal irrigation of sulfate to the sediments increases by up to a factor of five in the summer when benthic fauna are most active compared to winter when pore waters are diffusion controlled (Goldhaber and others, 1977; Aller, 1980a). Similarly, dissolved Fe and Mn, sourced from reduction of Fe/Mn oxides (the sedimentary source and temporary sink for Mo at FOAM), are both reported to increase during the summer when rates of microbial activity and associated Fe and Mn reduction increase, with partial escape to the overlying water column via diffusion and biogenic reworking (Aller, 1980b). Such a situation, where oxidants are seasonally introduced to formerly reduced layers, and degradation products are lost to the overlying water column, could result in authigenic Mo release from organic matter to the pore fluids and overlying water column on a seasonal basis, particularly during late summer/fall (Aller, 1980a,b). These factors, along with rapid sedimentation, could prevent the large authigenic enrichments expected in sediments with appreciable pore water sulfide.

Obviously our results only allow speculation regarding the potential role of bioturbation and seasonal variation in favoring only very low authigenic Mo enrichments, but the role of

seasonal controls on trace metal enrichment, including their relationships to infaunal activity, remain exciting areas of research worthy of further attention.

Anticipated Application To Studies of the Geologic Record

The fingerprinting of persistent pore water sulfide accumulation in the geologic record has important implications related to fluctuations in marine sulfate concentrations through time. For instance, dramatic increases in seawater sulfate may have been associated with the Paleoproterozoic Lomagundi carbon isotope excursion (e.g., Planavsky and others, 2012), Neoproterozoic negative carbon isotope excursions such as the Shuram anomaly (e.g., Fike and others, 2006), and the relative stabilization of seawater sulfate toward modern-like values in the Paleozoic (Gill and others, 2007). During periods of relatively higher sulfate and the stabilization of the sulfate reservoir, the penetration of marine sulfate into sedimentary pore fluids beneath oxic pore fluids and bottom waters represents a critical and currently under-studied step in the evolution of the marine redox state. One broader expectation is that temporal records of Fe speciation starting in oxic Paleozoic basins will reveal a lagged transition expressed in Fe_{py}/Fe_{HR} from limited pore water sulfide accumulation in phase with the protracted growth and stabilization of the marine sulfate reservoir. However, interestingly, a recent compilation of Fe_{py}/Fe_{HR}, where Fe_{HR}/Fe_T ratios are dominantly <0.38, suggests that even early Paleozoic sediments do not show signatures of frequent pore water sulfide accumulation (Sperling and others, 2015), begging the questions of when sulfide first began to dominate organic-rich, continental margin sediments. Comparisons of the extent of pore water sulfide accumulation during Precambrian oxidation events to that within the generally well-oxygenated Phanerozoic ocean may also act as a baseline for understanding the extent of seawater sulfate increases and oxygen penetration depths during these intervals. During the Phanerozoic, a trend toward

restriction of sulfide to marine pore fluids and the rise of animals may have broader implications for the evolution of bacterial-eukaryotic thiotrophic-respiratory symbiosis, as animals increased their burrowing depths (Tarhan and others, 2015). Regardless of any complications, it is clear the combined Fe speciation and Mo concentration data provides novel insight (Scott and Lyons, 2012).

CONCLUSIONS

A modified version of the Fe-extraction scheme of Poulton and Canfield (2005) was applied to modern sulfidic continental margin sediments in an effort to integrate Fe speciation and Mo concentration data toward a comprehensive view of the factors controlling pore water sulfide accumulation in sediments beneath an oxic water column and the resulting proxies that might track these conditions through time. The FOAM site and Long Island Sound more generally have played an essential role in our understanding of Fe reactivity toward sulfide and the development of a commonly applied Fe speciation scheme (Canfield and Berner, 1987; Canfield, 1989; Canfield and others, 1992) and the earlier DOP approach (Berner 1970; Raiswell and others, 1988; Canfield and others, 1992) — in large part through proximity to Yale University and the research group of Bob Berner. Based on previous work (Canfield and others, 1992; Raiswell and Canfield, 1998; Poulton and Canfield, 2011) and well documented pore water sulfide concentrations in excess of 3 mM, we expected $Fe_{HR}/Fe_T < 0.38$ (Raiswell and Canfield 1998), Fe_T/Al ratios of ~0.5 (Lyons and Severmann 2006), $Fe_{py}/Fe_{HR} > 0.8$, and Mo concentrations 2-25 ppm (Scott and Lyons 2012). The Fe speciation results fit the predicted range, with almost the entire 'highly reactive' Fe pool reacted with H_2S to form pyrite. Most importantly, the combined Fe data allow us to distinguish between settings where appreciable H_2S is limited to the pore waters versus euxinic environments where sulfide, by definition, extends into the water column. These results ultimately are the foundation for our understanding of the Fe paleoredox proxy —

that is, that anoxic settings (ferruginous and euxinic) are characterized by 'extra' reactive iron tied specifically to the redox conditions in the water column and associated Fe recycling/remobilization (Canfield and others, 1996; reviewed in Lyons and Severmann, 2006). Then, the degree to which the reactive iron is sulfidized points to ferruginous versus euxinic settings specifically. This additional iron, as we see at FOAM, is absent under oxic deposition, but high degrees of conversion of the reactive Fe to pyrite then delineate sulfidic pore waters.

Molybdenum concentrations, by contrast, did not fall within the typical range for sulfidic pore fluids (Scott and Lyons, 2012), despite Mo and Mn pore water profiles indicating Mo delivery to the sediments via oxides and abundant pore water H_2S that should allow for conversion of molybdate to particle reactive thiomolybdates and corresponding authigenic Mo accumulation. Calculation of authigenic enrichments based on the pore water Mo profiles indicate that there is indeed an authigenic Mo flux to the sediments but that episodic and generally high sedimentation rates and periodic re-oxidation of the sediments through biogenic reworking likely prevent expression of sedimentary Mo enrichments beyond typical lithologic values near 1-2 ppm.

We emphasize that recognizing sulfidic pore fluids beneath an oxic water column is most easily done when using combined Fe speciation and trace metal proxies such as Mo, similar to efforts designed to determine the specific redox state of anoxic water columns (e.g., Reinhard and others, 2013). Though Fe speciation proved to be the most robust indicator of sedimentary redox at FOAM, there are ambiguities introduced by high sedimentation rates, including similar Fe relationships under rapidly accumulating euxinic conditions (Lyons, 1997; Lyons and Severmann, 2006). Presence versus absence of lamination during the Phanerozoic, when infaunal organisms are prevalent under oxic conditions, can help us distinguish between anoxic and oxic deposition,

as can a ubiquity of reactive Fe in oxide phases. Added perspective comes with the inclusion of trace metal data, such as Mo. From FOAM, we learn that high bulk accumulation rates can stifle trace metal enrichment but that repeated re-oxidation of the surface sediments may be equally important. These are all essential environmental parameters that can be extrapolated back in time through integrated use of the associated proxies with the added benefit of a deeper understanding of the evolving ecological interactions among micro- and macro-organisms.

REFERENCES

Algeo, T.J., and Lyons, T.W., 2006, Mo-total organic carbon covariation inmodern anoxic marine environments: implications for analysis of paleoredox and paleohydrographic conditions: Paleoceanography, v. 21.

Algeo, T. J., & Maynard, J. B., 2004, Trace-element behavior and redox facies in core shales of Upper Pennsylvanian Kansas-type cyclothems: Chemical Geology, v. 206, p. 289-318.

Aller, R. C., 1980a, Diagenetic processes near the sediment–water interface of Long Island Sound: I. Decomposition and nutrient element geochemistry (S, N, P): In Estuarine Physics and Chemistry: Studies in Long Island Sound, Advances in Geophysics, v. 22 (ed. B. Saltzman), p. 237-350. Academic Press, New York.

Aller, R. C., 1980b, Diagenetic processes near the sediment–water interface of Long Island Sound: II. Fe and Mn: In Estuarine Physics and Chemistry: Studies in Long Island Sound, Advances in Geophysics, v. 22 (ed. B. Saltzman), p. 351–415. Academic Press, New York.

Aller, R. C., and Rude, P. D., 1988, Complete oxidation of solid phase sulfides by manganese and bacteria in anoxic marine settings: Geochimica et Cosmochimica Acta, v. 52, p. 751-765.

Anderson, R. F., Lyons, T. W., and Cowie, G. L., 1994, Sedimentary record of a shoaling of the oxic/anoxic interface in the Black Sea. Marine Geology, v. 116, p. 373-384.

Anderson, T.H., and Taylor, G.T., 2001, Nutrient pulses, plankton blooms, and seasonal hypoxia in western Long Island Sound: Estuaries, v. 24, p. 228-243.

Anderson T.F., and Raiswell R., 2004, Sources and mechanisms for the enrichment of highly reactive iron in euxinic Black Sea sediments: American Journal of Science, v. 304, p. 203-233.

Archer, C., and Vance, D., 2008, The isotopic signature of the global riverine molybdenum flux and anoxia in the ancient oceans: Nature Geoscience, v. 1, p. 597–600.

Arnold, G.L., Anbar, A.D., Barling, J. and Lyons, T.W., 2004, Anoxia in Mid-Proterozoic oceans: Science, v. 304, p. 87–90.

Barling, J., Arnold, G.L., and Anbar, A.D., 2001, Natural mass-dependent variations in the isotopic composition of molybdenum: Earth and Planetary Science Letters, v. 193, p. 447–457.

Barling, J., and Anbar, A.D., 2004, Molybdenum isotope fractionation during adsorption by manganese oxides. Earth and Planeary Science Letters, v. 217, p. 315–329.

Beck, M., Dellwig, O., Schnetger, B., and Brumsack, H. J., 2008, Cycling of trace metals (Mn, Fe, Mo, U, V, Cr) in deep pore waters of intertidal flat sediments: Geochimica et Cosmochimica Acta, v. 72, p. 2822-2840.

Benninger, R.K., Aller, R.C., Cochran, J.K., and Turekian, K.K., 1979, Effects of biological sediment mixing on the Pb chronology and trace metal distribution in a long island sound sediment core: Earth and Planetary Science Letters, v. 43, p. 241-259

Berner, R. A., 1970, Sedimentary pyrite formation: American Journal of Science, v. 268, p. 2–23.

Berner, R. A., 1978, Sulfate reduction and the rate of deposition of marine sediments: Earth and Planetary Science Letters, v. 37, p. 492-498.

Berner, R. A., 1980, Early diagenesis: A theoretical approach (No. 1). Princeton University Press.

Berner, R. A., Baldwin, T., qne Holdren Jr, G. R., 1979, Authigenic iron sulfides as paleosalinity indicators: Journal of Sedimentary Research, v. 49.4

Berner, R. A., and Westrich, J. T., 1985, Bioturbation and the early diagenesis of carbon and sulfur: American Journal of Science, v. 285, p. 193-206.

Bertine, K.K., and Turekian, K.K., 1973, Molybdenum in marine deposits: Geochimica et Cosmochimica Acta: v. 37, p. 1415-1434.

Boesen, C., and Postma, D., 1988, Pyrite formation in anoxic environments of the Baltic: American Journal of Science, v. 288, p. 575–603.

Bostick, B.C., Fendorf, S., and Helz, G.R., 2003, Differential adsorption of molybdate and tetrathiomolybdate on pyrite (FeS_2): Environmental Science and Technology, v. 37, p. 285–291.

Boudreau, B. P., and Canfield, D. E., 1988, A provisional diagenetic model for pH in anoxic porewaters: Application to the FOAM site: Journal of Marine Research., v. 46, p. 429 455.

Broecker, W.S., Peng, T.H., and Beng, Z., 1982, Tracers in the Sea. Lamont-Doherty Geological Observatory, Columbia University.

Brüchert, V., and Pratt, L. M., 1996, Contemporaneous early diagenetic formation of organic and inorganic sulfur in estuarine sediments from St. Andrew Bay, Florida, USA: Geochimica et Cosmochimica Acta, v. 60, p. 2325-2332.

Canfield, D. E., 1989, Reactive iron in marine sediments: Geochimica et Cosmochimica Acta, v. 53, p. 619–632.

Canfield, D. E., and Berner, R. A.,1987, Dissolution and pyritization of magnetite in anoxic marine sediments: Geochimica et Cosmochimica Acta, v. 51, p. 645-659.

Canfield, D. E., Raiswell, R., and Westrich, J. T., Reaves, C. M., & Berner, R. A., 1986, The use of chromium reduction in the analysis of reduced inorganic sulfur in sediments and shales: Chemical Geology, v. 54, p. 149-155.

Canfield, D. E., and Raiswell, R., 1991, Pyrite formation and fossil preservation, in Allison, P. A., and Briggs, D. E. G., editors, Taphonomy: Releasing the Data Locked in the Fossil Record: New York, Plenum, p. 337–387.

Canfield, D. E., Raiswell, R., and Bottrell, S. H., 1992, The reactivity of sedimentary iron minerals towards sulfide: American Journal of Science, v. 292, p. 659–683.

Canfield, D.E., Poulton, S.W., and Narbonne, G.M., 2007, Late-Neoproterozoic deep-ocean oxygenation and the rise of animal life: Science, v. 315, p. 92–95.

Cline, J. D., 1969, Spectrophotometric determination of hydrogen sulfide in natural waters: Limnology and Oceanography, v. 14, p. 454-458.

Crusius, J., and Anderson, R.F., 1991, Immobility of ^{210}Pb in Black Sea sediments: Geochimica et Cosmochimica Acta, v. 55, p. 327-333.

Crusius, J., Calvert, S., Pedersen, T., and Sage, D., 1996, Rhenium and molybdenum enrichments in sediments as indicators of oxic, suboxic, and sulfidic conditions of deposition: Earth and Planetary Science Letters, v. 145, p. 65–78.

Dahl, T. W., Hammarlund, E. U., Anbar, A. D., Bond, D. P. G., Gill, B. C., Gordon, G. W., Knoll, A. H., Nielsen, A. T., Schovsbo, N. H., and Canfield, D. E., 2010, Devonian rise in atmospheric oxygen correlated to the radiations of terrestrial plants and large predatory fish: Proceedings of the National Academy of Sciences, v. 107, 17911-17915.

Dahl, T. W., Chappaz, A., Fitts, J. P., and Lyons, T. W., 2013, Molybdenum reduction in a sulfidic lake: Evidence from X-ray absorption fine-structure spectroscopy and implications for the Mo paleoproxy: Geochimica et Cosmochimica Acta, v. 103, p. 213 231.

Diaz, R. J., and Rosenberg, R., 2008, Spreading dead zones and consequences for marine ecosystems: Science, v. 321, p. 926-929.

Erickson, B.E., and Helz, G.R., 2000, Molybdenum(VI) speciation in sulfidic waters: stability and lability of thiomolybdates: Geochimica et Cosmochimica Acta, v. 64, p. 1149–1158.

Emerson, S. R., and Huested, S. S., 1991, Ocean anoxia and the concentrations of molybdenum and vanadium in seawater: Marine Chemistry, v. 34, p. 177-196.

Ferdelman, T.G., 1988, The distribution of sulfur, iron, manganese, copper, and uranium in a salt marsh sediment core as determined by a sequential extraction method: Masters thesis, Univ. Delaware.

.Fike, D. A., Grotzinger, J.P., Pratt, L.M., and Summons, R.E., 2006, Oxidation of the Ediacaran ocean: *Nature*, v. *444*, p. 744-747.

Fischer, J.P., Ferdelman, T.G., D'Hondt, S., Røy, H. and Wenzhöfer, F., 2009, Oxygen penetration deep into the sediment of the South Pacific gyre: *Biogeosciences*, v. 6, p. 1467–1478.

Froelich, P., Klinkhammer, G. P., Bender, M. A. A., Luedtke, N. A., Heath, G. R., Cullen, D., and Maynard, V., 1979, Early oxidation of organic matter in pelagic sediments of the eastern equatorial Atlantic: suboxic diagenesis: Geochimica et Cosmochimica Acta, v. 43, p. 1075-1090.

Gagnon, C., Mucci, A., and Pelletier, E´., 1995, Anomalous accumulation of acid-volatile sulphides (AVS) in a coastal marine sediment, Saguenay Fjord, Canada: Geochimica et Cosmochimica Acta, v. 59, p. 2663–2675.

Gill, B.C., Lyons, T.W., and Saltzman, M.R., 2007, Parallel, high-resolution carbon and sulfur isotope records of the evolving Paleozoic marine sulfur reservoir: Palaeogeography, Palaeoclimatology, Palaeoecology, v. 256, p. 156-173.

Gill, B.C., Lyons, T.W., Young, S.A., Kump, L.R., Knoll, A.H., and Saltzman, M.R., 2011, Geochemical evidence for widespread euxinia in the Later Cambrian ocean: Nature, v. 469, p. 80-83.

Goldberg, T., Archer, C., Vance, D., and Poulton, S.W., 2009, Mo isotope fractionation during adsorption of Fe (oxyhydr)oxides: Geochimica et Cosmochimica Acta, v. 73, p. 6502–6516.

Golberg, T., Archer, C., Vance, D., Thamdrup, B., McAnena, A., and Poulton, S.W., 2012, Controls on Mo isotope fractionations in a Mn-rich anoxic marine sediment, Gullmar Fjord, Sweden: Chemical Geology, v. 296-297, p. 73-82.

Goldhaber, M. B., Aller, R. C., Cochran, J. K., Rosenfeld, J. K., Martens, C. S., and Berner, R. A., 1977, Sulfate reduction, diffusion, and bioturbation in Long Island Sound sediments; report of the FOAM Group: American Journal of Science, v. 277, p. 193-237.

Helz, G.R., Miller, C.V., Charnock, J.M., Mosselmans, J.F.W., Patrick, R.A.D., Garner, D.D., and Vaughan, D.J., 1996, Mechanism of molybdenum removal from the sea and its concentration in black shales: EXAFS evidence: Geochimica et Cosmochimica Acta, v. 60, p. 3631–3642.

Huerta-Diaz, M.A., and Morse, J.W., 1992, Pyritization of trace metals in anoxic marine sediments. Geochimica et Cosmochima Acta, v. 56, p. 2681–2702.

Hurtgen, M.T., Lyons, T.W., Ingall, E.D., and Cruse, A.M., 1999, Anomalous enrichments of iron monosulfide in euxinic marine sediments and the role of H_2S in iron sulfide transformations: examples from Effingham Inlet, Orca Basin, and the Black Sea: American Journal of Science, v. 299, p. 556–588.

Johnston, D. T., Poulton, S. W., Goldberg, T., Sergeev, V. N., Podkovyrov, V., Vorob'eva, N. G., Bekker, A., Knoll, A.H., 2012, Late Ediacaran redox stability and metazoan evolution. Earth and Planetary Science Letters, 335-336, p. 25–35.

Kendall, B., Reinhard, C. T., Lyons, T. W., Kaufman, A. J., Poulton, S. W., and Anbar, A. D., 2010, Pervasive oxygenation along late Archaean ocean margins. Nature Geoscience, 3, p. 647-652.

Kraal, P., Burton, E. D., and Bush, R. T., 2013, Iron monosulfide accumulation and pyrite formation in eutrophic estuarine sediments: *Geochimica et Cosmochimica Acta*, v. *122*, p. 75-88.

Krishnaswami, S., Monaghan, M. C., Westrich, J. T., Bennett, J. T., and Turekian, K. K., 1984, Chronologies of sedimentary processes in sediments of the FOAM site, Long Island Sound, Connecticut. American Journal of Science, v. 284, p. 706-733.

Lee, Y. J., and Lwiza, K., 2005, Interannual variability of temperature and salinity in shallow water: Long Island Sound, New York: Journal of Geophysical Research: Oceans (1978–2012), v. 110, p. 187 199.

Lee, Y. J., and Lwiza, K. M., 2008, Characteristics of bottom dissolved oxygen in long Island Sound, New York: Estuarine, Coastal and Shelf Science, v. 76, p. 187-200.

Li, C., Love, G. D., Lyons, T. W., Fike, D. A., Sessions, A. L., and Chu, X., 2010, A stratified redox model for the Ediacaran ocean: Science, v. 328, p. 80-83.

Lyons, T. W., 1997, Sulfur isotopic trends and pathways of iron sulfide formation in upper Holocene sediments of the anoxic Black Sea: Geochimica et Cosmochimica Acta, v. 61, p. 3367–3382.

Lyons, T. W., and Berner, R. A., 1992, Carbon-sulfur-iron systematics of the uppermost deep water sediments of the Black Sea: Chemical Geology, v. 99, 1-27.

Lyons, T. W., Berner, R. A., and Anderson, R. F., 1993, Evidence for large pre-industrial permutations of Black Sea chemocline: Nature, v. 365, p. 538–540.

Lyons, T.W., Werne, J.P., Hollander, D.J., and Murray, R.W., 2003, Contrasting sulfur geochemistry and Fe/Al and Mo/Al ratios across the last oxic-to-anoxic transition in the Cariaco Basin, Venezuela: Chemical Geology, v. 195, p. 131–157.

Lyons, T.W., and Kashgarian, M., 2005, Paradigm lost, paradigm found—The Black Sea-black shale connection as viewed from the anoxic basin margin: *Oceanography*, v. 18, p. 86-99.

Lyons, T. W., and Severmann, S., 2006, A critical look at iron paleoredox proxies: new insights from modern euxinic marine basins: Geochimica et Cosmochimica Acta, v. 70, p. 5698-5722.

März, C., Poulton, S. W., Beckmann, B., Küster, K., Wagner, T., and Kasten, S., 2008, Redox sensitivity of P cycling during marine black shale formation: Dynamics of sulfidic and anoxic, non-sulfidic bottom waters: Geochimica et Cosmochimica Acta, v. 72, p. 3703-3717.

März, C., Poulton, S. W., Brumsack, H. J., and Wagner, T., 2012, Climate-controlled variability of iron deposition in the Central Arctic Ocean (southern Mendeleev Ridge) over the last 130,000years. Chemical Geology, v. 330-331, p. 116-126.

McManus, J., Berelson, W.M., Severmann, S., Poulson, R.L., Hammond, D.E., Klinkhamer, G.P., and Holm, C., 2006, Molybdenum and uranium geochemistry in continental margin sediments: paleoproxy potential: Geochimica et Cosmochimica Acta, v. 18, p. 4643–4662.

Miller, C. A., Peucker-Ehrenbrink, B., Walker, B. D., and Marcantonio, F., 2011, Re-assessing the surface cycling of molybdenum and rhenium. Geochimica et Cosmochimica Acta, v. 75, p. 7146-7179.

Morford, J. L., Emerson, S. R., Breckel, E. J., and Kim, S. H., 2005, Diagenesis of oxyanions (V, U, Re, and Mo) in pore waters and sediments from a continental margin: Geochimica et Cosmochimica Acta, v. 69, p. 5021-5032.

Morford, J.L., and Emerson, S., 1999, The geochemistry of redox sensitive trace metals in sediments: Geochimica et Cosmochimica Acta, v. 63, p. 1735–1750.

Morford, J.L., Martin, W.R., Kalnejais, L.H., François, R., Bothner, M., and Karle, I. M., 2007, Insights on geochemical cycling of U, Re and Mo from seasonal sampling in Boston Harbor, Massachusetts, USA: Geochimica et Cosmochimica Acta, v. 71, p. 895-917.

Morford, J.L., Martin, W.R., François, R., and Carney, C.M., 2009, A model for uranium, rhenium, and molybdenum diagenesis in marine sediments based on results from coastal locations: Geochimica et Cosmochimica Acta, v. 73, p. 2938-2960.

Owens, J.D., Reinhard, C.T., Rohrssen, M., Love, G.D. and Lyons, T.W., 2016, Empirical links between trace metal cycling and marine microbial ecology during a large perturbation to Earth's carbon cycle: Earth and Planetary Science Letters, v. 449, p.407-417.

Planavsky, N.J., Bekker, A., Hofmann, A., Owens, J.D., and Lyons, T.W., 2012, Sulfur record of rising and falling marine oxygen and sulfate levels during the Lomagundi event: Proceedings of the National Academy of Sciences, v. 109, p. 18300-18305.

Poulson Brucker, McManus, J., Severmann, S., and Berelson, W.M., 2009, Molybdenum behavior during early diagenesis: insights from Mo isotopes: Geochemistry, Geophysics, Geosystems, v. 10, Q06010.

Poulson, R.L., Siebert, C., McManus, J., and Berelson, W.M., 2006, Authigenic molybdenum isotope signatures in marine sediments: Geology, v. 34, p. 617–620.

Poulton, S.W., and Canfield, D.E., 2005, Development of a sequential extraction procedure for iron: implications for iron partitioning in continentally derived particulates: Chemical Geology, v. 214, p. 209–221.

Poulton, S.W., and Canfield, D. E., 2011, Ferruginous conditions: a dominant feature of the ocean through Earth's history: Elements, v. 7, p. 107-112.

Poulton S.W., Fralick P.W., and Canfield D.E., 2004, The transition to a sulphidic ocean ~1.84 billion years ago: Nature, v. 431, p. 173-177.

Poulton S.W., and Raiswell R., 2002, The lowtemperature geochemical cycle of iron: From continental fluxes to marine sediment deposition: American Journal of Science, v. 302, p. 774-805.

Raiswell, R., Buckley, F., Berner, R. A., and Anderson, T. F., 1988, Degree of pyritization of iron as a paleoenvironmental indicator of bottom-water oxygenation: Journal of Sedimentary Petrology, v. 58, p. 812–819

Raiswell, R., and Canfield, D. E., 1996, Rates of reaction between silicate iron and dissolved sulfide in Peru Margin sediments: Geochimica et Cosmochimica Acta, v. 60, p. 2777-2787.

Raiswell R., and Canfield D.E., 1998, Sources of iron for pyrite formation in marine sediments: American Journal of Science, v. 298, p. 219-245l.

Raiswell, R., Canfield, D. E., and Berner, R. A., 1994, A comparison of iron extraction methods for the determination of degree of pyritisation and the recognition of iron-limited pyrite formation: Chemical Geology, v. 111, p. 101–111.

Raiswell, R., Vu, H. P., Brinza, L. and Benning, L. G., 2010, The determination of labile Fe in ferrihydrite by ascorbic acid extraction: methodology, dissolution kinetics and loss of solubility with age and de-watering: Chemical Geology, v. 278, p. 70-79.

Reinhard, C.T., Raiswell, R., Scott, C., Anbar, A.D., and Lyons, T.W., 2009, A Late Archean sulfidic sea stimulated by early oxidative weathering of the continents: Science, v. 326, p. 713–716

Reinhard, C. T., Planavsky, N. J., Robbins, L. J., Partin, C. A., Gill, B. C., Lalonde, S. V.,Bekker, A., Konhauser, K. O., & Lyons, T. W., 2013, Proterozoic ocean redox and biogeochemical stasis: Proceedings of the National Academy of Sciences, v. 110, p. 5357-5362.

Rhoads, D.C., and Morse, J.W., 1971, Evolutionary and ecologic significance of oxygen deficient marine basins: Lethaia, p. 4.4, p. 413-428.

Scheiderich, K., Helz, G.R., and Walker, R.J., 2010, Century-long record of Mo isotopic composition in sediments of a seasonally anoxic estuary (Chesapeake Bay): Earth and Planetary Science Letters, v. 289, p. 189-197.

Scott, C., Lyons, T.W., Bekker, A., Poulton, S.W., Shen, Y., Chu, X., and Anbar, A.D., 2008, Tracing the stepwise oxygenation of the Proterozoic ocean: Nature, v. 452, p. 456–460.

Scott, C., and Lyons, T. W., 2012, Contrasting molybdenum cycling and isotopic properties in euxinic versus non-euxinic sediments and sedimentary rocks: Refining the paleoproxies: Chemical Geology, v. 324, p. 19-27.

Scott, C.T., Bekker, A., Reinhard, C.T., Schnetger, B., Krapez, B., Rumble III, D., and Lyons, T.W., 2011, Late Archean euxinic conditions before the rise of atmospheric oxygen: Geology, v. 39, p. 119-122.

Scholz, F., Severmann, S., McManus, J., and Hensen, C., 2014, Beyond the Black Sea paradigm: The sedimentary fingerprint of an open-marine iron shuttle: Geochimica et Cosmochimica Acta, v. 127, p. 368-380.

Seeberg-Elverfeldt, J., Schlüter, M., Feseker, T., and Kölling, M., 2005, Rhizon sampling of pore waters near the sediment/water interface of aquatic systems: Limnology and Oceanography: Methods, v. 3, p. 361-371.

Severmann, S., Lyons, T. W., Anbar, A., McManus, J., and Gordon, G., 2008, Modern iron isotope perspective on the benthic iron shuttle and the redox evolution of ancient oceans: Geology, v. 36, p. 487-490.

Siebert, C., Nägler, J.F., von Blanckenburg, F., and Kramers, J.D., 2003. Molybdenum isotope records as a potential new proxy for paleoceanography: Earth and Planetary Science Letters, v. 211, p. 159-171.

Siebert, C., McManus, J., Bice, A., Poulson, R., and Berelson, W.M., 2006, Molybdenum isotope signatures in continental margin marine sediments. Earth and Planetary Science Letters, v. 241, p. 723–733.

Sperling, E.A., Wolock, C.J., Morgan, A.S., Gill, B.C., Kunzmann, M., Halverson, G.P., Macdonald, F.A., Knoll, A.H. and Johnston, D.T., 2015. Statistical analysis of iron geochemical data suggests limited late Proterozoic oxygenation. Nature, v. 523, p. 451-454.

Tarhan, L. G., Droser, M. L., Planavsky, N. J. and Johnston, D. T., 2015, Protracted development of bioturbation through the early Palaeozoic Era: Nature Geoscience, v., p. 865-869

Taylor, S.R., and McLennan, S.M., 1995, The geochemical evolution of the continental crust: Reviews of Geophysics, v. 33, p. 241–265.

Toth, D. J., and Lerman, A., 1977, Organic matter reactivity and sedimentation rates in the ocean: American Journal of Science, v. 277, p. 465-485.

Turekian, K.K., and Wedepohl, K.H., 1961, Distribution of the elements in some major units of the Earth's crust: Geol. Soc. Am. Bull., v. 72, p. 175–192.

Turekian, K.K., Cochran, J.K., Benninger, L.K., and Aller, R.C., 1980, The sources and sinks of nuclides in Long Island Sounds. In Saltzman, B. ed., Estuarine physics and chemistry: Studies in Long Island Sound: Advances in Geophysics, v. 22 p. 129-164.

US Environmental Protection Agency, 1998, Long Island Sound Study: Phase III Actions of Hypoxia Management. Report No. EPA 902-R-98-002, United States Environmental Protection Agency. Stamford, CT, USA.

Vaquer-Sunyer, R., and Duarte, C. M., 2008, Thresholds of hypoxia for marine biodiversity: Proceedings of the National Academy of Sciences, v. 105, p. 15452-15457.

Vorlicek T.P., and Helz G.R., 2002, Catalysis by mineral surfaces: Implications for Mo geochemistry in anoxic environments: Geochimica et Cosmochimica Acta, v. 66, p. 3679–3692.

Vorlicek, T. P., Kahn, M. D., Kasuya, Y., and Helz, G. R., 2004, Capture of molybdenum in pyrite forming sediments: role of ligand-induced reduction by polysulfides: Geochimica et Cosmochimica Acta, v. 68, p. 547-556.

Wang, D., Aller, R. C., and Sañudo-Wilhelmy, S. A., 2011, Redox speciation and early diagenetic behavior of dissolved molybdenum in sulfidic muds. Marine Chemistry, v. 125, p. 101 107.

Wasylenki, L.E., Rolfe, B.A., Weeks, C.L., Spiro, T.G., and Anbar, A.D., 2008, Experimental investigation of the effects of temperature and ionic strength on Mo isotope fractionation during adsorption to manganese oxides: Geochimica et Cosmochimica Acta, v. 72, p. 5997–6005.

Westrich, J.T., 1983, Consequences and controls of bacterial sulfate reduction in marine sediments. Ph.D. dissert. Yale University.

Wijsman, J.W.M., Middelburg, J.J., and Heip, C.H.R., 2001, Reactive iron in Black Sea sediments: implications for iron cycling: Marine Geology, v. 172, p. 167–180.

Zheng, Y., Anderson, R. F., van Geen, A., and Fleisher, M. Q., 2002, Remobilization of authigenic uranium in marine sediments by bioturbation: Geochimica et Cosmochimica Acta, v. 66, p. 1759-1772.

Zopfi, J., Ferdelman, T.G., and Fossing, H., 2004, Distribution and fate of sulfur intermediates sulfite, tetrathionate, thiosulfate, and elemental sulfur – in marine sediments. In: Sulfur biochemistry past and present (eds. J.P. Amend, K.J. Edwards, and T.W. Lyons): Geological Society of America Special Paper, v. 379, p. 97-116.

SUPPLEMENTAL MATERIALS

Table S1. Results for Fe speciation, degree of pyritization (DOP), and bulk sedimentary Fe and Al concentrations.

Depth (cm)	Fe_{asc} (wt %)	Fe_{dith} (wt %)	Fe_{mag} (wt %)	Fe_{py} (wt %)	Fe_{HCl} (wt %)	Fe_T (wt %)	Al_T (wt %)	Fe_{HR}/Fe_T	Fe_{py}/Fe_{HR}	Fe_T/Al	DOP	TOC (wt %)
0.5	0.02	< D.L.	0.09	0.68	1.37	3.18	5.82	0.25	0.86	0.55	0.33	1.75
2	<D.L.	0.11	0.06	0.65	1.14	3.44	6.61	0.24	0.79	0.52	0.36	1.85
4	0.06	0.13	0.05	0.31	1.18	3.16	6.43	0.18	0.55	0.49	0.21	1.20
6	0.03	0.10	0.06	0.36	1.33	2.96	5.67	0.19	0.65	0.52	0.22	1.22
8	0.01	0.04	0.02	0.35	1.05	3.13	6.45	0.14	0.84	0.48	0.25	1.31
10	0.01	0.03	0.02	0.60	0.94	2.72	5.51	0.24	0.91	0.49	0.39	1.01
12	0.01	0.02	0.06	0.66	1.02	2.77	5.71	0.27	0.86	0.48	0.39	2.50
14	< D.L.	< D.L.	0.01	0.74	1.16	3.03	6.03	0.25	0.98	0.50	0.39	1.21
16	0.01	0.02	0.01	0.65	0.94	3.11	6.19	0.22	0.94	0.50	0.41	0.71
18	0.02	0.03	0.03	0.69	1.00	2.53	4.95	0.31	0.89	0.51	0.41	1.04
20	0.05	0.04	0.07	0.71	1.25	3.21	6.04	0.27	0.82	0.53	0.36	1.32
22	< D.L.	< D.L.	0.06	0.93	0.92	3.32	6.67	0.30	0.94	0.50	0.50	1.42
24	0.01	0.00	0.05	1.06	1.24	3.12	4.85	0.36	0.95	0.64	0.46	1.52
26	< D.L.	0.00	0.07	0.83	1.12	3.69	7.38	0.24	0.93	0.50	0.43	1.65
28	< D.L.	< D.L.	0.04	0.93	1.51	3.45	7.01	0.28	0.96	0.49	0.38	1.24
30	< D.L.	0.00	0.02	0.86	0.97	3.03	5.69	0.28	0.99	0.53	0.47	1.45
32	0.04	0.02	0.08	0.68	1.21	3.17	6.12	0.26	0.83	0.52	0.36	1.41
34	0.03	0.01	0.08	0.59	1.24	2.79	5.89	0.26	0.83	0.47	0.32	0.87
36	< D.L.	0.00	0.03	0.70	1.10	3.19	6.09	0.23	0.96	0.52	0.39	1.54
38	< D.L.	0.01	0.07	0.69	1.20	3.06	5.87	0.25	0.90	0.52	0.36	1.91
40	0.03	0.03	0.08	0.66	1.17	3.00	5.73	0.27	0.83	0.52	0.36	1.00
42	0.02	0.01	0.06	0.55	1.14	3.28	6.47	0.19	0.87	0.51	0.33	1.47
44	0.02	0.01	0.07	0.71	1.13	3.04	5.70	0.27	0.88	0.53	0.39	1.64
46	0.01	0.00	0.09	0.81	0.99	3.31	6.48	0.27	0.89	0.51	0.45	1.49
48	0.02	0.01	0.06	0.60	0.77	3.16	5.84	0.22	0.86	0.54	0.44	1.42
50	0.00	0.00	0.02	0.85	0.84	2.84	5.22	0.31	0.97	0.54	0.50	1.27

D.L. = Detection limit

Table S2. Sedimentary and pore water Mo and U concentrations and Mo isotope composition.

Depth (cm)	Pore water Mo (nM)	Pore water U (nM)	Bulk Mo (ppm)	Bulk U (ppm)
0.5	157.40	23.86	1.14	2.50
2	139.75	18.68	1.11	2.54
4			1.11	2.26
6	296.53	14.25	0.96	2.30
8			1.02	2.18
10	79.94	11.13	0.96	2.02
12			1.2	2.2
14	115.08	11.75	1.02	2.26
16			1.30	2.21
18	35.92	13.19	1.07	1.89
20			0.90	2.40
22	2.99	5.77		2.26
24			0.87	2.25
26	4.48	6.74		2.54
28			1.01	250
30	13.89	7.78	0.96	2.13
32			0.86	2.31
34		6.37		
36			1.00	2.08
38	34.22	5.30	0.85	2.13
40			1.10	2.35
42	14.35	8.75	1.02	2.26
44			0.99	2.36
46	14.75	4.96	1.07	2.35
48			1.00	2.27
50	8.40	7.16	1.17	2.22

CHAPTER 4

A Holocene history of dynamic water column redox conditions in the Landsort Deep, Baltic Sea

ABSTRACT

The modern Baltic Sea is the world's largest anthropogenically forced anoxic basin. Using integrated geochemical records collected during Integrated Ocean Drilling Program (IODP) Expedition 347 from the deepest and one of the most reducing sub-basins in the Baltic Sea, Landsort Deep, we explore the degree and frequency of natural anoxia through the Baltic Holocene. A marked decrease in carbon-to-sulfur ratios (C/S) from the cores indicate the transition from the Baltic Ice Lake to the current brackish sea, which occurred about 8.5 kyrs B.P. Following this, laminations throughout sediments recording brackish deposition suggest sustained anoxia or extreme low oxygen, while high molybdenum (Mo) concentrations of >100 ppm and iron (Fe) geochemistry suggest water column sulfide accumulation, or euxinia, that persisted beyond seasonal timescales during deposition of two distinct sapropel units. Sedimentary Mo isotope values range from +1.11 to -0.50‰, which are distinctly fractionated from modern Baltic seawater (+2.26 to +2.67‰) and thus indicate that each of the sapropels experienced only weak and/or oscillatory euxinia — in contrast to the more stable euxinic conditions of more restricted basins. A shift in δ^{98}Mo starting above the lower sapropel to a distinctly more negative range suggests particularly weak and oscillatory euxinia, with an enhanced contribution of manganese (Mn) redox cycling to Mo deposition relative to the lower portion of the profile. This conclusion is supported by extreme sedimentary Mn enrichments of up to 15 wt.%. We interpret the combined data to indicate episodic but major Baltic inflow events of saline and oxygenated North Sea water into the anoxic Landsort Deep that limited the concentrations and residence time of water column sulfide and caused episodic oxide deposition. Considering the temporal overlap between the most reducing conditions and periods of redox instability, we hypothesize that major Baltic inflows, as is observed today, lead to short-term instability while simultaneously

supporting longer-term Baltic anoxia by strengthening the halocline. Ultimately, our results indicate that periods more reducing than the modern Baltic Sea have occurred naturally over the Holocene, but the characteristic dynamic saline inputs have historically prevented the relatively more widespread and stable anoxia observed in other classic restricted basins and will likely continue to do so.

INTRODUCTION

The Baltic Sea is currently the world's largest and most variable low oxygen basin (Diaz and Rosenberg, 2008). Oxygen variation occurs on centennial, decadal, and seasonal timescales (Carstensen and others, 2014; Conley and others, 2009; Zillén and others, 2008), with water column redox ranging from sulfide accumulation (euxinia), in the extreme, to milder reducing conditions characterized by dissolved manganese accumulation (Carstensen and others, 2014; Dellwig and others, 2012). Today's oxygen deficiency is linked, in part, to human-induced nutrient loading together with climate change (Kabel and others, 2012), but the Baltic Sea has experienced known intervals of natural oxygen deficiency since the most recent establishment as a brackish basin ~8.5-8.0 thousand years ago (ka) (Boesen and Postma, 1988; Fehr and others, 2008; Jilbert and others, 2015; Jilbert and Slomp, 2013; Sohlenius and others, 2001; Sternbeck and Sohlenius, 1997; Sternbeck and others, 2000; Zillén and others, 2008). This transition was facilitated by flooding of the shallow Öresund Straits in response to rising global sea-level, which provided an additional entrance and exit for both North Sea saline marine waters and Scandinavian freshwater drainage (Mohrholz and others, 2015; Zillén and others, 2008). Together, the spatiotemporal range of observed redox states and the intermittent ventilation of oxygen-depleted bottom waters distinguish the Baltic Sea from classic modern settings of intense, persistent oxygen deficiency, such as the Black Sea and Cariaco Basin. As the world's largest anthropogenically forced oxygen-depleted basin, the Baltic Sea is more representative of the

patterns of oxygen loss seen, with increasing frequency, in many coastal regions today (Diaz and Rosenberg, 2008). Currently, however, comprehensive geochemical proxy records of the full Holocene history in the Baltic are limited, thus precluding quantitative comparisons of the natural anoxic baseline relative to the current, human-impacted anoxic conditions.

The most temporally extensive Baltic sedimentary records to-date were recovered from Landsort Deep during the Integrated Ocean Drilling Program (IODP) Expedition 347 (fig. 1), capturing the transition from the glacio-lacustrine laminated clay sediments of the Baltic Ice Lake to the present laminated organic-rich Baltic Sea (Andrén and others, 2015a). The Deep's distance from the sill (fig. 1) and a water depth of 459 m (the deepest Baltic sub-basin) prime it to respond relatively intensely to larger scale changes in overall long-term Baltic redox conditions (Carstensen and others, 2014). A detailed reconstruction of Holocene redox transitions and a comparison of the degree (euxinic > ferruginous > manganeous > oxygenated) and frequency (semi-permanent > oscillatory > seasonal) of reducing conditions relative to those observed today would be a key step toward unraveling the processes that regulate Baltic oxygen depletion. Herein, we employ a series of geochemical proxies that are progressively sensitive to specific redox regimes — manganese, iron, and molybdenum — to reconstruct a high-resolution history of redox transitions in the Landsort Deep.

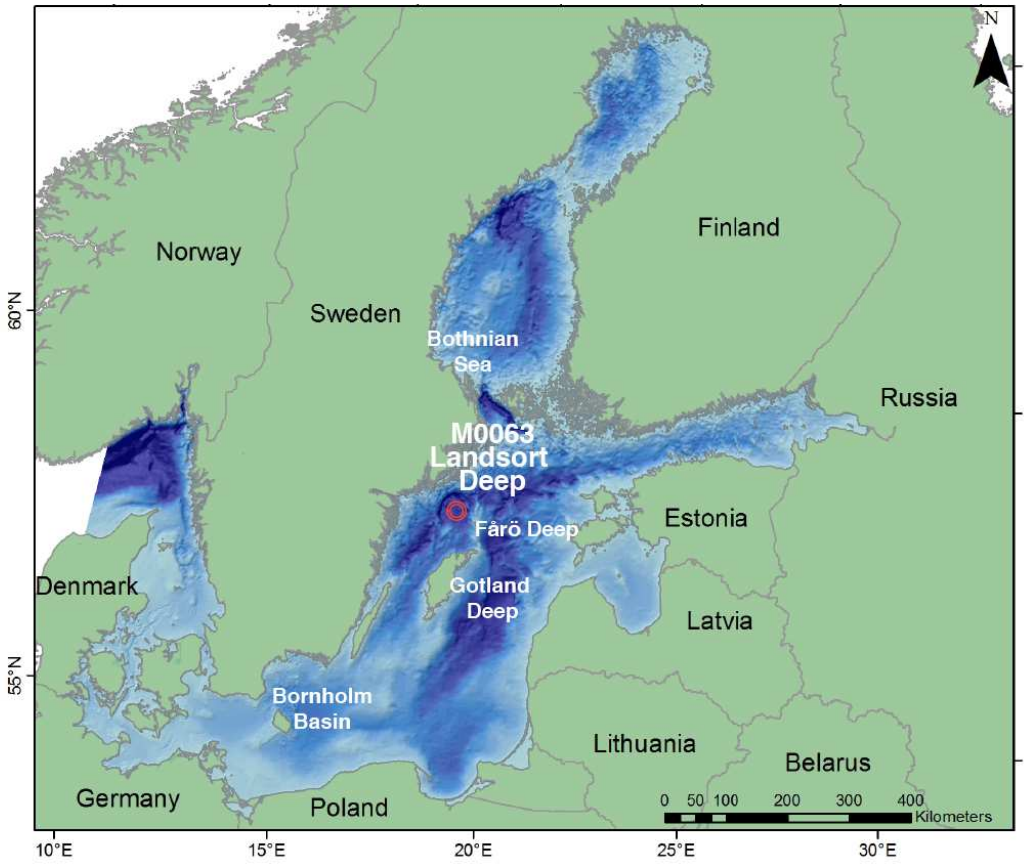

Figure 1. Baltic Sea map showing IODP Expedition 347 site M0063, or Landsort Deep, the focus of this study.

BACKGROUND

Baltic Basin

The Baltic Basin has experienced dynamic physical and chemical oceanographic conditions since the Late Weichselian deglaciation. Following the last glacial maximum about 22 ka, the Baltic ice lobe, which extended over the Öresund Strait into Denmark and covered the Baltic Sea since 55 ka, began retreating north (Andrén and others, 2011). The freshwater Baltic Ice Lake formed at ~16 ka as glacial melt water from the retreating ice sheet filled the Baltic basin. At the same time, ice blockage and isostatic rebound from ice retreat across the Öresund Strait severed any connection to the North Sea (Andrén and others, 2011; Björck, 2008; Houmark□Nielsen and Henrik Kjær, 2003). Around 11.7 ka (Walker and others, 2009), the dam

was breached and the Baltic Ice Lake drained into the North Sea, with estimates for the drop in lake level reaching 25 m over a period of as little as 1-2 years (Björck and others, 1996; Jakobsson and others, 2007). The resulting Yoldia Sea formed a brief and weak connection to the North Sea perhaps for only 350 years (Andrén and others, 2007; Andrén and Sohlenius, 1995; Wastegård and others, 1995). Then, isostatic rebound again dammed the Baltic Basin from the open ocean by 10.7 ka, forming the Ancylus Lake (Andrén and others, 2011). Beginning at 9.8 ka (Andrén and others, 2000a; Andrén and others, 2000b; Andrén and others, 2011; Berglund and others, 2005), eustatic sea level rise from the melting Antarctic and Laurentide ice sheets (Lambeck and Chappell, 2001) gradually flooded the Danish straights. Later, at 8.5-8.0 ka, the Öresund Strait flooded, establishing the brackish Littorina Sea stage, which lasted until 3.0 ka (Björck and others, 2008). The following 1.5 ka, or Post-Littorina stage, was characterized by a declining salinity and onset of the modern silled Baltic system (Andrén and others, 2000a; Sohlenius and others, 1996; Sohlenius and Westman, 1998). Today, saline waters from the North Sea enter and exit the basin through the narrow and shallow Danish straights, with a present mean water depth of ~20 and 11 meters in the Great Belt and Öresund Strait, respectively (Mohrholz and others, 2015).

Three main periods of Holocene low oxygen conditions are inferred from the presence of laminated sediments at ca. 8.0-4.0 ka, 2.0-0.8 ka, and over the last 200 years (Zillén and others, 2008). These periods correspond roughly with the Holocene Thermal Maximum (HTM; ~9.0-5.0 ka ago), the Medieval Climate Anomaly (MCA; ~1.2-0.8 ka), and the modern historical period (Zillén and others, 2008) — with past anoxia linked to salinity changes and varying freshwater inputs into the basin during the HTM (Conley and others, 2009; Gustafsson and Westman, 2002; Middelburg, 1991) and warmer temperatures associated with the MCA (Kabel and others, 2012). Unlike the first two intervals of oxygen depletion, the most recent period is clearly attributable to

human activities in the region in combination with a warmer climate (Carstensen and others, 2014; Kabel and others, 2012). Increased nutrient discharge from expanding agriculture and industrialization in response to increased population and the industrial revolution amplified eutrophication and resulted in the expansion of oxygen-depleted bottom waters. There are sediment laminations and redox sensitive trace metal enrichments in sediments beginning roughly with the onset of the 19th century (Zillén and others, 2008), and direct water column measurements record oxygen depletion near the beginning of the 20th century (Carstensen and others, 2014). Studies suggest that the onset of reducing conditions occurred more rapidly for the current anoxic era relative to those of the past (Jilbert and Slomp, 2013), which was followed by a tenfold increase in the area of reducing bottom waters over the last century (Carstensen and others, 2014).

Today, these is a lateral salinity gradient from south to north, with surface salinity near 8-10 PSU in the southern Baltic and 3-5 PSU to the north in the Gulf of Finland (Matthäus, 2006), and a vertical gradient of ~4-5 PSU in the Baltic proper. Circulation of seawater in and out of the Baltic occurs as a gyre trending counterclockwise through the basin (Döös and others, 2004). In the Landsort Deep, the focus of this study, the resulting halocline is at ~80 m water depth (Dellwig and others, 2012). Sporadic but substantial incursions of marine water from the North Sea, termed major Baltic inflows (MBIs), are barotropic events driven by special conditions of large-scale atmospheric circulation over the North Atlantic (Mohrholz and others, 2015). These MBIs drive bottom-water oxygenation events, providing oxygen-rich and saline North Sea waters to formerly anoxic waters of the Baltic deeps (Carstensen and others, 2014). At the same time, introduction of these saline bottom waters maintains long-term Baltic anoxia by strengthening the halocline (Carstensen and others, 2014). The average residence time of Baltic water today is ~30 years (Döös and others, 2004; Stigebrandt and Gustafsson, 2003), but this estimate varies with

distance from the sill (Carstensen and others, 2014). Today, Landsort Deep is a euxinic basin with dissolved sulfide concentrations of <13.5 μM (Dellwig and others, 2012; Nägler and others, 2011), and MBIs occur on decadal timescales (Carstensen and others, 2014). The latest MBI occurred in late 2014 and was the third strongest since 1880 (Mohrholz and others, 2015).

Geochemical Techniques

Iron proxies — The amount of 'highly reactive' mineral-bound Fe (Fe_{HR}) in sediments, defined as being reactive with hydrogen sulfide on short diagenetic time scales, relative to the amount of total Fe (Fe_T) can be used to identify anoxic conditions in modern and ancient water columns (Raiswell and Canfield, 1998). Furthermore, the extent to which the Fe_{HR} has been sulfidized to form pyrite (Fe_{py}) allows us to distinguish between ferruginous and euxinic conditions (Canfield and others, 1992; Poulton and Canfield, 2005; Raiswell and Canfield, 1998). Fe_{HR} is typically defined as the sum of Fe bound in amorphous and crystalline Fe(oxyhydr)oxides, siderite, Fe monosulfides, and pyrite. Under anoxic conditions, an enhanced input of Fe_{HR} can be decoupled from the typical detrital input, leading to ratios that exceed the upper detrital limit recognized as 0.38 (Raiswell and Canfield, 1998) and Fe_T/Al ratios beyond the detrital baseline of ~0.4-0.6 (Lyons and Severmann, 2006). If dissolved sulfide is persistently available in the water column, syngenetic iron sulfide typically leads to Fe_{py}/Fe_{HR} ratios of greater than 0.8 (Canfield and others, 1996; Poulton and Canfield, 2011). From these observations, the combination of Fe_{HR}/Fe_T >0.38, Fe_T/Al >0.4-0.6, and Fe_{py}/Fe_{HR} >0.8 is commonly used to infer euxinic conditions, and this approach has proven utility throughout the geologic record (Poulton and Canfield, 2011). Though not yet observed in modern marine settings, indications of anoxia in the water column combined with Fe_{py}/Fe_{HR} ratios of <0.8 suggest that availability of water column sulfide is limiting pyrite formation, thus suggesting iron-rich or ferruginous conditions (Canfield and others, 2008; Poulton and Canfield, 2011).

Molybdenum and manganese proxies — Molybdenum is the most abundant transition metal in the modern ocean with a concentration of ~104 nM (Miller and others, 2011); however, due to its brackish salinity, concentrations in the Baltic Sea are closer to 20 nM (Neubert and others, 2008; Noordmann and others, 2014). The primary Mo species under oxic conditions is molybdate (MoO_4^{2-}), which has an affinity for adsorption to Mn and Fe oxides — the main pathway of Mo deposition to sediments in the modern ocean (Barling and Anbar, 2004). However, under sulfide-rich conditions, MoO_4^{2-} is converted to particle reactive thiomolybdates ($MoO_{4-x}S_x^{2-}$) (Erickson and Helz, 2000) and reactive Mo-polysulfide species (Dahl and others, 2013) and is efficiently buried — frequently in association with organic matter (Algeo and Lyons, 2006). In euxinic water columns with >100 μM persistent total dissolved sulfide accumulation, high sedimentary Mo enrichments of >25 ppm and often >100 ppm point uniquely to stably euxinic conditions (Scott and Lyons, 2012). Enrichments at the low end of this range can occur when connection to the open ocean is restricted, as in the modern Black Sea, and uptake and burial can be nearly quantitative (Erickson and Helz, 2000). Comparatively low Mo concentrations (<25 ppm), but above average crustal values (~2 ppm), typically reflect burial coupled to Mn/Fe oxides and are diagnostic of a non-euxinic water column (Scott and Lyons, 2012). Furthermore, sediments underlying water columns with high and stable water column sulfide concentrations can record the Mo isotope composition of contemporaneous seawater, which today is ~2.4‰, because these systems experience near-quantitative tetrathiomolybdate formation and consequent Mo uptake and burial (Siebert et al., 2003). This relationship is observed in the modern Black Sea (Neubert and others, 2008).

During conversion of MoO_4^{-2} to tetrathiomolybdate, a large isotope fractionation can be seen among the transient intermediate species (Tossell, 2005), which can be as high as -3.1 ‰ (Azrieli-Tal and others, 2014). This effect can result in sedimentary Mo isotope data that are

negatively fractionated beneath waters with unstable euxinia with total dissolved sulfide concentrations of <100 μM (Azrieli-Tal and others, 2014; Neubert and others, 2008). Diagnostic negative Mo isotope fractionations as large as -2.9‰ (Barling and others, 2001; Wasylenki and others, 2008) and -2.2‰ (Goldberg and others, 2009) are also associated with Mo adsorption to Mn and Fe oxides, respectively.

Sampling and Lithological Descriptions

Because details for the coring protocols and lithologic descriptions for IODP Expedition 347 are published elsewhere (Andrén and others, 2015a), we provide only a summary below (stratigraphic column in fig. 2). Relevant intervals for Holes C and E of site M0063, Landsort Deep, were cored using an advanced piston-coring device. The lithology at site M0063 was divided into seven units and multiple subunits. Unit I (Hole C 0-25.9 mbsf) captures the brackish conditions of the Littorina Sea and the Baltic Sea since the most recent connection to the open ocean and is generally organic-rich and black in color. Laminations are present throughout Unit I in all intervals and are particularly prominent from 4.1 to 6.7 mbsf and 17.8 to 25.9 mbsf. Units II (Hole C 25.9-34.24 mbsf) and III (Hole C 34.24-41.5 mbsf) contain Ancylus Lake sediments and are defined by a dark grey color, Liesegang bands (which were avoided during sampling), and a series of basin slumping events. Unit IV (Hole C 41.5-48.62 mbsf) is interpreted, based on the presence of diatoms from 41-43 mbsf relative to their absence in surrounding sediments, as recording a weak brackish phase — most probably the Yoldia Sea. Similar to Units II and III, Unit IV is gray in color with black FeS bands. Units V and VI (Hole C 48.62-92.16 mbsf) are similarly gray to brown in color, but in this case show a distinct pattern of fining-upward rhythmic couplets interpreted to reflect a transition from ice-distal to ice-proximal glacio-lacustrine settings likely within the Baltic Ice Lake and marked by possible slumping events. Unit

VII (92.16-93.30 mbsf) consists of angular, poorly sorted, pebble-sized clasts in a sandy diamicton resulting from deposition as debris flows or subglacial till (Andrén and others, 2015a).

METHODS

Samples from Hole E were collected and sealed in N_2-flushed bags onboard the ship immediately following collection and stored frozen prior to analysis. Cores from Hole C were capped and sealed immediately following retrieval and stored at 4°C prior to sample collection, which occurred 4-5 months later at MARUM in Bremen, Germany. At Bremen, samples were collected within a few hours of core splitting and immediately sealed in N_2 flushed bags and stored frozen prior to analyses, minimizing oxidation of redox sensitive Fe minerals important for this study. Sediment analyses took place at the University of California-Riverside and Yale University. Fresh material was used exclusively for each analysis described below; sediments showing signs of oxidation (graying or browning from the formerly black color of iron monosulfides) were scraped away.

We used classic methods for extraction of iron monosulfide or acid volatile sulfide (AVS) (Berner and others, 1979; Chanton and Martens, 1985; Hurtgen and others, 1999; Lyons, 1997; Morse and Cornwell, 1987) and chromium reducible sulfur (CRS) (Canfield et al., 1987), in each case using a split of freshly thawed sample. Concentrations of both CRS and AVS were measured via the methylene blue method using a spectrophotometer at wavelength of 660 nm (Cline, 1969). Assuming negligible concentrations of [S^0], pyritic sulfur was determined by subtracting the AVS from CRS. In a few samples, likely due to heterogeneities and incomplete mixing, AVS concentrations slightly exceed those determined for CRS from the same sample. In such cases, pyritic sulfur was recorded as zero, though we acknowledge that this is unlikely to be the case. Iron present as AVS and CRS was calculated from the measured S concentrations using

the stoichiometries FeS and FeS_2, respectively. These calculated Fe contents are represented throughout the text as Fe_{AVS} and Fe_{py}.

To further characterize the Fe pools present, a modified chemical extraction method was used: $MgCl_2$, ascorbate (Fe_{asc}), dithionite (Fe_{dith}), oxalate (Fe_{ox}) and Na-acetate (Fe_{NaAc}) representing sorbed Fe, labile Fe oxides, crystalline Fe oxides, magnetite, and Fe carbonates, respectively (Ferdelman, 1988; Kostka and Luther, 1994; Poulton and Canfield, 2005; Raiswell and others, 1994; Raiswell and others, 2010). In each case, the chemical reagents were deoxygenated with N_2 for >15 minutes prior to addition to the sample, and the headspace of each centrifuge tube was replaced with N_2 prior to shaking. Only fresh and wet — not dried powdered sediment (Raiswell and others, 1994; Raiswell and others, 2010) — was used, and sample exposure time to the atmosphere was limited to minutes during initial weighing and subsequent reagent additions. Powdering sediment samples has been shown previously to increase the Fe_{dith} extractable fraction explicitly, likely due to the increase in surface area (Raiswell and others, 1994). For our purposes, this step would artificially inflate the Fe_{dith} fraction and likely other oxide fractions relative to that naturally available for reaction with dissolved sulfide to form iron sulfides. Subsamples for individual analyses were carefully homogenized, but the bulk sample was kept heterogeneous in order to avoid mixing of oxidized and un-oxidized portions of the sample.

Details for the sequential Fe chemical extraction scheme follow: (1) ascorbate at pH 7.5 for 24 hours, (2) dithionite at pH 4.8 for 2 hours, and (3) oxalate at pH of 3.2 for 6 hours. Furthermore, a fresh sediment sample was used for two separate extractions: (1) $MgCl_2$ at pH 7.05 for 24 hours and (2) Na-acetate extraction at pH 4.5 for 24 hours (Poulton and Canfield, 2005). All Fe extracts were quantified via an Agilent 7500c quadrupole inductively coupled plasma-mass spectrometer (ICP-MS) upon dilution with 0.24 M nitric acid. An initial survey of

all samples collected onboard the ship from Hole E (thus minimizing the likelihood of oxidation) revealed that concentrations for $MgCl_2$-extracted Fe were all below the detection limit; this step was omitted from subsequent extraction series. Separate sub-sample duplicates assessed for precision revealed relative whole analysis standard deviations in most cases <0.01 wt.%, but in a few cases <0.1 wt.%; we point out, however, that heterogeneities are expected, as bulk samples were not homogenized prior to taking a sub-sample for the sequential Fe-extraction procedure.

A separate aliquot of fresh, wet sample was removed at the same time as the split for the Fe sequential extraction scheme and dried at 60°C for the determination of water content. Iron concentration data are reported on dry sediment basis. Due to the low salinity, dry sediment weight was not salt corrected. This dried sediment split was then homogenized and used for measurements of each total carbon, total inorganic carbon (TIC), and a total acid digest for major and trace metal analyses. Total carbon was determined using an Eltra CS-500 carbon-sulfur analyzer. Total inorganic carbon determinations were made measuring CO_2 concentrations from carbon liberated during an addition of 2.5 N HCl to the sample. Total organic carbon (TOC) was determined by difference of the total carbon and total inorganic carbon. The geostandard AR4007 was analyzed routinely, with values within reported ranges and deviating by <5%.

A multi-acid digest procedure was used for determination of bulk sediment metal concentrations. Dried samples were ashed at 450-650°C and digested using trace metal grade HF:HNO_3:HCl, with the metals solubilized at the end in 0.24 M HNO_3 acid. Total digests were measured for major elements (Al, Fe, Mn) and trace elements (Mo) via an Agilent 7500c quadrupole ICP-MS using a multi-element standard solution in a 0.24 M HNO_3 matrix. Total digest geostandards (NIST 2702, USGS SCO-1, and USGS SGR-1) were routinely compared for accuracy, with all elements analyzed deviating by <5% from the reported values. All values for

Al, Fe, Mn, Mo, Fe_{asc}, Fe_{dith}, Fe_{ox}, Fe_{NaAc}, Fe_{AVS}, Fe_{CRS}, TOC, and TIC can be found in Supplementary Table 1.

Molybdenum isotope measurements were performed at the Metal Geochemistry Center at Yale University, New Haven, Connecticut. The resulting 0.24 M HNO_3 solution from total digest was evaporated and re-constituted in 7 M HCl. An aliquot of the acid split was doped with a Mo double spike according to the Mo concentration determined previously via ICP-MS in order to maintain a constant sample-to-spike ratio. This aliquot was also used for chromatographic separation. The ^{97}Mo-^{100}Mo double spike solution was prepared gravimetrically from Oak Ridge Laboratory metal powders as previously described (Asael and others, 2013). A two-stage column procedure was applied for Mo purification: the sample was run through an anion resin (AG-MP-1M) to separate Mo and Fe from the matrix followed by purification through a cation resin (AG50W-X8) to separate Mo from any remaining Fe. Molybdenum isotope compositions are reported using the δ notation, where:

$$\delta^{98}\text{Mo}\ (‰) = 1000\cdot[(^{98}\text{Mo}/^{95}\text{Mo})_{sample}/(^{98}\text{Mo}/^{95}\text{Mo})_{NIST}*0.99975 - 1]\ . \qquad \text{(equation 1)}$$

δ^{98}Mo is calculated relative to NIST 3134 (Lot 130418) with a value of -0.25 ‰ (Nägler and others, 2014). A calibration of the NIST standard relative to Rochester (Lot 862309E) gave:

$$\delta^{98}\text{Mo}_{ROCH} = \delta^{98}\text{Mo}_{\ NIST3137} - 0.32 \pm 0.12\ ‰. \qquad \text{(equation 2)}$$

For each sample, the target Mo concentration was 200 ppb during MC-ICP-MS analysis. For nearly all samples, the 1σ was <0.05 ‰. Duplicates (n=5) of reference standard NOD-1 yielded an average δ^{98}Mo value of -0.29 ‰ and 1σ of 0.04 ‰, similar to previously reported values (Asael and others, 2013). Values for Mo isotope measurements and associated error can be

found in Supplementary Table 2. We analyzed duplicates or more from 48 individual samples, resulting in $1\sigma < 0.11$ ‰ and mostly <0.06 ‰.

RESULTS

Carbon and Sulfur

Starting near ~26.75 mbsf, TOC concentrations increase up section from <0.5 wt.% to >2 wt.% (fig. 2a). This switch in TOC occurs in concert with an increase in diatom abundance inferred to record the transition from the Ancylus Lake into the Littorina Sea (Andrén and others, 2015a). There are two peaks in TOC above ~26.75 mbsf that indicate two sapropels at ~19.5-26.75 mbsf and ~4.3-7.3 mbsf, with maxima between 7-8 wt.%. Peaks in TIC abundance also occur within these sapropels. A similar trend to that of TOC is observed for total inorganic sulfur (TIS), which represents the sum of sulfur from the AVS and CRS extractions (fig. 2b). C/S ratios were calculated using the ratio of TOC to TIS (fig. 2c).

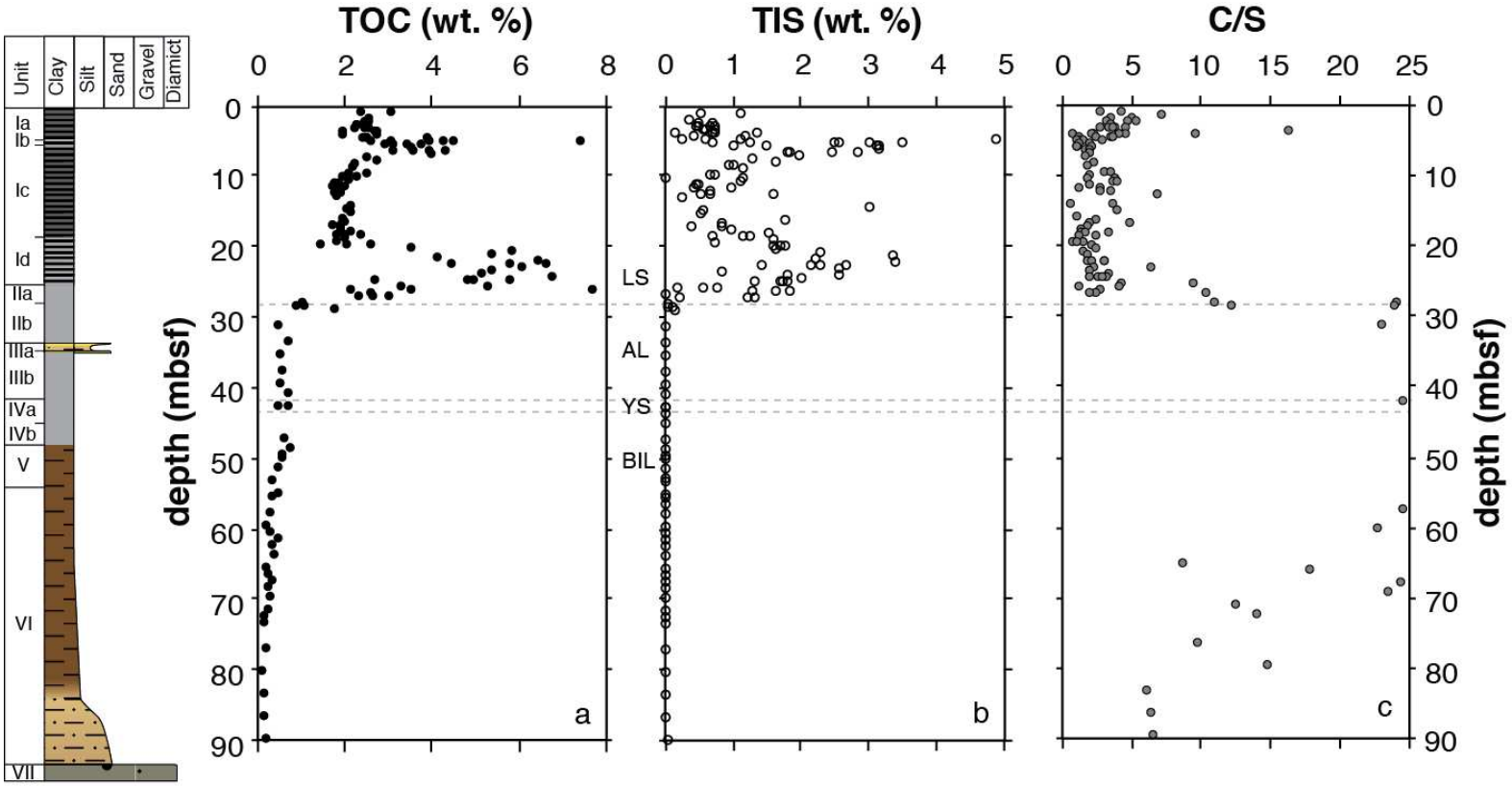

Figure 2. M0063 down core profiles of a.) total organic carbon (TOC), b.) total inorganic sulfur (TIS), which is the sum of CRS and AVS, and c.) total organic carbon-to-inorganic sulfur (C/S) ratios. C/S ratios below 30 mbsf often exceed 25. The dashed lines separate the Baltic Ice Lake (BIL), Yoldia Sea (YS), Ancylus Lake (AL), and Baltic Sea, as inferred from the sedimentological descriptions in the M0063 summary (Andrén and others, 2015a). Sediment depth is displayed as meters below sea floor (mbsf). Stratigraphic column is adapted from Andrén and others, (2015), and stresses the laminations and color changes described in the *Samples and Lithologic Descriptions* section of this manuscript.

Iron and Manganese

As products of glacial runoff in an oxic setting, Fe_T/Al and Fe_{HR}/Fe_T from the Baltic glacial lake clays below 26.75 mbsf provide an integrated detrital sediment record for the catchment area (Goldschmidt, 1933) (fig. 3a). Though Baltic detrial Fe_T/Al values have previously been reported as 0.6-0.65 (Fehr and others, 2008), to be conservative we will interpret anoxia from Fe_T/Al ratios above the highest value from the ice lake sediments, which is 0.75 (vertical dashed line fig. 3a). Importantly, a baseline of 0.65 is consistent with most of our samples and if applied would have little impact on our final interpretations. For Fe_{HR}/Fe_T ratios (Fe_{HR} defined here as the sum of Fe_{AVS}, Fe_{CRS}, Fe_{ox}, Fe_{NaAc}, Fe_{asc}, and Fe_{dith}), we identify the presence of past water column anoxia using a threshold value of 0.38 as previously determined (Raiswell and Canfield, 1998) and commonly applied in the literature (Poulton and Canfield, 2011) — and consistent with the Landsort Deep lacustrine sediments below 26.75 mbsf.

Starting near the lacustrine-brackish boundary at ~26.75 mbsf and moving up section, there is a distinct increase in Fe_T/Al and Fe_{HR}/Fe_T ratios above the detrital background, with large peaks in close association with the sapropel units and some outside of sapropel deposition, and in association with peaks in Mo concentration (fig. 3; fig. 4; fig. 5a,b). The Fe_T/Al values approach 1 in the lower sapropel and 1.4 in the upper sapropel, both of which are well above the detrital baseline. Between 7.4-3.4 mbsf, there are cases where Fe_{HR} exceeds Fe_T, in which case Fe_{HR}/Fe_T is plotted as 1. This artifact may reflect sample heterogeneity, as sample splits for individual analyses come from unhomogenized bulk samples.

For intervals with elevated Fe_{HR}/Fe_T and Fe_T/Al, we use $(Fe_{py}+Fe_{AVS})/Fe_{HR}$ values of >0.6 as the threshold for delineating past euxinia. Supporting this choice, a crossplot of $(Fe_{py}+Fe_{AVS})/Fe_{HR}$ versus Mo (not shown) indicates that Mo concentrations >25 ppm, which are

typical of euxinic deposition (Scott and Lyons, 2012), are nearly exclusively associated with $(Fe_{py}+Fe_{AVS})/Fe_{HR}$ values >0.6. Alternatively, Mo concentrations >10 ppm could indicate short-lived/intermittent or weakly euxinic episodes, which may be supported by coupled increases in Mo >10 ppm in association with elevated Fe_{HR}/Fe_T and Fe_T/Al, which are noted in figure 3d. However, our approach of a euxinic/ferruginous $(Fe_{py}+Fe_{AVS})/Fe_{HR}$ threshold of ~0.6 is conservative in that it minimizes the likelihood of false ferruginous interpretations. We also note that the Fe_{asc} and Fe_{dith} data from the samples collected onshore indicate that some post-drilling oxidation of Fe-sulfides has occurred, and thus Fe_{asc} and Fe_{dith} are not included in the Fe_{HR} pool for calculations of $(Fe_{py}+Fe_{AVS})/Fe_{HR}$ for the onshore sample set. This omission also minimizes the likelihood of spurious ferruginous signals. However, comparison with offshore $(Fe_{py}+F_{AVS})/Fe_{HR}$ ratios that include Fe_{dith} and Fe_{asc} suggests little difference (green vs black points fig. 3c).

In the brackish sediments, Mn enrichments also mirror the sapropels, with values of up to 15 wt.% in the upper sapropel and near 7 wt.% in the lower sapropel (Figure 5c). These concentrations are four orders of magnitude higher than the estimated global crustal average of 0.085 wt.% (Turekian and Wedepohl, 1961) and up to five orders of magnitude above those observed for the underlying Baltic lacustrine sediments. This comparison indicates that the Baltic Mn enrichments are not a result of detrital input but instead reflect intensive Mn redox cycling persistent throughout brackish deposition.

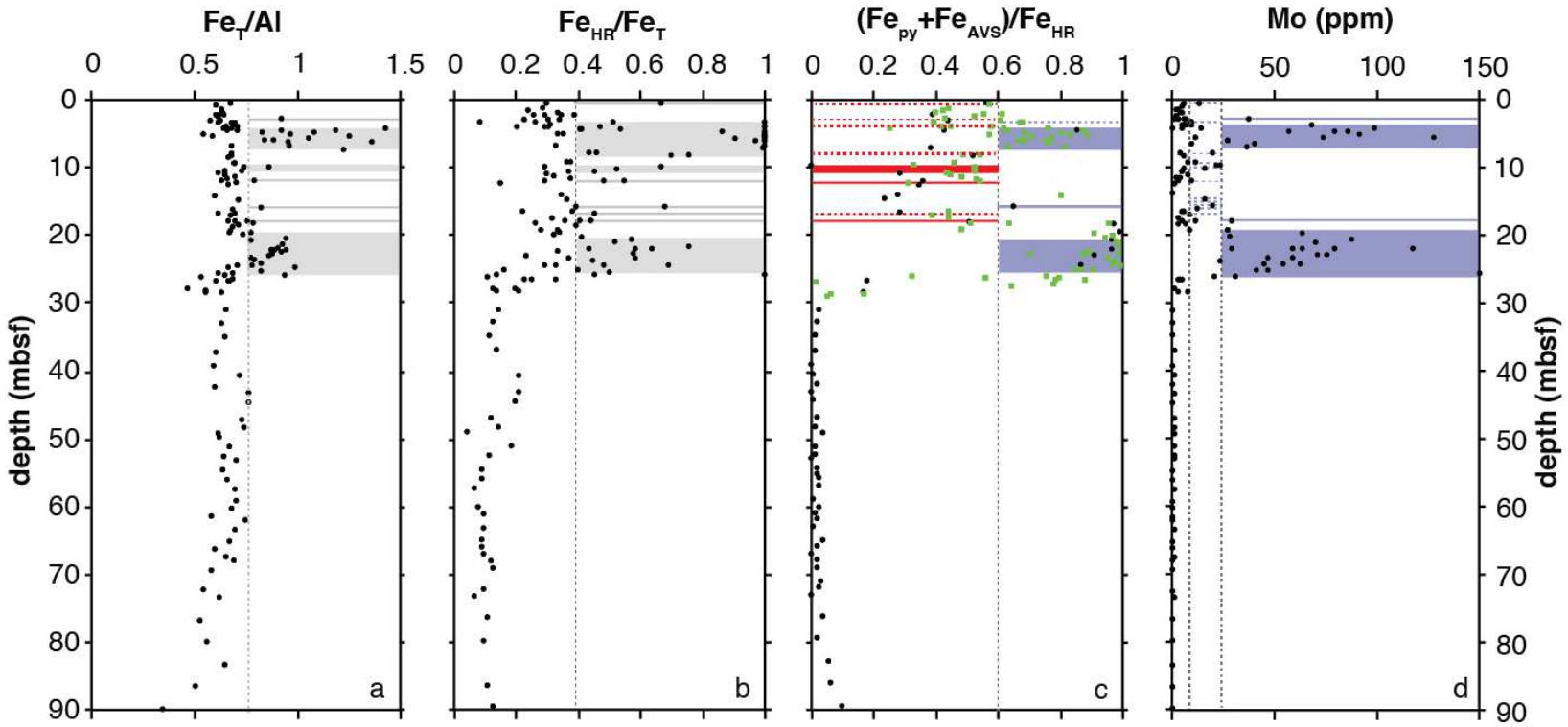

Figure 3. M0063 down core profiles displaying: a.) Total Fe-to-Al ratios (Fe_T/Al), with dashed line representing our locally established Landsort Deep Fe_T/Al detrital baseline of 0.75 determined from the ice lake sediments; b.) 'Highly reactive' Fe-to-total Fe ratios (Fe_{HR}/FeT), with vertical dashed line representing the previously established anoxic baseline of 0.38 (Raiswell and Canfield, 1998); c.) The sum of CRS-derived Fe and AVS-derived Fe-to-'highly reactive' Fe ($(Fe_{py}+Fe_{AVS})/Fe_{HR}$), with vertical dashed line representing the ferruginous-euxinic baseline of 0.6 determined specifically for this study. Green squares indicate samples collected onshore where Fe_{HR} does not include Fe_{dith} and Fe_{asc} due to indications of post-drilling Fe-sulfide oxidation; d.) Mo concentrations. The colored boxes/lines indicate specific water column redox conditions inferred from the data as, anoxic (grey), ferruginous (red), and euxinic (purple). Dashed lines in (c) represent intervals not inferred as anoxic from both Fe_T/Al and Fe_{HR}/Fe_T and dashed lines in (d) represent possible euxinic conditions indicated by 10-25 ppm Mo, which together overlap with each of the increases in Fe_T/Al or Fe_{HR}/Fe_T above detrital baselines.

Molybdenum

Molybdenum concentrations rise above 1 ppm at the transition from lacustrine to brackish sedimentation in the Landsort Deep, reaching values >100 ppm in the intervals associated with sapropel deposition from ~19.5-26.3 mbsf and 4.30-7.34 mbsf (fig. 3d, fig. 4, fig. 5b). For Mo isotopes, we performed 123 individual measurements for 52 samples. Our results show that, although sedimentary Mo is in general a mixture of detrital and authigenic sources, the Mo in the lacustrine interval is mainly of detrital origin as indicated by the Mo concentrations of <1 ppm, which are typical of average continental crust. Therefore, no Mo isotope measurements were performed for the lacustrine sediments. The δ^{98}Mo have a total range of -0.5 to +1.11‰ (fig. 5d). From ~20-26 mbsf, overlapping with the lower sapropel, δ^{98}Mo values are variable within a distinct range of +0.10 to +0.62‰ relative to the remainder of the profile. Starting at 20 mbsf, there is an upward shift to more negative values, with a range of -0.50 to +0.29‰ and one outlier of 1.11‰ at 4.62 mbsf. From ~4.8 to 8 mbsf, overlapping with the upper sapropel, δ^{98}Mo values show a distinctly negative range of -0.50 to -0.11‰.

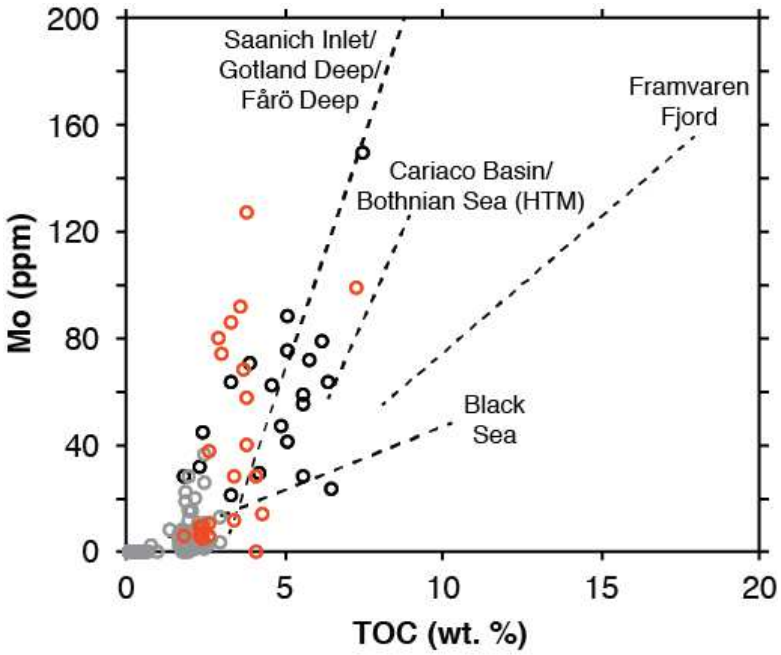

Figure 4. Crossplot of Mo concentration against total organic carbon (TOC). Colors correspond to the upper (red) and lower sapropels (black) and all other intervals (grey). Dashed lines represent Mo vs TOC slopes for other modern and past euxinic basins as determined in previous studies (Algeo and Lyons, 2006; Jilbert and others, 2015; Jilbert and Slomp, 2013). The line for the Bothnian Sea refers specifically to the Holocene Thermal Maximum or HTM (Jilbert and others, 2015). Sapropel intervals correspond to that of figure 2.

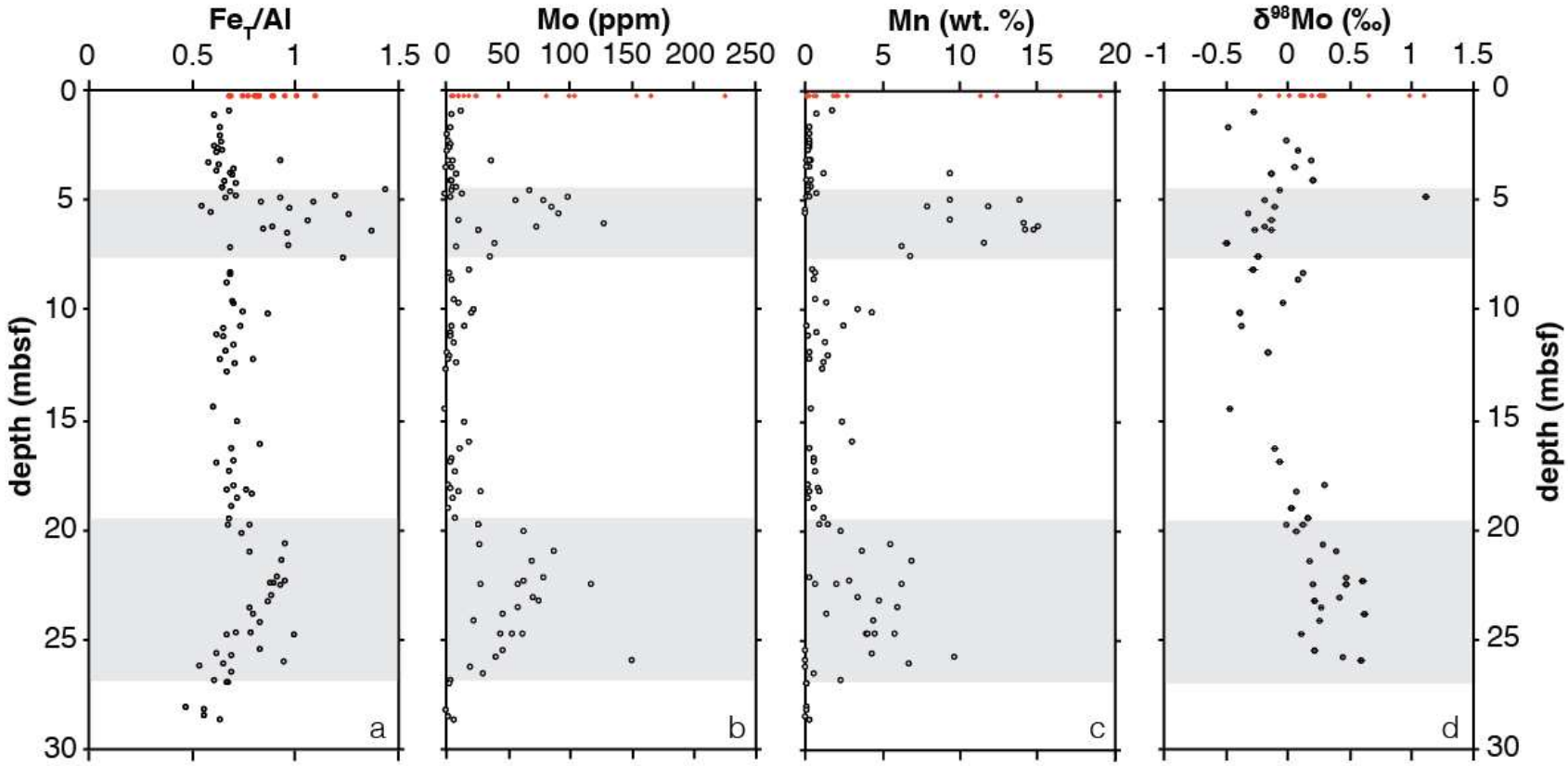

Figure 5. M0063 down core profiles showing the upper 30 mbsf for a.) Fe_T/Al from figure 3a; b.) Mo concentrations from figure 3d c.) Mn concentrations; d.) Mo isotope values ($\delta^{98}Mo$). Error bars are shown in part d, but are typically smaller than the data points. Red dots at the top of each panel show data from Noordman et al. (2015) for the upper 15 cm of Landsort Deep, representing the modern-recent euxinic period not captured in this study. The shaded grey areas indicate the sapropels from 26.75 to 19.5, and 7.3 to 4.3 mbsf, as indicated from TOC in figure 2.

Pore Waters

Interstitial waters were analyzed as part of the IODP Expedition 347 and are described in detail in the expedition report (Andrén and others, 2015a). We use these interstitial water data to complement our corresponding sedimentary data and for the calculation of saturation indices, particularly for rhodochrosite. Briefly, pore water Mn concentrations increase moving upward in the profile to a peak value of ~1.5 mM (fig. 6b). Pore water alkalinity shows a broad peak in association with the brackish sediments, with a peak value of ~58 meq/L at ~14.5 mbsf (fig. 6b).

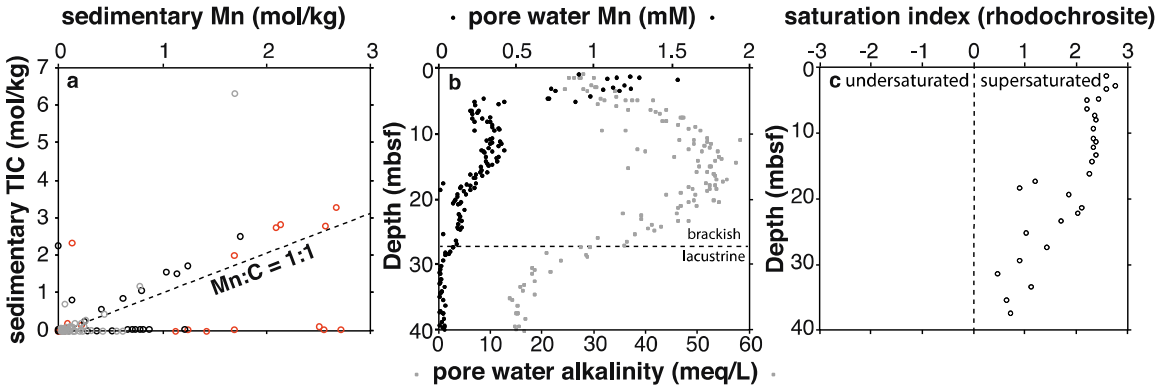

Figure 6. a.) Crossplot of total inorganic carbon (TIC) and Mn concentrations. As in Figure 4, the colors correspond the lower sapropel (black), upper sapropel (red), and all other intervals (grey), with sapropel intervals corresponding to that of figure 2a. The dashed line represents the relationship expected for rhodochrosite assuming a chemical formula of $MnCO_3$. b.) Pore water Mn (black circles) and alkalinity (grey squares) concentrations for the upper 40 mbsf from all holes at site M0063 (Andrén and others, 2015b). Dashed line represents the lacustrine-brackish boundary, as depicted in figure 2 and described in the text. c.) Saturation indices for rhodochrosite calculated using PHREEQC (Parkhurst and Appelo, 1999) and using pore water data from Hole C at site M0063 (Andrén and others, 2015b).

DISCUSSION

Salinity Variations

The diatom and sedimentological records from Landsort Deep, as described in detail in the IODP report for Site M0063 of Expedition 347 (Andrén and others, 2015a), indicate a fresh-

to-weakly brackish transition at 43 mbsf (Baltic Ice Lake-to-Yoldia Sea), a switch from brackish to fresh conditions at 41 mbsf (Yoldia Sea-to-Ancylus Lake), and a fresh-to-brackish shift near 26.75 mbsf (Ancylus Lake to Littorina Sea). Ratios of total organic carbon to total inorganic sulfur (C/S) can provide an independent indicator of salinity transitions because sulfate is typically the main factor limiting pyrite formation in freshwater lacustrine settings (Berner and Raiswell, 1983). This assumption holds true only for sediments with TOC values of >1 wt.%. At lower TOC values, organic matter may be the limiting factor, thus complicating the distinction between marine and non-marine deposition (Berner and Raiswell, 1983). Our results show a switch to TOC values of >1 wt.% at ~26.75 mbsf; below this concentration detailed fluctuations in C/S cannot be used to track salinity fluctuations (fig. 2). A general change from C/S ratios of >10 to values <5 at ~26.75 mbsf, however, is consistent with sedimentological and paleontological evidence for a switch from lacustrine to brackish deposition — marking a transition to a high TOC sapropel. In general, C/S ratios for sediments above 26.75 mbsf are <5 and specifically near the 2.8±0.8 value typical for normal (oxic) marine deposition (Berner, 1982). The shift in C/S is interpreted to capture the transition from the Ancylus Lake to Littorina Sea, occurring at ~8.5 kyrs B.P. (Andrén and others, 2011). The Yoldia Sea record of brackish deposition (<350 years) at ~41-43 mbsf, as inferred from brackish diatom abundance (Andrén and others, 2015a), is not seen in our C-S geochemical proxy — reflecting poor sample resolution (n=2) and/or limiting sulfate and organic matter.

Anoxic Indicators

In this discussion and those that follow, we explore the use of geochemical proxies as tracers of past oxygen-deficiency and, in that discussion, open the door to the possibility that multiple geochemical tracers might collectively speak more convincingly to temporal stability of such conditions and the related controlling factors.

Iron and molybdenum proxies — The persistence of laminations indicates likely sustained water column anoxia throughout deposition of the Baltic brackish phase. Furthermore, Fe_T/Al and Fe_{HR}/Fe_T ratios provide evidence for anoxic deposition for the two sapropels, as well as multiple, likely short-lived, redox oscillations outside of the sapropel deposition (fig. 3, 5). Adding to this framework, $(Fe_{py}+Fe_{AVS})/Fe_{HR}$ and Mo concentrations suggest euxinia during sapropel deposition and multiple euxinic and potential ferruginous candidates in the surrounding brackish intervals (fig. 3, 5). The combination of Fe_{HR}/Fe_T >0.38 and Mo concentrations approaching or exceeding 100 ppm constrains euxinia for the two sapropels as being the predominant condition and thus likely occurring beyond seasonal timescales (Raiswell and Canfield, 1998; Scott and Lyons, 2012). Two distinct sapropels with inferred anoxic water column conditions have been recognized previously in the Landsort Deep past (Lepland and Stevens, 1998), and past water column euxinia has more specifically been inferred for periods throughout the Holocene at other Baltic sub-basins (Boesen and Postma, 1988; Fehr and others, 2008; Jilbert and Slomp, 2013; Lenz and others, 2015; Sohlenius and others, 2001; Sternbeck and Sohlenius, 1997; Sternbeck and others, 2000). These intervals overlap roughly with the Holocene Thermal Maximum (HTM) from ~9-5 kyrs B.P. and the Medieval Climate Anomaly (MCA) from ca. 1.25-0.80 kyrs. B.P. (Zillén and others, 2008). The presence of laminations in intervals lacking geochemical indications of anoxia likely reflect the persistence of local water column redox conditions not reducing enough to support dissolved iron or sulfide accumulation — but instead low oxygen or even anoxia that could not support benthic habitation (Dashtgard and MacEachern, 2016). Alternatively, ferruginous conditions may have prevailed during these periods, which have been shown in the modern Peruvian oxygen minimum zone to not support enhanced 'highly reactive' iron deposition in the absence of a ferruginous-oxic transition (Scholz and others, 2014).

Crossplots of Mo versus TOC can speak to the relative basin-wide extent of euxinic seafloor under different redox regimes in the Baltic by revealing the impact of the water column Mo reservoir size on local sedimentary Mo enrichments (Algeo and Lyons, 2006). The relationship of Mo versus TOC in our samples from the two Landsort Deep sapropels are similar, and both data sets are consistent with those from other euxinic sub-basins of the Baltic Proper — past and present (fig. 4) (Jilbert and Slomp, 2013). Furthermore, our results from Landsort Deep show a Mo-TOC relationship similar to that seen in the intermittently restricted Saanich Inlet, and our high Mo concentrations and Mo-TOC are easily distinguished from those of more restricted modern euxinic basins (fig. 4) (Algeo and Lyons, 2006). During exposure to sulfide, dissolved water column molybdate is progressively converted to tetrathiomolybdate (Erickson and Helz, 2000). Near-complete tetrathiomolybdate formation from molybdate occurs when water column total dissolved sulfide is stable at concentrations >100 μM (Erickson and Helz, 2000). Subsequent efficient scavenging under restricted conditions can draw down the water column Mo reservoir when renewal rates are low relative to burial. Such efficient Mo uptake can result in markedly low sedimentary Mo concentrations despite elevated TOC and independent indications for euxinia based on Fe geochemistry (Algeo and Lyons, 2006). Figure 4 shows examples of modern basins with progressively more restricted conditions with respect to Mo: Baltic Sea, Saanich Inlet < Cariaco Basin < Framvaren Fjord < Black Sea (Algeo and Lyons, 2006; Jilbert and Slomp, 2013). Intriguingly, a different Mo-TOC trend than that of the Holocene Baltic Proper is observed in the more northern Bothnian Sea (fig. 4) — specifically in association with the HTM (Jilbert and others, 2015). During this time, Bothnian sediments contain Mo enrichments indicative of euxinia and a Mo-TOC relationship more similar to the modern Cariaco Basin. Considering that the Bothnian Sea is oxic today, local evidence for stable euxinia extended beyond the Baltic Proper suggests the likelihood of more expansive euxinia in the Baltic generally during the HTM

relative to today. Ultimately, however, relatively high Mo/TOC ratios in the Landsort Deep and the Baltic Proper generally indicate a high rate of Mo supply compared to the burial sink throughout the Holocene regardless of relative changes in the extent of seafloor euxinia in the Baltic generally — consistent with strong seawater exchange and a relatively small fraction of seafloor characterized by euxinia (Jilbert and others, 2015; Jilbert and Slomp, 2013).

Interestingly, the intervals with clearly elevated Fe_T/Al and Fe_{HR}/Fe_T ratios have $(Fe_{py}+Fe_{AVS})/Fe_{HR}$ and Mo concentration typical of euxinia but show a range of magnitudes in Fe_T/Al, suggesting controls on Fe deposition in addition to the persistence of euxinic water column conditions. Multiple factors can influence primary differences in Fe_T/Al and Fe_{HR}/Fe_T ratios among or within basins. Importantly, the observed Fe_T/Al peaks of 1.4 and 0.95 within the two Landsort Deep sapropels (fig. 4) are high compared to other modern euxinic basins (Lyons and Severmann, 2006) but are comparable to the modern Landsort Deep sediments with values as high as 1 (Noordmann and others, 2014). The diagnostic Fe enrichments are largely controlled by the rate at which Fe is transported from source regions, such as oxygen-poor sediments and bottom waters that are reducing but not sulfidic, to regions such as the Landsort Deep that are euxinic (for example, Lyons and Severmann, 2006). In these euxinic settings, the 'shuttled' Fe is captured in the water column through syngenetic pyrite formation. If we consider the small area of the Landsort deep relative to the surrounding potential source region, the large source-to-sink ratio is expected to favor high Fe_T/Al and Fe_{HR}/Fe_T ratios in both sapropel intervals (Lenz and others, 2015; Raiswell and Anderson, 2005). In this view, relative to conditions during deposition of the upper sapropel, the lower Fe_T/Al ratios of the lower sapropel may reflect more widespread euxinic conditions in the Landsort Deep (providing a larger Fe sink relative to the source area) or an expansion of sulfidic pore fluids and water columns in the Baltic more generally (thus decreasing the Fe source area to Landsort Deep) — or both. This interpretation is supported by

detailed analyses of Fe_T/Al ratios along shelf-to-basin transects that capture past euxinic regimes at the nearby Gotland Deep. In this case, maximum Fe_T/Al ratios do not correspond to the time of most expansive bottom water euxinia — but instead record the initial onset and expansion of euxinia (Lenz and others, 2015). Together, the Fe_T/Al and Mo-TOC relationship indicate that the extent of euxinia at Landsort Deep and likely the Baltic in general varied between deposition of the two sapropels, but the concentrations and timescales of water column sulfide accumulation euxinia consistently remained below distributions that would have significantly drawn down the Baltic Mo reservoir.

Stability of Reducing Conditions

Given that our Fe_T/Al results suggest potential differences between the past euxinic episodes represented by the sapropels in Landsort Deep, we apply a combination of Mn concentration and Mo isotope data to evaluate the relative stabilities and magnitudes of water-column total dissolved sulfide concentrations as recorded in these two intervals.

Manganese concentrations — Our measured bulk sedimentary Mn concentrations associated with sapropel deposition, up to 7 and 15 wt.%, are extreme in a global context but are comparable to observations in the modern Baltic; Mn concentrations in sediments from the modern Landsort and Gotland Deeps range up to 10-18 wt.% (Lepland and Stevens, 1998; Noordmann and others, 2014; Sternbeck and Sohlenius, 1997) and even as high as 25 wt.% (Lenz and others, 2014). We suggest, as others have for Mn enrichments in modern Landsort Deep sediments (Lenz and others, 2014; Scholz and others, 2013), that the extreme enrichments observed during brackish deposition generally, but for the euxinic sapropels in particular, fingerprint oscillations between oxic and anoxic conditions in a system that was dominantly euxinic (Lepland and Stevens, 1998). As was argued in that past work, we attribute these oscillations to major Baltic inflow (MBIs) events characterized by oxygenated marine waters

from the North Sea. As Mn concentrations are twice as high in the upper sapropel compared to lower, this interpretation would require relatively less stable redox conditions during upper sapropel deposition. MBIs are barotrophic events during which saline and oxygenated water from the North Sea enters the Baltic beneath the halocline (Mohrholz and others, 2015). A record of MBIs over the last century indicates that the area of Baltic seafloor anoxia decreases during such events due to replacement of previously anoxic bottom waters with oxygenated North Sea water, but anoxia resumes soon afterward due to an associated strengthening of the halocline from the input of relatively higher salinity waters from the marine North Sea compared to the brackish Baltic Sea (Carstensen and others, 2014).

Sedimentary Mn enrichments are linked to MBIs through oxidation of dissolved Mn^{2+} within the anoxic Landsort Deep waters and associated deposition in the sediments as oxide mineral phases (Lenz and others, 2014; Lenz and others, 2015; Scholz and others, 2013). During burial, the oxides are re-reduced and accumulate in pore waters as dissolved Mn^{2+} or, in the presence of pore water sulfide or appreciable alkalinity, precipitate as sulfide or carbonate minerals such as hauerite or rhodochrosite (Berner, 1984; Lepland and Stevens, 1998; Sternbeck and Sohlenius, 1997). Indeed, a link is observed in our samples between total inorganic carbon (TIC) and Mn that falls along a slope similar to that for stoichiometric $MnCO_3$ (fig. 6a), suggesting the formation of Mn carbonate is a relevant Mn sink in our sediments. Importantly, however, our interpretation of MBI-associated redox oscillations from the enhanced Mn concentrations generally requires the delivery of Mn oxides to the sediments with subsequent conversion to Mn carbonate in anoxic pore waters rather than direct carbonate precipitation in the water column.

In order to establish that the source for Mn for carbonate precipitation originated from the pore waters rather than the water column, we calculated saturation indices for rhodochrosite using

measured pore water Mn^{2+} and alkalinity profiles from our IODP Expedition 347 sediments from M0063 collected in the Landsort Deep (Andrén and others, 2015a) (fig. 6b,c). The pore waters host intensive dissolved Mn^{2+} enrichments, up to 1.5 mM at the top of the profile (fig. 6b), providing evidence for dissolution of Mn oxides as a source of dissolved Mn^{2+} to the pore fluids. Calculated using PHREEQC (Parkhurst and Appelo, 1999) and the MINTEQ databases, saturation indices indicate that rhodochrosite is supersaturated in pore waters spanning the brackish interval and extending into the lacustrine sediments (fig. 6c). These calculations favor the deposition, burial, dissolution, and diffusion of Mn that was originally associated with oxides but was subsequently reprecipitated in carbonate phases. A diagenetic origin for the Mn carbonate is generally supported by similar calculations from pore waters in modern Landsort Deep sediments (Lenz and others, 2014) and previous work that measured carbon isotope values for Mn carbonate from Landsort Deep (Suess, 1979). These efforts revealed carbonate carbon isotope values as low as -13‰, requiring a mix of seawater and organic matter remineralization as a carbonate source.

Lastly, we point out that the extreme enrichments in Mn, interpreted to represent redox oscillations, are most prominent in association with Fe and Mo indications of the most strongly reducing conditions (fig. 6). This seemingly counterintuitive observation is partially linked to anoxic/euxinic conditions allowing for enhanced water column Mn accumulation. Given the requirement for redox oscillations for enhanced Mn burial, however, we suggest that the frequency/stamina of MBIs is also a major factor. It is well known from observations of the current anoxic period over the last century that, while the MBIs punctuate anoxia, they also provide the input of saline waters from the North Sea to the brackish Baltic. This seawater is essential for maintaining the halocline that facilitates anoxia through stronger vertical stratification (Carstensen et al., 2014). In other words, these MBIs limit the maximum reducing

potential by providing oxygen-rich North Sea waters and simultaneously sustain longer-term anoxia through the introduction of seawater to Baltic bottom waters. As a proof of concept, a prolonged period lacking MBIs from 1982-1993 was marked by a decrease in the strength of Baltic haloclines in individual sub-basins as well as a decrease in the area of low oxygen bottom waters throughout the Baltic Sea, including the Landsort Deep (Carstensen et al., 2014). The frequency of these events also controls the delivery of Mn oxides to the sediments and simultaneously renews molybdate supplies to the water column, consistent with our Mo-TOC relationships suggesting an ample Mo supply to the basin. The role of MBIs as both instigators of short-term redox oscillations and as a requirement for sustained long-term anoxia again separates the Baltic from more stably reducing settings, suggesting that strongly stable euxinia throughout the Baltic is unlikely in the past — and in the future.

Mo isotopes — Our Mo isotope results offer an independent constraint on redox stability, while also providing constraints on the concentrations of water column total dissolved sulfide during sapropel deposition. Our sedimentary Mo isotope data range from -0.50 to +1.11‰, which is highly fractionated from the +2.24 to +2.67‰ values of modern Baltic seawater and similar to the -0.24 to +1.12‰ values seen in Landsort Deep sediments from the modern euxinic era (Nägler and others, 2011; Neubert and others, 2008; Noordmann and others, 2014). Two known processes allow for such large negative δ^{98}Mo fractionations: euxinic conditions with water column total dissolved sulfide concentrations of <100 μM or burial of Mo initially delivered to the sediments through adsorption to Mn and/or Fe oxides. In the case of the sapropels at Landsort Deep — where Mo concentrations and Fe speciation indicate euxinia and the associated highly enriched Mn concentrations indicate likely widespread Mn-oxide burial — both of these possibilities are likely. As such, it is difficult to distinguish between two processes with overlapping fractionation relationships. Regardless, extreme Mn redox cycling relative to other

modern anoxic settings as well as low water column dissolved sulfide concentrations and residence times are both consistent with dynamic redox conditions, such as those characterizing the modern Landsort Deep. This combination is our preferred interpretation for both of the euxinic sapropels and modern Landsort Deep sediments.

First, if water column total dissolved sulfide is <100 μM or only accumulates periodically, thus introducing kinetic challenges to quantitative tetrathiomolybdate formation (Erickson and Helz, 2000), a δ^{98}Mo fractionation during conversion of molybdate to thiomolybdates can be captured in the sediments and can approach extreme fractionations from seawater of up to -3.1‰ (Azrieli-Tal and others, 2014). In contrast, when total dissolved sulfide concentrations are stable at levels >100 μM, as in the modern deep Black Sea, quantitative conversion of molybdate to tetrathiomolybdate occurs (Neubert and others, 2008). At the same time, near-quantitative water column Mo depletion is observed across the chemocline, with the net result that the δ^{98}Mo of the sediments matches the ambient seawater (Arnold and others, 2004; Barling and others, 2001; Neubert and others, 2008). The δ^{98}Mo range of both Landsort Deep euxinic sapropels, but particularly the upper sapropel, approach the most negative δ^{98}Mo value (-0.7‰) predicted from previous efforts modeling of dissolved Mo speciation and isotope fractionations under extreme sulfide limitation (Azrieli-Tal and others, 2014). As such, our data are generally in the range anticipated with water column sulfide limitation inhibiting quantitative tetrathiomolybdate formation (fig. 6d). This conclusion is consistent with observations from the modern Landsort Deep where total dissolved sulfide values are observed below the 100 μM switchpoint that favors quantitative tetrathiomolybdate formation (Dellwig and others, 2012; Nägler and others, 2011; Neubert and others, 2008; Noordmann and others, 2014). Ultimately, oxygenated MBIs limit the timescales and concentration of water column sulfide accumulation within while simultaneously increasing the supply of dissolved molybdate to the Landsort Deep.

As a result, vertical water column profiles show relatively little dissolved Mo depletion across the euxinic chemocline and modern sedimentary Mo isotope data range from -0.24 to +1.12‰ (Nägler and others, 2011; Neubert and others, 2008; Noordmann and others, 2014). Building on the suggestion from Mo-TOC ratios that Mo reservoir drawdown is not a major factor in the Baltic, the observed low δ^{98}Mo values from all three Landsort Deep euxinic periods indicate that at no point in the past has the Landsort Deep been similar to more restricted modern euxinic basins where water column dissolved sulfide is stable at concentrations of hundreds of μM or higher (Algeo and Lyons, 2006).

Sorption of molybdate to Mn oxides provides an alternative, or in this case complementary, mechanism for transport of Mo to the sediments, especially considering the up to 15 wt.% Mn observed in the euxinic sapropels and the inferred oxidation of dissolved water column Mn during MBIs. There is an overlap in the δ^{98}Mo fractionation during Mo sorption to Mn-oxides, -2.9 to -2.5‰ (Arnold and others, 2004; Wasylenki and others, 2008), and that associated with incomplete conversion of molybdate to tetrathiomolybdate, which is potentially up to -3.1‰ (Azrieli-Tal and others, 2014). Following burial and reductive dissolution of the Mn oxides during diagenesis, quantitative conversion of molybdate to tetrathiomolybdate in sulfidic pore waters could then capture the negative isotope signature from oxide adsorption. The adsorption of Mo to Fe oxides and delivery to the sediments is also a relevant sedimentary Mo source. Oxidation of water column dissolve Fe could occur during MBIs or other redox oscillations, and adsorption of Mo to Fe oxides exerts large Mo isotope fractionations, ranging from -0.83 to -2.19‰ relative to the seawater signature depending on the specific Fe oxide mineralogy involved (Goldberg and others, 2009). Evidence that Fe and Mn oxide deposition is an important sedimentary Mo source even during euxinic sapropel deposition comes from similarities in δ^{98}Mo data from the euxinic sapropels and those from intervals outside of the

inferred euxinic layers (fig. 5). Molybdenum concentrations in the non-euxinic intervals are often greater than the 2 ppm crustal average but <25 ppm, indicating a likely oxide source for Mo transport to the sediments, which is subsequently sequestered upon reaction with pore water dissolved sulfide and organic carbon (Scott and Lyons, 2012).

A clear trend in the δ^{98}Mo toward more negative values is observed moving upward within the brackish portion of the profile (fig. 5d), with δ^{98}Mo values shifting from a range of +0.10 to +0.62‰ within the lower sapropel to +0.29 to -0.50‰ beginning directly above the lower sapropel (other than one outlier of +1.11‰). The δ^{98}Mo range in the upper sapropel, -0.50 to -0.07‰ (again, barring one outlier), is distinctly more negative than in the lower sapropel (fig. 5d). Using our Mn concentration and Mo isotope data in combination with the known Mo isotope fractionations associated with Mo burial through both reaction with water column sulfide and adsorption to oxides, we can estimate the potential role of Mo delivered with Mn oxides versus Mo isotope fractionations during exposure to low and variable water column total dissolved sulfide concentrations of <100 μM. This exercise is not intended to quantify precisely the Mn versus euxinic sources of Mo but rather to demonstrate that their relative roles within the euxinic water columns during deposition of the two sapropels can be approximated. The following simple equation permits this mass balance approximation:

$$\delta^{98}Mo_{sed} = \delta^{98}Mo_{eux} \times (1\text{-}f_{\mathbf{Mn}}) + \mathbf{\Delta}^{98}Mo_{sw\text{-}ox} \times f_{\mathbf{Mn}} \ . \qquad \text{(equation 3)}$$

Here, $\delta^{98}Mo_{eux}$ represents the sedimentary Mo isotope value following fractionation from seawater associated with non-quantitative tetrathiomolybdate conversion under euxinic conditions with low total dissolved sulfide concentrations (<100 μM), which, as mentioned, becomes progressively more negative relative to seawater with decreasing sulfide concentration and thus shorter residence time (Azrieli-Tal and others, 2014). The variable $f_{\mathbf{Mn}}$ represents the contribution

of sedimentary Mo from Mn oxide relative to euxinic deposition. For simplicity, we choose to represent the Mo isotope fractionations related to Mn oxides ($\mathbf{\Delta}^{98}Mo_{sw\text{-}ox}$) as the maximum fractionation for Mo sorption to these oxide phases — that is, -2.9‰ from a seawater value of +2.4‰. Maintaining a constant value for $\mathbf{\Delta}^{98}Mo_{sw\text{-}ox}$ is appropriate despite the known dynamic seawater conditions through the Baltic Holocene, as Mo isotope fractionations during adsorption to Mn oxides change little with the range of temperatures and salinities we can expect in this region (Wasylenki and others, 2008). Changes in the fraction of Fe versus Mn oxide Mo delivery to the sediments are also possible (Barling and Anbar, 2004; Goldberg and others, 2009; Wasylenki and others, 2008). Opposite to predictions from such variations, however, the upper sapropel has the highest Fe (now largely present as pyrite) and the most negative $\delta^{98}Mo$ (fig. 5). Lastly, it could be assumed that a Mo flux to the sediments coupled to Mn oxides is substantial enough to deplete water column Mo. For our samples, this scenario is unlikely, as such a scenario would result in bulk sedimentary Mo isotope values closest to seawater in association with highest sedimentary Mn concentrations — the opposite of our observations (Figure 5).

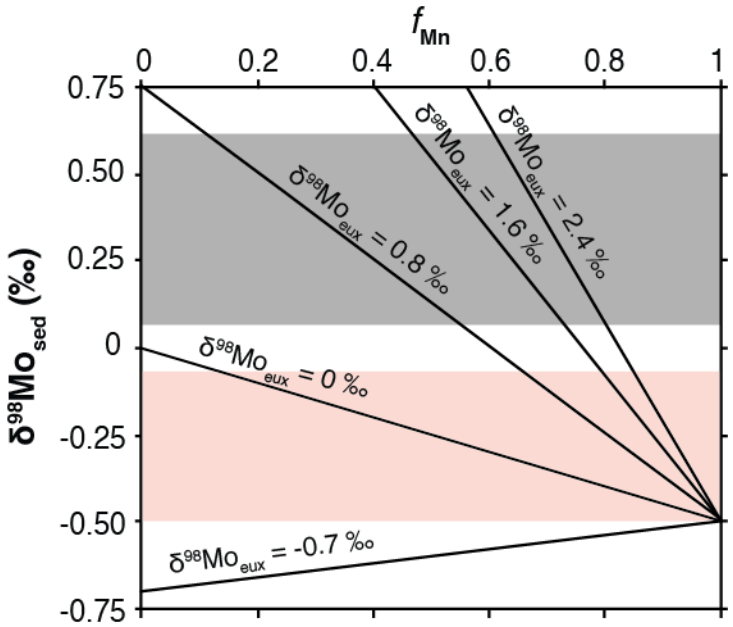

Figure 7. Two end member-mixing model between sedimentary Mo ($\delta^{98}Mo_{sed}$) sourced from varied inputs of Mn-oxides (f_{Mn}) relative to euxinic deposition ($\delta^{98}Mo_{eux}$). Boxes are our measured δ^{98}Mo intervals from the sapropel intervals with the red representing the upper sapropel (barring one outlier) and the black the lower sapropel (fig. 5d). Justification and description of variables are given in the text. Sensitivity tests at varied $\delta^{98}Mo_{eux}$ represent progressive decreases in the concentration and residence of water column total dissolved sulfide at concentrations <100 μM.

Our model calculations demonstrate that the range in δ^{98}Mo from the lower sapropel cannot be explained by mixed Mn oxide and euxinic Mo burial if $\delta^{98}Mo_{eux}$ is approaching the lowest possible values of -0.7 ‰ as constrained from published modeling efforts (Azrieli-Tal and others, 2014) (fig. 7). We also observe that under no constant $\delta^{98}Mo_{eux}$ value does a simple doubling of f_{Mn}, as is observed from the lower to upper sapropel (fig. 5c), explain the shift in the $\delta^{98}Mo_{sed}$ values between the lower and upper sapropel without requiring Mn oxides as nearly the sole sedimentary Mo source in the upper scenario. A scenario demanding nearly all Mo as sourced from Mn oxides, and little from euxinic burial, is unlikely given our independent constraints on euxinic deposition in both sapropels based on Fe speciation, the Mo versus TOC relationship, and modern observations of euxinia at Landsort Deep. Instead, the relatively more

negative $\delta^{98}Mo_{sed}$ in the upper sapropel likely requires more negative $\delta^{98}Mo_{eux}$ values along with increased f_{Mn} compared to the lower sapropel. Decreases in $\delta^{98}Mo_{eux}$ point to a decrease in the absolute concentration and residence time of dissolved sulfide in the water column during deposition of the upper relative to lower sapropel. Considering that both extreme Mn redox cycling and low dissolved sulfide concentrations and residence times are consistent with dynamic redox conditions, we suggest that both of these factors likely contributed to the more negative $\delta^{98}Mo$ range observed in the upper euxinic sapropel compared to the lower. Ultimately, relatively more positive $\delta^{98}Mo$, lower Mn concentrations, and lower Fe_T/Al in the lower sapropel support more expansive and stable euxinia at Landsort Deep and likely the Baltic generally during the HTM relative to the MCA.

Modern and Past Anoxia Comparison

Given the framework from previous studies of Fe, Mn, and Mo from sediments capturing the current euxinic period at Landsort Deep, we can further compare all three main Holocene Baltic anoxic events in the context of their relative stability and extent of reducing conditions. Figure 5 presents Fe_T/Al, Mn, Mo, and $\delta^{98}Mo$ data from the upper 15 cm of Landsort Deep published by Noordman and others (2015) (upper red dots), which includes the transition to the current euxinic era not captured in our study. Overall, the data suggest that the modern euxinic era represents a distinct redox state relative to the past euxinic periods. Modern Mn concentrations are as high as 18.8 wt.% and generally in the range >8 wt.%, and $\delta^{98}Mo$ ranges from -0.24 to +1.12‰ but is generally <0.29‰. Similar to our interpretation of the upper sapropel (MCA), the high Mn concentrations and distinctly more negative $\delta^{98}Mo$ suggest that the current euxinic period has lower sulfide concentrations and residence times in the water column compared to HTM, the earliest euxinic interval captured in our core. Our interpretations of relatively higher and more stable sulfide concentrations at Landsort Deep during the HTM than

today may also extend to other portions of the Baltic. In the Bothnian Sea, sedimentary Mo enrichments from the HTM are consistent with euxinia, while the modern Bothnian Sea is oxic. (Jilbert and others, 2015), supporting the conclusion that euxinic conditions were most expansive during the HTM. Ultimately, this comparison implies that despite a rapid expansion of anoxia in the modern Baltic relative to the anoxic periods of the past (Jilbert and Slomp, 2013), the current anoxic period at Landsort Deep may not yet have reached its maximum reducing potential if past events are a reliable guide.

SUMMARY AND CONCLUSION

Following the most recent transition from lacustrine-to-brackish deposition, the lamination record at Landsort Deep indicates a generally anoxic water column persistently to the present, while the results of combined Fe, Mn, and Mo geochemistry provide evidence for multiple transitions between euxinic, ferruginous, and less reducing conditions. Euxinic deposition is clearly represented within two sapropel intervals with TOC contents of up to 8 wt.%. Highly enriched Mn concentrations throughout most of the brackish profile, but within the sapropels in particular, indicate that oxygenated and saline massive Baltic inflows from the North Sea commonly disrupted anoxic deposition throughout the past, similar to what we observe today (Carstensen and others, 2014). A comparison of Fe_T/Al, Mn, Mo, and $\delta^{98}Mo$ data from both sapropels to sedimentary data from the current Landsort Deep (Lenz and others, 2014; Neubert and others, 2008; Noordmann and others, 2014) indicate that euxinic water column conditions during the Holocene Thermal Maximum was most stable and likely the most reducing over the course of the Holocene.

Though our results clearly demonstrate potential variations in the strength of reducing conditions at Landsort Deep specifically, our Mo data also indicate that past euxinia has never approached the high and stable sulfide concentrations observed in other modern euxinic basins,

such as the Black Sea. As we see in the Baltic today, there is a stratigraphic overlap between the indications of the most reducing conditions, as recorded in Fe speciation and Mo concentration data, and signatures of redox oscillations expressed through Mn concentrations and Mo isotopes. This seemingly contradictory temporal relationship is likely a result of both more expansive anoxia in the Baltic generally during these periods but with major Baltic inflows (MBIs) of North Sea saline and oxygen-rich waters acting to provide punctuated and short-lived replacement of formerly anoxic bottom waters. MBIs simultaneously strengthen the halocline through input of marine North Sea water to brackish Baltic Sea bottom waters, providing the stratified water-column conditions necessary for maintenance of long-term Baltic anoxia. Though our records indicate variations in Baltic water column redox throughout the Holocene, the dual effect from MBIs of short-term oxidation of anoxic bottom waters and sustaining long-term anoxia implies that, as in the past, the future Baltic is unlikely to reach the reducing conditions observed in more restricted modern basins. As such, the unique expressions of Fe, Mn, and Mo geochemistry observed here and elsewhere in the Baltic Sea are characteristically different from more restricted modern euxinic basins and provide a another euxinic example that can be extended to similar basins and redox controls through the geologic record.

REFERENCES CITED

Algeo, T. J. and Lyons, T. W., 2006, Mo–total organic carbon covariation in modern anoxic marine environments: Implications for analysis of paleoredox and paleohydrographic conditions: Paleoceanography, v. 21, p.

Andrén, E., Andrén, T. and Kunzendorf, H., 2000a, Holocene history of the Baltic Sea as a background for assessing records of human impact in the sediments of the Gotland Basin: The Holocene, v. 10, p. 687-702.

Andrén, E., Andrén, T. and Sohlenius, G., 2000b, The Holocene history of the southwestern Baltic Sea as reflected in a sediment core from the Bornholm Basin: Boreas, v. 29, p. 233-250.

Andrén, E., Clarke, A., Telford, R., Weckström, K., Vilbaste, S., Aigars, J., Conley, D., Johnsen, T., Juggins, S. and Korhola, A., 2007, Defining reference conditions for coastal areas in the Baltic Sea. Nordic Council of Ministers.

Andrén, T., Björck, S., Andrén, E., Conley, D., Zillén, L. and Anjar, J. (2011) The development of the Baltic Sea Basin during the last 130 ka, The Baltic Sea Basin. Springer, p. 75-97.

Andrén, T., Jørgensen, B. B., Cotterill, C., Green, S., Andrén, E., Ash, J., Bauersachs, T., Cragg, B., Fanget, A.-S., Fehr, A., Granoszewski, W., Groeneveld, J., Hardisty, D., Herrero-Bervera, E., Hyttinen, O., Jensen, J. B., Johnson, S., Kenzler, M., Kotilainen, A., Kotthoff, U., Marshall, I. P. G., Martin, E., Obrochta, S., Passchier, S., Quintana Krupinski, N., Riedinger, N., Slomp, C., Snowball, I., Stepanova, A., Strano, S., Torti, A., Warnock, J., Xiao, N. and Zhang, R., 2015a, M0063, v. In Andrén, T., Jørgensen, B.B., Cotterill, C., Green, S., and the Expedition 347 Scientists, Proc. IODP, 347: College Station, TX (Integrated Ocean Drilling Program), p.

Andrén, T., Jørgensen, B. B., Cotterill, C., Green, S., Andrén, E., Ash, J., Bauersachs, T., Cragg, B., Fanget, A.-S., Fehr, A., Granoszewski, W., Groeneveld, J., Hardisty, D., Herrero-Bervera, E., Hyttinen, O., Jensen, J. B., Johnson, S., Kenzler, M., Kotilainen, A., Kotthoff, U., Marshall, I. P. G., Martin, E., Obrochta, S., Passchier, S., Quintana Krupinski, N., Riedinger, N., Slomp, C., Snowball, I., Stepanova, A., Strano, S., Torti, A., Warnock, J., Xiao, N. and Zhang, R., 2015b, Site M0063: In Andrén, T., Jørgensen, B.B., Cotterill, C., Green, S., and the Expedition 347 Scientists, Proc. IODP, 347: College Station, TX (Integrated Ocean Drilling Program), v., p.

Andrén, T. and Sohlenius, G., 1995, Late Quaternary development of the north-western Baltic Proper—Results from the clay-varve investigation: Quaternary International, v. 27, p. 5-10.

Arnold, G. L., Anbar, A., Barling, J. and Lyons, T., 2004, Molybdenum isotope evidence for widespread anoxia in mid-Proterozoic oceans: Science, v. 304, p. 87-90.

Asael, D., Tissot, F. L., Reinhard, C. T., Rouxel, O., Dauphas, N., Lyons, T. W., Ponzevera, E., Liorzou, C. and Chéron, S., 2013, Coupled molybdenum, iron and uranium stable

isotopes as oceanic paleoredox proxies during the Paleoproterozoic Shunga Event: Chemical Geology, v. 362, p. 193-210.

Azrieli-Tal, I., Matthews, A., Bar-Matthews, M., Almogi-Labin, A., Vance, D., Archer, C. and Teutsch, N., 2014, Evidence from molybdenum and iron isotopes and molybdenum–uranium covariation for sulphidic bottom waters during Eastern Mediterranean sapropel S1 formation: Earth and Planetary Science Letters, v. 393, p. 231-242.

Barling, J. and Anbar, A., 2004, Molybdenum isotope fractionation during adsorption by manganese oxides: Earth and Planetary Science Letters, v. 217, p. 315-329.

Barling, J., Arnold, G. L. and Anbar, A., 2001, Natural mass-dependent variations in the isotopic composition of molybdenum: Earth and Planetary Science Letters, v. 193, p. 447-457.

Berglund, B. E., Sandgren, P., Barnekow, L., Hannon, G., Jiang, H., Skog, G. and Yu, S.-Y., 2005, Early Holocene history of the Baltic Sea, as reflected in coastal sediments in Blekinge, southeastern Sweden: Quaternary International, v. 130, p. 111-139.

Berner, R. A., 1982, Burial of organic carbon and pyrite sulfur in the modern ocean: its geochemical and environmental significance: Am. J. Sci, v. 282, p. 451-473.

Berner, R. A., 1984, Sedimentary pyrite formation: an update: Geochimica et Cosmochimica Acta, v. 48, p. 605-615.

Berner, R. A., Baldwin, T. and Holdren Jr, G. R., 1979, Authigenic iron sulfides as paleosalinity indicators: Journal of Sedimentary Research, v. 49, p.

Berner, R. A. and Raiswell, R., 1983, Burial of organic carbon and pyrite sulfur in sediments over Phanerozoic time: a new theory: Geochimica et Cosmochimica Acta, v. 47, p. 855-862.

Björck, S., 2008, The late Quaternary development of the Baltic Sea basin: Assessment of climate change for the Baltic Sea Basin, v., p. 398-407.

Björck, S., Andrén, T. and Jensen, J. B., 2008, An attempt to resolve the partly conflicting data and ideas on the Ancylus-Littorina transition: Polish Geological Institute Special Papers, v. 23, p. 21-26.

Björck, S., Kromer, B., Johnsen, S., Bennike, O., Hammarlund, D., Lemdahl, G., Possnert, G., Rasmussen, T. L., Wohlfarth, B. and Hammer, C. U., 1996, Synchronized terrestrialatmospheric deglacial records around the North Atlantic: Science, v. 274, p. 1155-1160.

Boesen, C. and Postma, D., 1988, Pyrite formation in anoxic environments of the Baltic: American Journal of Science, v. 288, p. 575-603.

Canfield, D. E., Lyons, T. W. and Raiswell, R., 1996, A model for iron deposition to euxinic Black Sea sediments: American Journal of Science, v. 296, p. 818-834.

Canfield, D. E., Poulton, S. W., Knoll, A. H., Narbonne, G. M., Ross, G., Goldberg, T. and Strauss, H., 2008, Ferruginous conditions dominated later Neoproterozoic deep-water chemistry: science, v. 321, p. 949-952.

Canfield, D. E., Raiswell, R. and Bottrell, S. H., 1992, The reactivity of sedimentary iron minerals toward sulfide: American Journal of Science, v. 292, p. 659-683.

Carstensen, J., Andersen, J. H., Gustafsson, B. G. and Conley, D. J., 2014, Deoxygenation of the Baltic Sea during the last century: Proceedings of the National Academy of Sciences, v. 111, p. 5628-5633.

Chanton, J. P. and Martens, C. S., 1985, The effects of heat and stannous chloride addition on the active distillation of acid volatile sulfide from pyrite-rich marine sediment samples: Biogeochemistry, v. 1, p. 375-382.

Cline, J. D., 1969, Spectrophotometric determination of hydrogen sulfide in natural waters: Limnology and Oceanography, v. 14, p. 454-458.

Conley, D. J., Björck, S., Bonsdorff, E., Carstensen, J., Destouni, G., Gustafsson, B. G., Hietanen, S., Kortekaas, M., Kuosa, H. and Markus Meier, H., 2009, Hypoxia-related processes in the Baltic Sea: Environmental science & technology, v. 43, p. 3412-3420.

Dahl, T. W., Chappaz, A., Fitts, J. P. and Lyons, T. W., 2013, Molybdenum reduction in a sulfidic lake: Evidence from X-ray absorption fine-structure spectroscopy and implications for the Mo paleoproxy: Geochimica et Cosmochimica Acta, v. 103, p. 213-231.

Dashtgard, S. E. and MacEachern, J. A., 2016, Unburrowed mudstones may record only slightly lowered oxygen conditions in warm, shallow basins: Geology, v., p. G37648. 37641.

Dellwig, O., Schnetger, B., Brumsack, H.-J., Grossart, H.-P. and Umlauf, L., 2012, Dissolved reactive manganese at pelagic redoxclines (part II): Hydrodynamic conditions for accumulation: Journal of Marine Systems, v. 90, p. 31-41.

Diaz, R. J. and Rosenberg, R., 2008, Spreading dead zones and consequences for marine ecosystems: Science, v. 321, p. 926-929.

Döös, K., Meier, H. E. M. and Döscher, R., 2004, The Baltic haline conveyor belt or the overturning circulation and mixing in the Baltic: AMBIO: A Journal of the Human Environment, v. 33, p. 261-266.

Erickson, B. E. and Helz, G. R., 2000, Molybdenum (VI) speciation in sulfidic waters:: stability and lability of thiomolybdates: Geochimica et Cosmochimica Acta, v. 64, p. 1149-1158.

Fehr, M. A., Andersson, P. S., Hålenius, U. and Mörth, C.-M., 2008, Iron isotope variations in Holocene sediments of the Gotland Deep, Baltic Sea: Geochimica et Cosmochimica Acta, v. 72, p. 807-826.

Ferdelman, T. G., 1988, The distribution of sulfur, iron, manganese, copper and uranium in a salt marsh sediment core as determined by a sequential extraction method. University of Delaware, MS thesis.

Goldberg, T., Archer, C., Vance, D. and Poulton, S. W., 2009, Mo isotope fractionation during adsorption to Fe (oxyhydr) oxides: Geochimica et Cosmochimica Acta, v. 73, p. 6502-6516.

Goldschmidt, V., 1933, Grundlagen der quantitativen Geochemie: Fortschr. Mineral. Krist. Petrog, v. 17, p. 112.

Gustafsson, B. G. and Westman, P., 2002, On the causes for salinity variations in the Baltic Sea during the last 8500 years: Paleoceanography, v. 17, p. 12-11-12-14.

Houmark□Nielsen, M. and Henrik Kjær, K., 2003, Southwest Scandinavia, 40–15 kyr BP: palaeogeography and environmental change: Journal of Quaternary Science, v. 18, p. 769-786.

Hurtgen, M. T., Lyons, T. W., Ingall, E. D. and Cruse, A. M., 1999, Anomalous enrichments of iron monosulfide in euxinic marine sediments and the role of H2S in iron sulfide transformations: examples from Effingham Inlet, Orca Basin, and the Black Sea: American Journal of Science, v. 299, p. 556-588.

Jakobsson, M., Björck, S., Alm, G., Andrén, T., Lindeberg, G. and Svensson, N.-O., 2007, Reconstructing the Younger Dryas ice dammed lake in the Baltic Basin: Bathymetry, area and volume: Global and Planetary Change, v. 57, p. 355-370.

Jilbert, T., Conley, D. J., Gustafsson, B. G., Funkey, C. P. and Slomp, C. P., 2015, Glacio-isostatic control on hypoxia in a high-latitude shelf basin: Geology, v. 43, p. 427-430.

Jilbert, T. and Slomp, C. P., 2013, Rapid high-amplitude variability in Baltic Sea hypoxia during the Holocene: Geology, v. 41, p. 1183-1186.

Kabel, K., Moros, M., Porsche, C., Neumann, T., Adolphi, F., Andersen, T. J., Siegel, H., Gerth, M., Leipe, T. and Jansen, E., 2012, Impact of climate change on the Baltic Sea ecosystem over the past 1,000 years: Nature Climate Change, v. 2, p. 871-874.

Kostka, J. E. and Luther, G. W., 1994, Partitioning and speciation of solid phase iron in saltmarsh sediments: Geochimica et Cosmochimica Acta, v. 58, p. 1701-1710.

Lambeck, K. and Chappell, J., 2001, Sea level change through the last glacial cycle: Science, v. 292, p. 679-686.

Lenz, C., Jilbert, T., Conley, D., Wolthers, M. and Slomp, C., 2014, Are recent changes in sediment manganese sequestration in the euxinic basins of the Baltic Sea linked to the expansion of hypoxia?: Biogeosciences Discussions, v. 11, p. 9889-9918.

Lenz, C., Jilbert, T., Conley, D. J. and Slomp, C. P., 2015, Hypoxia□driven variations in iron and manganese shuttling in the Baltic Sea over the past 8 kyr: Geochemistry, Geophysics, Geosystems, v. 16, p. 3754-3766.

Lepland, A. and Stevens, R. L., 1998, Manganese authigenesis in the Landsort Deep, Baltic Sea: Marine geology, v. 151, p. 1-25.

Lyons, T. W., 1997, Sulfur isotopic trends and pathways of iron sulfide formation in upper Holocene sediments of the anoxic Black Sea: Geochimica et Cosmochimica Acta, v. 61, p. 3367-3382.

Lyons, T. W. and Severmann, S., 2006, A critical look at iron paleoredox proxies: new insights from modern euxinic marine basins: Geochimica et Cosmochimica Acta, v. 70, p. 5698-5722.

Matthäus, W., 2006, The History of Investigation of Salt Water Inflows Into the Baltic Sea: From Early Beginning to Recent Results. Institut für Meereskunde Warnemhunde.

Middelburg, J. J., 1991, Organic carbon, sulphur, and iron in recent semi-euxinic sediments of Kau Bay, Indonesia: Geochimica et Cosmochimica Acta, v. 55, p. 815-828.

Miller, C. A., Peucker-Ehrenbrink, B., Walker, B. D. and Marcantonio, F., 2011, Re-assessing the surface cycling of molybdenum and rhenium: Geochimica et Cosmochimica Acta, v. 75, p. 7146-7179.

Mohrholz, V., Naumann, M., Nausch, G., Krüger, S. and Gräwe, U., 2015, Fresh oxygen for the Baltic Sea—An exceptional saline inflow after a decade of stagnation: Journal of Marine Systems, v. 148, p. 152-166.

Morse, J. W. and Cornwell, J. C., 1987, Analysis and distribution of iron sulfide minerals in recent anoxic marine sediments: Marine Chemistry, v. 22, p. 55-69.

Nägler, T., Neubert, N., Böttcher, M., Dellwig, O. and Schnetger, B., 2011, Molybdenum isotope fractionation in pelagic euxinia: Evidence from the modern Black and Baltic Seas: Chemical Geology, v. 289, p. 1-11.

Nägler, T. F., Anbar, A. D., Archer, C., Goldberg, T., Gordon, G. W., Greber, N. D., Siebert, C., Sohrin, Y. and Vance, D., 2014, Proposal for an international molybdenum isotope measurement standard and data representation: Geostandards and Geoanalytical Research, v. 38, p. 149-151.

Neubert, N., Nägler, T. F. and Böttcher, M. E., 2008, Sulfidity controls molybdenum isotope fractionation into euxinic sediments: Evidence from the modern Black Sea: Geology, v. 36, p. 775-778.

Noordmann, J., Weyer, S., Montoya-Pino, C., Dellwig, O., Neubert, N., Eckert, S., Paetzel, M. and Böttcher, M., 2014, Uranium and molybdenum isotope systematics in modern

euxinic basins: Case studies from the central Baltic Sea and the Kyllaren fjord (Norway): Chemical Geology, v., p.

Parkhurst, D. L. and Appelo, C., 1999, User's guide to PHREEQC (Version 2): A computer program for speciation, batch-reaction, one-dimensional transport, and inverse geochemical calculations, v., p.

Poulton, S. W. and Canfield, D. E., 2005, Development of a sequential extraction procedure for iron: implications for iron partitioning in continentally derived particulates: Chemical Geology, v. 214, p. 209-221.

Poulton, S. W. and Canfield, D. E., 2011, Ferruginous conditions: a dominant feature of the ocean through Earth's history: Elements, v. 7, p. 107-112.

Raiswell, R. and Anderson, T., 2005, Reactive iron enrichment in sediments deposited beneath euxinic bottom waters: constraints on supply by shelf recycling: Geological Society, London, Special Publications, v. 248, p. 179-194.

Raiswell, R., Canfield, D. and Berner, R., 1994, A comparison of iron extraction methods for the determination of degree of pyritisation and the recognition of iron-limited pyrite formation: Chemical Geology, v. 111, p. 101-110.

Raiswell, R. and Canfield, D. E., 1998, Sources of iron for pyrite formation in marine sediments: American Journal of Science, v. 298, p. 219-245.

Raiswell, R., Vu, H. P., Brinza, L. and Benning, L. G., 2010, The determination of labile Fe in ferrihydrite by ascorbic acid extraction: methodology, dissolution kinetics and loss of solubility with age and de-watering: Chemical Geology, v. 278, p. 70-79.

Scholz, F., McManus, J. and Sommer, S., 2013, The manganese and iron shuttle in a modern euxinic basin and implications for molybdenum cycling at euxinic ocean margins: Chemical Geology, v. 355, p. 56-68.

Scholz, F., Severmann, S., McManus, J. and Hensen, C., 2014, Beyond the Black Sea paradigm: The sedimentary fingerprint of an open-marine iron shuttle: Geochimica et Cosmochimica Acta, v. 127, p. 368-380.

Scott, C. and Lyons, T. W., 2012, Contrasting molybdenum cycling and isotopic properties in euxinic versus non-euxinic sediments and sedimentary rocks: refining the paleoproxies: Chemical Geology, v. 324, p. 19-27.

Sohlenius, G., Emeis, K.-C., Andrén, E., Andrén, T. and Kohly, A., 2001, Development of anoxia during the Holocene fresh–brackish water transition in the Baltic Sea: Marine geology, v. 177, p. 221-242.

Sohlenius, G., Sternbeck, J., Andrén, E. and Westman, P., 1996, Holocene history of the Baltic Sea as recorded in a sediment core from the Gotland Deep: Marine geology, v. 134, p. 183-201.

Sohlenius, G. and Westman, P., 1998, Salinity and redox alternations in the northwestern Baltic proper during the late Holocene: Boreas, v. 27, p. 101-114.

Sternbeck, J. and Sohlenius, G., 1997, Authigenic sulfide and carbonate mineral formation in Holocene sediments of the Baltic Sea: Chemical Geology, v. 135, p. 55-73.

Sternbeck, J., Sohlenius, G. and Hallberg, R. O., 2000, Sedimentary trace elements as proxies to depositional changes induced by a Holocene fresh-brackish water transition: Aquatic Geochemistry, v. 6, p. 325-345.

Stigebrandt, A. and Gustafsson, B. G., 2003, Response of the Baltic Sea to climate change—theory and observations: Journal of Sea Research, v. 49, p. 243-256.

Suess, E., 1979, Mineral phases formed in anoxic sediments by microbial decomposition of organic matter: Geochimica et Cosmochimica Acta, v. 43, p. 339-352.

Turekian, K. K. and Wedepohl, K. H., 1961, Distribution of the elements in some major units of the earth's crust: Geological Society of America Bulletin, v. 72, p. 175-192.

Walker, M., Johnsen, S., Rasmussen, S. O., Popp, T., Steffensen, J. P., Gibbard, P., Hoek, W., Lowe, J., Andrews, J. and Björck, S., 2009, Formal definition and dating of the GSSP (Global Stratotype Section and Point) for the base of the Holocene using the Greenland NGRIP ice core, and selected auxiliary records: Journal of Quaternary Science, v. 24, p. 3-17.

Wastegård, S., Andrén, T., Sohlenius, G. and Sandgren, P., 1995, Different phases of the Yoldia Sea in the north-western Baltic Proper: Quaternary International, v. 27, p. 121-129.

Wasylenki, L. E., Rolfe, B. A., Weeks, C. L., Spiro, T. G. and Anbar, A. D., 2008, Experimental investigation of the effects of temperature and ionic strength on Mo isotope fractionation during adsorption to manganese oxides: Geochimica et Cosmochimica Acta, v. 72, p. 5997-6005.

Zillén, L., Conley, D. J., Andrén, T., Andrén, E. and Björck, S., 2008, Past occurrences of hypoxia in the Baltic Sea and the role of climate variability, environmental change and human impact: Earth-Science Reviews, v. 91, p. 77-92.

SUPPLEMENTARY MATERIALS

Table S1. Original geochemical data from this study.

Depth (mbsf)	TOC wt.%	TIC wt.%	TOC /TIS	Fe_{asc} wt.%	Fe_{dith} wt.%	Fe_{ox} wt.%	Fe_{NaAc} wt.%	Fe_{py} wt. %	Fe_{AVS} wt. %	Fe_{HR}/Fe_T	$(Fe_{py}+Fe_{AVS})/Fe_{HR}$	Mn wt %	Al wt.%	Fe_T wt.%	Mo ppm
0.70	3.08	0.00	2.73	0.27	0.11	0.39	0.89	0.00	1.96	0.66	0.54	1.72	8.06	5.46	13.65
0.87	2.36	0.06	4.34	0.09	0.03	0.16	0.47	0.14	0.67	0.29	0.56	0.71	8.28	5.02	5.56
1.47	2.56	0.04	7.20	0.16	0.00	0.19	0.63	0.00	0.62	0.28	0.43	0.32	8.08	5.10	4.55
1.81	2.53	0.01	5.00	0.08	0.04	0.21	0.46	0.40	0.08	0.23	0.42	0.26	8.03	5.10	2.33
2.04	2.46	0.03	3.53	0.14	0.03	0.12	0.84	0.60	0.02	0.33	0.39	0.30	7.71	4.92	3.30
2.30	2.45	0.00	5.42	0.22	0.05	0.54	0.41	0.05	0.69	0.38	0.38	0.26	8.41	5.11	4.64
2.37	2.28	0.01	4.70	0.14	0.05	0.19	0.37	0.00	0.85	0.29	0.60	0.27	8.11	5.06	3.55
2.42	2.40	0.02	3.27	0.08	0.04	0.13	0.67	0.32	0.64	0.34	0.54	0.17	8.11	5.23	3.57
2.56	2.28	0.02	3.47	0.08	0.03	0.18	0.45	0.47	0.21	0.25	0.52	0.21	8.55	5.26	1.82
2.97	2.55	0.09	4.61	0.14	0.07	0.23	0.66	0.31	0.34	0.22	0.42	0.38	7.87	7.27	37.30
3.05	2.46	0.00	3.34	0.12	0.06	0.39	0.41	0.56	0.16	0.33	0.42	0.15	8.79	5.11	6.58
3.08	2.25	0.02	3.80	0.07	0.04	0.11	0.48	0.15	0.72	0.30	0.60	0.26	8.03	5.03	2.53
3.34	1.95	0.81	2.74	0.14	0.13	0.30	1.00	0.43	0.37	1.00	0.38	0.33	0.94	0.66	0.80
3.37	2.71	0.00	3.71	0.11	0.05	0.11	0.33	0.41	0.46	0.26	0.67	0.12	8.46	5.22	6.03
3.55		7.56		0.46	0.23	0.35	0.62	0.45	1.49	0.51	0.67	9.29	9.06	6.19	9.41
3.59	2.71	0.18	16.30	0.08	0.00	0.16	0.11	0.12	0.05	0.08	0.39	1.20	7.90	5.47	9.77
3.91	1.93	0.07	4.66	0.23	0.07	0.29	0.62	0.01	0.71	0.31	0.44	0.37	8.42	5.54	5.09
3.99	2.73	0.00	2.28	0.21	0.06	0.30	1.22	1.03	0.02	0.47	0.41	0.13	7.93	5.63	5.50
4.15	2.51	0.06	4.13	0.13	0.04	0.28	0.39	0.19	0.68	0.29	0.57	0.35	8.51	5.48	6.75
4.21	2.52	0.00	9.69	0.32	0.15	0.39	0.33	0.22	0.01	0.20	0.24	0.21	8.63	5.57	9.53
4.30	3.87	0.02	0.79	0.70	1.23	0.34	2.99	3.29	1.90	1.00	0.61	0.21	4.11	5.89	68.54
4.31	2.42	0.00	2.15	0.04	0.15	0.21	0.15	0.83	0.31	0.30	0.76	0.18	8.11	5.54	5.93

Depth (mbsf)	TOC wt.%	TIC wt.%	TOC /TIS	Fe_{asc} wt.%	Fe_{dith} wt.%	Fe_{ox} wt.%	Fe_{NaAc} wt.%	Fe_{py} wt. %	Fe_{AVS} wt. %	Fe_{HR}/Fe_T	$(Fe_{py}+Fe_{AVS})/Fe_{HR}$	Mn wt %	Al wt.%	Fe_T wt.%	Mo ppm
4.56	4.27	3.65	1.22	0.11	1.23	0.20	0.31	2.75	0.57		0.87		0.00	0.00	0.00
4.59	4.47	2.80	3.54	0.17	0.07	0.25	0.54	0.90	0.40	0.40	0.62	0.76	7.65	5.43	14.27
4.60	2.57	0.00	3.69	0.12	0.05	0.45	0.62	0.34	0.54	0.41	0.41	0.10	7.87	5.21	4.80
4.62	7.38	0.00	2.44	0.13	0.04	0.14	0.26	2.57	0.13	0.53	0.83	0.27	6.60	6.11	98.70
4.83	3.06	0.12	1.20	0.33	0.74	0.21	0.63	1.19	2.07	1.00	0.80	13.78	3.80	4.13	79.57
4.85	3.92	0.02	1.57	0.36	0.38	0.18	0.99	1.93	0.49	0.86	0.68	9.29	5.54	4.61	57.15
5.06	2.90	0.00	2.91	0.10	0.14	0.23	0.46	0.85	0.03	0.33	0.56	7.83	9.57	5.20	
5.15	3.41	3.42	1.08	0.12	0.71	0.29	0.27	1.44	2.63	1.00	0.88	11.77	3.60	3.50	85.51
5.31	3.10	0.00	2.05	0.09	0.02	0.17	0.12	1.28	0.07	0.35	0.83	0.00	8.08	4.78	
5.41	3.74	0.04	1.20	0.51	0.57	0.17	1.70	1.01	3.40	1.00	0.70	0.00	3.06	3.84	91.01
5.67	3.50	2.41	1.11	0.09	1.09	0.23	0.71	2.45	0.61	1.00	0.76	9.31	4.52	4.77	11.44
5.94	3.91	0.04	2.10	0.07	0.16	0.09	0.65	1.06	1.11	0.90	0.75	14.07	3.82	3.39	127.49
6.05	3.12	0.01	1.09	0.44	0.35	0.19	1.58	1.30	2.38	1.00	0.67	14.97	6.26	5.27	73.93
6.13	4.28	3.34	1.75	0.11	1.14	0.35	0.88	1.91	0.45	1.00	0.66	14.13	2.73	3.73	27.47
6.23	3.57	3.95	1.97	0.17	0.64	0.25	0.38	1.24	0.67	0.97	0.75	14.71	3.43	3.29	27.63
6.80	3.97	3.31	1.99	0.08	0.84	0.38	0.13	1.38	0.72	1.00	0.80	11.51	3.51	3.39	40.00
6.88	2.49	0.00	1.95	0.20	0.11	0.24	0.43	1.10	0.01	0.32	0.62	6.18	8.54	5.85	9.46
7.34	2.75	0.02	1.67	0.42	0.16	1.36	1.74	0.69	1.50	0.99	0.37	6.81	4.83	5.93	36.74
8.03		0.24		0.29	0.17	0.44	0.81	0.59	0.57	0.43	0.48	0.45	8.76	5.97	19.75
8.13	2.25	0.11	2.35	0.00	0.49	0.36	0.62	0.55	0.56	0.45	0.53	0.63	8.35	5.69	4.29
8.48	2.17	0.00	1.88	0.27	0.08	0.91	0.72	0.00	2.01	0.75	0.50	0.53	7.97	5.30	6.01
9.37	2.08	0.10	3.08	0.14	0.06	0.23	0.87	0.28	0.62	0.37	0.45	0.61	8.03	5.58	7.64
9.47	2.52	0.11	3.49	0.08	0.06	0.26	1.12	0.61	0.03	0.36	0.32	1.36	8.29	5.79	11.51
9.87	1.95	0.00		0.09	0.13	0.41	1.13	0.00	0.00	0.29	0.00	3.42	8.26	6.16	23.66
9.91	2.29	1.40	2.01	0.21	0.10	0.36	1.48	0.06	1.87	0.67	0.51	4.30	6.72	5.80	21.37

Depth (mbsf)	TOC wt.%	TIC wt.%	TOC /TIS	Fe_{asc} wt.%	Fe_{dith} wt.%	Fe_{ox} wt.%	Fe_{NaAc} wt.%	Fe_{py} wt. %	Fe_{AVS} wt. %	Fe_{HR}/Fe_T	$(Fe_{py}+Fe_{AVS})/Fe_{HR}$	Mn wt %	Al wt.%	Fe_T wt.%	Mo ppm
10.49	2.09	0.53	1.87	0.16	0.10	0.35	1.01	0.48	0.98	0.52	0.52	2.47	7.65	5.60	15.70
10.62	1.78	0.07	3.79	0.11	0.09	0.36	0.76	0.00	0.82	0.37	0.42	0.15	8.50	5.53	5.40
10.88	1.85	0.00	3.63	0.11	0.17	0.90	0.79	0.14	0.60	0.45	0.27	0.77	9.79	6.03	5.13
10.97	1.73	0.04	3.99	0.45	0.07	0.32	0.59	0.05	0.66	0.29	0.44	0.20	8.86	5.78	4.97
11.32	1.99	0.00	2.06	0.18	0.10	0.35	0.61	0.82	0.03	0.32	0.47	1.26	8.60	6.00	7.41
11.69	1.85	0.04	2.75	0.13	0.07	0.28	0.65	0.16	0.84	0.37	0.52	0.33	8.21	5.43	2.24
11.98	1.89	0.35	1.17	0.39	0.09	0.44	1.07	1.06	0.68	0.54	0.53	1.47	7.76	6.17	4.32
12.01	1.76	0.00	2.70	0.08	0.20	0.74	0.70	0.22	0.70	0.48	0.35	0.31	8.65	5.48	3.17
12.17	1.82	0.25	3.46	0.42	0.09	0.27	0.83	0.44	0.03	0.29	0.30	1.20	8.16	5.76	9.48
12.56	1.83	0.00	6.81	0.07	0.04	0.18	0.34	0.15	0.18	0.14	0.34	1.10	10.10	6.72	1.03
13.90	2.13	1.76	0.71	0.23	0.21	0.43	0.64	1.05	3.15		0.80				
14.24	2.02	0.00	3.64	0.18	0.08	0.64	0.61	0.42	0.14	0.34	0.27	0.42	10.00	6.00	0.53
14.85	2.14	0.01	4.01	0.10	0.37	0.42	0.75	0.45	0.03	0.36	0.23	2.35	8.21	5.90	15.87
15.88	1.95	0.01	1.11	0.23	0.08	0.65	0.86	0.00	3.06	0.67	0.63	3.07	8.77	7.25	19.56
16.07	2.02	0.00	2.42	0.22	0.13	0.57	0.72	0.46	0.53	0.39	0.43	0.32	9.00	6.18	12.18
16.63	1.73	0.14	2.03	0.16	0.05	0.26	1.02	0.71	0.06	0.38	0.38	0.60		5.61	5.80
16.74	1.88	0.00	4.89	0.09	0.08	0.34	0.44	0.31	0.06	0.21	0.28	0.54	9.90	6.13	4.68
17.12	1.89	0.08	1.93	0.14	0.06	0.44	1.01	0.62	0.47	0.45	0.43	0.63		5.82	8.30
17.80	2.11	0.00	1.39	0.02	0.01	0.10	0.00		0.85	0.31	0.95	0.17		5.91	2.61
17.95	1.83	0.00	1.46	0.45	0.06	0.29	0.79	1.09	0.00	0.35	0.50	0.81	9.58	6.38	5.11
18.02	2.01	0.00	1.73	0.19	0.10	0.29	0.66	0.40	1.22	0.40	0.63	0.25	8.79	6.69	28.62
18.15	2.37	0.00	3.43	0.09	0.10	0.17	0.90		1.21	0.43	0.49	0.91	7.23	5.69	11.28
18.35	2.01	0.00	1.27	0.02	0.02	0.01	0.05	1.37	0.03	0.26	0.94	0.23	8.04	5.76	6.37
18.76	1.82	0.03	2.45	0.22	0.08	0.30	0.84		0.75	0.39	0.47	0.52		5.76	3.01
19.31	1.44	0.01	0.83	0.03	0.00	0.11	0.05	1.50	0.00	0.27	0.90	1.22	9.01	6.11	8.98

Depth (mbsf)	TOC wt.%	TIC wt.%	TOC /TIS	Fe_{asc} wt.%	Fe_{dith} wt.%	Fe_{ox} wt.%	Fe_{NaAc} wt.%	Fe_{py} wt. %	Fe_{AVS} wt. %	Fe_{HR}/Fe_T	$(Fe_{py}+Fe_{AVS})/Fe_{HR}$	Mn wt %	Al wt.%	Fe_T wt.%	Mo ppm
19.55	2.60	0.21	1.61	0.02	0.05	0.08	0.00	0.98	0.86	0.33	0.96	0.90		5.91	26.90
19.60	2.05	0.00	1.15	0.01	0.01	0.04	0.03	1.22	0.67	0.34	0.96	1.52	8.65	5.84	27.37
19.93	3.52	0.65	2.17	0.03	0.03	0.05	0.05	1.28	0.26	0.32	0.94	2.26		5.23	63.72
20.44	5.83		2.53	0.02	0.00	0.04	0.01	1.98	0.05	0.41	0.97	5.48		5.11	27.86
20.83	5.38	0.01	1.60	0.02	0.03	0.01	0.15	2.88	0.09	0.57	0.93	3.64	7.20	5.60	87.75
21.20	4.13	2.04	1.85	0.03	0.00	0.04	0.00	1.63	0.62	0.52	0.98	6.89		4.44	70.12
21.95	6.43	0.01	1.90	0.31	0.03	0.06	0.32	2.94	0.02	0.75	0.89	0.29	4.92	4.47	78.97
22.19	6.58	0.00	3.08	0.25	0.02	0.05	0.27		0.49	0.58	0.87	2.88	4.46	4.23	63.09
22.25		0.97		0.13	0.04	0.09	0.79		0.00	0.64	0.69	0.69	5.21	4.57	117.58
22.27	5.79	0.00	2.17	0.03	0.04	0.00	0.10		0.01	0.43	0.93	2.07	6.47	5.78	58.57
22.32	4.42	1.79	3.11	0.01	0.00	0.03	0.00	0.95	0.57	0.33	0.98	6.24		4.71	28.99
22.84	6.05	1.01	2.35	0.03	0.03	0.04	0.09	2.15	0.20	0.57	0.94	3.43		4.37	71.32
23.07	5.35	0.01	6.39	0.03	0.02	0.04	0.10	0.13	1.20	0.23	0.88	4.77	7.76	6.70	75.57
23.36				0.05	0.03	0.04	0.01	1.54	0.04	0.36	0.97	5.98		4.56	58.69
23.63	5.15	0.30	2.00	0.04	0.01	0.02	0.07	2.23	0.03	0.58	0.96	1.36		4.05	46.91
24.01	6.74	1.25	3.37	0.07	0.01	0.02	0.00	1.73	0.02	0.44	0.99	4.37		4.02	23.74
24.50	4.80	0.01	2.67	0.13	0.04	0.10	0.15	1.55	0.03	0.48	0.86	3.92	4.99	3.91	62.64
24.53	2.67	1.87	2.02	0.05	0.00	0.04	0.10	1.10	0.11	0.29	0.90	5.74		4.67	44.42
24.58	5.78	0.01	3.29	0.08	0.03	0.06	0.18	1.25	0.56	0.69	0.84	4.05	3.16	3.13	54.63
24.63	4.93	0.01	2.89	0.23	0.03	0.10	0.20		0.01	0.32	0.84	4.46	8.49	5.66	
25.29		2.71		0.15	0.03	0.14	0.21		0.00	0.15	0.31	0.00	4.25	3.51	46.53
25.42	3.28	0.04	4.35	0.10	0.03	0.13	0.19	0.35	0.60	0.40	0.75	4.31	5.35	3.30	
25.54	5.28	3.01	9.44	0.15	0.17	0.09	0.58	0.16	0.65	0.50	0.55	9.60		3.30	41.11
25.81	7.66	0.02	4.16	0.16	0.22	0.12	0.32	1.57	0.07	0.45	0.79	0.00	5.41	5.10	149.67

Depth (mbsf)	TOC wt.%	TIC wt.%	TOC /TIS	Fe_{asc} wt.%	Fe_{dith} wt.%	Fe_{ox} wt.%	Fe_{NaAc} wt.%	Fe_{py} wt. %	Fe_{AVS} wt. %	Fe_{HR}/Fe_T	$(Fe_{py}+Fe_{AVS})/Fe_{HR}$	Mn wt %	Al wt.%	Fe_T wt.%	Mo ppm
25.94	2.12	0.01	1.29	0.05	0.01	0.13	0.08	1.44	0.00	1.00	0.87	6.66	2.31	1.50	
26.05	3.50	0.00	2.72	0.08	0.02	0.21	0.11	1.12	0.00	0.14	0.78	0.00	20.30	10.86	20.70
26.30	2.60	0.01		0.16	0.02	0.17	0.39	0.00	0.00	0.10	0.00	0.56	8.14	5.61	31.12
26.66	3.01	0.00	2.47	0.09	0.01	0.18	0.14	1.05	0.01	0.25	0.77	2.27	9.29	5.63	4.45
26.75	2.33	0.00	10.44	0.08	0.05	0.39	0.44	0.18	0.02	0.22	0.18	0.08	7.92	5.27	2.62
26.75	2.66	0.00	2.03	0.17	0.07	0.37	0.29	1.14	0.00	0.32	0.63	0.11	8.63	5.82	3.51
27.90	1.04	0.00	24.13	0.09	0.08	0.50	0.27	0.04	0.00	0.19	0.05	0.07	9.82	4.62	
27.98	1.07	0.02	10.99	0.17	0.04	0.26	0.21	0.08	0.01	0.12	0.16	0.07		4.93	0.72
28.27	0.87	0.00	23.97	0.09	0.06	0.64	0.33	0.03	0.01	0.20	0.04	0.00	9.41	5.24	3.09
28.47	1.78	0.00	12.27	0.04	0.03	0.42	0.18	0.12	0.01	0.13	0.17	0.30	9.48	6.02	7.85
31.04	0.45	0.00	23.08	0.05	0.04	0.42	0.32	0.01	0.01	0.14	0.03	0.04	9.47	6.20	0.45
33.01	0.72	0.00	71.20	0.03	0.03	0.33	0.27	0.01	0.00	0.12	0.02	0.03	8.68	5.52	0.58
34.96	0.52	0.00	53.69	0.06	0.04	0.42	0.22	0.01		0.11	0.01	0.02	10.34	6.71	0.52
37.17	0.55	0.00	39.45	0.06	0.05	0.40	0.28	0.01		0.13	0.02	0.01	9.96	6.04	0.96
39.25	0.54	0.00	163.57	0.07	0.03	0.00	0.27	0.00		0.00		0.01	11.62	6.91	0.61
40.73	0.69	0.00	48.77	0.07	0.08	0.66	0.43	0.01		0.20	0.01	0.03	8.55	6.18	0.67
42.23	0.71	0.00	31.92	0.09	0.06	0.62	0.38	0.02			0.02		0.00	0.00	0.48
42.25	0.47		24.52					0.02		0.00		0.05	10.31	6.18	
43.25		0.00		0.10	0.07	0.62	0.38			0.20	0.00	0.07	7.62	5.82	0.97
44.55		0.00		0.08	0.06	0.66	0.33	0.01		0.19	0.01	0.03	7.81	6.00	0.61
47.05	0.61	0.00	42.23	0.03	0.05	0.26	0.31	0.01		0.12	0.02	0.03	7.86	5.77	0.73
48.35	0.77	0.00	63.02	0.04	0.03	0.50	0.29	0.01		0.14	0.01	0.04	8.62	6.40	0.68
49.25	0.56	0.00	39.20	0.04	0.03	0.03	0.20	0.01		0.04	0.04	0.05	12.89	7.97	0.64
49.60	0.55		44.66					0.01				0.02	8.70	5.43	
51.25	0.46	0.00	29.89	0.04	0.03	0.70	0.20	0.01		0.18	0.01	0.03	8.01	5.40	0.76

Depth (mbsf)	TOC wt.%	TIC wt.%	TOC /TIS	Fe_{asc} wt.%	Fe_{dith} wt.%	Fe_{ox} wt.%	Fe_{NaAc} wt.%	Fe_{py} wt. %	Fe_{AVS} wt. %	Fe_{HR}/Fe_T	$(Fe_{py}+Fe_{AVS})/Fe_{HR}$	Mn wt %	Al wt.%	Fe_T wt.%	Mo ppm
52.60		0.00		0.02	0.03	0.52	0.13	0.01		0.11	0.01	0.04	10.00	6.47	0.67
53.05	0.34	0.00	31.03	0.02	0.02	0.00	0.00	0.01				0.02	8.41	5.94	0.64
54.65	0.49	0.00	40.90	0.02	0.02	0.39	0.09	0.01		0.08	0.02	0.02	9.65	6.19	0.58
55.25	0.33	0.00	32.08	0.02	0.02	0.37	0.06	0.01			0.02		0.00	0.00	
55.95		0.00		0.02	0.01	0.41	0.10	0.01		0.09	0.02	0.02	9.76	6.45	0.50
57.25	0.29	0.00	24.61	0.02	0.00	0.29	0.08	0.01		0.06	0.03	0.04	9.67	6.76	0.65
59.10	0.19	0.00	63.80	0.01	0.04	0.25	0.04	0.00			0.01	0.06	6.91	4.89	0.51
60.25	0.28	0.00	22.77	0.02	0.01	0.36	0.08	0.01		0.07	0.02	0.05	9.57	6.56	0.55
61.25	0.46	0.00	71.16	0.01	0.09	0.38	0.05	0.01		0.09	0.01	0.03	10.26	5.98	0.62
61.90	0.34	0.00	49.16	0.01	0.01	0.26	0.06	0.01			0.02	0.08	8.74	6.54	0.51
63.25	0.37	0.00	136.89	0.02	0.04	0.38	0.09	0.00		0.09	0.00	0.04	8.26	5.76	0.63
65.15	0.21	0.00	8.67	0.01	0.07	0.36	0.09	0.02		0.09	0.04	0.04	9.47	6.38	0.46
66.15	0.23	0.00	17.82	0.01	0.01	0.37	0.10	0.01		0.09	0.02	0.04	9.81	5.90	0.60
67.25	0.32	0.00	186.80	0.01	0.07	0.35	0.10	0.00		0.09	0.00	0.03	8.94	5.88	1.11
67.95	0.23	0.00	24.42	0.01	0.01	0.38	0.09	0.01		0.11	0.02	0.01	6.42	4.47	0.45
69.25	0.27	0.00	23.50	0.01	0.08	0.35	0.07	0.01		0.12	0.02	0.02	7.26	4.23	0.55
71.15	0.23		12.60	0.01	0.03	0.38	0.07	0.02			0.03			0.00	
72.15	0.17	0.00	14.00	0.01	0.01	0.28	0.08	0.01		0.09	0.03	0.02	8.11	4.45	0.47
73.25	0.16	0.00	146.23	0.01	0.04	0.21	0.08	0.00		0.06	0.00	0.03	9.15	5.68	0.99
76.55	0.20	0.00	9.81	0.01	0.03	0.41	0.04	0.02		0.10	0.03	0.03	9.60	5.08	0.62
79.75	0.12	0.00	14.81	0.01	0.02	0.26	0.05	0.01		0.09	0.02	0.02	6.54	3.68	0.08
83.05	0.14	0.00	6.11	0.01	0.03	0.28	0.04	0.02			0.05	0.07	8.01	5.20	0.56
86.35	0.17	0.00	6.44	0.00	0.02	0.28	0.04	0.02		0.10	0.06	0.02	7.09	3.59	0.52
89.65	0.20	0.00	6.63	0.00	0.03	0.19	0.04	0.03		0.12	0.09	0.00	6.72	2.32	0.51

Table S2. Molybdenum isotope data from this study.

Sample Depth (mbsf)	$\delta^{98/95}$Mo (‰)	1s
0.70	-0.28	0.03
0.70	-0.25	0.04
0.70	-0.24	0.03
1.47	-0.46	0.03
1.47	-0.49	0.03
2.04	-0.02	0.03
2.04	0.06	0.04
2.56	0.19	0.03
2.56	0.08	0.02
2.97	0.18	0.03
2.97	0.18	0.02
3.34	0.06	0.03
3.34	0.03	0.03
3.55	-0.13	0.03
3.55	-0.11	0.03
3.99	0.19	0.03
4.30	-0.04	0.04
4.30	-0.07	0.02
4.62	1.19	0.03
4.62	1.11	0.03
4.62	1.00	0.03
4.62	1.17	0.05
4.85	-0.13	0.03
4.85	-0.19	0.03
5.15	-0.09	0.03
5.15	-0.11	0.03
5.41	-0.38	0.05
5.41	-0.49	0.05
5.41	-0.32	0.03
5.41	-0.32	0.02
5.67	-0.13	0.04
6.05	-0.17	0.03
6.05	-0.19	0.03
6.13	-0.14	0.03
6.23	-0.45	0.04
6.23	-0.24	0.02
6.23	-0.27	0.02
6.8	-0.50	0.03
6.8	-0.43	0.03
7.34	-0.25	0.05
7.34	-0.25	0.04
8.03	-0.12	0.03

Sample Depth (mbsf)	$\delta^{98/95}$Mo (‰)	1s
8.03	-0.28	0.04
8.13	0.11	0.03
8.13	0.14	0.03
8.48	0.07	0.03
8.48	0.06	0.04
8.48	0.07	0.03
8.48	-0.01	0.03
9.47	-0.03	0.03
9.47	-0.05	0.02
9.91	-0.37	0.03
9.91	-0.39	0.03
10.49	-0.38	0.03
10.49	-0.36	0.03
11.69	-0.16	0.03
11.69	-0.04	0.03
14.24	-0.47	0.03
14.24	-0.43	0.03
14.24	-0.41	0.03
14.24	-0.48	0.04
14.24	-0.49	0.05
14.24	-0.51	0.03
14.24	-0.44	0.02
16.07	-0.11	0.03
16.07	-0.10	0.03
16.74	-0.05	0.04
16.74	-0.08	0.03
17.8	0.34	0.03
17.8	0.29	0.03
18.02	0.07	0.02
18.02	0.09	0.03
18.76	0.15	0.03
18.76	0.03	0.03
19.31	0.16	0.03
19.31	0.10	0.03
19.31	0.17	0.03
19.545	-0.02	0.02
19.545	0.06	0.03
19.60	0.12	0.03
19.60	0.14	0.03
19.60	0.11	0.04
19.925	0.04	0.04
19.925	0.07	0.03
20.44	0.28	0.03
20.44	0.28	0.03

Sample Depth (mbsf)	$\delta^{98/95}$Mo (‰)	1s
20.44	0.27	0.03
20.83	0.41	0.03
20.83	0.38	0.03
21.2	0.17	0.03
21.95	0.46	0.03
21.95	0.50	0.03
22.19	0.59	0.03
22.19	0.59	0.03
22.25	0.47	0.03
22.25	0.47	0.03
22.32	0.23	0.03
22.32	0.20	0.02
22.32	0.21	0.03
22.84	0.43	0.03
22.84	0.43	0.03
22.84	0.41	0.03
23.07	0.22	0.03
23.07	0.22	0.03
23.36	0.26	0.02
23.36	0.30	0.03
23.36	0.23	0.03
23.63	0.69	0.03
23.63	0.62	0.03
23.63	0.46	0.03
23.63	0.57	0.07
24.01	0.30	0.03
24.01	0.25	0.03
24.01	0.24	0.03
24.53	0.13	0.03
24.53	0.10	0.03
25.29	0.21	0.03
25.29	0.23	0.03
25.54	0.43	0.02
25.54	0.44	0.03
25.81	0.59	0.03
25.81	0.59	0.03
25.81	0.11	0.06
Sample		
NOD-A-1	-0.25	0.05
NOD-A-1	-0.33	0.04
NOD-A-1	-0.24	0.04
NOD-A-1	-0.33	0.04

Sample Depth (mbsf)	$\delta^{98/95}$Mo (‰)	1s
NOD-A-1	-0.28	0.03
Average	-0.29	0.04
Standard Deviation	0.04	
External precision 1STD on δ^{98}Mo = 0.04 ‰		

CHAPTER 5

Spatiotemporal variations in the degree and frequency of Baltic Sea Holocene anoxia

ABSTRACT

The modern Baltic Sea is the world's largest anthropogenically forced anoxic basin, with sub-basins displaying anoxia with increasing degree (oxygenated < manganeous < euxinic) and frequency (seasonal < variable < semi-permanent) with increasing distance from the sill at the Danish Straits. Here, we apply Fe-Mn-Mo geochemistry to specifically define the degree and frequency of past spatiotemporal patterns of anoxia through the Baltic Holocene relative to modern Baltic redox regimes. We provide two new records from southern Baltic sub-basins from Integrated Ocean Drilling Program Expedition 347, Bornholm Basin and Little Belt, which we assimilate with published paleoredox records from Baltic Proper sub-basins. Similar to previous studies, we observe two prominent sapropel units with variable evidence for anoxic conditions at each sub-basin, roughly overlapping with the transition from the Ancylus Lake to Littorina Sea and, immediately following, the Holocene Thermal Maximum (HTM), as well as a later event during the Medieval Climate Anomaly. Our data indicate, similar to today, that each past anoxic event is characterized by redox conditions that became progressively more reducing with increasing distance from the sill. The earliest anoxic period was the most widespread and reducing (episodic low oxygen < ferruginous < semi-permanent euxinia), but the temporal transition to anoxia was dynamic at various sub-basins relative to evidence for the well-known lacustrine-to-brackish transition that marked the shift from the Ancylus Lake to the Littorina Sea. The more recent Medieval Climate Anomaly is linked to the same general relationship, but the sill proximal to sill distal redox transect is characterized by relatively less reducing conditions more similar to the modern Baltic Sea (i.e., seasonally low oxygen, episodic euxinia, and semi-permanent euxinia that is less stable and expansive than during the HTM). Ultimately, our results provide the first characterization of specific paleoredox regimes in southern Baltic sub-basins, while emphasizing the importance of salinity as a driver of specific paleoredox regimes on both

long and short timescales. Furthermore, we demonstrate that redox regimes both similar to and different than the modern Baltic have occurred naturally over the Holocene.

INTRODUCTION

As the world's largest anthropogenically forced low oxygen basin, the Baltic Sea's bottom water oxygen availability is regulated by a combination of climatic warming, eutrophication, salinity, and physical controls (Carstensen and others, 2014). Among these, increased nutrient input from land and associated cyanobacteria blooms are most prominently responsible for the 10× increase in Baltic low oxygen/anoxic bottom waters observed over the last century, while it has only been over the last 20 years that increased respiration resulting from human-induced warming is observable (Carstensen and others, 2014). Importantly, however, even in the absence of anthropogenic factors, salinity gradients and variations from combined natural climate variations, unique circulation, and hydrography prime the Baltic Sea for the development of low oxygen bottom waters (Mohrholz and others, 2015). The Baltic Sea is silled at the Danish straits (Figure 1a,b), forcing freshwater output from runoff and saline input from the North Sea through the same location. This restriction supports the development of a strong halocline — limiting physical mixing between surface and bottom waters and thus restricting bottom water renewal to lateral advection. Such restricted and stratified conditions are particularly prone to the development of oxygen depleted bottom waters (Figure 1d,e,f red lines), as is observed in other silled basins including the Black Sea, Cariaco Basin, Framvaren Fjord, and Saanich Inlet. Like these other restricted basins, the modern Baltic water column is reducing enough within some sub-basins for the accumulation of hydrogen sulfide, or euxinia (Carstensen and others, 2014; Noordmann and others, 2014). These are extreme reducing conditions that preclude the presence of animals and result in characteristic sedimentary sequestration of redox-sensitive metals (for

example, Mo, Fe) (Algeo and Lyons, 2006; Lyons and Severmann, 2006; Poulton and Canfield, 2011).

Importantly, however, the Baltic is unique relative to these other settings as the halocline is highly dynamic, with a gradient in the magnitudes, timescales, and depths of salinity fluctuations from proximal to distal position relative to the sill (Figure 1c,d,e blue lines). Baltic Sea salinity gradients and short-term oscillations are largely a function of isolated climatic events known as Major Baltic Inflows (MBIs). During these events, saline and oxygen-rich marine waters from the North Sea are introduced into the Baltic beneath the halocline (Carstensen and others, 2014). The large catchment area — 4× the size of the sea — and associated runoff produce a positive freshwater balance to the Baltic Sea, rendering such events necessary for maintaining the Baltic salt balance and the halocline that facilitates the anoxic conditions in multiple sub-basins. MBIs are both barotropic and baroclinic events in which wind and air pressure cause a sea level difference between the Kattegat and Arkona Basin on opposing sides of the sill (Figure 1), forcing temporary net inflow of North Sea saline and oxygenated water into the Baltic (Franck and others, 1987; Matthäus, 2006; Mohrholz and others, 2015). Depending on the scale of the MBI and the season of occurrence, nearly the entire Baltic Sea may become temporarily oxygenated. This process oxidizes reduced redox-sensitive chemical species accumulated in the formerly anoxic bottom waters (e.g., Mn(II), Fe(II), H_2S), while simultaneously introducing the saline water that maintains the halocline and the resulting stratification responsible for the return to anoxic bottom waters and their long-term maintenance. Ultimately, halocline stability and frequency of bottom water renewal act to regulate the maximum reducing potential of bottom waters within individual Baltic sub-basins. This combination results in a spatial gradient in anoxic conditions with relatively more intense and stable anoxia with increasing distance from the sill (Figure 1c,d,e red lines).

The importance of natural physical and climate forcing on Baltic water column chemistry are evident from modern observations (Figure 1) but are further emphasized from events within the Baltic since the last glacial maximum and throughout the Holocene. Immediately following the last glacial maximum (~22 ka), the Baltic Basin initially hosted an ice lake, which eventually underwent a permanent switch to a brackish basin following global sea level rise — the Ancylus Lake-to-Littorina Sea transition — at approximately 8.5 ka. Following this transition and associated halocline formation, two major pre-anthropogenic Baltic anoxic periods are known through sedimentary laminations and geochemical signatures (Zillén and others, 2008). These events roughly overlap with the Holocene Thermal Maximum (8-4 ka) and Medieval Climate Anomaly (1.2-0.8 ka) and co-occur with the widespread enhanced deposition of organic matter and sediment laminations in many sub-basins (Zillén and others, 2008).

In this work we use high-resolution cores from the recent IODP 347 and combined sedimentology, sedimentary Mn-Fe-Mo relationships, and pore water geochemistry to constrain the paleosalinity influence on specific paleoredox regimes from two southern Baltic sub-basins over the course of the Holocene — Little Belt (Site M0059) and Bornholm Basin (Site M0065) (Figure 1). These specific paleosalinity variations include the transition from the freshwater Ancylus Lake to the brackish Littorina Sea (Andrén and others, 2011), higher salinity during the Holocene Thermal Maximum relative to today (Gustafsson and Westman, 2002), and episodic Major Baltic Inflows of saline and oxygenated North Sea water (Carstensen and others, 2014). No previous study has evaluated paleoredox conditions from southern Baltic sub-basins using proxies that are sensitive to the range of redox conditions observed in the modern Baltic. Today there is an observed lateral transition in the degree and frequency of anoxic water column conditions in sub-basins moving away from the sill — from Little Belt to Bornholm Basin to the Landsort

Deep. The corresponding redox gradient spans from seasonally low oxygen conditions to variable euxinia to semi-persistent euxinia (Figure 1).

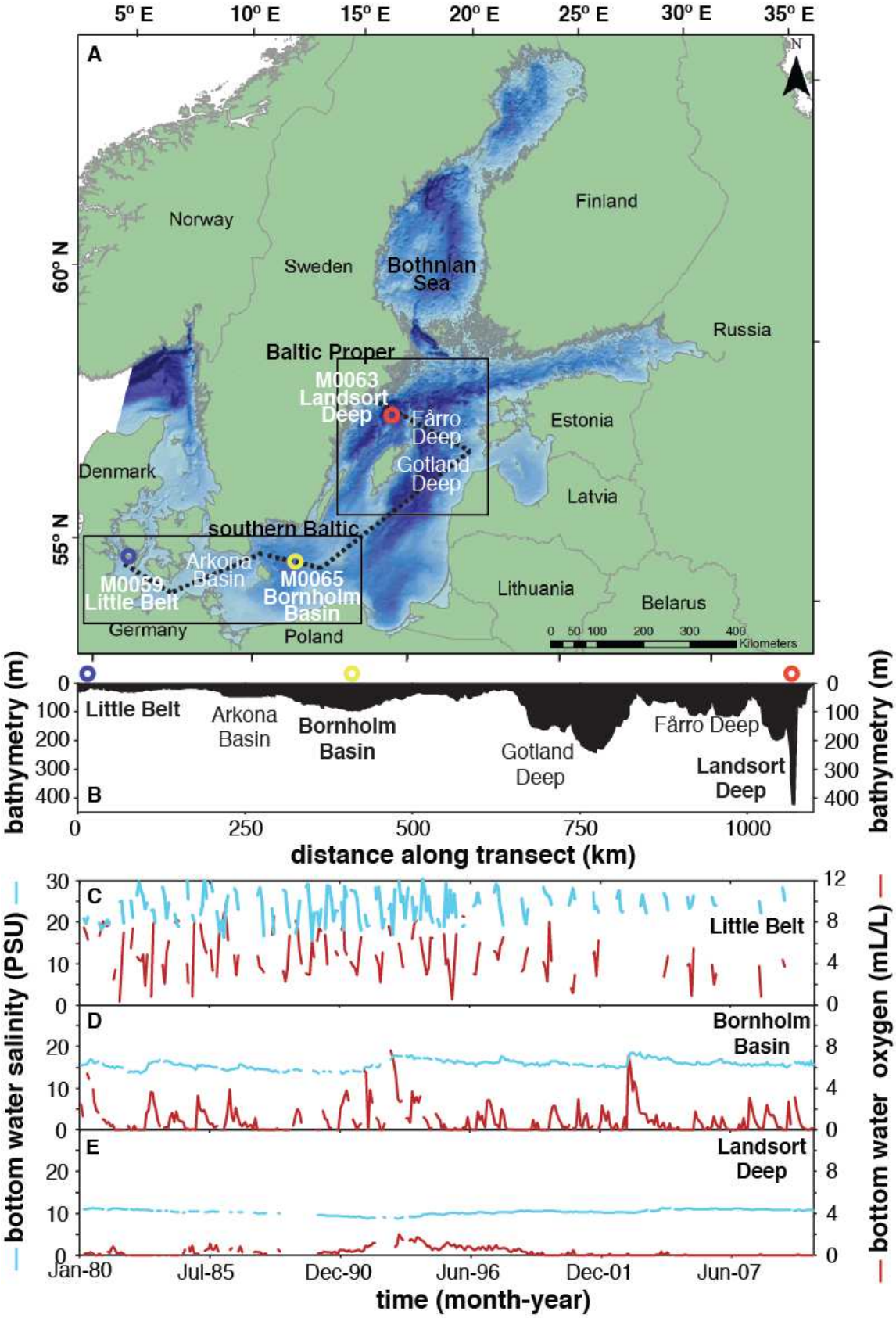
5° E
10° E
15° E
20° E
25° E
30° E
35° E
A
N
60° N
55° N
Norway
Sweden
Finland
Bothnian Sea
Russia
Baltic Proper
M0063
Landsort Deep
Fårro Deep
Gotland Deep
Estonia
Latvia
Denmark
southern Baltic
Arkona Basin
M0059
Little Belt
M0065
Bornholm Basin
Lithuania
Belarus
Germany
Poland
0 50 100 200 300 400
Kilometers
bathymetry (m)
Little Belt
Arkona Basin
Bornholm Basin
Gotland Deep
Fårro Deep
Landsort Deep
B
distance along transect (km)
bottom water salinity (PSU)
bottom water oxygen (mL/L)
C
Little Belt
D
Bornholm Basin
E
Landsort Deep
Jan-80
Jul-85
Dec-90
Jun-96
Dec-01
Jun-07
time (month-year)

Figure 1. (A) Map showing relevant drilling localities from IODP Expedition 347 and other locations discussed in the text. (B) Bathymetry from transect shown in part A (dashed line). C, D, and E represent the mean monthly (1980-2010) bottom water salinity and oxygen concentrations at Little Belt, Bornholm Basin, Landsort Deep, respectively. Chemical data are from the Baltic Environmental Database of the Baltic Nest Institute, Stockholm University, specifically from stations 450, BY5, and BY31. Landsort Deep is shown as a general representative of Baltic Proper sub-basins.

BACKGROUND

Paleoredox Proxy Geochemistry

The combination of Fe-Mn-Mo geochemistry is calibrated for the determination of anoxia occurring on various timescales. Brief descriptions of the proxy systematics and threshold values are provided below, and Table 1 provides our favored interpretations of the combined proxies as calibrated from modern settings.

	Fe_T/Al	Fe_{py}/Fe_{HR} & [Mo]	interpretation
sediment homogenous	<0.65	<<1 <2 ppm	WC: oxic PW: non-sulfidic
		>0.7 2-25 ppm	WC: oxic PW: sulfidic
	>0.65	>0.7 >25 ppm	WC: episodic anoxia with faunal recolonization
		>0.7 <25 ppm	WC: oxic PW: Fe-S remobilization
sediment laminated	<0.65	<<1 <2 ppm	WC: reducing but not anoxic PW: non-sulfidic
		>0.7 2-25 ppm	WC: reducing but not anoxic PW: sulfidic
	>0.65	<<1 <2 ppm	WC: ferruginous PW: non-sulfidic
		<<1 2-25 ppm	WC: ferruginous PW: sulfidic
		>0.7 >100 ppm	WC: persistent euxinia
		>0.7 25-100 ppm	WC: episodic euxinia
		>0.7 <25 ppm	WC: ferruginous PW: Fe-S remobilization

Table 1. Interpretations for combined Fe-Mo proxy results as justified in the text. Values near the specified thresholds should be interpreted with caution. WC: water column redox; PW: pore water redox.

Ratios of total Fe-to-aluminum (Fe_T/Al) and 'highly reactive' Fe-to-total Fe (Fe_{HR}/Fe_T) are complementary proxies for determining ancient water column anoxia at levels that support the accumulation of dissolved iron or hydrogen sulfide. 'Highly reactive' Fe represents operationally

defined Fe-bearing minerals that are reactive toward hydrogen sulfide on short diagenetic timescales (Berner and Canfield, 1989; Canfield, 1989; Canfield and Berner, 1987; Canfield and others, 1996; Canfield and others, 1992; Poulton and Canfield, 2005; Raiswell and Canfield, 1998). These are specifically Fe-(oxy)hydroxides (hematite, ferrihydrite, lepidocrocite), magnetite, and Fe-carbonate (siderite) — all representing potential Fe sulfide precursors — as well as sulfide products pyrite, mackinawite, and greigite (Canfield and Berner, 1987; Canfield and others, 1992; Poulton and Canfield, 2005; Raiswell and others, 1994; Raiswell and others, 2010). Comparisons of Fe_T/Al and Fe_{HR}/Fe_T data from the stable euxinic Black Sea and other similar settings relative to oxic continental margin and deep ocean sediments indicate that 'highly reactive' Fe is enriched relative to typical detrital fluxes under anoxic conditions through a process coined the 'Fe shuttle' (Canfield and others, 1996; Lyons and Severmann, 2006; Lyons and others, 2003; Raiswell and Canfield, 1998). In general, sedimentary Fe cycling drives shelf-to-basin transport of 'highly reactive' Fe, but this process is enhanced under low oxygen conditions, and anoxic — especially euxinic — conditions represent a particularly efficient Fe trap, allowing for elevated Fe_T/Al and Fe_{HR}/Fe_T. Detrital values for Fe_{HR}/Fe_T are typically < 0.38 in oxic settings (Raiswell and Canfield, 1998), and detrital Fe_T/Al in the Baltic has been specifically calibrated as < 0.65 (Fehr and others, 2008). Values clearly above these thresholds are candidates for ancient water column anoxia.

Under anoxic conditions marked by sediments showing elevated Fe_T/Al and Fe_{HR}/Fe_T, the ratios of pyritized Fe-to-'highly reactive' Fe (Fe_{py}/Fe_{HR}) and Mo concentrations can be further applied to distinguish euxinic from ferruginous (iron-rich) systems. Values for Fe_{py}/Fe_{HR} greater than ~0.7 in settings with independent indications of anoxia indicate that the majority of the 'highly reactive' Fe has been converted to pyrite, which is favored by syngenetic pyrite formation in the water column — as is observed in the euxinic Black Sea (Canfield and others, 1996; Lyons

and Severmann, 2006; Poulton and Canfield, 2011). Indications of anoxia from Fe speciation but with Fe_{py}/Fe_{HR} less than ~0.7 suggest a ferruginous water column (Poulton and Canfield, 2011). Similarly, when coupled with a lack of enrichments in Fe_T/Al and Fe_{HR}/Fe_T, ratios of Fe_{py}/Fe_{HR} are a proxy for past pore water sulfide accumulation (see chapter 3 for details).

Molybdate is the dominant dissolved Mo species in oxic seawater and is largely sourced from rivers, with modern concentrations near 104 nM in oxic marine waters (Miller and others, 2011) but with values near ~20 nM in the brackish Baltic Sea (Noordmann and others, 2014). Molybdenum concentrations are <2 ppm in typical continental crust but become elevated in the presence of dissolved sulfide (Scott and Lyons, 2012). The largest Mo sink in modern seawater, however, is sorption to Mn and Fe oxides, which deliver molybdate to the sediments followed by burial and dissolution of the oxides during anoxic diagenesis (Bertine and Turekian, 1973; Kashiwabara and others, 2009; Krishnaswami, 1976). If sulfide is present at appreciable levels, molybdate will convert efficiently if not quantitatively to tetrathiomolybdate and other polysulfide species (Azrieli-Tal and others, 2014; Dahl and others, 2013; Erickson and Helz, 2000), which can be buried effectively in association with organic matter (Algeo and Lyons, 2006). This 'oxide shuttle' process ultimately accounts for Mo fixation in sulfidic sediments underlying an oxic water column with concentrations typically in a range between 2-25 ppm (Scott and Lyons, 2012) — complimenting $Fe_{HR}/Fe_T < 0.38$, $Fe_T/Al < 0.65$, $Fe_{py}/Fe_{HR} > 0.7$ that fingerprint the same conditions of sulfidic pore fluids beneath oxic bottom waters. Sediments underlying euxinic waters — where progressive reaction between molybdate and sulfide to form tetrathiomolybdate occurs in the water column — have Mo concentrations elevated beyond this range. Sediments beneath waters marked by temporally varying euxinia have values typically from 25 to 100 ppm, and values > 100 ppm are often observed in settings with stable water column sulfide at appreciable levels (Scott and Lyons, 2012).

In stable euxinic settings with total sulfide concentrations beyond 100 μM (Erickson and Helz, 2000), the near-quantitative scavenging of water column Mo with free sulfide results in sedimentary Mo isotope signatures that typically mirror that of seawater (δ^{98}Mo = ~2.3‰; (Arnold and others, 2004; Neubert and others, 2008)). Under conditions with unstable euxinia and/or total sulfide concentrations < 100 μM, Mo concentrations are often still elevated relative to oxic settings. However, a negative Mo isotope fractionation of up to 3.1‰ linked to incomplete conversion of molybdate to tetrathiomolybdate is captured in the sediments (Azrieli-Tal and others, 2014; Tossell, 2005). In the Black Sea, elevated and stable water column hydrogen sulfide concentrations in a restricted setting allow for sedimentary Mo isotope values that mimic that of coeval seawater (Arnold and others, 2004; Barling and others, 2001). This strength of signal capture can be contrasted with the modern Baltic Sea — Landsort and Gotland Deep, specifically — where large Mo isotope offsets are observed in sediments underlying euxinic waters with low water column sulfide concentrations (Nägler and others, 2011; Neubert and others, 2008; Noordmann and others, 2014). Importantly, however, sorption of Mo to oxide phases also exerts similarly large Mo isotope offsets from seawater ranging up to 2.9‰ ((Barling and others, 2001; Wasylenki and others, 2008) and 2.2‰ (Goldberg and others, 2009), for Mn and Fe, respectively. Due to the overlap in fractionations, oxide-associated Mo isotope fractionations can be difficult to distinguish from fractionations related to low and unstable water column sulfide concentrations (Hardisty and others, In Press; Nägler and others, 2011; Neubert and others, 2008; Noordmann and others, 2014).

Sediment Description

Because of poor recovery of the sediment-water interface, the cores from this study do not capture the present anoxic conditions but instead provide a detailed record of the Holocene prior to the last couple of centuries. The sedimentology and paleontology of Sites M0059 and

M0065 are described in detail in the IODP Expedition Reports (Andrén and others, 2015b, d) and are displayed in Figure 2, but a summary of the relevant details is provided below. A summary of the sedimentology of Landsort Deep site M0063 specifically can be found in a previous chapter in the dissertation, with details also available in the IODP Expedition Report (Andrén and others, 2015c).

Cores from site M0059 at Little Belt span ~85 meters below the seafloor (mbsf) and are composed of seven units, as well as multiple sub-units. Subunits Ia and Ib are the focus of this study and span from 0-47.1 and 47.1-53.7 mbsf, respectively. Both subunits consist of black to greenish well-sorted clay. Subunit Ia contains millimeter-scale laminations, minor bioturbation, shell fragments, foraminifera throughout (albeit at low diversity), and a relatively diverse brackish-marine diatom assemblage. This subunit likely represents deposition in the Littorina Sea. Subunit Ib is characterized by centimeter-scale laminations and lacks both bioturbation and foraminifera. The diatom assemblages are lacustrine in origin and suggest that the upper portion of this subunit represents the transition from the lacustrine Ancylus Lake to the brackish Littorina Sea. Unit II contains an uncomformity, possibly reflecting a low-stand. Units III-VI capture a combination of glacial lake sediments characterized by rhythmically banded clays and dropstones, a possible braided glacial outwash network, diamicton representing a possible glacial till deposit, and an interbedded glacial deposit capturing variations in clast size reflecting ice advance and retreat. Unit VII is Cretaceous-age carbonate bedrock.

The core from Site M0065 at Bornholm Basins spans ~47 mbsf and consists of three units. Unit I, a focus of this study, spans from 0-9 mbsf and consists largely of bioturbated organic-rich clay with weak laminations, a brackish-marine diatom assemblage of medium diversity, and benthic formanifera of brackish affinity down to 8.9 mbsf. In the bottom 10 cm of

Unit I, foraminifera are absent, and the sediment is characterized by a lack of bioturbation and, instead, prominent millimeter-scale lamination. Unit II spans from 12.6-9.0 mbsf and is a dark clay featuring prominent 2-3 mm-scale very fine dark gray laminae. Unit II lacks bioturbation and is characterized by combinations of lacustrine, lacustrine-brackish, and brackish diatoms and lacks foraminifera outside of one marine species at ~12.1 mbsf. Unit II likely represents the gradual and pulsed transition between the Ancylus Lake and Littorina Sea — the Initial Littorina Sea — recorded in previous work (Björck and others, 2008; Sohlenius and others, 2001). Unit III is interpreted as a glacial lake deposit with rhythmically banded clays indicating ice-proximal deposition in the lower portion and contorted structures indicating slumping along a slope section in the upper portion.

METHODS

Samples from M0059C,E and M0065C were collected and sealed in N_2-flushed bags onboard the ship immediately following core recovery and stored frozen prior to analysis. Cores from M0059A,B,D and M0065A,B were capped and sealed immediately following retrieval and stored at 4°C prior to sampling, which occurred 4-5 months later at MARUM in Bremen, Germany. Samples were collected within a few hours of core splitting, immediately sealed in N_2-flushed bags, and stored frozen prior to analyses — thus minimizing oxidation of redox-sensitive Fe minerals important for this study. Sediments were analyzed at the University of California-Riverside and Yale University. As described below, we used exclusively fresh material for analysis, scraping and discarding any oxidized sediments.

We used splits of freshly thawed sample for extraction of iron monosulfide (acid-volatile sulfide or AVS) (Berner and others, 1979; Chanton and Martens, 1985; Hurtgen and others, 1999; Lyons, 1997; Morse and Cornwell, 1987) and for the chromium reducible sulfur (CRS) extraction (Canfield et al., 1987). CRS and AVS concentrations were measured via the methylene blue

method using a spectrophotometer at wavelength of 660 nm (Cline, 1969), as well as gravimetrically following conversion of ZnS to Ag_2S. Pyritic sulfur was determined by subtracting the AVS from CRS, which was also used to calculate the associated Fe concentrations (Fe_{AVS} and Fe_{py}) assuming FeS and FeS_2 stoichiometries, respectively.

A modified chemical extraction method was used for characterization of distinctive, operationally defined 'highly reactive' Fe pools: ascorbate (Fe_{asc}), dithionite (Fe_{dith}), oxalate (Fe_{ox}), and Na-acetate (Fe_{NaAc}) — representing labile Fe-oxides, crystalline Fe-oxides, magnetite, and Fe-carbonate, respectively (Ferdelman, 1988; Kostka and Luther, 1994; Poulton and Canfield, 2005; Raiswell and others, 1994; Raiswell and others, 2010). Immediately prior to the extractions, the chemical reagents were deoxygenated with N_2 for > 15 minutes, and the headspace of each centrifuge tube was replaced with N_2 prior to shaking. We used fresh and wet sediment exclusively, and sample exposure time to the atmosphere was limited to minutes during initial weighing and subsequent reagent additions. Subsamples for individual analyses were carefully homogenized. The sequential Fe chemical extraction scheme was performed as follows: (1) Na-acetate extraction at pH 4.5 for 24 hours (Poulton and Canfield, 2005), (2) ascorbate at pH 7.5 for 24 hours (Raiswell and others, 2010), (3) dithionite at pH 4.8 for 2 hours (Poulton and Canfield, 2005), and (4) oxalate at pH of 3.2 for 6 hours (Poulton and Canfield, 2005). All Fe extracts were quantified via an Agilent 7500c quadrupole inductively coupled plasma-mass spectrometer (ICP-MS) following dilution with 0.24 M nitric acid. Sample duplicates assessed for precision revealed total error mostly <0.1 wt.%; we point out, however, that heterogeneities are expected, as samples were not homogenized prior to taking a split for the sequential Fe-extraction procedure.

Total carbon, TIC, and TOC were determined using an Eltra CS-500 carbon-sulfur analyzer. The geostandard AR4007 was analyzed routinely, with values deviating by < 5% relative to the reported ranges. Bulk sediment metal concentrations were determined through a multi-acid digest procedure using dried samples ashed at 450-650°C and digested using trace metal grade HF:HNO_3:HCl, with the metals solubilized at the end in 0.24 M HNO_3 acid. Total digests were measured for major elements (Al, Fe, and Mn) and trace elements (Mo) via an Agilent 7900c quadrupole ICP-MS using a multi-element standard solution in a 0.24 M HNO_3 matrix. Total digests of geostandards (NIST 2702, USGS SCO-1, and USGS SGR-1) were routinely compared for accuracy, with all elements analyzed within reported ranges. All values for Al, Fe, Mn, Mo, Fe_{asc}, Fe_{dith}, Fe_{ox}, Fe_{NaAc}, Fe_{AVS}, Fe_{CRS}, TOC, and TIC can be found in Supplementary Tables 1 and 2.

Molybdenum isotope measurements were performed at the Metal Geochemistry Center at Yale University, New Haven, Connecticut. The resulting 0.24 M HNO_3 solution from each total digest was evaporated and re-constituted in 7 M HCl. An aliquot of the acid split was doped with a Mo double spike according to the Mo concentration determined previously via ICP-MS in order to maintain a constant sample-to-spike ratio. This aliquot was also used for chromatographic separation. The ^{97}Mo-^{100}Mo double spike solution was prepared gravimetrically from Oak Ridge Laboratory metal powders as previously described (Asael and others, 2013). A two-stage column procedure was applied for Mo purification: the sample was run through an anion resin (AG-MP-1M) to separate Mo and Fe from the matrix followed by purification through a cation resin (AG50W-X8) to separate Mo from any remaining Fe. Molybdenum isotope compositions are reported using the δ notation, where:

$$\delta^{98}\text{Mo}\ (‰) = 1000\cdot[(^{98}\text{Mo}/^{95}\text{Mo})_{\text{sample}}/(^{98}\text{Mo}/^{95}\text{Mo})_{\text{NIST}}*0.99975 - 1]. \qquad \text{(equation 1)}$$

$\delta^{98}Mo$ is calculated relative to NIST 3134 (Lot 130418) with a value of -0.25 ‰ (Nägler and others, 2014). A calibration of the NIST standard relative to Rochester (Lot 862309E) gave:

$$\delta^{98}Mo_{ROCH} = \delta^{98}Mo_{NIST3137} - 0.32 \pm 0.12 \text{ ‰}. \quad \text{(equation 2)}$$

Duplicates (n=6) of reference standard NOD-1 yielded an average $\delta^{98}Mo$ value of -0.63 ‰ and 1σ of 0.18 ‰, similar to previously reported values (Asael and others, 2013). Values for Mo isotope measurements and associated error can be found in Supplementary Table 3. Measurement error for individual samples was <-0.07 ‰ and mostly <-0.04 ‰.

RESULTS

We specifically discuss the results from Bornholm Basin and Little Belt. Though it is not a focus of this study, total organic carbon (TOC) and diatom abundances are shown from Landsort Deep (Andrén and others, 2015e; Hardisty and others, In Press) to provide a context for correlating the sill-distal sub-basins from the Baltic Proper to the sill-proximal southern Baltic sub-basins of this study. Diatom abundances from previously published work are shown in Figure 2 (Andrén and others, 2015b, c, d). At Little Belt, total organic carbon (TOC) is < 1 wt. % from the bottom of the core until 51.82 mbsf, where TOC increases to 3.75 wt.% and gradually increases up the remainder of the core (Figure 2). Superimposed on this increasing TOC trend are two sapropel units at 51.2-44.6 and 7.7-5.9 mbsf, with peak values of ~6.2 and 7.8 wt. %, respectively. At Bornholm Basin, TOC values are below 0.7 wt. % from the bottom of the profile up to 12.75 mbsf where they begin to steadily increase above this value for the remainder of the profile (Figure 3). There are two peaks above this baseline between 12.3 and 8.3 mbsf and 5.17 and 3.34 mbsf to values of ~4.7 and 9.8 wt.%, respectively.

At Little Belt, concentrations of redox-sensitive elements do not change in response to the elevated TOC contents of the sapropels (Figure 3). Fe_T/Al and Mo concentrations are

generally near 0.65 and < 25 ppm, respectively, however, each shows one increase to a higher value, but are isolated and not associated with sapropel deposition. Manganese concentrations show a broad peak from 47.5 to 11 mbsf, with values oscillating but peaking as high as 1.5 wt. %. Mo isotope values range from +0.18 to +1.47 ‰.

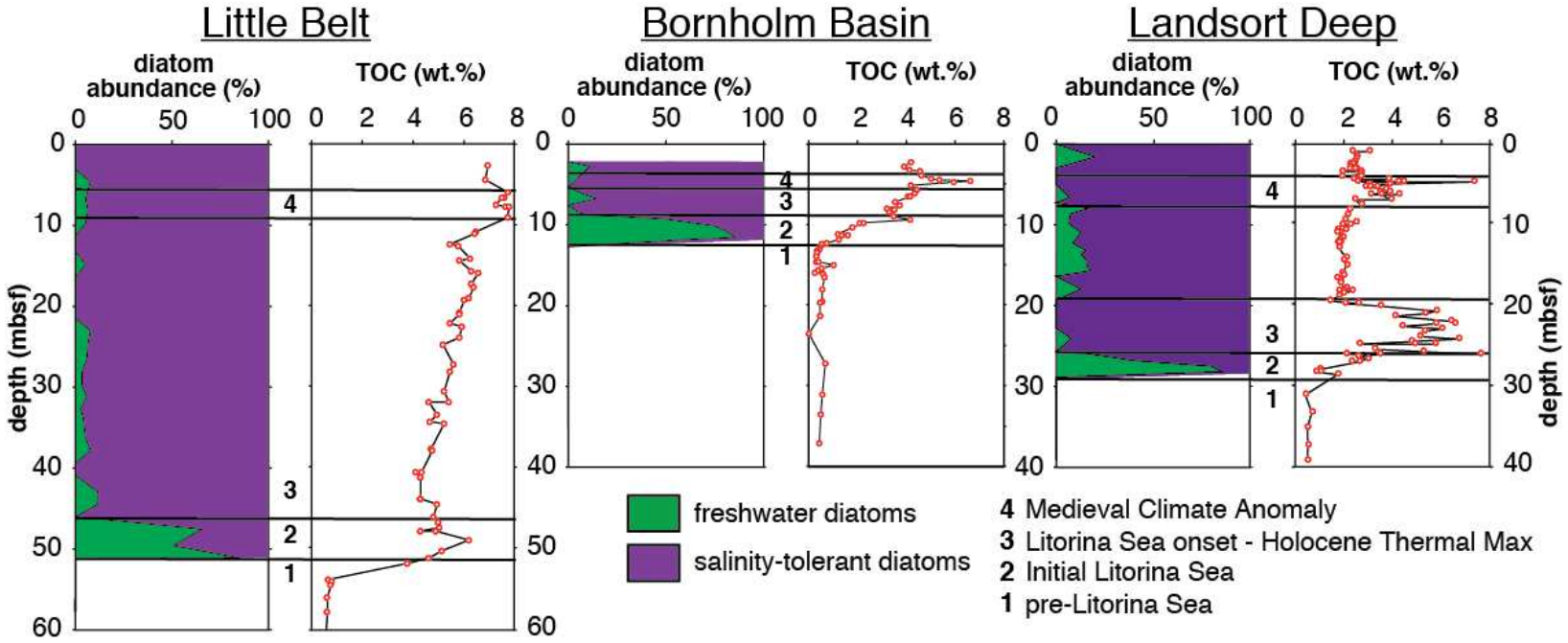

Figure 2. The abundance of freshwater versus salinity-tolerant diatoms (Andrén and others, 2015b, c, d) and total organic carbon concentrations from Little Belt and Bornholm Basin from this study and Landsort Deep from a previous study (Hardisty and others, In Press). The sites are shown here with increasing distance from the sill from left to right, with locations shown in Figure 1. Also shown are the distinct stages discussed in the text. Landsort Deep is included to represent the Baltic Proper, allowing for correlation between the Baltic Proper and southern Baltic sub-basins.

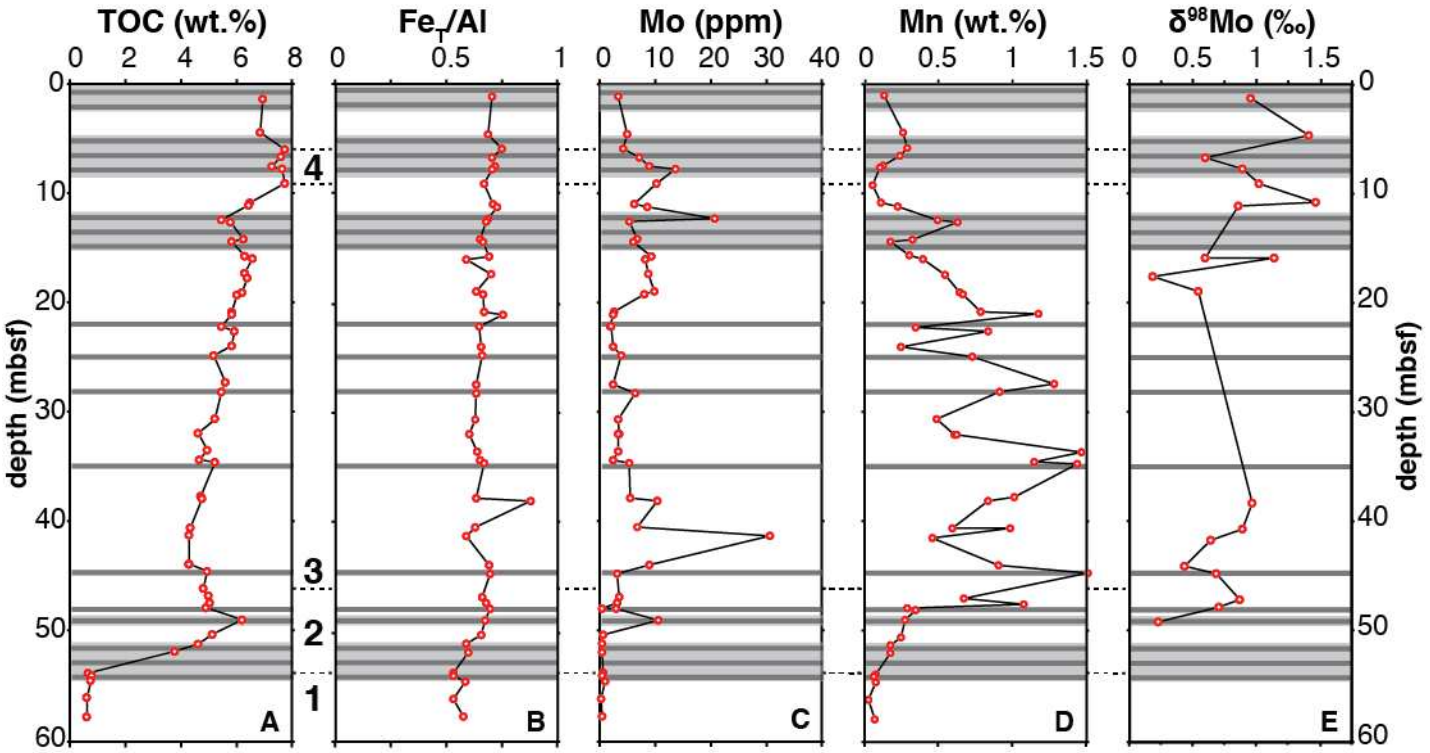

Figure 3. The composition of **(A)** total organic carbon, **(B)** total iron-to-alumninum, **(C)** molybdenum, **(D)** manganese, and **(E)** molybdenum isotopes. The grey bars mark portions of the cores where the bioturbation index is marked as 0 in the IODP Expedition Report (Andrén and others, 2015b), indicating undisturbed lamination. The temporal intervals discussed in the text and displayed in Figure 2 are numbered and marked with dashed lines. These correspond to: (1) Ancylus Lake, (2) Initial Littorina Sea, (3) Littorina Sea onset and Holocene Thermal Maximum, and (4) Medieval Climate Anomaly.

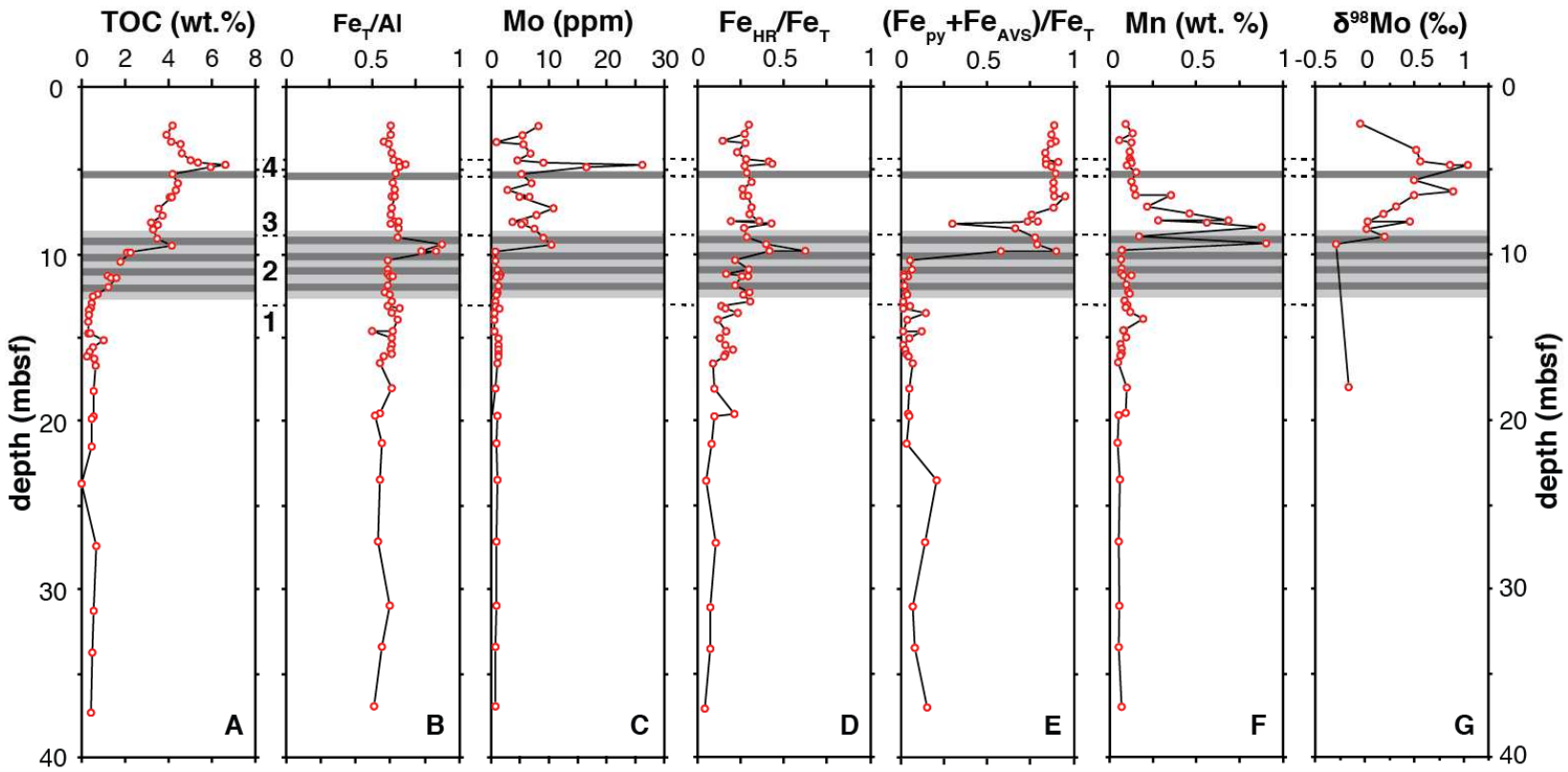

Figure 4. Bornholm Basin sedimentary compositions of **(A)** total organic carbon, **(B)** total iron-to-aluminum, **(C)** molybdenum, **(D)** 'highly reactive' iron-to-total iron, **(E)** sulfidized iron-to-total iron, **(F)** manganese, and **(G)** molybdenum isotopes. The grey bars mark portions of the cores where the bioturbation index is marked as 0 in the IODP Expedition Report. The dashed lines and numbers represent the boundaries inferred in Figure 2 and justified in the text: (1) Ancylus Lake, (2) Initial Littorina Sea, (3) Littorina Sea onset and Holocene Thermal Maximum, and (4) Medieval Climate Anomaly.

At Bornholm Basin, multiple anoxic indicators fluctuate in association with the two sapropels defined by elevated TOC (Figure 4). Fe_T/Al maintains a baseline < 0.65 outside of the two intervals where TOC peaks, with values increasing above anoxic thresholds to 0.90 and 0.69 mbsf in the lower and upper sapropels, respectively. Fe_{HR}/Fe_T remains < 0.38 outside of the sapropels. Fe_{HR}/Fe_T increases to 0.62 and 0.43 in the lower and upper sapropel, respectively, as well as one point at 8.1 mbsf with a value of 0.43. $(Fe_{py}+Fe_{AVS})/Fe_{HR}$ values are < 0.2 from the bottom of the profile up to 10.3 mbsf, where values begin to increase to > 0.7 for most of the overlying profile. Molybdenum concentrations are generally < 2 ppm from the bottom of the profile until near 9.8 mbsf. Above this, Mo concentrations increase to values still < 25 ppm, other than one value in the upper sappropel at 4.65 of 26.84 ppm. There is a co-variation between Mo concentrations and TOC in the upper sapropel (Figure 5). Manganese concentrations increase exclusively from 9.8 to 6.6 mbsf, overlapping with but extending beyond the lower sapropel. Molybdenum isotope values range from -0.29 to +1.04 ‰ but are distinctly more positive from 6.54-3.85 mbsf (Figure 4).

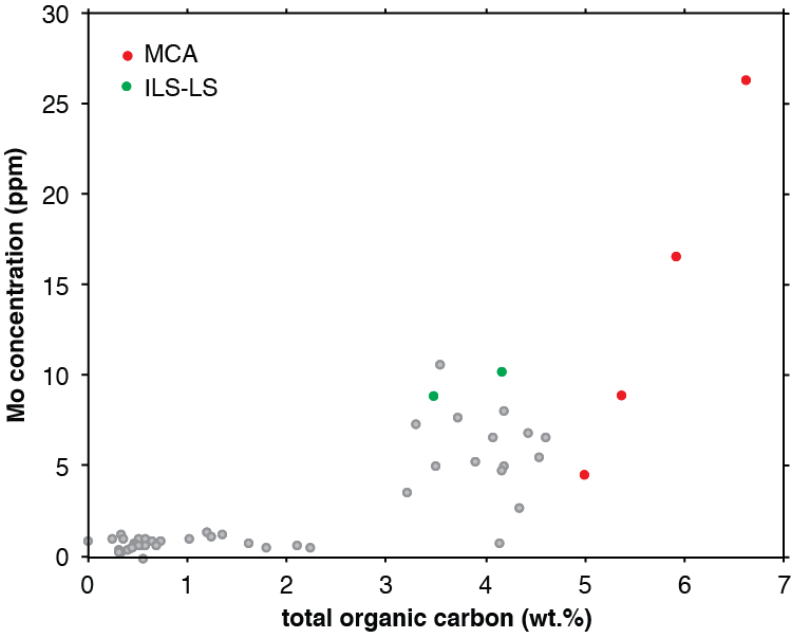

Figure 5. Comparison of Mo concentrations and total organic carbon at Bornholm Basin. Using the stratigraphic correlations from Figure 2, the Medieval Climate Anomaly (MCA) is shown in red, the Initial Littorina Sea-Littorina Sea boundary (ILS-LS) is in green, and all other intervals are in grey.

The profiles for pore water dissolved Fe are shown from Little Belt, Bornholm Basin, and Landsort Deep (Figure 6). These results are extracted from the IODP Expedition 347 Report (Andrén and others, 2015b, c, d)

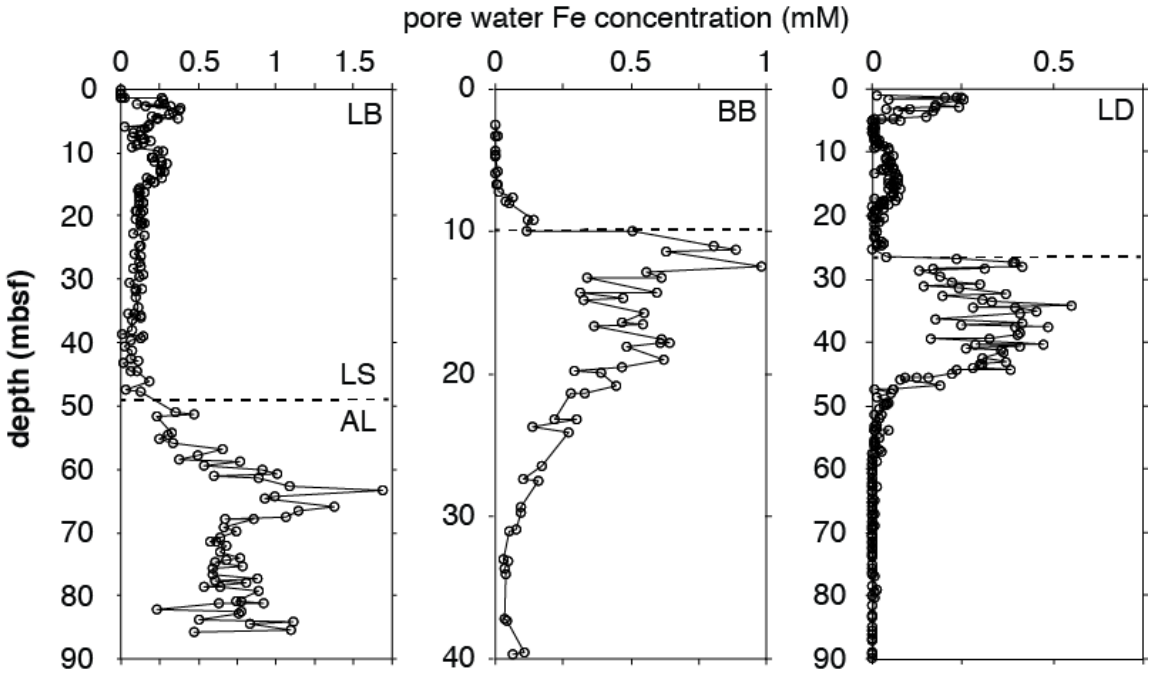

Figure 6. The pore water Fe concentrations from Little Belt (LB), Bornholm Basin (BB), and Landsort Deep (LD). Data are from the IODP 347 Expedition Report (Andrén and others, 2015b, c, d). The dashed line from each site marks the horizon in the profile with the first indications of pore water sulfide accumulation, as constrained from Mo concentrations and $(Fe_{py}+Fe_{AVS})/Fe_{HR}$. In each case this change occurs near the transition from the Ancylus Lake (AL) to the Littorina Sea (LS).

DISCUSSION

Salinity transitions and correlations between sub-basins

Prior to placing our southern Baltic sub-basins in the context of a comprehensive Baltic paleoredox discussion, we must first establish core characteristics that can be used to correlate between our sites, Little Belt and Bornholm Basin, and further link them to sub-basins of the Baltic Proper. In our correlations, we use Landsort Deep to represent Baltic Proper sites, as it has

been compared directly to other Baltic Proper sub-basins in recent work that employed the same paleoredox indicators (Hardisty and others, In Press). Using diatom abundances and total organic carbon contents, we are able to discern the Ancylus Lake (AL), Initial Littorina Sea (ILS), Littorina Sea (LS) onset, Holocene Thermal Maximum (HTM), and Medieval Climate Anomaly (MCA).

The combinations of the carbon and diatom records from this study indicate periods of variable salinity and organic matter preservation, which are already well known from the Baltic. These intervals are markers that can be used to correlate syndepositional periods and events between sub-basins from this and previous studies. First, the Little Belt, Bornholm Basin, and Landsort Deep contain a systematic shift in diatom assemblage that indicates a transition from lacustrine to brackish/marine water column conditions (Figure 2). In each case, the sediments with low TOC and little-to-no diatoms are most parsimoniously linked with sediments of the pre-Littorina stage representing the Ancylus Lake (Sohlenius and others, 2001). Above this interval, lacustrine diatoms are more common than brackish diatoms (Andrén and others, 2015a; Andrén and others, 2015c). This interval is linked to the Initial Littorina Stage, the transition period between the lacustrine Ancylus Lake and brackish Littorina Sea, which lasted from ~9.8-8.5 ka and is characterized by only pulsed inputs of saline waters into the Baltic Basin (Andrén and others, 2011; Björck and others, 2008; Sohlenius and others, 2001). The shift in sedimentary Mo to concentrations greater than the detrital value of 2 ppm but < 25 ppm in Little Belt and the Bornholm Basin, alongside the increase in $(Fe_{py}+Fe_{AVS})/Fe_T$ toward 1 and increasing TOC (Figures 3 and 4), marks the initial presence of appreciable pore water sulfide (See chapter 3). This transition likely fingerprints the input of seawater and associated sulfate into the basin during the Initial Littorina Sea, which promoted sulfate reduction, Fe limitation during

sedimentary pyrite formation, and subsequent pore water sulfide accumulation (Berner, 1984; Berner and Raiswell, 1984; Canfield and others, 1992; Scott and Lyons, 2012). The following interval, where salinity-tolerant diatoms become relatively more abundant, marks the onset of the Littorina Sea and the brackish conditions that still exist today (Sohlenius and others, 2001). Importantly, a previous study comparing the ILS-LS transition between Arkona Basin, Bornholm Basin, and Gotland Deep found that there is a lag between salinification of the southern and northern sub-basins (Sohlenius and others, 2001). This relationship is also likely true for the southern sub-basins of this study relative to Landsort Deep (representing the Baltic Proper).

Notably, each of the three cores contains two peaks in TOC relative to the background, which can be correlated to other Baltic sub-basins (Figure 2). First, a peak in TOC in our southern Baltic sub-basins, specifically Little Belt and Bornholm Basin, occurs in the inferred Initial Littorina Stage and, in the case of Bornholm Basin, near the onset of the Littorina Sea (Figure 2). This same pattern has been observed previously from the Arkona Basin — located between Little Belt and Bornholm Basin (Figure 1) — and occurs in association with the Initial Littorina Sea stage (Sohlenius and others, 2001). Similar to Bornholm Basin, there is a peak in TOC at Landsort Deep that occurs near the onset of the Littorina Sea (Figure 2). Importantly, however, in the case of Landsort Deep and other sub-basins of the Baltic Proper, the TOC peak continues beyond the onset of the Littorina Sea through an interval that overlaps with the Holocene Thermal Maximum, lasting from 8-4 ka years ago (Hardisty and others, In Press; Jilbert and Slomp, 2013). The HTM was marked by higher sea level and reduced freshwater input relative to today, and previous work evaluating Baltic surface salinity suggest that this was the most saline period in the Baltic Sea from relative to the last 4 ka (Gustafsson and Westman, 2002).

The last peak in TOC from the three sub-basins is likely syndepositional with the Medieval Climate Anomaly, which occurred from 1.2-0.8 ka, and has been observed previously in both Fårö and Gotland Deep (Jilbert and Slomp, 2013). Enhanced productivity and burial during this interval is linked to warmer sea surface temperatures (Kabel and others, 2012).

Diagenetic considerations

Before interpreting specific paleoredox settings and their implications, we must consider the potential for diagenetic influences on our proxy records. We specifically focus on potential tracers of anoxia in Bornholm Basin, as it is the only site from this study with distinct intervals with Fe and Mo geochemical indications of anoxia. Records of Fe geochemistry, Mo concentrations, and Mo isotopes from Little Belt largely fall within a range expected from variations in pore water sulfide accumulation and sedimentary Mo input via Mn and Fe oxides (discussed in the next section). Relevant questions from Bornholm Basin include whether trends in sedimentary Mo concentration from the MCA and ILS reflect water column or pore water sulfide variations and whether Fe geochemistry from the ILS-LS transition reflects water column redox or post-depositional Fe and S migration in anoxic pore waters.

First, in the upper sapropel at Bornholm Basin correlated with the MCA (Figure 2), there is an increase in sedimentary Mo concentrations to a value slightly above 25 ppm (Figure 4). This value could reflect the presence of low and variable water column sulfide concentrations (Scott and Lyons, 2012), or alternatively, the presence of pore water sulfide with significant sedimentary delivery of Mo adsorbed to Mn/Fe oxides (Poulson Brucker and others, 2009; Scott and Lyons, 2012). Deciphering between these two possibilities is critical prior to any interpretations about water column paleoredox variations and can be clarified with Fe geochemistry, Mo versus TOC observations, and Mo isotopes. We note that Fe geochemistry provides subtle indications of water

column redox variations in this same interval. Specifically, increases in Fe_T/Al and Fe_{HR}/Fe_T associated with elevated $(Fe_{py}+Fe_{AVS})/Fe_{HR}$ (Figure 4) collectively support the possibility of at least short-lived euxinia. Further, an evaluation of Mo versus TOC from the upper sapropel reveals co-variation between the two (Figure 5), which is most often observed in sediments underlying a euxinic water column (Algeo and Lyons, 2006). Finally, we note that Mo isotope values for this interval are the most positive recorded in the entire profile (Figure 4). These values are unexpected for an interval with a prominent oxide-delivered Mo flux to the sediments, as both Fe and Mn oxides fractionate Mo isotopes to more negative values, by up to 2.9 (Barling and others, 2001; Wasylenki and others, 2008) and 2.2 ‰ (Goldberg and others, 2009), respectively. A non-oxide origin for the sedimentary Mo from this interval is also supported by a lack of associated Mn enrichment (Figure 4). Instead, the Mo isotope values are in a range consistent with variable water column sulfide concentrations of < 100 μM with a large fractionation factor reflecting only partial conversion of molybdate to tetrathiomolybdate (Azrieli-Tal and others, 2014) — a result observed in euxinic portions of the Landsort Deep today and in the recent past (Hardisty and others, In Press; Noordmann and others, 2014). Alternatively, the values approach those often observed in continental margin settings with low oxygen bottom waters and sulfidic pore waters, which are usually near +1.6 ‰ (Poulson Brucker and others, 2009). Though these independent data support multiple interpretations, together, the proxies point to a system that was at least intermittently anoxic, with likely but infrequent accumulation of water column sulfide at low levels.

We further acknowledge that Mo and Fe geochemical evidence from the lower sapropel corresponding to the Littorina Sea also does not have a straightforward interpretation. The Mo concentrations in this interval are < 10 ppm, which, alone, is most consistent with sulfide

accumulation in the pore waters but not the water column (Scott and Lyons, 2012). However, in this case independent proxy evidence from Fe geochemistry indicates water column euxinia (Figure 4), as Fe_T/Al and Fe_{HR}/Fe_T values are both elevated to values indicative of an anoxic water column in combination with $(Fe_{py}+Fe_{AVS})/Fe_{HR}$ values that approach 1 (Table 1). Together, the Mo and Fe properties suggest either a euxinic water column allowing for near-complete scavenging of dissolved water column Mo, resulting in muted sedimentary Mo concentrations, or a ferruginous water column with sulfidic pore fluids. The first scenario is analogous to that in the modern Black Sea, where high sulfide levels and restricted circulation combine to facilitate near-quantitative Mo removal, and can be tested through evaluation of our sedimentary Mo isotope data. The δ^{98}Mo of sediments is expected to mimic that of seawater in a euxinic system where near-complete scavenging of the water column Mo has occurred (Nägler and others, 2011; Neubert and others, 2008). Instead, the Mo isotopes from the ILS interval at Bornholm Basin are the most negative observed in the entire profile (Figure 4) — highly fractionated from seawater and distinctly in a range expected for Mo delivery to the sediments in association with initial uptake via Mn/Fe oxides (Barling and Anbar, 2004; Wasylenki and others, 2008). This interpretation is supported by Mn concentrations in this interval being the highest in the profile (Figure 4). Another possibility is that $(Fe_{py}+Fe_{HR})/Fe_T$ indications of sulfide accumulation in this interval are the result of pore water migration of dissolved sulfide from overlying, more saline (and relatively sulfate-rich) pore fluids into the zone with elevated 'highly reactive' Fe from a ferruginous water column. This is not supported, however, as the directly overlying interval has relatively low $(Fe_{py}+Fe_{HR})/Fe_T$ — most consistent with pore water and sedimentary 'highly reactive' Fe availability that would prevent pore water sulfide accumulation (Figure 4; Table 1). Considering the strong evidence against water column euxinia and pore water sulfide migration during the ILS at Bornholm Basin, we suggest that the combination the Mo and Fe geochemical

data are most parsimoniously linked to a ferruginous water column overlying syndepositionally sulfidic pore fluids.

Further, given our interpretation of pore water sulfide accumulation during the ILS at Bornholm Basin, we must also address the possibility of post-depositional enrichments in Fe_T/Al and Fe_{HR}/Fe_T in this same interval. Changes in Fe_T/Al and Fe_{HR}/Fe_T require the addition of 'extra Fe' to the sediments, either through an anoxic water column and the associated 'Fe shuttle' (Lyons and Severmann, 2006) or upward pore water Fe migration from underlying sediments (Berner, 1969). Given that Bornholm Basin (as well as Landsort Deep and Little Belt) contains elevated pore water dissolved Fe concentrations in Ancylus Lake sediments, which sharply decrease at the Initial Littorina Sea boundary (Figure 6), it is possible that the diffusion of Ancylus Lake pore water Fe to the overlying sulfidic Littorina pore waters caused post-depositional Fe enrichments. We will further consider this possibility.

In order to assess the possibility of Fe diffusing upward into sulfidic sediments and its potential authigenic Fe contribution to Fe_T/Al, we use Fick's First law of diffusion, as applied to sediments (Berner, 1980), to calculate Fe_{auth} at the AL-ILS transition in Bornholm Basin. For comparison, we include similar data from Little Belt and Landsort Deep:

$$Fe_{auth} = \frac{J}{\omega\rho}$$

$$J = -\varphi D_s \frac{\Delta C}{\Delta z} \ ,$$

where $\boldsymbol{\varphi}$ = porosity, $\mathbf{D_s}$ = diffusion coefficient with a value of 5.268×10^{-6} cm^2/sec for Fe^{2+} (Li and Gregory, 1974), $\boldsymbol{\Delta C}$ = change in pore water concentration across sulfide interface, $\boldsymbol{\Delta z}$ =

depth interval from which ΔC is measured, $\boldsymbol{\omega}$ = sedimentation rate (cm/sec), and $\boldsymbol{\rho}$ = sediment density (g/cm^3)

In our calculation, we model the mass flux (J) of Fe across the dissolved Fe-sulfide front from the Ancylus Lake to overlying sulfidic pore waters, assuming complete precipitation of pore water dissolved Fe as Fe sulfides. To provide a liberal maximum Fe_{auth} estimate, we use the maximum observed pore water Fe concentration from the Ancylus Lake sediments to represent ΔC. Also, although the Δz for the observed large ΔC is presently on the scale of > 0.5 m at all sites (Figure 6), we use a Δz of 5 cm at each site to account for the likely profile smoothing that occurred via diffusion over time. This is a liberal estimate, as this distance is likely much smaller than reality and Fe_{auth} increases with decreasing Δz — that is, a steeper concentration gradient. The mass flux can then be used, in combination with the sediment density ($\boldsymbol{\rho}$), porosity ($\boldsymbol{\varphi}$), sedimentation rate ($\boldsymbol{\omega}$), and the minimum Al concentration among samples with observed elevated Fe_T/Al, to estimate a potential range of authigenic Fe_T/Al enrichments (Table 2).

Table 2. Values and associated sources for calculations shown in Figure 7.

Basin	**ΔC** (mM)[a]	$\boldsymbol{\rho}$ (g/cm^3)[b]	$\boldsymbol{\varphi}$ [b]	$\boldsymbol{\omega}$ (cm/sec)[c]	$\mathbf{Al_{min}}$ (wt.%)[d]
Little Belt	1.70	0.75	0.8	0.35	4.9
Bornholm Basin	0.98	1.5	0.8	0.21	7.5
Landsort Deep	0.56	0.8	0.8	0.12	3.8

[a]Figure 4, [b]Andrén and others, (2015b, c, d), [c]Mort and others, (2010), [d]Supplementary Data Tables 1 and 2, Hardisty and others, (In Press)

In all cases, calculations suggest that the observed Fe_T/Al cannot be entirely or at all explained by upward Fe migration into sulfidic sediments (Figure 7). Most importantly, the model results indicate that upward Fe migration could contribute to the observed Fe_T/Al enrichments at Bornholm Basin and Landsort Deep but cannot account for the full enrichments. Further, our liberal model estimates are best highlighted by the calculated Fe_{auth} increase in

Fe_T/Al by ~0.21 at Little Belt, a location where no significant increases in Fe_T/Al are observed through the whole profile. This emphasizes that our Fe_{auth} calculations from Bornholm Basin and Landsort Deep are likely also overestimates. Together, these outcomes ultimately imply that a substantial portion of the observed Fe_T/Al enrichments at both Bornholm Basin and Landsort Deep in the period following Ancylus Lake deposition likely resulted from primary water column redox dynamics and the associated Fe shuttle, thus permitting interpretation related to water column redox variations.

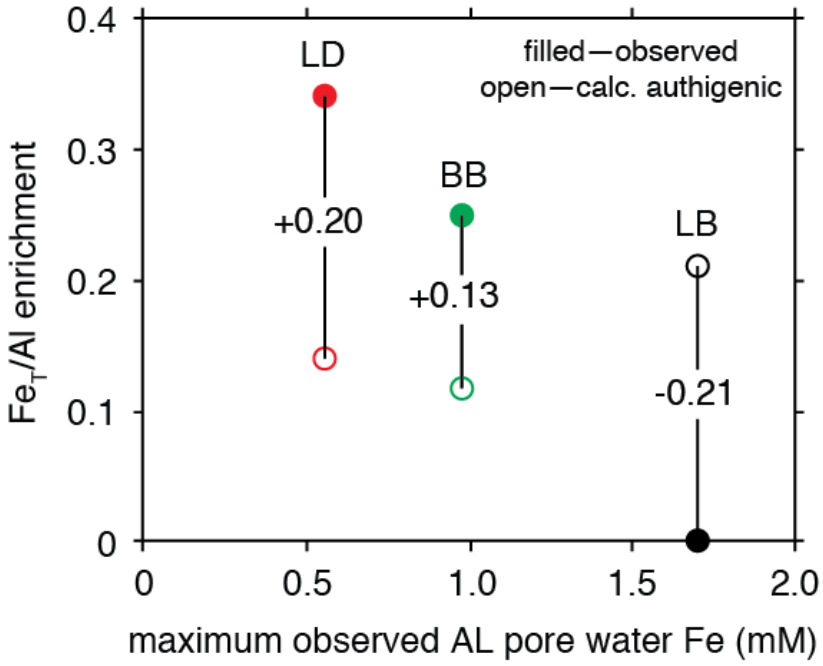

Figure 7. Comparison of observed (filled) and calculated authigenic (open) Fe_T/Al enrichments at Little Belt (LB), Bornholm Basin (BB), and Landsort Deep (LD). Observed Fe_T/Al enrichments represent the maximum from the interval directly overlying the Ancylus Lake-Littorina Sea transition relative to a detrital baseline of 0.65 (Fehr and others, 2008). Maximum pore water Fe concentrations come from the Ancylus Lake (AL) sediments and represent ΔC in equation 2.

Baltic Holocene paleoredox

Together with previously published paleoredox records from the Baltic Proper (Hardisty and others, In Press; Jilbert and Slomp, 2013; Sohlenius and others, 2001) and the more northern Bothnian Sea (Jilbert and others, 2015), our southern Baltic paleoredox records can be used to comprehensively assess the spatiotemporal dynamics of Holocene Baltic anoxia to compare to the present. A conceptual illustration of Baltic paleoredox during the intervals identified in this study and by others is shown in Figure 8.

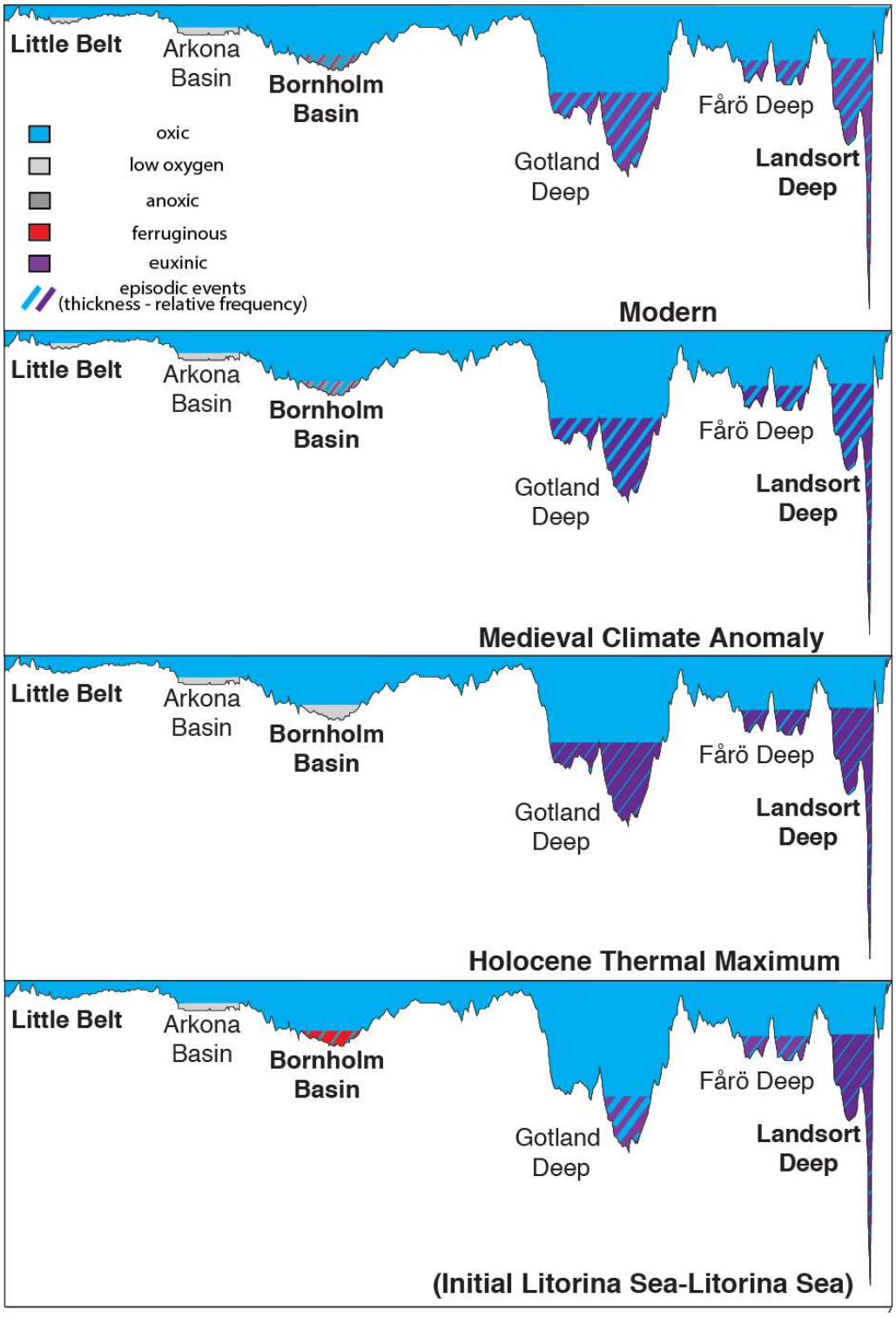
Little Belt
Arkona Basin
Bornholm Basin
Gotland Deep
Fårö Deep
Landsort Deep
oxic
low oxygen
anoxic
ferruginous
euxinic
episodic events
(thickness - relative frequency)
Modern
Little Belt
Arkona Basin
Bornholm Basin
Gotland Deep
Fårö Deep
Landsort Deep
Medieval Climate Anomaly
Little Belt
Arkona Basin
Bornholm Basin
Gotland Deep
Fårö Deep
Landsort Deep
Holocene Thermal Maximum
Little Belt
Arkona Basin
Bornholm Basin
Gotland Deep
Fårö Deep
Landsort Deep
(Initial Litorina Sea-Litorina Sea)

Figure 8. Representations of the generalized water column redox conditions at sub-basins from this (bold) and previous studies based on paleoredox data for Arkona Basin, Gotland Deep, Fårö Deep, and Landsort Deep. Paleoredox proxies discussed in the text are used to infer the specific paleoredox conditions, spanning low oxygen (sediment laminations), anoxic (Fe geochemistry), ferruginous (Fe geochemistry), euxinic (Fe and Mo geochemistry), and episodic oxygenation events (Mn and Mo geochemistry). The relative frequency of oxygenation of euxinic bottom waters at Gotland and Fårö Deeps is extrapolated from that inferred from manganese and molybdenum isotope compositions of Landsort Deep (Hardisty and others, In Press). This approach is justified at Gotland Deep by the presence of modern water column chemistry and accompanying modern sedimentary Mo, Mn, and Fe geochemistry, including Mo isotopes, that are similar to those of Landsort Deep. Outside of Gotland Deep at the ILS-LS transition, the haloclines marking the vertical onset of water column redox changes are placed at the depths seen in the modern sub-basins. At Gotland Deep during the ILS-LS, a previous study has specifically inferred a deeper halocline, which is represented in the figure (Sohlenius and others, 2001). This may be true for other sub-basins of the Baltic Proper, but constraints are lacking. Further, during the HTM, higher bottom water salinity and reduced freshwater runoff to the Baltic (Gustafsson and Westman, 2002) may have resulted in haloclines at different positions relative to today — likely shallower. Also, the present-day bathymetries are used in each scenario shown, although we acknowledge that both glacio-isostatic rebound of the Baltic seafloor and different sea level would have caused these to be different during the ILS-LS transition and HTM.

Initial Littorina Sea through Holocene Thermal Maximum

Anoxic conditions are inferred from geochemical proxy records and laminations in association with the Initial Littorina Sea-to-Littorina Sea transition at each Bornholm Basin (this study and (Sohlenius and others, 2001)), Landsort Deep (Hardisty and others, In Press; Zillén and others, 2008), Gotland Deep (Jilbert and Slomp, 2013; Sohlenius and others, 2001; Zillén and others, 2008), Fårö Deep (Jilbert and Slomp, 2013), and the Bothnian Sea. In the southern sub-basins specifically, we observe oxic/seasonally low oxygen at Little Belt based on sediment laminations lacking clear geochemical anoxic indicators (Figure 3 and 8) and ferruginous conditions at Bornholm Basin (Figures 4 and 8). Geochemical records from previous studies have indicated euxinic conditions in the Baltic Proper (Hardisty and others, In Press; Jilbert and Slomp, 2013; Sohlenius and others, 2001) and Bothnian Sea (Jilbert and others, 2015) at the ILS-IS boundary and after (Figure 8) — a condition clearly more reducing than that in the southern Baltic sub-basins at this time. Like today, it appears that conditions were progressively more reducing with increasing distance from the sill at the ILS-LS boundary and during the HTM. As has been suggested in previous work, the formation of a halocline in association with the salinification of the Baltic Basin best explains the onset of anoxia from this time period (Sohlenius and others, 2001; Zillén and others, 2008), and our study provides specific constraints on the degree and frequency of anoxia as related to salinification.

The occurrence of a ferruginous water column at Bornholm Basin during the ILS-LS transition — as justified in the diagenetic discussion — is significant because these conditions contrast starkly with that observed in the modern Bornholm, which is currently episodically euxinic (Figures 1 and 8). A previous study has identified reducing conditions at Bornholm Basin in association with the ILS-LS transition (Sohlenius and others, 2001); however, ours is the first

study to specifically define the redox regime at Bornholm Basin during this time and the first clear identification of a ferruginous marine-connected basin in the recent past more generally. The ferruginous conditions at Bornholm Basin appear during the ILS and disappear near the ILS-LS transition, which can be contrasted with the Baltic Proper sub-basins such as Landsort Deep, where euxinia is first noted near the ILS-LS transition (Figure 8). We suggest that this spatiotemporal redox difference is a product of rising sea level and resulting halocline formation, MBI frequency, and associated sulfate input into the Baltic Basin.

The progressive input of saline water from the North Sea along with rising sea level leading up to the ILS-LS transition would first allow for a more developed halocline at southern Baltic sub-basins, like Bornholm Basin (Sohlenius and others, 2001). One potential explanation for the observation of ferruginous — as opposed to euxinic — water column conditions at Bornholm Basin during the ILS that precede euxinic indications in the Baltic Proper is limited sulfate input into the basin. Sulfate limitation from the low sulfate concentrations associated with only weak and sporadic pulses of saline water input to the Baltic during this period could limit sulfate reduction to sedimentary pore fluids — as is inferred from our proxy record. Further, similar to those of today, episodic major Baltic inflows (MBIs) of oxygenated and saline marine water from the North Sea likely provided a mechanism for the interruption of anoxic conditions, thus preventing water column sulfide accumulation, as well as oxidation of dissolved Fe accumulated in the water column. Following sedimentary delivery, Fe oxides could then react with pore water sulfide to form pyrite, thus explaining our 'conflicted' Fe and Mo geochemical proxy indications from this interval. A modern analogy for this scenario comes from observations of the Fe geochemistry of sediments beneath the modern ferruginous Peruvian oxygen minimum zone (OMZ). Here, indications of anoxia only occur at the edge of the OMZ where a ferruginous-

oxic boundary exists (Scholz and others, 2014), similar to the possible ferruginous-oxic boundary resulting from MBIs. Additional support for this interpretation comes from elevated Mn concentrations in tandem with the most negative Mo isotope values in the entire profile found within this interval (Figure 4) — both pointing to Mn oxide delivery to the sediments. Enhanced Mn oxide delivery is observed in sediments from later time periods in the Baltic Proper and has been linked to the oxidation of dissolved water column Mn following oxygenated MBIs (Hardisty and others, In Press).

The onset of the Littorina Sea marks a period of increasing salinity and sulfate in the Baltic from rising sea level and decreased freshwater input (Gustafsson and Westman, 2002), combined with lower sill depths from muted glacio-isostatic rebound relative to today (Jilbert and others, 2015). At this transition and through the HTM (Figure 8), ferruginous indications disappear from Bornholm Basin, but sedimentary Mn enrichments continue (Figure 4), Baltic Proper sub-basins become clearly euxinic (Hardisty and others, In Press; Jilbert and Slomp, 2013; Sohlenius and others, 2001), and euxinia can be identified as far north as the Bothnian Sea (Jilbert and others, 2015). Together, these lines of evidence illustrate that the factors increasing salinity during this time acted to strengthen and expand the halocline in the Baltic Proper and Bothnian Sea, and associated euxinia expanded spatially beyond even that observed in these regions today (Hardisty and others, In Press; Jilbert and others, 2015). Supporting this inference, previously published Mo isotope and Mn records from the Landsort Deep HTM suggest that euxinia was more stable with higher water column dissolved sulfide concentrations relative to today (Hardisty and others, In Press). However, our observations from Bornholm Basin indicate that the increased salinity and oxygenated North Sea water input during MBIs simultaneously promoted relatively more frequent oxic conditions in sill-proximal southern Baltic sub-basins. Implicit in our

observations is that the glacio-isostatic and salinity controls responsible for the expansion and stabilization of euxinia in Baltic Proper sub-basins during the HTM had the opposite effect in southern Baltic sub-basins, leading to more oxic conditions relative to the directly preceding interval.

Many factors likely acted to control the spatiotemporal variability in the degree and frequency of anoxia during the ILS-LS and HTM, including the Baltic phosphorous budget (Jilbert and others, 2015), glacio-isostatic rebound (Jilbert and others, 2015), and salinity (Sohlenius and others, 2001; Zillén and others, 2008). Our data most specifically highlight the importance of salinity as related to the frequency and scale of MBIs and halocline development as a major control on the specific paleoredox regimes and their spatial extent during the ILS-LS and HTM. This conclusion is supported by the importance of MBIs and associated halocline strength as a key control on the frequency and degree of reducing conditions in modern Baltic sub-basins (Carstensen and others, 2014). Further, already well-established differences between the salinity of the Baltic basin during the Ancylus Lake-Littorina Sea transition and the HTM relative to today (Gustafsson and Westman, 2002) likely best explain the presence of redox regimes not observed at the same localities today. As illustrated in Figure 8, these paleoredox scenarios are specifically, ferruginous conditions at Bornholm Basin, relatively higher and more stable water column sulfide concentrations in some Baltic Proper sub-basins (Hardisty and others, In Press), and the expansion of euxinia into the presently oxic Bothnian Sea (Jilbert and others, 2015).

Medieval Climate Anomaly

The paleoredox conditions from the southern Baltic, Baltic Proper, and Bothnian Sea during the period interpreted to reflect the MCA appear to be most directly comparable to those observed today (Figure 8). At Little Belt, laminations are observed but without geochemical

indications of anoxic conditions, as during the HTM (Figure 3). This combination specifically implies low oxygen conditions persisting seasonally or longer that largely excluded benthic fauna — a situation similar to that observed today (Figures 1 and 8). At Bornholm Basin, slightly enriched Fe_T/Al is observed with Mo concentrations near 25 ppm, which — as discussed in detail in the diagenetic discussion — may indicate variable euxinia. This interpretation is directly comparable to the modern Bornholm Basin. Modern water column observations at Bornholm Basin reflect a basin with the potential for short-term anoxia and episodic euxinia (Figure 1). These water column observations are consistent with Mo concentrations from modern Bornholm Basin sediments near 35 ppm (Mort and others, 2010), supporting variably euxinic conditions (Scott and Lyons, 2012) and similar to what is observed during the MCA from this study. This series of calibrations from both modern water columns and sediments provides strong evidence that the degree and frequency of water column anoxia during the MCA were most comparable to what is observed today in southern sill-proximal sub-basins. This interpretation is further buttressed by paleoredox inferences from the Baltic Proper (Hardisty and others, In Press) and Bothnian Sea (Jilbert and others, 2015) that are similar to what is observed in the modern sub-basins.

During the MCA, semi-permanent euxinic conditions are inferred from multiple Baltic Proper sub-basins — Landsort Deep (Hardisty and others, In Press), Faro Deep (Jilbert and Slomp, 2013), and Gotland Deep (Jilbert and Slomp, 2013) — based on the presence of large Mo enrichments >100 ppm and Fe speciation consistent with euxinia, as is observed today in these sub-basins. At Landsort Deep, combined Mo isotopes and large Mn enrichments similar to those in modern Landsort Deep sediments specifically imply semi-permanent euxinia punctuated by oxygenated MBIs during the MCA (Hardisty and others, In Press) — consistent with modern

water column observations at this site (Figure 1). Further, the MCA and modern Mn and Mo geochemistry at Landsort Deep varies from that of the HTM, where results indicate euxinia more stable than following intervals. Beyond the Baltic Proper, similarities in Baltic water column redox today and during the MCA are further suggested by a lack of anoxic geochemical proxy indications in the more northern Bothnian Sea, which is presently oxic (Jilbert and others, 2015). Together with previous studies, our results from Bornholm Basin and Little Belt provide evidence for a sill-proximal to sill-distal paleoredox transect during the MCA that was similar to today's, that is, seasonally low oxygen transitioning laterally to variable euxinia and then semi-permanent euxinia.

The similar redox conditions between the modern and MCA relative to earlier periods is likely a result of more comparable salinity (Gustafsson and Westman, 2002), bathymetry (Jilbert and others, 2015), and temperature regimes (Kabel and others, 2012). Indeed, some studies have even speculated that anthropogenic nutrient loading, as we see today, may have played a key role in driving anoxia during this period (Zillén and others, 2008).

CONCLUSIONS

This study focused on the Holocene paleosalinity and paleoredox records from Baltic sub-basins along a transect moving away from the sill — Little Belt to Bornholm Basin to Landsort Deep (Baltic Proper) — to compare past water column anoxic events and controls to those of the modern. In contrast to previous Baltic paleoredox studies from multiple sub-basins, our combined Fe-Mn-Mo paleoredox proxy approach is sensitive to the range in frequency and degree of redox conditions observed along this same transect in the modern — that is, seasonally low oxygen, variable euxinia, semi-permanent euxinia, from sill proximal to sill distal.

In the past, as today, our paleoredox records imply a prominent salinity influence on Baltic anoxia and the existence of past sill-proximal to sill-distal redox gradients. These characteristics can be broken down into three stages: (1) the salinity transition from the Ancylus Lake to Littorina Sea, (2) higher salinity during the HTM relative to the MCA and today, and (3) the episodic input of oxygenated and saline North Sea water via Massive Baltic Inflows throughout the Holocene. We ultimately suggest that previous natural Baltic anoxic periods have been distinctly different and often more reducing than the modern — specifically those associated with the Ancylus Lake-Littorina Sea transition and Holocene Thermal Maximum. These sill-proximal to sill-distal paleoredox regimes were marked by a progression from oxic or seasonally low oxygen waters to ferruginous to euxinia relatively more expansive and stable than today. Water column redox conditions similar to the modern also occurred, specifically during the Medieval Climate Anomaly.

REFERENCES

Algeo, T. J. and Lyons, T. W., 2006, Mo–total organic carbon covariation in modern anoxic marine environments: Implications for analysis of paleoredox and paleohydrographic conditions: Paleoceanography, v. 21, p.

Andrén, T., Björck, S., Andrén, E., Conley, D., Zillén, L. and Anjar, J. (2011) The development of the Baltic Sea Basin during the last 130 ka, The Baltic Sea Basin. Springer, p. 75-97.

Andrén, T., Jørgensen, B. B., Cotterill, C., Green, S., Andrén, E., Ash, J., Bauersachs, T., Cragg, B., Fanget, A.-S., Fehr, A., Granoszewski, W., Groeneveld, J., Hardisty, D., Herrero-Bervera, E., Hyttinen, O., Jensen, J. B., Johnson, S., Kenzler, M., Kotilainen, A., Kotthoff, U., Marshall, I. P. G., Martin, E., Obrochta, S., Passchier, S., Quintana Krupinski, N., Riedinger, N., Slomp, C., Snowball, I., Stepanova, A., Strano, S., Torti, A., Warnock, J., Xiao, N. and Zhang, R., 2015a, M0063, v. In Andrén, T., Jørgensen, B.B., Cotterill, C., Green, S., and the Expedition 347 Scientists, Proc. IODP, 347: College Station, TX (Integrated Ocean Drilling Program), p.

Andrén, T., Jørgensen, B. B., Cotterill, C., Green, S., Andrén, E., Ash, J., Bauersachs, T., Cragg, B., Fanget, A.-S., Fehr, A., Granoszewski, W., Groeneveld, J., Hardisty, D. S., Herrero-Bervera, E., Hyttinen, O., Jensen, J. B., Johnson, S., Kenzler, M., Kotilainen, A., Kotthoff, U., Marshall, I. P. G., Martin, E., Obrochta, S., Passchier, S., Quintana Krupinski, N., Riedinger, N., Slomp, C., Snowball, I., Stepanova, A., Strano, S., Torti, A., Warnock, J., Xiao, N. and Zhang, R., 2015b, Site M0059: In Andrén, T., Jørgensen, B.B., Cotterill, C., Green, S., and the Expedition 347 Scientists, Proc. IODP, 347: College Station, TX (Integrated Ocean Drilling Program), v. 347, p.

Andrén, T., Jørgensen, B. B., Cotterill, C., Green, S., Andrén, E., Ash, J., Bauersachs, T., Cragg, B., Fanget, A.-S., Fehr, A., Granoszewski, W., Groeneveld, J., Hardisty, D. S., Herrero-Bervera, E., Hyttinen, O., Jensen, J. B., Johnson, S., Kenzler, M., Kotilainen, A., Kotthoff, U., Marshall, I. P. G., Martin, E., Obrochta, S., Passchier, S., Quintana Krupinski, N., Riedinger, N., Slomp, C., Snowball, I., Stepanova, A., Strano, S., Torti, A., Warnock, J., Xiao, N. and Zhang, R., 2015c, Site M0063: In Andrén, T., Jørgensen, B.B., Cotterill, C., Green, S., and the Expedition 347 Scientists, Proc. IODP, 347: College Station, TX (Integrated Ocean Drilling Program), v., p.

Andrén, T., Jørgensen, B. B., Cotterill, C., Green, S., Andrén, E., Ash, J., Bauersachs, T., Cragg, B., Fanget, A.-S., Fehr, A., Granoszewski, W., Groeneveld, J., Hardisty, D. S., Herrero-Bervera, E., Hyttinen, O., Jensen, J. B., Johnson, S., Kenzler, M., Kotilainen, A., Kotthoff, U., Marshall, I. P. G., Martin, E., Obrochta, S., Passchier, S., Quintana Krupinski, N., Riedinger, N., Slomp, C., Snowball, I., Stepanova, A., Strano, S., Torti, A., Warnock, J., Xiao, N. and Zhang, R., 2015d, Site M0065: In Andrén, T., Jørgensen, B.B., Cotterill, C., Green, S., and the Expedition 347 Scientists, Proc. IODP, 347: College Station, TX (Integrated Ocean Drilling Program), v. 347, p.

Andrén, T., Jørgensen, B. B., Cotterill, C., Green, S., Andrén, E., Ash, J., Bauersachs, T., Cragg, B., Fanget, A.-S., Fehr, A., Granoszewski, W., Groeneveld, J., Hardisty, D. S., Herrero-Bervera, E., Hyttinen, O., Jensen, J. B., Johnson, S., Kenzler, M., Kotilainen, A.,

Kotthoff, U., Marshall, I. P. G., Martin, E., Obrochta, S., Passchier, S., Quintana Krupinski, N., Riedinger, N., Slomp, C., Snowball, I., Stepanova, A., Strano, S., Torti, A., Warnock, J., Xiao, N. and Zhang, R., 2015e, M0063, v. In Andrén, T., Jørgensen, B.B., Cotterill, C., Green, S., and the Expedition 347 Scientists, Proc. IODP, 347: College Station, TX (Integrated Ocean Drilling Program), p.

Arnold, G. L., Anbar, A., Barling, J. and Lyons, T., 2004, Molybdenum isotope evidence for widespread anoxia in mid-Proterozoic oceans: science, v. 304, p. 87-90.

Asael, D., Tissot, F. L., Reinhard, C. T., Rouxel, O., Dauphas, N., Lyons, T. W., Ponzevera, E., Liorzou, C. and Chéron, S., 2013, Coupled molybdenum, iron and uranium stable isotopes as oceanic paleoredox proxies during the Paleoproterozoic Shunga Event: Chemical Geology, v. 362, p. 193-210.

Azrieli-Tal, I., Matthews, A., Bar-Matthews, M., Almogi-Labin, A., Vance, D., Archer, C. and Teutsch, N., 2014, Evidence from molybdenum and iron isotopes and molybdenum–uranium covariation for sulphidic bottom waters during Eastern Mediterranean sapropel S1 formation: Earth and Planetary Science Letters, v. 393, p. 231-242.

Barling, J. and Anbar, A., 2004, Molybdenum isotope fractionation during adsorption by manganese oxides: Earth and Planetary Science Letters, v. 217, p. 315-329.

Barling, J., Arnold, G. L. and Anbar, A., 2001, Natural mass-dependent variations in the isotopic composition of molybdenum: Earth and Planetary Science Letters, v. 193, p. 447-457.

Berner, R. A., 1969, Migration of iron and sulfur within anaerobic sediments during early diagenesis: American Journal of Science, v. 267, p. 19-42.

Berner, R. A., 1980, Early diagenesis: A theoretical approach. Princeton University Press.

Berner, R. A., 1984, Sedimentary pyrite formation: an update: Geochimica et Cosmochimica Acta, v. 48, p. 605-615.

Berner, R. A., Baldwin, T. and Holdren Jr, G. R., 1979, Authigenic iron sulfides as paleosalinity indicators: Journal of Sedimentary Research, v. 49, p.

Berner, R. A. and Canfield, D. E., 1989, A new model for atmospheric oxygen over Phanerozoic time: Am. J. Sci, v. 289, p. 333-361.

Berner, R. A. and Raiswell, R., 1984, C/S method for distinguishing freshwater from marine sedimentary rocks: Geology, v. 12, p. 365-368.

Bertine, K. K. and Turekian, K. K., 1973, Molybdenum in marine deposits: Geochimica et Cosmochimica Acta, v. 37, p. 1415-1434.

Björck, S., Andrén, T. and Jensen, J. B., 2008, An attempt to resolve the partly conflicting data and ideas on the Ancylus-Littorina transition: Polish Geological Institute Special Papers, v. 23, p. 21-26.

Canfield, D. E., 1989, Reactive iron in marine sediments: Geochimica et Cosmochimica Acta, v. 53, p. 619-632.

Canfield, D. E. and Berner, R. A., 1987, Dissolution and pyritization of magnetite in anoxie marine sediments: Geochimica et Cosmochimica Acta, v. 51, p. 645-659.

Canfield, D. E., Lyons, T. W. and Raiswell, R., 1996, A model for iron deposition to euxinic Black Sea sediments: American Journal of Science, v. 296, p. 818-834.

Canfield, D. E., Raiswell, R. and Bottrell, S. H., 1992, The reactivity of sedimentary iron minerals toward sulfide: American Journal of Science, v. 292, p. 659-683.

Carstensen, J., Andersen, J. H., Gustafsson, B. G. and Conley, D. J., 2014, Deoxygenation of the Baltic Sea during the last century: Proceedings of the National Academy of Sciences, v. 111, p. 5628-5633.

Chanton, J. P. and Martens, C. S., 1985, The effects of heat and stannous chloride addition on the active distillation of acid volatile sulfide from pyrite-rich marine sediment samples: Biogeochemistry, v. 1, p. 375-382.

Cline, J. D., 1969, Spectrophotometric determination of hydrogen sulfide in natural waters: Limnology and Oceanography, v. 14, p. 454-458.

Dahl, T. W., Chappaz, A., Fitts, J. P. and Lyons, T. W., 2013, Molybdenum reduction in a sulfidic lake: Evidence from X-ray absorption fine-structure spectroscopy and implications for the Mo paleoproxy: Geochimica et Cosmochimica Acta, v. 103, p. 213-231.

Erickson, B. E. and Helz, G. R., 2000, Molybdenum (VI) speciation in sulfidic waters:: stability and lability of thiomolybdates: Geochimica et Cosmochimica Acta, v. 64, p. 1149-1158.

Fehr, M. A., Andersson, P. S., Hålenius, U. and Mörth, C.-M., 2008, Iron isotope variations in Holocene sediments of the Gotland Deep, Baltic Sea: Geochimica et Cosmochimica Acta, v. 72, p. 807-826.

Ferdelman, T. G., 1988, The distribution of sulfur, iron, manganese, copper and uranium in a salt marsh sediment core as determined by a sequential extraction method. University of Delaware, MS thesis.

Franck, H., Matthäus, W. and Sammler, R., 1987, Major inflows of saline water into the Baltic Sea during the present century: Gerlands Beiträge zur Geophysik, v. 96, p. 517-531.

Goldberg, T., Archer, C., Vance, D. and Poulton, S. W., 2009, Mo isotope fractionation during adsorption to Fe (oxyhydr) oxides: Geochimica et Cosmochimica Acta, v. 73, p. 6502-6516.

Gustafsson, B. G. and Westman, P., 2002, On the causes for salinity variations in the Baltic Sea during the last 8500 years: Paleoceanography, v. 17, p. 12-11-12-14.

Hardisty, D. S., Riedinger, N., Planavsky, N. J., Asael, D., Andrén, T., Jørgensen, B. B. and Lyons, T. W., In Press, A Holocene history of dynamic water column redox conditions in the Landsort Deep, Baltic Sea American Journal of Science, v., p.

Hurtgen, M. T., Lyons, T. W., Ingall, E. D. and Cruse, A. M., 1999, Anomalous enrichments of iron monosulfide in euxinic marine sediments and the role of H2S in iron sulfide transformations: examples from Effingham Inlet, Orca Basin, and the Black Sea: American Journal of Science, v. 299, p. 556-588.

Jilbert, T., Conley, D. J., Gustafsson, B. G., Funkey, C. P. and Slomp, C. P., 2015, Glacio-isostatic control on hypoxia in a high-latitude shelf basin: Geology, v. 43, p. 427-430.

Jilbert, T. and Slomp, C. P., 2013, Rapid high-amplitude variability in Baltic Sea hypoxia during the Holocene: Geology, v. 41, p. 1183-1186.

Kabel, K., Moros, M., Porsche, C., Neumann, T., Adolphi, F., Andersen, T. J., Siegel, H., Gerth, M., Leipe, T. and Jansen, E., 2012, Impact of climate change on the Baltic Sea ecosystem over the past 1,000 years: Nature Climate Change, v. 2, p. 871-874.

Kashiwabara, T., Takahashi, Y. and Tanimizu, M., 2009, A XAFS study on the mechanism of isotopic fractionation of molybdenum during its adsorption on ferromanganese oxides: Geochemical Journal, v. 43, p. e31-e36.

Kostka, J. E. and Luther, G. W., 1994, Partitioning and speciation of solid phase iron in saltmarsh sediments: Geochimica et Cosmochimica Acta, v. 58, p. 1701-1710.

Krishnaswami, S., 1976, Authigenic transition elements in Pacific pelagic clays: Geochimica et Cosmochimica Acta, v. 40, p. 425-434.

Lyons, T. W., 1997, Sulfur isotopic trends and pathways of iron sulfide formation in upper Holocene sediments of the anoxic Black Sea: Geochimica et Cosmochimica Acta, v. 61, p. 3367-3382.

Lyons, T. W. and Severmann, S., 2006, A critical look at iron paleoredox proxies: new insights from modern euxinic marine basins: Geochimica et Cosmochimica Acta, v. 70, p. 5698-5722.

Lyons, T. W., Werne, J. P., Hollander, D. J. and Murray, R., 2003, Contrasting sulfur geochemistry and Fe/Al and Mo/Al ratios across the last oxic-to-anoxic transition in the Cariaco Basin, Venezuela: Chemical Geology, v. 195, p. 131-157.

Matthäus, W., 2006, The History of Investigation of Salt Water Inflows Into the Baltic Sea: From Early Beginning to Recent Results. Institut für Meereskunde Warnemhunde.

Miller, C. A., Peucker-Ehrenbrink, B., Walker, B. D. and Marcantonio, F., 2011, Re-assessing the surface cycling of molybdenum and rhenium: Geochimica et Cosmochimica Acta, v. 75, p. 7146-7179.

Mohrholz, V., Naumann, M., Nausch, G., Krüger, S. and Gräwe, U., 2015, Fresh oxygen for the Baltic Sea—An exceptional saline inflow after a decade of stagnation: Journal of Marine Systems, v. 148, p. 152-166.

Morse, J. W. and Cornwell, J. C., 1987, Analysis and distribution of iron sulfide minerals in recent anoxic marine sediments: Marine Chemistry, v. 22, p. 55-69.

Mort, H. P., Slomp, C. P., Gustafsson, B. G. and Andersen, T. J., 2010, Phosphorus recycling and burial in Baltic Sea sediments with contrasting redox conditions: Geochimica et Cosmochimica Acta, v. 74, p. 1350-1362.

Nägler, T., Neubert, N., Böttcher, M., Dellwig, O. and Schnetger, B., 2011, Molybdenum isotope fractionation in pelagic euxinia: Evidence from the modern Black and Baltic Seas: Chemical Geology, v. 289, p. 1-11.

Nägler, T. F., Anbar, A. D., Archer, C., Goldberg, T., Gordon, G. W., Greber, N. D., Siebert, C., Sohrin, Y. and Vance, D., 2014, Proposal for an international molybdenum isotope measurement standard and data representation: Geostandards and Geoanalytical Research, v. 38, p. 149-151.

Neubert, N., Nägler, T. F. and Böttcher, M. E., 2008, Sulfidity controls molybdenum isotope fractionation into euxinic sediments: Evidence from the modern Black Sea: Geology, v. 36, p. 775-778.

Noordmann, J., Weyer, S., Montoya-Pino, C., Dellwig, O., Neubert, N., Eckert, S., Paetzel, M. and Böttcher, M., 2014, Uranium and molybdenum isotope systematics in modern euxinic basins: Case studies from the central Baltic Sea and the Kyllaren fjord (Norway): Chemical Geology, v., p.

Poulson Brucker, R. L., McManus, J., Severmann, S. and Berelson, W. M., 2009, Molybdenum behavior during early diagenesis: Insights from Mo isotopes: Geochemistry, Geophysics, Geosystems, v. 10, p.

Poulton, S. W. and Canfield, D. E., 2005, Development of a sequential extraction procedure for iron: implications for iron partitioning in continentally derived particulates: Chemical Geology, v. 214, p. 209-221.

Poulton, S. W. and Canfield, D. E., 2011, Ferruginous conditions: a dominant feature of the ocean through Earth's history: Elements, v. 7, p. 107-112.

Raiswell, R., Canfield, D. and Berner, R., 1994, A comparison of iron extraction methods for the determination of degree of pyritisation and the recognition of iron-limited pyrite formation: Chemical Geology, v. 111, p. 101-110.

Raiswell, R. and Canfield, D. E., 1998, Sources of iron for pyrite formation in marine sediments: American Journal of Science, v. 298, p. 219-245.

Raiswell, R., Vu, H. P., Brinza, L. and Benning, L. G., 2010, The determination of labile Fe in ferrihydrite by ascorbic acid extraction: methodology, dissolution kinetics and loss of solubility with age and de-watering: Chemical Geology, v. 278, p. 70-79.

Scholz, F., Severmann, S., McManus, J. and Hensen, C., 2014, Beyond the Black Sea paradigm: The sedimentary fingerprint of an open-marine iron shuttle: Geochimica et Cosmochimica Acta, v. 127, p. 368-380.

Scott, C. and Lyons, T. W., 2012, Contrasting molybdenum cycling and isotopic properties in euxinic versus non-euxinic sediments and sedimentary rocks: refining the paleoproxies: Chemical Geology, v. 324, p. 19-27.

Sohlenius, G., Emeis, K.-C., Andrén, E., Andrén, T. and Kohly, A., 2001, Development of anoxia during the Holocene fresh–brackish water transition in the Baltic Sea: Marine geology, v. 177, p. 221-242.

Tossell, J., 2005, Calculating the partitioning of the isotopes of Mo between oxidic and sulfidic species in aqueous solution: Geochimica et Cosmochimica Acta, v. 69, p. 2981-2993.

Wasylenki, L. E., Rolfe, B. A., Weeks, C. L., Spiro, T. G. and Anbar, A. D., 2008, Experimental investigation of the effects of temperature and ionic strength on Mo isotope fractionation during adsorption to manganese oxides: Geochimica et Cosmochimica Acta, v. 72, p. 5997-6005.

Zillén, L., Conley, D. J., Andrén, T., Andrén, E. and Björck, S., 2008, Past occurrences of hypoxia in the Baltic Sea and the role of climate variability, environmental change and human impact: Earth-Science Reviews, v. 91, p. 77-92.

SUPPLEMENTARY MATERIALS

Table S1. Geochemical data from Little Belt (M0059).

depth (mbsf)	TOC (wt.%)	Al (ppm)	Mn (ppm)	Fe (ppm)	Mo (ppm)
1.10		47959.29	1289.59	33623.15	3.29
2.60	6.96				
4.45	6.84	44409.00	2556.51	30483.24	5.05
5.90	7.75	41656.24	2851.26	31168.40	4.24
6.52	7.60	46193.31	3333.72	32523.27	7.12
7.40	7.28	48288.18	1249.47	34560.92	8.94
7.70	7.66	39449.84	979.56	27706.90	13.64
9.15	7.76	45290.29	1863.92	30177.96	10.16
10.80	6.48	42766.66	1013.72	30228.76	6.32
11.15	6.44	48623.74	2229.18	35161.69	8.65
12.35	5.43	55942.45	4916.98	38296.24	20.71
12.55	5.79	49914.07	6247.33	33804.06	5.38
14.15	6.27	40703.70	2293.08	26321.42	6.78
14.40	5.82	48982.84	1720.16	32392.49	6.04
15.65	6.27	41653.84	2517.17	28603.73	9.37
15.90	6.58	54987.08	3943.77	32215.63	8.28
17.35	6.27	45716.32	5371.40	31822.80	8.80
17.75	6.40				
18.95	6.19	49860.65	6408.90	31486.23	9.79
19.20	6.03	49802.77	6581.13	32996.49	8.00
20.75	5.80	50981.49	9240.04	32632.44	3.26
21.00	5.81	50429.63	11657.01	37780.46	2.42
22.20	5.47	50336.89	3445.58	31526.69	1.81
22.50	5.90	53080.13	8310.03	35875.15	5.81
24.00	5.85	53257.01	2430.93	33497.64	2.52
24.85	5.19	54216.17	7263.34	35718.57	3.90
27.30	5.58	55971.37	12747.21	35751.12	2.62
28.10	5.46	53535.88	9107.33	33868.43	6.49
30.60	5.23	51408.13	4846.30	32198.05	3.40
31.90	5.39	54216.05	6042.93	32521.04	3.44
32.00	4.62	52069.18	6169.94	33887.99	3.37
33.52	4.96	54034.78	14584.79	34407.87	3.29
34.35	4.67	45750.35	11410.38	29582.62	2.48
34.65	5.23	62249.79	14304.71	41388.67	5.24

depth (mbsf)	TOC (wt.%)	Al (ppm)	Mn (ppm)	Fe (ppm)	Mo (ppm)
37.70		52771.68	9438.48	33215.33	5.52
37.95	4.77	50778.87	8323.27	44397.24	10.50
40.50		57209.68	5865.22	35711.99	7.74
40.55	4.09	46547.32	9766.23	30009.77	6.84
41.30	4.27	61378.97	4552.60	35912.37	30.85
43.89	4.26	54093.26	9026.74	37268.88	9.04
44.60	4.93	48077.14	14993.38	33265.65	3.23
46.20	4.78				
46.80	5.00	56786.57	6673.64	37279.39	3.43
47.46	5.03	58320.75	10699.65	39326.81	3.21
47.90		59320.01	3425.51	40998.53	2.91
48.90	6.18	55157.98	2726.19	37120.06	10.56
50.37	5.14	59361.33	2427.38	38764.84	0.53
51.20	4.63	59725.95	1711.14	34954.14	0.46
51.82	3.75	49396.64	1692.40	29409.94	0.46
53.81	0.64	55789.66	725.08	29363.64	0.54
54.05	0.78	57579.06	617.62	30415.63	0.43
54.50	0.73	53769.29	722.59	31255.50	0.89
56.15	0.59	19077.95	241.91	10046.80	0.17
57.79	0.57	57511.82	685.78	32938.75	0.47
61.10	0.52	58407.84	654.48	28800.82	0.48
63.80	0.58	63190.61	770.84	33822.54	0.52
64.40		64682.75	616.57	35580.80	0.43
66.45		86562.69	572.51	49064.75	0.47
71.57		60068.90	669.76	32103.89	0.49
73.37		68474.66	600.30	38462.36	0.43
73.66	0.54	51385.54	672.43	25015.75	0.49
74.35	0.73	72601.05	651.28	38372.87	0.38
77.55	0.71	52297.43	749.17	25199.21	0.53
77.72	0.43	45813.78	636.62	21189.17	1.01
81.07		46418.59	623.21	20862.90	0.60

Table S2. Geochemical data from Bornholm Basin (M0065).

depth (mbsf)	TOC (wt.%)	Total S (wt.%)	Fe_{dith} (ppm)	Fe_{NaAc} (ppm)	Fe_{asc} (ppm)	Fe_{ox} (ppm)	Fe_{py} (ppm)	Fe_{AVS} (ppm)	Al (ppm)	Mn (ppm)	Fe (ppm)	Mo (ppm)
2.25	4.19	1.34	100.81	235.92	301.87	920.57	11550.18		72912.99	948.97	44083.69	8.11
2.82	3.91	1.39	71.55	418.30	320.16	873.26	10677.93		74503.18	1362.50	44962.48	5.36
3.15	4.13	1.54	160.62	227.91	10.09	512.13	7214.97	4.61	98383.87	572.30	55740.80	0.75
3.34	4.55	1.48	72.30	465.83	310.74	869.87	10518.79		74066.66	1294.19	43952.43	5.51
3.85	4.62	1.52	78.45	499.38	392.75	780.26	8525.60		73132.54	1185.04	44493.14	6.68
4.25	5.01	1.76	124.68	574.32	504.79	871.09	10428.97		71853.15	1185.83	44518.80	4.48
4.46	5.37	2.22	259.87	504.94	284.01	761.10	16965.37		70723.94	1236.50	45841.84	8.91
4.65	6.62	2.50	319.06	977.81	1138.57	919.44	16794.71		67537.02	1282.79	46590.59	26.18
4.70	5.93	2.18	325.61	630.92	176.25	545.82	10745.40	6.29	69536.25	1019.65	45482.00	16.48
5.17	4.18	1.71	52.73	469.60	265.00	861.42	13067.73		80998.37	1531.84	51282.47	5.08
5.66	4.44	1.75	46.22	355.99	386.52	964.70	12452.38		73508.82	1273.90	45341.69	6.83
6.16	4.34	1.63	81.68	297.52	346.35	783.11	10695.34		74792.01	1416.76	46903.86	2.72
6.54	4.08	1.64	107.29	391.99	308.00	756.20	11323.75		79449.06	1509.32	48515.23	6.58
6.55	4.17	1.70	193.05	234.47	84.79	302.03	13613.05	6.14	78493.70	3535.29	49106.08	4.82
7.14	3.55	1.41	85.14	259.87	417.83	1077.23	12815.84		76570.28	2187.72	46730.05	10.60
7.66	3.73	1.23	479.14	848.42	822.33	1272.52	10150.50		74515.04	4635.46	45140.99	7.69
7.98	3.21	1.37	377.15	1112.93	868.23	1471.12	10085.23		62709.13	6855.06	39187.03	3.60
8.00			301.56	605.70	264.81	1067.62	8248.82	5.05	83777.36	2809.00	54188.09	5.62
8.10	3.51	0.88	1522.89	6770.69	3453.19	2019.05	5704.17		75490.04	5613.53	45411.72	5.10
8.49	3.31	1.46	506.08	1256.82	1008.26	1502.62	8099.88		70928.04	8771.60	45908.84	7.33
8.98	3.48	1.64	362.87	1074.48	902.18	1165.53	11646.62		81709.21	1719.05	52791.75	8.95
9.38	4.17	4.02	363.76	2286.95	1363.10	1388.60	19115.65		69323.95	9013.85	62216.02	10.31
9.80	2.11	2.97	247.80	1445.91	626.04	1559.65	32241.71	11.21	75119.47	737.40	58441.98	0.66
9.85	2.25	3.14	1960.12	4558.86	1767.28	3436.47	15690.04		76211.46	718.18	65849.42	0.61
10.37	1.79	0.11	1555.29	3506.70	1483.21	3670.91	537.82		82994.98	665.44	48823.54	0.58

depth (mbsf)	TOC (wt.%)	Total S (wt.%)	Fe_{dith} (ppm)	Fe_{NaAc} (ppm)	Fe_{asc} (ppm)	Fe_{ox} (ppm)	Fe_{py} (ppm)	Fe_{AVS} (ppm)	Al (ppm)	Mn (ppm)	Fe (ppm)	Mo (ppm)
10.84		0.13	1977.42	4206.47	1475.69	4196.08	800.60		71881.05	728.01	42348.59	0.94
11.20	1.20	0.00	389.06	2709.00	702.47	5413.11	136.81	5.29	94559.68	678.06	55698.28	1.41
11.26	1.36	0.08	1875.26	4934.53	2828.26	4830.12	554.92		85269.04	1291.31	51033.08	1.24
11.28	1.61	0.01	1577.80	5644.51	1447.94	4112.23	181.02		82064.38	801.97	50584.07	0.81
11.81	1.24	0.04	1687.82	4376.16	1615.56	4425.82	210.83		95165.93	982.84	56000.59	1.11
12.32	0.74	0.18	1523.36	5907.70	2643.30	4034.98	372.70		84699.22	1081.12	48053.56	0.94
12.40	0.53	0.00	1733.84	4822.92	1392.96	6431.51	523.13		94040.82	1188.01	56026.15	0.83
12.79	0.46	0.00	1723.53	6786.34	913.69	6219.82	132.36		84230.15	888.19	51570.48	0.54
13.15	0.44	0.07	242.49	1909.16	404.65	3680.56	326.23	6.07	78976.10	1047.09	46416.06	0.53
13.21	0.34	0.00	1267.58	2184.45	1032.39	4736.24	91.54		87163.06	933.39	57177.92	1.24
13.55	0.34	0.02	2175.64	1858.50	405.57	6201.16	1744.27		86745.24	1221.70	52794.00	0.34
13.94	0.32	0.00	2005.08	576.95	314.62	3766.13	233.27		89240.61	1944.49	57607.21	0.40
14.55	0.41	0.04	1831.57	633.42	223.70	4363.92	914.19	7.11	95945.35	816.62	47482.11	0.38
15.02	1.03	0.02	2639.81	1340.17	290.16	2250.81	302.50		86186.72	973.70	52331.79	1.05
15.47	0.52	0.02	3056.67	1820.17	447.14	3130.01	95.83		85280.06	657.37	51836.40	1.03
15.71	0.37	0.02	5454.06	607.66	635.18	3684.49	215.51		84596.60	712.74	51186.92	1.06
15.93	0.25	0.00	3729.70	1918.62	301.30	3368.90	285.40		96426.77	706.32	58828.26	1.03
16.12	0.59	0.01	2119.68	1419.80	566.74	2636.58	281.37		78926.27	641.51	44753.41	1.03
16.45	0.65	0.06	438.12	729.24	351.39	2986.60	323.73	5.09	96784.30	518.11	52341.97	0.88
17.95	0.57	0.05	382.13	764.10	572.04	2601.69	214.69	6.94	73861.83	1023.26	45007.91	0.62
19.50	0.55	0.00	4188.90	944.34	549.54	3003.06	329.65		78002.11	933.98	42183.45	0.00
19.70	0.48	0.02	779.69	593.99	385.66	2964.14	233.54	5.40	94825.84	528.36	48595.88	0.86
21.25	0.46	0.00	837.64	518.46	245.89	2814.91	139.35	4.04	98375.06	474.60	54606.66	0.71
23.55	0.01	0.00	379.62	336.37	169.16	1241.13	542.80	3.37	93392.10	595.74	50687.38	0.91
27.20	0.69	0.05	713.34	373.44	215.50	2979.03	683.92	3.23	87549.67	549.89	46441.18	0.72
31.05	0.57	0.03	560.60	435.66	160.54	2696.98	272.95	3.69	91870.83	576.23	54790.74	0.71

depth (mbsf)	TOC (wt.%)	Total S (wt.%)	Fe_{dith} (ppm)	Fe_{NaAc} (ppm)	Fe_{asc} (ppm)	Fe_{ox} (ppm)	Fe_{py} (ppm)	Fe_{AVS} (ppm)	Al (ppm)	Mn (ppm)	Fe (ppm)	Mo (ppm)
33.55	0.52	0.00	628.03	361.50	202.12	2432.10	298.19	6.05	90612.75	534.57	49885.42	0.63
37.05	0.45	0.11	210.05	581.79	133.97	779.13	299.14	3.18	85223.36	725.62	43342.98	0.50

Table S3. Molybdenum isotope values from Little Belt and Bornholm Basin.

Site	*mbsf*	δ^{98}Mo (SRM 3134) (‰)	1 sigma
M0059	1.1	0.96	0.03
M0059	4.45	1.41	0.04
M0059	6.52	0.60	0.03
M0059	7.7	0.88	0.03
M0059	9.15	1.02	0.04
M0059	10.8	1.47	0.03
M0059	11.15	0.85	0.03
M0059	17.35	0.18	0.04
M0059	18.95	0.54	0.04
M0059	37.95	0.96	0.04
M0059	40.5	0.89	0.03
M0059	41.3	0.63	0.03
M0059	43.89	0.43	0.03
M0059	44.6	0.68	0.03
M0059	46.8	0.86	0.03
M0059	47.46	0.70	0.03
M0059	48.9	0.22	0.02
M0065	2.25	-0.05	0.03
M0065	3.85	0.52	0.03
M0065	4.46	0.56	0.03
M0065	4.65	0.86	0.04
M0065	4.7	1.04	0.03
M0065	5.66	0.50	0.03
M0065	6.16	0.90	0.03
M0065	6.54	0.50	0.02
M0065	7.14	0.32	0.03
M0065	7.66	0.20	0.03
M0065	7.98	0.03	0.03
M0065	8	0.46	0.04
M0065	8.49	0.02	0.03
M0065	8.98	0.21	0.03
M0065	9.38	-0.29	0.03
M0065	17.95	-0.16	0.03

FINAL REMARKS AND SYNTHESIS

The foundation of this work was inspired by two simple observations: **(1)** The low oxygen marine systems most prominent today are characterized by the cycling of redox sensitive elements such as manganese, iodine, and nitrogen — which occurs within systems of extreme low but present oxygen. In spite of this, the best calibrated, and hence most commonly applied, paleoredox proxies are based on the cycling of iron and sulfur and associated geochemical cycles, which in the modern ocean occurs only in extreme settings like the persistently euxinic Black Sea. **(2)** In the midst of a growing understanding of the chemical composition — specifically oxygen and associated redox-sensitive elements — of the atmosphere and oceans through the Precambrian, no record of surface ocean redox conditions existed. This is despite that the Precambrian surface ocean hosted both the evolution of oxygenic photosynthesis prior to widespread atmosphere and deep ocean oxygenation as well as the first eukaryotes and animals.

Prior to this work, a widely held view was that Precambrian surface ocean redox conditions were in equilibrium with the atmosphere and therefore mimicked temporal atmospheric oxygen concentrations and trends. In the preceding chapters, I have exposed that such a view is oversimplified and outlined a means for assessing the distribution of shallow ocean redox conditions through time using iodine in carbonate. The new view of the Precambrian surface ocean is that oxygen concentrations and the depth of the oxycline varied dramatically within a dominantly anoxic ocean starting in the Paleoproterozoic through the end-Proterozoic. Absolute surface ocean oxygen concentrations were likely above that necessary to sustain animals, but I emphasize that

this instability in oxygen concentrations should be considered prominently in the debate regarding potential redox controls on the emergence of animal life. The middle Proterozoic, the time period preceding the first evidence for animals, shows the greatest evidence for such instability. Future work should focus on determining the exact oxygen concentrations necessary to sustain an aerobic iodine cycle in the modern ocean, building on the modern water column observations discussed here and placing more quantitative constraints on the dynamics in past surface ocean oxygen levels from this work. Beyond the Precambrian surface ocean — as conditions promoting iodine redox cycling are best representative of modern low oxygen systems — the calibration of the iodine proxy within this dissertation provides a metric for comparing modern and past low oxygen systems within a relevant modern framework.

Another product of the iodine work is that the redox sensitivity of iodine and exclusive association of the oxidized iodine species in carbonates makes the proxy particularly well suited for examining carbon diagenetic history of carbonate and origins of associated geochemistry (e.g $\delta^{13}C_{carb}$). This dissertation demonstrates this utility in modern-recent carbonate and provides evidence that even in ancient carbonate where modern analogues are few — specifically Proterozoic dolomite and carbonate associated with the extreme negative Shuram $\delta^{13}C_{carb}$ excursion — that the seawater versus pore water origins of geochemical signals from carbonatse can be assessed.

Further, this work presents the most detailed constraints on natural water column spatiotemporal redox conditions in the Baltic Sea over the Holocene relative to the

current anthropogenic-induced anoxic era — aided through extensive cores and detailed sample taking during participation in IODP Expedition 347. I demonstrate — using sediments from modern reducing basins Landsort Deep and Bornholm Basin — that the Baltic Sea has been more reducing in the past than it is today. Importantly, however, past Baltic redox regimes have never experienced stable euxinia with elevated water column sulfide concentrations approaching that observed in the modern Black Sea. Within the Baltic today, the stability and degree of anoxia varies within individual sub-basins according to distance from the sill. I also demonstrate that this has been true for past anoxic periods, with redox regimes ranging from euxinia with low sulfide concentrations and residence times, seasonal-episodical euxinia, ferruginous waters, and low but present oxygen. This was achieved using a unique combination of Fe-Mn-Mo geochemistry and the outlined approach represents a way forward in inferring paleoredox regimes relevant to that more typical of low oxygen systems today.